





This is to certify that the

dissertation entitled

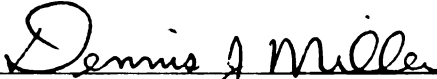
HYDROGEN INHIBITION IN
STEAM GASIFICATION OF
ANNEALED SARAN CHAR

presented by

Michael Gerard Lussier Jr.

has been accepted towards fulfillment
of the requirements for

Ph.D. degree in Chemical Engineering


Major professor

Date 10/29/98

**LIBRARY
Michigan State
University**

PLACE IN RETURN BOX to remove this checkout from your record.
TO AVOID FINES return on or before date due.
MAY BE RECALLED with earlier due date if requested.

DATE DUE	DATE DUE	DATE DUE
JUN 18 2001 JUN 20 01		

HYDROGEN INHIBITION IN STEAM GASIFICATION OF ANNEALED SARAN CHAR

by

Michael Gerard Lussier Jr.

A DISSERTATION

Submitted to
Michigan State University
in partial fulfillment of the requirements
for the degree of

DOCTOR OF PHILOSOPHY

Department of Chemical Engineering

1998

ABSTRACT

HYDROGEN INHIBITION IN STEAM GASIFICATION OF ANNEALED SARAN CHAR

by

Michael Gerard Lussier Jr.

Annealed Saran and coal chars were gasified in mixtures of $\text{H}_2\text{O}/\text{H}_2/\text{Ar}$ at 1123 K and varying pressures to varying extents of conversion, followed by transient kinetic desorption and TPD to 1773 K, in order to characterize hydrogen adsorbed onto char surfaces during gasification and to identify the mode(s) of hydrogen inhibition at varying extents of char conversion. Adsorbed hydrogen concentration on annealed Saran char was found to be independent of reactant gas composition and pressure, to increase from an initial surface concentration of 3×10^{-5} to 1.5×10^{-3} $\text{mmolH}_2(\text{STP})/\text{m}^2$ over the first 1% conversion, and to increase very gradually after this. Gasification rate declines significantly over the initial 1% carbon conversion and is inhibited mainly by dissociative hydrogen adsorption over this range.

1912

1913

1914

1915

1916

1917

1918

1919

1920

1921

1922

1923

1924

1925

1926

1927

1928

1929

1930

1931

1932

1933

1934

1935

Linearized Langmuir-Hinshellwood type rate expressions based on the three primary modes of hydrogen inhibition have been developed for all gasification data above 1% char conversion. The expression which indicates reverse oxygen exchange or "associative" hydrogen adsorption fits the data well, while the expression for dissociative hydrogen adsorption does not. Calculation of the equilibrium constant for oxygen exchange ($k_1/k_{-1}=0.029$) indicates a low fractional coverage of adsorbed oxygen complexes ($C(O)$), while the equilibrium constant for "associative" hydrogen adsorption ($k_3/k_{-3}=425 \text{ MPa}^{-1}$) stipulates a high fractional coverage of "associatively" adsorbed hydrogen. Because no "associatively" bound hydrogen was detected and because low concentrations of surface oxides were found during gasification, it is concluded that reverse oxygen exchange is the primary mode of hydrogen inhibition past 1% char conversion for Saran char. Active site propagation along graphitic zig-zag edges is proposed as the main source of surface carbon consumption for steady-state char gasification in steam.

I dedicate my PhD. Dissertation to my parents Michael and Roseann Lussier and my sister Amy Lussier, and to Jennifer Durst.

1. A
2. B
3. C
4. D
5. E
6. F
7. G
8. H
9. I
10. J
11. K
12. L
13. M
14. N
15. O
16. P
17. Q
18. R
19. S
20. T
21. U
22. V
23. W
24. X
25. Y
26. Z

ACKNOWLEDGEMENTS

I would like to thank my graduate advisor and project principal investigator, Dr. Dennis J. Miller, for his patience and high degree of involvement in my Doctorate research and dissertation work. Dr. Lawrence T. Drzal, Dr. Martin C. Hawley, Dr. Thomas J. Pinnavaia, and Dr. Robert E. Buxbaum must also be thanked for accepting the task of being my committee members.

I give thanks to Zhigang Zhang for all of his effort on the char gasification project, including work on TPD, nitrogen adsorption, unannealed char gasification, and data deconvolution programs. Thanks must also go to Radu Craciun for his help with using the X-ray diffractometer.

Julie Caywood, Faith Peterson, and Candice McMaster must all be thanked for their exceptional secretarial support, as well as Rob Selden for fabricating several intricate components of the experimental apparatus used in this investigation.

Finally, I would like to thank the United States Department of Energy for their financial support through grant #DE-FG22-93PC93213.

117 79

118 80

119 81

120 82

121 83

122 84

123 85

124 86

125 87

126 88

127 89

128 90

129 91

130 92

131 93

132 94

133 95

134 96

135 97

TABLE OF CONTENTS

LIST OF TABLES	xiii
LIST OF FIGURES	xiv
LIST OF NOMENCLATURE	xxi
Chapter 1. Introduction	1
1.1. Background	1
1.2. Literature Review	3
1.2.1. Hydrogen Chemisorption on Carbon	3
1.2.2. Hydrogasification of Chars	3
1.2.2.1. General Reaction Phenomena	3
1.2.2.2. Role of Oxygen	5
1.2.2.3. Structural Effects	5
1.2.3. Steam Gasification of Chars	7
1.2.3.1. General Reaction Phenomena	7
1.2.3.2. Role of Oxygen	9
1.2.3.3. Hydrogen Inhibition	12
1.2.4. Isotopic Studies	13
1.3. Previous Research in Our Laboratory	14
1.4. Research Objectives	19

1.4.1. Mechanism Identification	20
1.4.2. Isotope Effects	23
Chapter 2. Experimental	26
2.1. Starting Materials	27
2.1.1. Chars	27
2.1.2. Reactant Gases	28
2.2. Experimental Apparatus	29
2.2.1. High Pressure Reactor	29
2.2.1.1. Internal Microreactor	29
2.2.1.2. Flange Modifications	31
2.2.2. Flow Control and Mixing System	34
2.2.2.1. Gas Blending/Rapid Switching System	35
2.2.2.2. Low Dead Volume Steam Trap	36
2.2.3. High Temperature Reactor	38
2.2.4 Mass Spectrometer	38
2.3. Experimental Techniques	40
2.3.1. Gasification	44
2.3.1.1. Gasification Conditions	44
2.3.1.2. Gasification Procedure	45
2.3.2. Temperature Programmed Desorption	47
2.3.2.1. TPD Conditions	47

1930

1931

1932

203

203

203

203

203

203

203.0

204.0

204.1

204.2

204.3

204.3

204.3

204.3

204.3

204.3

204.3

204.3

204.3

2.3.2.2. TPD Procedure	48
2.3.3. Gas Detection and Calculation of Effluent Rates	49
2.3.3.1. Mass Spectrometer Calibration	50
2.3.3.1.1. Variation of Pressure at Capillary Inlet	51
2.3.3.1.2. Linearity of Response	56
2.3.3.1.3. Response as a Function of Time	56
2.3.3.1.4. Response as a Function of Carrier Gas Composition	59
2.3.3.1.5. Fragmentation Investigation	62
2.3.3.1.6. CD ₄ /CH ₄ Response Ratios	62
2.3.3.2. Mass Spectrometer Data Deconvolution	64
2.3.4. Char Characterization	66
2.3.4.1. Mercury Intrusion	67
2.3.4.2. Nitrogen Adsorption	67
2.3.4.3. X-ray Diffraction	68
Chapter 3. Gasification Experiments	69
3.1. Determination of Appropriate Gasification Temperature	70
3.2. Char Gasification in Steam	72
3.2.1. Evolution of Char Surface Area	72
3.2.2. Rate Dependence on Pressure, Composition, and Conversion	74
3.2.2.1. Annealed Char Steam Gasification	76
3.2.2.1.1. Annealed Saran Char Steam Gasification	76

1

3.2.2.1.2. Annealed Coal Char Gasification	101
3.2.2.2. Unannealed Char Steam Gasification	105
3.2.3. Isotopic Studies	108
3.3. Adsorbed Hydrogen Concentration	108
3.3.1. Transient Hydrogen Desorption	108
3.3.2. Adsorbed Hydrogen: Unit Weight Basis	110
3.3.3. Adsorbed Hydrogen: Unit Area Basis	118
Chapter 4. Model Fitting - Linear Regression Analysis	120
4.1. Char Gasification in Steam	122
4.1.1. Reverse Oxygen Exchange	123
4.1.1.1. Reverse Oxygen Exchange	123
4.1.1.2. Rapid Equilibrium Reverse Oxygen Exchange	127
4.1.2. "Associative" Hydrogen Adsorption	128
4.1.2.1. "Associative" Hydrogen Adsorption Only	131
4.1.2.2. "Associative" Hydrogen Adsorption and Reverse Oxygen Exchange	132
4.1.3. Dissociative Hydrogen Adsorption	138
4.1.3.1. Dissociative Hydrogen Adsorption Only	138
4.1.3.2. Dissociative Hydrogen Adsorption and Reverse Oxygen Exchange	142
4.2. Comparison of Hydrogen Inhibition Models	146
4.2.1. Linear Regression Parameters	146

40
41
42
43
44
45
46
47
48
49
50
51
52
53
54
55
56
57
58
59
60
61
62
63
64
65
66
67
68
69
70
71
72
73
74
75
76
77
78
79
80
81
82
83
84
85
86
87
88
89
90
91
92
93
94
95
96
97
98
99
100

4.2.2. Calculated Rate Constants	149
4.2.3. Theoretical Rate Curves	153
4.3. Methane Formation Only	160
Chapter 5. Char Properties During Gasification	162
5.1. Hydrogen Adsorption	162
5.1.1. Initial Rapid Adsorption	163
5.1.2. Gradual Adsorption over Time	165
5.2. Char Structure	165
5.2.1. Total Surface Area and Pore Structure	166
5.2.2. Domain Sizes via H/C Atom Ratio	167
5.2.3. X-ray Analysis	168
5.2.4. Char Morphology	175
5.2.5. Char Active Sites	177
5.2.5.1. Etch Pit Analysis	178
5.2.5.2. Active Site Propagation	181
5.2.5.3. Active Site Behavior with Conversion	184
5.2.5.4. Comparison to the "Universal" Mechanism	188
5.3. Rate Enhancement	189
5.3.1. Partial Combustion	190
5.3.2. Catalysis	191
Chapter 6. Conclusions/Recommendations	193

6.1. Char Gasification Mechanism Identification	193
6.2. Char Structure During Gasification	195
6.3. Recommendations	198
Appendices	200
A-1. Linearized Rate Expression for Dissociative Hydrogen Adsorption Including Explicit Adsorbed Hydrogen Term	202
A-2. Linearized Rate Expression for Reverse Oxygen Exchange and Dissociative Hydrogen Adsorption Including Explicit Adsorbed Hydrogen Term	203
B. Mass Spectrometer Controller Settings	204
C. Mass Spectrometer Data Deconvolution Programs	205
D. Annealed Saran Char Generalized Modulus Calculation	213
E-1. Linearized Rate Expression Derivation for Reverse Oxygen Exchange	217
E-2. Linearized Rate Expression Derivation for Rapid Equilibrium Reverse Oxygen Exchange	218
E-3. Linearized Rate Expression Derivation for “Associative” Hydrogen Adsorption	219
E-4. Linearized Rate Expression Derivation for “Associative” Hydrogen Adsorption and Reverse Oxygen Exchange	221
E-5. Linearized Rate Expression Derivation for Dissociative Hydrogen Adsorption	223
E-6. Linearized Rate Expression Derivation for Dissociative Hydrogen Adsorption and Reverse Oxygen Exchange	225
E-7. Linearized Rate Expression Derivation for Methane Formation Only - “Associative” Hydrogen Adsorption	227

E-8. Linearized Rate Expression Derivation for Methane Formation
Only - Dissociative Hydrogen Adsorption 228

References 229

231.

232.

233.

234.

235.

LIST OF TABLES

Table 1 - Char Ultimate Analysis	28
Table 2 - Number of Parameters in Various Kinetic Models of H ₂ O/H ₂ Gasification of Annealed Saran Char	146
Table 3 - Degrees of Freedom for Linear Regression of Various Kinetic Models of H ₂ O/H ₂ Gasification of Annealed Saran Char as a Function of Conversion	147
Table 4 - Regression Results for Linearized Rate Expressions	150
Table 5 - Comparison of Rate Constant Groups	152

Page 1 -

Page 2 -

Page 3 -

Page 4 -

Page 5 -

Page 6 -

Page 7 -

Page 8 -

Page 9 -

Page 10 -

Page 11 -

Page 12 -

Page 13 -

Page 14 -

Page 15 -

LIST OF FIGURES

Figure 1 - Various Edge Configurations on the Graphite Basal Plane . . .	6
Figure 2 - Edge Carbon Atoms Configurations of the Graphite Basal Plane	10
Figure 3 - Universal Gasification Mechanism Proposed by Chen, Yang, Kapteijn, and Moulijn [56]	11
Figure 4 - Hydrogasification Rate Curves for Saran Char	15
Figure 5 - Hydrogasification Rate Curves for Coal Char	16
Figure 6 - Hydrogasification Rate Curves for Chars Based on Total Surface Area	17
Figure 7 - Overall Experimental Apparatus	30
Figure 8 - High Pressure Vessel Internal Microreactor	32
Figure 9 - High Pressure Vessel Flange Modifications	33
Figure 10 - Low Dead Volume Steam Trap	37
Figure 11 - High Temperature Reactor	39
Figure 12 - Experimental Technique for Gasification and Subsequent Temperature Programmed Desorption of Chars	41
Figure 13 - High Pressure System Transient Response	43
Figure 14 - Vacuum Chamber Pressure vs. Capillary Inlet Pressure with Argon Purge Gas	52
Figure 15 - Background Partial Pressure of Various Masses vs. Vacuum Chamber Pressure (Argon)	54

Page 16

Page 17

Page 18

Page 19

Page 20

Page 21

Page 22

Page 23

Page 24

Page 25

Page 26

Page 27

Page 28

Page 29

Figure 16 - Background Partial Pressure of Various Masses vs. Vacuum Chamber Pressure (Ar/Kr)	55
Figure 17 - Linearity of Mass Spectrometer Response with Species Concentration	57
Figure 18 - Change in Mass Spectrometer Peak Heights over Five Hour Time Interval	58
Figure 19 - Partial Pressures of Carrier Gases in Vacuum Chamber vs. Carrier Gas Composition	60
Figure 20 - Partial Pressures of Key Components in Vacuum Chamber vs. Carrier Gas Composition	61
Figure 21 - Partial Pressure of CO ₂ and CO Fragments vs. Carrier Gas Composition and Inlet Percent CO ₂	63
Figure 22 - Arrhenius Plot of Annealed Saran Char Steam Gasification at 1.0 MPa	71
Figure 23 - Total Surface Area of Annealed Chars by Nitrogen Adsorption after Gasification in Steam at 1.0 MPa	73
Figure 24 - Equilibrium Composition of the Shift Reaction and Reactor Effluent Composition vs. Temperature	75
Figure 25 - Equilibrium Composition of the Methanation Reaction and Reactor Effluent Composition vs. Temperature	77
Figure 26 - CO + CO ₂ Evolution Rate from Several Runs of Annealed Saran Char Steam Gasification at 1.0 MPa in 40/0/60 H ₂ O/H ₂ /Ar	78
Figure 27 - CO + CO ₂ Evolution Rate from Annealed Saran Char Steam Gasification at 1.0 MPa in 40/0/60 H ₂ O/H ₂ /Ar; Several Runs at 2% Carbon Conversion	80
Figure 28 - CO + CO ₂ Evolution Rate from Annealed Saran Char Steam Gasification at 3.1 MPa	81

Page 3

Page 3

Page 3

Page 3

Page 3

Page 3

Page 3

Page 3

Page 3

Page 3

Page 3

Page 3

Page 3

Page 3

Figure 29 - CH ₄ Evolution Rate from Annealed Saran Char Steam Gasification at 3.1 MPa	82
Figure 30 - CO + CO ₂ Evolution Rate from Annealed Saran Char Steam Gasification at 1.0 MPa	83
Figure 31 - CH ₄ Evolution Rate from Annealed Saran Char Steam Gasification at 1.0 MPa	84
Figure 32 - CO + CO ₂ Evolution Rate from Annealed Saran Char Steam Gasification at 0.3 MPa	85
Figure 33 - CH ₄ Evolution Rate from Annealed Saran Char Steam Gasification at 0.3 MPa	86
Figure 34 - CO + CO ₂ Evolution Rate from Annealed Saran Char Steam Gasification	88
Figure 35 - CH ₄ Evolution Rate from Annealed Saran Char Steam Gasification	89
Figure 36 - CO + CO ₂ Evolution Rate from Annealed Saran Char Steam Gasification at 1.0 MPa with Cycled Reactant Gas Composition	91
Figure 37 - Quadratic Polynomial Least Squares Fit to Annealed Saran Char Total Surface Area Following Gasification in Steam	93
Figure 38 - Quadratic Polynomial Least Squares Fit to Annealed Coal Char Total Surface Area Following Gasification in Steam	94
Figure 39 - CO + CO ₂ Evolution Rate from Annealed Saran Char Steam Gasification at 1.0 MPa; Rate Per Unit Weight and Unit Surface Area Basis	95
Figure 40 - CH ₄ Evolution Rate from Annealed Saran Char Steam Gasification at 1.0 MPa; Rate Per Unit Weight and Unit Surface Area Basis	96

Figure 41

Figure 42

Figure 43

Figure 44

Figure 45

Figure 46

Figure 47

Figure 48

Figure 49

Figure 50

Figure 51

Figure 41 - CO + CO ₂ Evolution Rate from Annealed Saran Char Steam Gasification to Low Conversion; Rate Per Unit Weight and Unit Surface Area Basis	97
Figure 42 - CH ₄ Evolution Rate from Annealed Saran Char Steam Gasification to Low Conversion; Rate Per Unit Weight and Unit Surface Area Basis	98
Figure 43 - Evolution Rate from Annealed Saran Char Steam Gasification at 1.0 MPa; Rate Per Unit Weight and Unit Surface Area Basis	100
Figure 44 - Product Gas Evolution Rate from Annealed Coal Char Steam Gasification at 1.0 MPa	102
Figure 45 - CO + CO ₂ Evolution Rate from Annealed Coal Char Steam Gasification at 1.0 MPa; Unit Weight and Unit Surface Area Basis	103
Figure 46 - CH ₄ Evolution Rate from Annealed Coal Char Steam Gasification at 1.0 MPa; Unit Weight and Unit Surface Area Basis	104
Figure 47 - Product Gas Evolution Rate from Unannealed Saran Char Steam Gasification at 1000 K and 3.1 MPa	106
Figure 48 - Product Gas Evolution Rate from Unannealed Coal Char Steam Gasification at 1000 K and 3.1 MPa	107
Figure 49 - CO + CO ₂ Evolution Rate from Annealed Saran Char H ₂ O or D ₂ O Gasification at 3.1 MPa	109
Figure 50 - Step Change in Feed Gas Composition During Annealed Saran Char D ₂ O Gasification	111
Figure 51 - Temperature Programmed Desorption Profile of Hydrogen from Annealed Saran Char Following Gasification in Steam at 1123 K	112

Page 6

Page 6

Page 6

Page 6

Page 6

Page 6

Page 6

Page 6

Page 6

Page 6

Figure 52 - Hydrogen TPD Profile of Annealed Saran Char Following Hydrogasification at 3.1 MPa and Cooling in Argon or Hydrogen	114
Figure 53 - Adsorbed Hydrogen Concentration from Annealed Chars Following Gasification in Steam at 1123 K	115
Figure 54 - Product Gas Evolution Rate and Adsorbed Hydrogen Concentration from Annealed Saran Char Steam Gasification at Low Conversion	117
Figure 55 - Adsorbed Hydrogen Concentration on Surface Area Basis from Annealed Chars Following Steam Gasification at 1123 K	119
Figure 56 - Correlation Coefficient for Linear Regression of Annealed Saran Char Steam Gasification - Reverse Oxygen Exchange (ROE)	125
Figure 57 - F Statistic for Linear Regression of Annealed Saran Char Steam Gasification - Reverse Oxygen Exchange (ROE)	126
Figure 58 - Correlation Coefficient for Linear Regression of Annealed Saran Char Steam Gasification - ROE, and Rapid Reverse Oxygen Exch. (R-ROE)	129
Figure 59 - F Statistic for Linear Regression of Annealed Saran Char Steam Gasification - ROE, and Rapid Reverse Oxygen Exch. (R-ROE)	130
Figure 60 - Correlation Coefficient for Linear Regression of Annealed Saran Char Steam Gasification - "Associative" Hydrogen Adsorption (AHA)	133
Figure 61 - F Statistic for Linear Regression of Annealed Saran Char Steam Gasification - "Associative" Hydrogen Adsorption (AHA)	134

Page 62 -

Page 63 -

Page 64 -

Page 65 -

Page 66 -

Page 67 -

Page 68 -

Page 69 -

Page 70 -

Page 71 -

Page 72 -

Page 73 -

Figure 62 - Correlation Coefficient for Linear Regression of Annealed Saran Char Steam Gasification - ROE, AHA, and ROE + AHA	136
Figure 63 - F Statistic for Linear Regression of Annealed Saran Char Steam Gasification - ROE, AHA, and ROE + AHA . . .	137
Figure 64 - Correlation Coefficient for Linear Regression of Annealed Saran Char Steam Gasification - Dissociative Hydrogen Ads. (DHA), and ROE	140
Figure 65 - F Statistic for Linear Regression of Annealed Saran Char Steam Gasification - Dissociative Hydrogen Ads. (DHA), and ROE	141
Figure 66 - Correlation Coefficient for Linear Regression of Annealed Saran Char Steam Gasification - ROE, AHA, and ROE + DHA	144
Figure 67 - F Statistic for Linear Regression of Annealed Saran Char Steam Gasification - ROE, AHA, and ROE + DHA . . .	145
Figure 68 - CO + CO ₂ Evolution Rate from Annealed Saran Char Steam Gasification at 3.1 MPa and "n=1" Model	154
Figure 69 - CO + CO ₂ Evolution Rate from Annealed Saran Char Steam Gasification at 1.0 MPa and "n=1" Model	155
Figure 70 - CO + CO ₂ Evolution Rate from Annealed Saran Char Steam Gasification at 0.3 MPa and "n=1" Model	156
Figure 71 - CO + CO ₂ Evolution Rate from Annealed Saran Char Steam Gasification at 3.1 MPa and "n=0.5" Model	157
Figure 72 - CO + CO ₂ Evolution Rate from Annealed Saran Char Steam Gasification at 1.0 MPa and "n=0.5" Model	158
Figure 73 - CO + CO ₂ Evolution Rate from Annealed Saran Char Steam Gasification at 0.3 MPa and "n=0.5" Model	159

Figure 74

Figure 75

Figure 76

Figure 77

Figure 78

Figure 79

Figure 80

Figure 81

Figure 82

Figure 83

Figure 84

1

Figure 74 - Dependence of Methane Formation Rate on Hydrogen Partial Pressure in Annealed Saran Char Steam Gasification	161
Figure 75 - X-ray Spectra of 360 mesh Ultra "F" Graphite	170
Figure 76 - X-ray Spectra of 325 mesh Alpha Graphite	171
Figure 77 - X-ray Spectra of -10+60 mesh Alpha Graphite	172
Figure 78 - X-ray Spectra of -60+100 mesh Annealed Saran Char . . .	173
Figure 79 - Magnified View of X-ray Spectra of -60+100 mesh Annealed Saran Char	174
Figure 80 - CH ₄ Evolution Rate from Saran Char Hydrogasification, Temperature at or Normalized to 1123 K via E _A =75 Kcal/mol	176
Figure 81 - Round and Hexagonal Etch Pits of the Graphite Basal Plane	180
Figure 82 - Active Site Propagation along Graphite Zig-Zag Edge . .	183
Figure 83 - Active Site Propagation along Graphite Armchair Edge . .	185
Figure 84 - Round Etch Pit and Crystallite Converting to Hexagonal Features with Zig-Zag Edges	187



1
2
3
4
5
6
7
8
9
10
11
12
13
14
15
16
17
18
19
20
21
22
23
24
25
26
27
28
29
30
31
32
33
34
35
36
37
38
39
40
41
42
43
44
45
46
47
48
49
50
51
52
53
54
55
56
57
58
59
60
61
62
63
64
65
66
67
68
69
70
71
72
73
74
75
76
77
78
79
80
81
82
83
84
85
86
87
88
89
90
91
92
93
94
95
96
97
98
99
100

LIST OF NOMENCLATURE

C_F	=	"Free" Active Site Surface Concentration
C_T	=	Total Active Site Surface Concentration
$C(H)$	=	Hydrogen Surface Concentration
$C(H)$	=	Dissociatively Bound Hydrogen Concentration
$C(H)_2$	=	"Associatively" Bound Hydrogen Concentration
$C(H)_i$	=	Initial Hydrogen Surface Concentration
$C(O)$	=	Oxygen Surface Concentration
d	=	Interlayer Spacing
E_0^D	=	Deuterium Zero-Point Energy
E_0^H	=	Hydrogen Zero-Point Energy
F_{STAT}	=	F-Statistic
h	=	Planck's Constant
k	=	Shape Factor
k_{-1}	=	Reverse Oxygen Exchange Forward Rate Constant
k_1	=	Oxygen Exchange Forward Rate Constant
k_2	=	Gasification Rate Constant
K_3	=	"Associative" Hydrogen Adsorption Equilibrium Constant
k_3	=	"Associative" Hydrogen Adsorption Forward Rate Constant
k_{-3}	=	"Associative" Hydrogen Adsorption Reverse Rate Constant
K_4	=	Dissociative Hydrogen Adsorption Equilibrium Constant
k_4	=	Dissociative Hydrogen Adsorption Forward Rate Constant
k_{-4}	=	Dissociative Hydrogen Adsorption Reverse Rate Constant
k_b	=	Boltzman's Constant
k_{OR}	=	Overall Steam Gasification Rate Constant
K_{SH}	=	Shift Reaction Equilibrium Constant
n	=	Positive Integer
P_{H_2}	=	Hydrogen Partial Pressure
P_w	=	Water Partial Pressure
Q_{rot}^d	=	Deuterium Rotational Partition Function
Q_{vib}^d	=	Deuterium Vibrational Partition Function
Q_{elec}^d	=	Deuterium Electric Partition Function
Q_{trans}^d	=	Deuterium Translational Partition Function
Q_{rot}^H	=	Hydrogen Rotational Partition Function
Q_{vib}^H	=	Hydrogen Vibrational Partition Function
Q_{elec}^H	=	Hydrogen Electric Partition Function

$Q_{\text{trans}}^{\text{H}}$	=	Hydrogen Translational Partition Function
R	=	Gas Constant
r^2	=	Linear Regression Coefficient of Correlation
r_{CH_4}	=	CH_4 Evolution Rate
r_{CO}	=	CO Evolution Rate
$r_{\text{CO},i}$	=	Initial CO Evolution Rate
r_{CO}^{H}	=	CO Evolution Rate in Hydrogen Containing Species
r_{CO}^{D}	=	CO Evolution Rate in Deuterium Containing Species
T	=	Temperature
t	=	Ordered Domain Size
TSA	=	Total Surface Area
x	=	Percent Carbon Conversion
β	=	Peak Full Width at Half Max
λ	=	X-ray Wavelength
μ	=	Reduced Mass
ν	=	Frequency
θ	=	X-ray Scatter Angle
θ_{B}	=	X-ray Peak Width at Half Max

11. B

Inc
ated Sta
rises
State det
the rec o
the ab an
the and

Chapter 1

INTRODUCTION

1.1. Background

Increasing demand for pipeline and transportation fuels in the United States, coupled with a dwindling world supply of these fuels, indicates that gasification of coal may be the most viable solution. Future demands on current natural gas supplies will deplete them far more rapidly than current coal supplies. Natural gas is superior to coal as an energy source because it is a pipeline and transportation fuel, and burns much cleaner than coal. Benefits of coal gasification

in steam include the facts that it is simple to carry out, water is cheap and plentiful, and the effluent gases can be converted into many other products traditionally derived from petroleum.

Gasification of coal is not currently used on a wide scale because extreme conditions are needed to achieve reaction rates that are reasonably fast. Hydrogen is known to strongly inhibit steam gasification rate. The process by which hydrogen inhibits gasification is not yet well characterized, but if it were there would be great potential for minimizing this phenomenon.

The main objective of this investigation is to characterize the concentration and stability of hydrogen on coal char and Saran char during steam gasification and relate this to hydrogen inhibition. Gasification rate under varying conditions will be incorporated into linearized rate expressions that are based on the possible mode(s) of hydrogen inhibition. Regression parameters and rate constants calculated for the different rate expressions will be compared to determine which mode(s) of hydrogen inhibition are correct.

1.2.

1.2.1

1.2.1.1

1.2.1.2

1.2.1.3

1.2.1.4

1.2.1.5

1.2.1.6

1.2.1.7

1.2.1.8

1.2.1.9

1.2.1.10

1.2.1.11

1.2.1.12

1.2.2

1.2.2.1

1.2.2.2

1.2. Literature Review

1.2.1. Hydrogen Chemisorption on Carbon

Hydrogen that has chemisorbed onto a carbon surface is very stable, and is generally accepted as dissociative in nature. Prolonged outgassing at 1300 K will not remove all dissociatively adsorbed hydrogen [1-8]; temperatures approaching 1800 K are required [1]. Dissociatively adsorbed hydrogen can saturate a graphite surface at 1373 K and 3 millitorr hydrogen [5], and has an equilibrium constant of $253 \text{ atm}^{-1/2}$ at 973 K [6]. This constant, however, can be strongly affected by impurities in the carbon which may act as hydrogen dissociation sites. Dissociatively bound hydrogen (C(H)) will form a peak starting at about 1200 K during temperature programmed desorption (TPD), while another peak can be observed at about 900-1100 K due to associatively bound hydrogen (C(H)₂) following exposure of carbon samples to gases containing hydrogen.

1.2.2. Hydrogasification of Chars

1.2.2.1. General Reaction Phenomena

Understanding methane formation by direct attack of carbon by molecular hydrogen is important because it occurs during steam

2013
2014
2015
2016
2017
2018
2019
2020
2021
2022
2023
2024
2025
2026
2027
2028
2029
2030
2031
2032
2033
2034
2035
2036
2037
2038
2039
2040
2041
2042
2043
2044
2045
2046
2047
2048
2049
2050
2051
2052
2053
2054
2055
2056
2057
2058
2059
2060
2061
2062
2063
2064
2065
2066
2067
2068
2069
2070
2071
2072
2073
2074
2075
2076
2077
2078
2079
2080
2081
2082
2083
2084
2085
2086
2087
2088
2089
2090
2091
2092
2093
2094
2095
2096
2097
2098
2099
2100

gasification of chars when hydrogen partial pressures are high [9].

Hydrogasification is also the first major step in the HYDROCARB process, which results in very pure fuel grade carbon black [10,11].

Kinetic studies by Blackwood et al. [12-16] have shown that hydrogasification is first order in hydrogen partial pressure, and is not a strong function of char type [12,17,18]. Several researchers performing mechanistic studies have suggested successive dissociative hydrogen chemisorption onto adjacent carbon atoms [19,20], with the cleavage of the bond between adjacent carbons being the rate limiting step [21]. Several others have suggested associative hydrogen chemisorption of two hydrogen molecules onto the same carbon atom [8,22,23], with the cleavage of carbon-carbon bonds also being rate limiting [22].

The rate of this reaction decreases rapidly with conversion when char samples are uncatalyzed [13,15,23-29]. Several two-stage reactions have been proposed to explain this phenomenon, most of which include initial rapid methanation of highly reactive surface carbon followed by slow reaction of the highly aromatic char base structure. Blackwood et al. [17] identify the reactive carbon, or "secondary" carbon, as amorphous and already partially enriched with hydrogen, and/or adjacent to oxygen functional groups [30]. Heating rate, final temperature, and

Page 99

Page 100

2.2.2

Page 101

Page 102

Page 103

Page 104

Page 105

Page 106

Page 107

Page 108

Page 109

Page 110

2.2.3

Page 111

Page 112

Page 113

Page 114

Page 115

Page 116

Page 117

purge gas composition during char preparation, as well as storage methods, largely determine the nature of these reactive surface carbons.

1.2.2.2. Role of Oxygen

It is generally believed that the major source of active sites in all uncatalyzed char gasification reactions comes from the desorption of oxygen functional groups from the char surface. These groups desorb in the form of carbon monoxide and carbon dioxide when samples are heated to reaction temperatures [15,31-38], and in the form of water during hydrogasification [15]. Hydrogasification rate has been shown to be a strong function of the oxygen content of various chars [12,15,39], and initial rate a strong function of oxygen surface concentration [36,40]. Hydrogasification rate can be increased by an order of magnitude by addition of 0.1% oxygen to the reactant gas [41].

1.2.2.3. Structural Effects

Initial gasification of highly reactive carbon is not the only reason why uncatalyzed rate decreases so dramatically with conversion. Figure 1 shows the various configurations of carbon atoms on the graphite basal plane. A strong preference for reaction of hydrogen with edge carbon atoms, as opposed to basal plane carbon atoms, has been shown [42]. Further probing into the reactivity of edge carbon atoms by

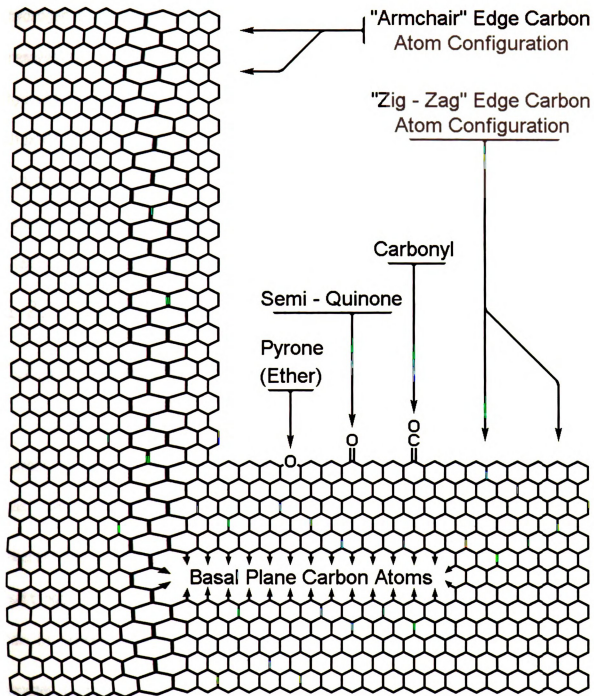


Figure 1: Various carbon atom configurations and oxygen functional groups of the graphite basal plane.

00000

00000

00000

00000

00000

00000

00000

00000

00000

1.2.3

1.2.3

00000

00000

00000

00000

00000

00000

00000

00000

00000

00000

00000

00000

etch pit analysis of graphite by Yang et al. [6,21,43,44] shows that hydrogen binds more strongly to the "zig-zag" edge carbon atoms and removes the "armchair" edge carbon atoms more easily in hydrogasification and steam gasification, while oxygen and carbon dioxide show no edge preference in gasification [6,43]. Therefore, as hydrogasification or gasification in steam proceeds, the more highly reactive armchair edge carbon atoms are consumed, leaving the more stable zig-zag edge carbon atoms.

1.2.3. Steam Gasification of Chars

1.2.3.1. General Reaction Phenomena

Steam gasification of chars consists of the reaction of steam with carbon to form a mixture of carbon monoxide and hydrogen, or "synthesis gas", which can then be converted into a spectrum of products [45].



Huttinger et al. [8,46,47] state that the uninhibited forward reaction can be broken down into the following two major steps.



C_F indicates a free carbon site, which is a surface carbon atom that is not saturated with chemical bonds. Carbon dioxide and methane are also



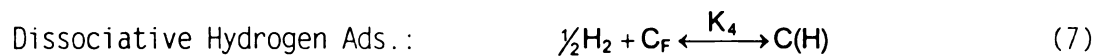
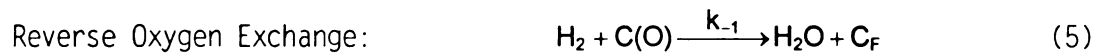
172
173
174
175
176
177
178
179
180
181
182
183
184
185
186
187
188
189
190
191
192
193
194
195
196
197
198
199
200

formed to a much lesser extent during steam gasification. Carbon dioxide is formed in the gas phase by the shift reaction, not at the carbon surface [8].



Under normal conditions methane is formed at the carbon surface; it is neither homogeneously formed nor decomposed [8].

There are three major mechanisms by which steam gasification is inhibited [8,46,47].



Selection of any one of these inhibition reactions when developing a rate expression gives an equation that has been supported by several researchers [8,46]

Basic Rate Expression:
$$r_{\text{CO}} = \frac{k_1 C_T P_W}{1 + (k_1/k_2) P_W + f(k) P_{\text{H}_2}^n} \quad (8)$$

Dissociative hydrogen adsorption gives a value of 0.5 for n in Equation 8, which has been found to be the case for low temperatures, low hydrogen pressures and subatmospheric steam pressures [6,43,48,49].

Reverse oxygen exchange and “associative” hydrogen adsorption both give

1.2.3

1.2.3

1.2.3

1.2.3

1.2.3

1.2.3

1.2.3

1.2.3

1.2.3

1.2.3

1.2.3

1.2.3

1.2.3

1.2.3

1.2.3

1.2.3

1.2.3

1.2.3

1.2.3

1.2.3

1.2.3

1.2.3

values of 1 for n in the basic rate expression, which was reported in early studies [50-54].

1.2.3.2. Role of Oxygen

A mechanism that has been cited as universal to all carbon gasification has been recently proposed by Chen, Yang, Kapteijn, and Moulijn [55,56]. At least two different types of oxygen surface complexes were identified by Kapteijn and Moulijn [56] by studying the exponential decay of CO curves following transient step changes in feed gas. The first type of complexes are semi-quinone and carbonyl, which are fairly stable at reaction temperature and can be seen in Figure 1. Molecular orbital calculations by Chen and Yang [55] have shown that the lowest energy conformation for the other type of complex is an off-plane oxygen atom bound to a carbon atom which is adjacent to the semi-quinone or carbonyl complex. The off-plane oxygen atom is bonded to a carbon atom that is in the "caved-in" or "sheltered" position on the zig-zag edge of a graphitic basal plane (see Figure 2), and lowers the bond energy of the adjacent "exposed" carbon atom by about 30%. This mechanism, shown in Figure 3, is said by both sets of workers to be universal to the reaction of char to all oxygen containing reactant gases, however neither group studied the effect of hydrogen on this off-plane oxygen atom.



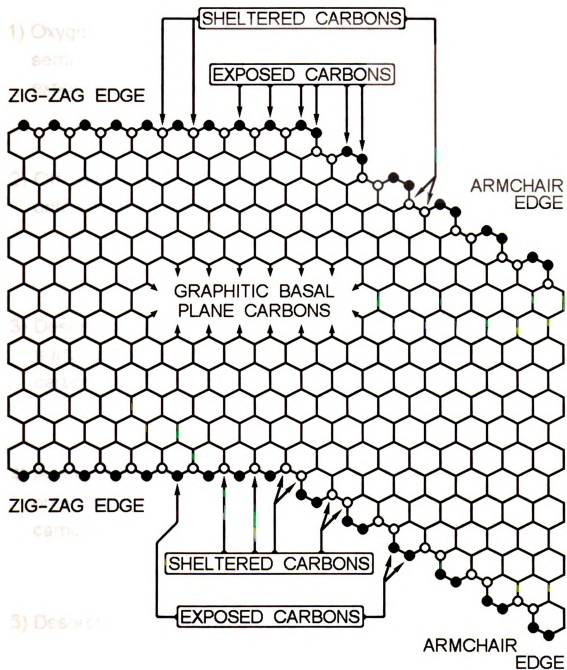


Figure 2: Edge carbon atom configurations of the graphite basal plane.

1) O
se
ex

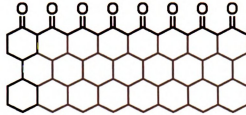
2) O
on

3) De
su
ca

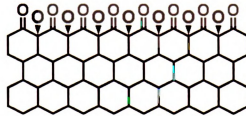
4) Ac
on
ca

5) De
to
su

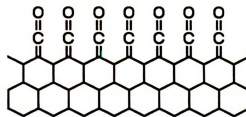
- 1) Oxygen adsorption to form semi-quinone groups on exposed edge carbons:



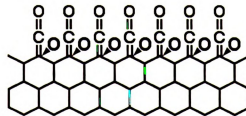
- 2) Off-plane oxygen adsorption onto sheltered edge carbons:



- 3) Desorption of semi-quinone surface groups to form carbonyl surface groups:



- 4) Adsorption of off-plane oxygen onto carbons that anchor carbonyl surface groups:



- 5) Desorption of carbonyl groups to leave semi-quinone surface groups:

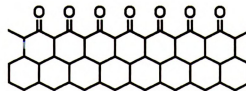


Figure 3: Universal gasification mechanism proposed by Chen, Yang, Kapteijn, and Moulijn [56].

1000

1000

1000

1000

1000

1000

1000

1000

1000

1000

1000

1000

1000

1000

1000

1000

1000

1000

1000

1.2.3.3. Hydrogen Inhibition

The presence of hydrogen greatly reduces the rate of gasification in steam as well as hydrogasification rate [50-54]. Steam gasification of chars rate drops by an order of magnitude with the addition of only 1 ppm hydrogen [49]. Gasification with carbon dioxide is also inhibited to this degree by hydrogen at low pressures [5,6,43]. During char gasification in steam, carbon dioxide and methane formation rates are decreased as well as carbon monoxide and hydrogen formation rates due to hydrogen inhibition [8].

"Associative" hydrogen adsorption has been found by Hermann and Huttinger [45,47] to contribute to inhibition in steam gasification of chars at higher pressures. Their TPD studies show a hydrogen desorption peak at 900-1100 K following gasification, indicative of $C(H)_2$ surface groups. Much larger peaks were found above 1273 K, proving that dissociative hydrogen inhibition still dominates. These investigators, and others [24,27,57], have reported reaction rates approaching zero at carbon conversions as low as 40% in steam/hydrogen mixtures. Gasification rate has also been shown by Huttinger and Merdes [8] to be greatly reduced after exposure of carbon to hydrogen in sequential steam/hydrogen/steam reactions. The rate is reported not to return to



11

12

13

14

15

16

17

18

19

20

21

22

23

24

25

26

27

28

29

30

its previous value after the second gasification in steam is initiated, suggesting irreversible blockage of active sites on char surfaces.

1.2.4. Isotopic Studies

Relatively few gasification studies have been performed using isotopes, even though isotope effects in chemical reactions have been discussed in several texts [58,59]. Gasification rates of graphite in H_2O are reported to be twice as high as in D_2O . Yates and McKee concluded that breakage of the $HO-H$ bond is involved in the rate limiting transition state complex [60], while Mims and Pabst concluded that the difference in rate is due to a shift in the oxygen exchange equilibrium constant [61]. Very small isotopic effects were found in the H_2 and D_2 gasification of graphite at 1473 K and 20 torr hydrogen [62]. H/D exchange has been shown to take place readily over carbon at 673 K [63].

Transient kinetic methods, isotopic studies using ^{13}C and ^{18}O , and TPD have been successfully combined by Kapteijn et al. [56,64] to clarify mechanisms in the CO_2 gasification of carbon. Similar methods have been used to identify reaction intermediates and intermediate rate constants in the catalytic conversion of CO/H_2 [65,66]. The experimental systems used are quite similar to the one proposed in this investigation. Low system transient responses (approaching one second)

were stressed in all investigations, as well as the use of mass spectrometry for rapid and continuous sample analysis.

1.3. Previous Research in Our Laboratory

The doctoral candidate has performed a kinetic study of the role of oxygen in hydrogasification of Saran char and coal char in partial fulfillment of the requirements for the Master of Science degree. During hydrogasification, the only oxygen present is that which is initially associated with the char sample. Even though steam gasification of chars has been studied much more extensively by other researchers, hydrogasification was chosen in order to focus on surface oxygen groups more closely.

Pertinent results of previous research are summarized in Figures 4-6. It can be seen in Figures 4 and 5 that hydrogasification rate decreases rapidly with carbon conversion, which is observed by other researchers [13,15,23-26]. Oxidation via partial combustion increases hydrogasification rate for 4-5% carbon conversion for intermittently oxidized chars, as well as heat pretreated chars. It does not increase the reaction rate when used as a pretreatment for as-received chars.

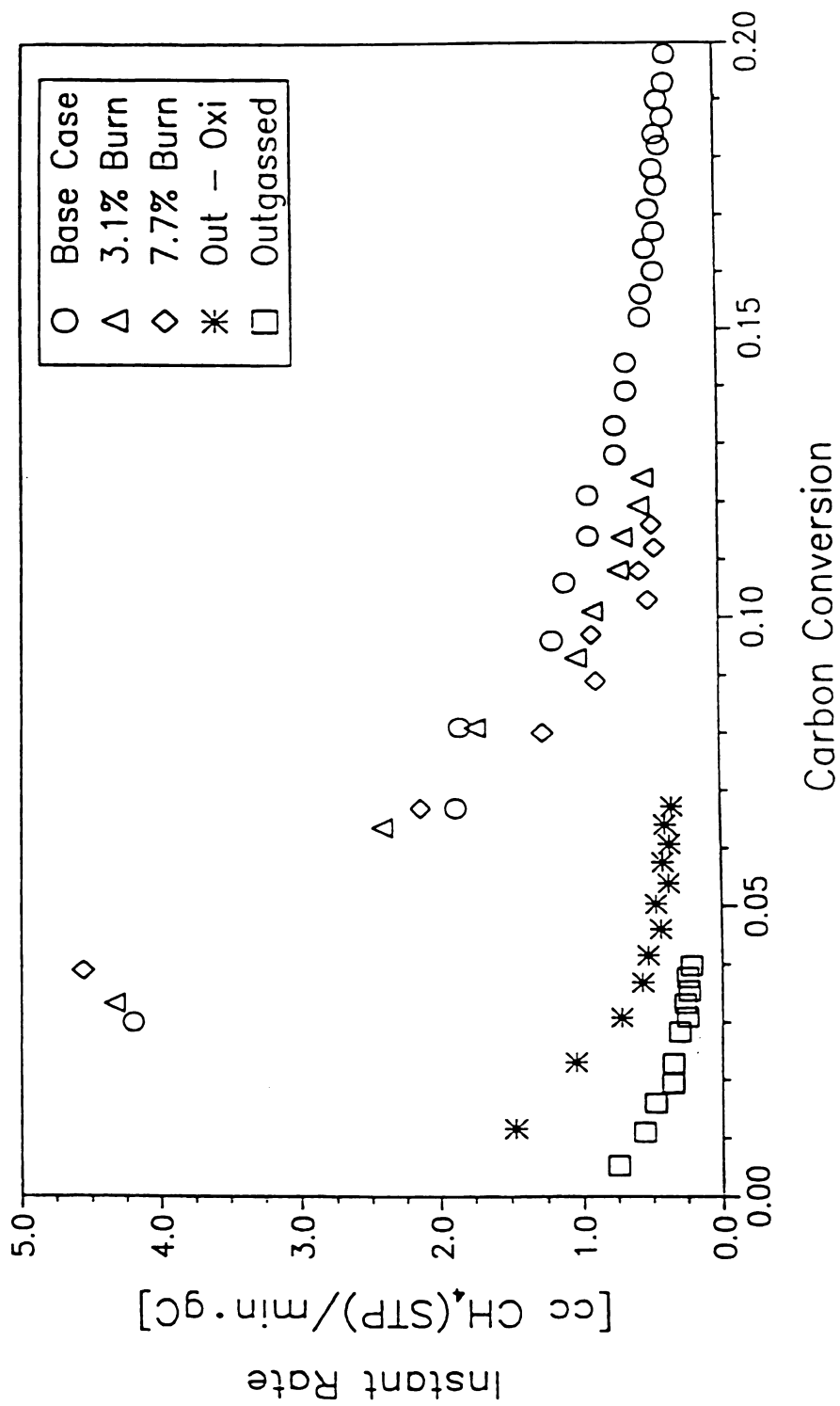


Figure 4: Hydrogasification rate curves for Saran char.

Base Case
5.1% Burn

0.00

1.00

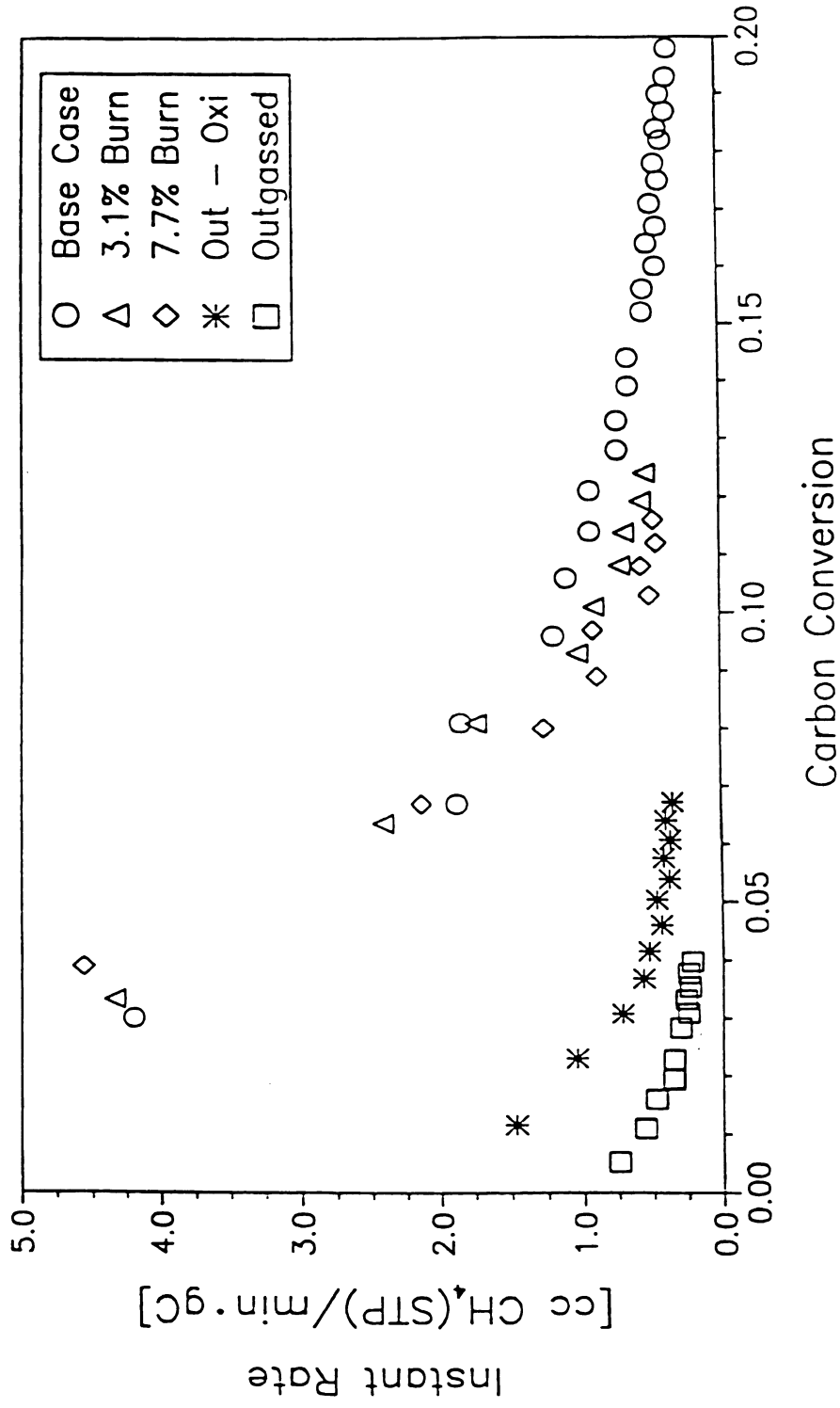


Figure 4: Hydrogasification rate curves for Saran char.

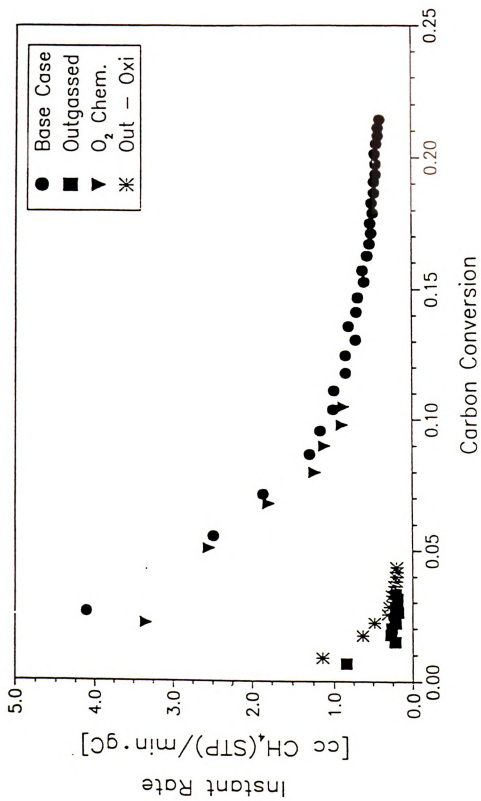


Figure 5: Hydrogasification rate curves for coal char.

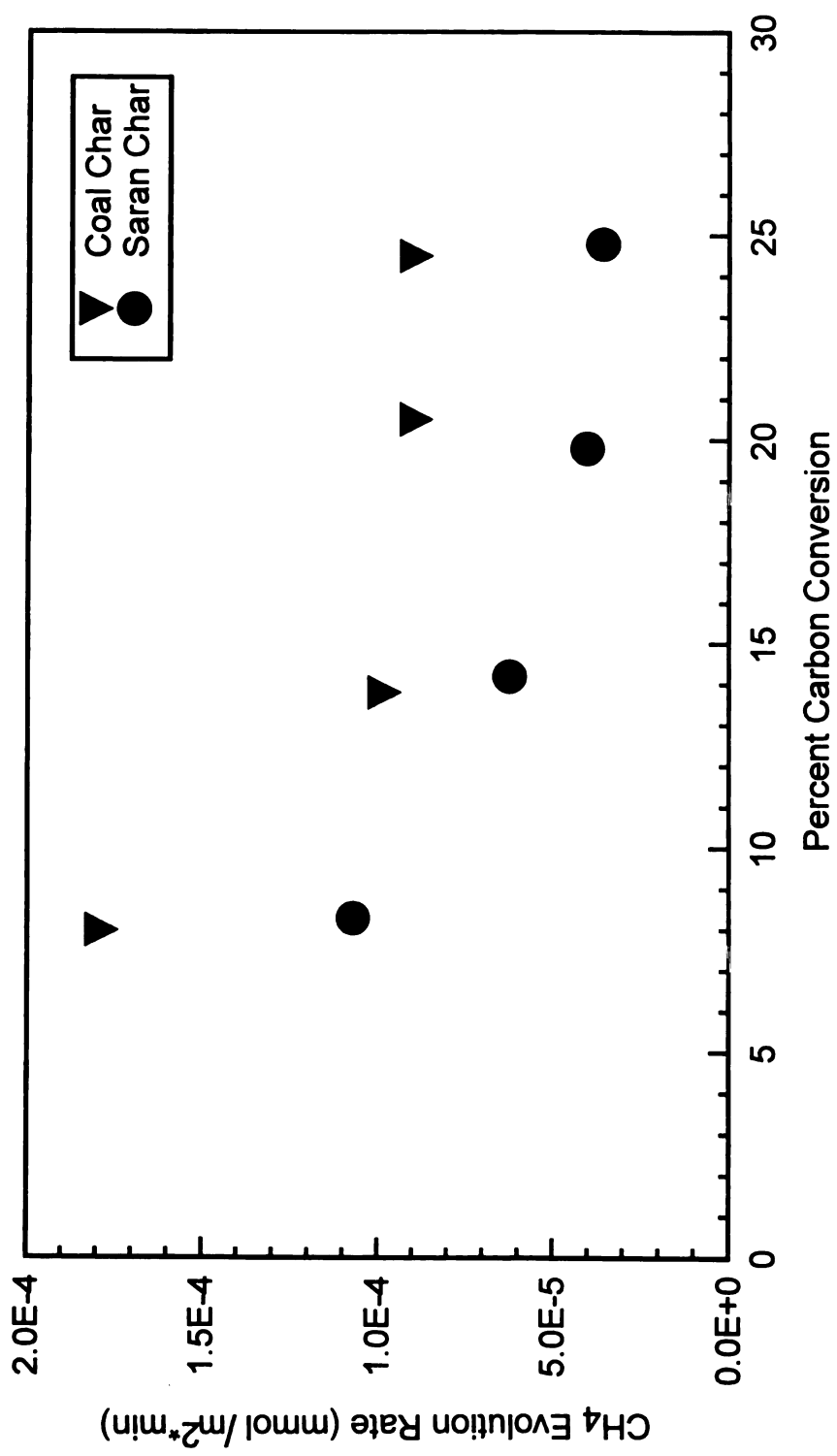


Figure 6: Hydrogasification rate curves for chars based on total surface area.

Figure 6 shows a hydrogasification rate curve based on total surface area that appears to reach a steady state at 15-20% carbon conversion.

This set of observations supports a hydrogasification reaction that is composed of three stages, in which each stage dominates during different ranges of carbon conversion. During the first stage, hydrogen reacts rapidly with the small amount of secondary carbon formed during char pyrolysis. This carbon is amorphous and tar-like; it contains a relatively high concentration of heteroatoms compared to the bulk of the char carbon. The second stage involves hydrogasification of base char carbon via active sites formed by functional group desorption, and reaction of carbons located primarily on the armchair edges of the base char. Active sites formed during the first reaction stage may propagate to the base char and contribute to hydrogasification during the second stage. Rate during the third stage is low because the carbon atoms that react are primarily those on the relatively unreactive zig-zag edges of the aromatic planes. Reaction rate is now roughly proportional to the char total surface area because there are very few active sites or armchair edges left, making the char surface relatively homogeneous, and the only source of functional groups is oxygen trapped in the bulk char.

Intermittent oxidative treatments fix oxygen functional groups on the char surface, increasing the number of active sites and therefore



increasing hydrogasification rate by a factor of 2-3. These extra active sites are consumed rapidly, so the rate returns back to its base level over the course of 4-5% carbon conversion. The oxidative pretreatment was not effective in increasing reaction rate because fixing oxygen functional groups on the char surface is balanced by the removal of the highly reactive secondary carbon.

1.4. Research Objectives

The main objective of the proposed research is to characterize the concentration, stability, and reactivity of hydrogen adsorbed on carbon surfaces at gasification conditions, and to relate this information quantitatively to the extent of hydrogen inhibition observed during gasification of chars. Though this problem has been studied for nearly a century, there is still unresolved conflict between well established researchers as to which mode of hydrogen inhibition dominates char gasification in steam. Mims and Pabst [61] state that product inhibition is due to reverse oxygen exchange, not hydrogen chemisorption. Hutter and Merdes [8] claim that inhibition caused by hydrogen chemisorption is much stronger than reverse oxygen exchange.

For the first time, the concentration of surface hydrogen will be included explicitly in linearized rate expressions that have been



14

derived from several possible reaction mechanisms. The rate expression that most closely matches collected data should reveal the actual mechanism(s) responsible for hydrogen inhibition. Chars of Saran and coal will be gasified in mixtures of $\text{H}_2\text{O}/\text{H}_2/\text{Ar}$ and mixtures of $\text{D}_2\text{O}/\text{D}_2/\text{Ar}$, ranging in composition from 40%/0%/60% to 0%/100%/0%. The first of the two specific objectives are to use TPD to determine the concentration, stability, and reactivity of hydrogen adsorbed onto char surfaces before and after gasification at a fixed temperature while varying reactant gas pressure, composition, and char conversions. The second specific objective is to use this information to determine rate constants and reaction mechanisms by matching rate data, adsorbed hydrogen concentration, and reactant gas partial pressures to linearized rate expressions.

1.4.1. Mechanism Identification

Comparison of actual experimental data with rate expressions developed from Equations 2-9 should reveal the relationship between adsorbed hydrogen and gasification rate at different gasification conditions, and identify to what extent the various proposed mechanisms contribute to hydrogen inhibition. Direct active site measurement has been done for steam gasification of chars by other researchers, however temperature programmed desorption was only done to 1373 K, and desorbed

1000

1000

1000

1000

1000

1000

1000

1000

1000

1000

1000

1000

1000

1000

1000

1000

1000

1000

1000

1000

1000

1000

1000

species concentration was not incorporated into rate expressions [45]. TPD will be performed to 1773 K in this investigation, therefore the concentration of C(H) surface groups will be measured and considered in the development of rate expressions for char gasification in steam/hydrogen mixtures.

There are three major types of surface carbon that contribute to the total number of active sites.

Active Site Balance:
$$[C_T] = [C_F] + [C(O)] + [C(H)] \quad (9)$$

A "free" surface carbon, denoted by C_F , is a carbon atom that is not saturated with chemical bonds. Carbons denoted by the symbol C(O) are bound to oxygen. Carbons that are bound to hydrogen are denoted C(H) in the active site balance, however this symbol may refer to either dissociatively bound C(H) groups or "associatively" bound C(H)₂ groups.

There are several linearized rate expressions that can be derived based on the three possible modes of inhibition. If reverse oxygen exchange is solely responsible for inhibition, then Equation 8 is correct with a value of n equal to 1, and the surface concentration of C(H) is not included in the expression. In this case, there is no correlation between adsorbed hydrogen and reaction rate.

If dissociative hydrogen adsorption is solely responsible for inhibition, then Equation 8 is correct with a value of n equal to 0.5. The linearized form is as follows (See Appendix A-1 for derivation):

$$\frac{C(H) - C(H)_i}{r_{COj} - r_{CO}} = \left(\frac{1}{k_1} \right) \frac{1}{P_w} + \frac{1}{k_2} \quad (10)$$

In this equation, instantaneous rate at any conversion has been subtracted from initial rate. A plot of the left side, which can be determined experimentally, versus $1/P_w$ will be linear. In this case, the value of the left side is not a function of hydrogen partial pressure, therefore the same plot should result for all hydrogen partial pressures.

If reverse oxygen exchange and dissociative hydrogen adsorption are both responsible for inhibition, the rate equation becomes slightly more complicated than Equation 8. The linearized form is as follows (See Appendix A-2 for derivation):

$$\frac{C(H) - C(H)_i}{r_{COj} - r_{CO}} = \left(\frac{k_{-1}}{k_1 k_2} \right) \frac{P_{H_2}}{P_w} + \frac{1}{k_2} \quad (11)$$

Instantaneous rate has also been subtracted from initial rate in this equation. A plot of the left side versus P_H/P_w should be linear if the assumptions leading to this rate expression are correct.

There are several other possible rate equations that would result from other combinations of the proposed mechanisms. Inclusion of

“associative” hydrogen adsorption as an inhibition mechanism, or inclusion of non-rapid oxygen exchange will result in more complicated rate expressions that must be analyzed by linear regression. Using the above methods and rate expressions, the unsteady state behavior of char gasification over the entire range of conversion will be able to be accounted for for the first time.

1.4.2. Isotope Effects

There are several ways in which rate may differ between char gasification in $\text{H}_2\text{O}/\text{H}_2$ and gasification in $\text{D}_2\text{O}/\text{D}_2$. Effects caused by differences in adsorption [58], as well as quantum-mechanical tunneling [67], should be negligible at elevated temperatures. If oxygen exchange is reversible and rapid, there will be an isotope effect on the equilibrium constant for this step. If gasification rate is proportional to the surface $\text{C}(\text{O})$ concentration, as it is in all proposed mechanisms, then the ratio of gasification rates should be the same as the ratio of the oxygen exchange equilibrium constants, which is about 1.3 at 1023 K [61].

Another way in which isotope effects may manifest themselves in char gasification is in the breakage of the bond(s) involved in the rate limiting step. Effects here are a result of differences between the masses of atoms or groups of atoms surrounding the bond in question, and

are more pronounced given a greater relative mass difference. A primary isotope effect will result if hydrogen or deuterium is on one or both ends of the bond. The rate ratio is calculated by taking the ratio of the partition functions, and the difference in zero-point energies between hydrogen and deuterium.

$$\frac{r_{\text{CO}}^{\text{H}}}{r_{\text{CO}}^{\text{D}}} = \left(\frac{Q_{\text{rot}}^{\text{H}} Q_{\text{vib}}^{\text{H}} Q_{\text{elec}}^{\text{H}} Q_{\text{trans}}^{\text{H}}}{Q_{\text{rot}}^{\text{D}} Q_{\text{vib}}^{\text{D}} Q_{\text{elec}}^{\text{D}} Q_{\text{trans}}^{\text{D}}} \right) \exp - \left[\frac{E_0^{\text{H}} - E_0^{\text{D}}}{RT} \right] \quad (12)$$

Since char gasification is a surface reaction, the only terms that will contribute significantly to the rate ratio should be the vibrational partition functions and the zero-point energy differences [58].

Vibrational partition functions are calculated with the following formulas [68]:

$$Q_{\text{vib}} = \frac{1}{1 - e^{-(h\nu/kb)T}} \quad (13)$$

$$\nu = \left(\frac{1}{2\pi} \right) \sqrt{\frac{k}{\mu}} \quad (14)$$

The ratio of vibrational frequencies is 1.41, however the ratio of vibrational partition functions is what contributes to the overall rate ratio. The contribution, which is a function of temperature, is 1.3 at 1073 K. This value is based on a bond stretching force constant of 5.75 N/cm which was derived from spectral data [69,70]. Zero-point energies are calculated with the following formula [58]:

$$E_0 = \frac{h\nu}{2} \quad (15)$$

The contribution to the rate ratio of the zero-point energy term is about 2.4 at 1073 K. This is also based on a bond stretching force constant of 5.75 N/cm. A secondary isotope effect will result if hydrogen or deuterium is bonded to another atom that is involved in the rate limiting bond breakage. In the case of a CH₂ or CD₂ group, the difference in mass is quite small compared to the total mass of each group 14/16, therefore a secondary isotope effect would have little influence on the rate ratio.

There are many reasons why observed rate ratios may only give very limited information about rate limiting reaction mechanisms. First, distinguishing between the relative contributions of various isotope effects is very difficult. Second, there may be differences between the zero-point energies of adsorbed and gaseous species, altering the contribution from this term. Third, there may be small contributions from other terms in the rate ratio equation or other phenomena that are unknown in the char gasification system. Because of these reasons, information gained by isotopic studies should be qualitative at best.

Chapter 2

EXPERIMENTAL

Detailed descriptions of starting materials, equipment, and experimental methods are given in this chapter. Equipment used in previous studies [71,72] has undergone several modifications and additions, including addition of a gas metering and blending system, a small packed bed reactor that fits inside the existing pressure vessel, a greatly modified reactor flange, a low dead volume steam trap, a high temperature ceramic reactor, and a mass spectrometer.

Experimental methods that allow characterization of surface hydrogen include the combination of steady-state gasification with transient step changes in reactant gas composition and temperature programmed desorption (TPD). Rate measurement characterizes char reactivity, while transient monitoring is performed immediately following gasification to characterize species that are loosely bound to char surfaces at reaction conditions. TPD to 1773 K is then performed in a separate reactor to characterize species that are more stable on char surfaces.

2.1. Starting Materials

2.1.1. Chars

Samples used in this study are chars of Dow Saran powder (MA 127) and Illinois #6 coal (PSOC 1493), which have also been used in previous studies [73,74]. Chars are prepared by heating the starting materials in ultra high purity nitrogen at 10 K/min to 1173 K for one hour in a quartz tube furnace. Chars are then crushed and sieved to -60+100 mesh particles. In order to facilitate the desired measurement of adsorbed species following gasification, chars are further pretreated by heating at 5 K/min to 1773 K in argon for 6 hours in order to anneal and clean sample surfaces. Char properties are given in Table 1.

Table 1: Ultimate analysis and surface area of chars (wt% dry basis)

Component (wt%)	Saran Char[75]	Coal Char[75]	Annealed SaranChar[76]	Annealed CoalChar[76]
Carbon	96.4	75.3	97.76	87.19
Hydrogen	0.5	0.5	0.019	< 0.001
Nitrogen	1.0	1.3	< 0.5	< 0.5
Sulfur	0.4	3.6	0.0023	1.36
Chlorine	na	na	< 0.0010	0.0062
Ash	0.1	17.3	0.46	15.00
Oxygen (diff.)	1.3	2.0	1.78	< 0.1
TSA (m ² /g)	1330	440	800	15
	(CO ₂ at 298 K)	(CO ₂ at 298 K)	(N ₂ at 77 K)	(N ₂ at 77 K)

2.1.2. Reactant Gases

All gases used are ultra high purity grade (99.999%) except for deuterium (Scott, 99.7% D), which contains 99.4% D₂ and 0.6% HD. Two argon gases are used: one is doped with 1.0% krypton for characterization of system transients during gasification and is used as the diluent along with hydrogen and steam, while the other is used as an inert only. All gases are further purified by flow through R&D Separations Model OT500-2 Oxygen/Moisture Traps to remove water and reduce oxygen to less than 10 ppb. HPLC grade H₂O and Sigma D₂O (99.9 atom% D), used for producing the reactant gas stream, are outgassed at

2.2.1

2.2.1

2.2.1

2.2.1

2.2.1

2.2.1

2.2.1

2.2.1

2.2.1

2.2.1

2.2.1

2.2.1

2.2.1

2.2.1

2.2.1

2.2.1

2.2.1

2.2.1

2.2.1

2.2.1

2.2.1

373 K for 30 minutes and stored under argon to minimize dissolved oxygen in the steam.

2.2. Experimental Apparatus

The required experimental apparatus consists of four major components: gas flow control and metering equipment, a high pressure gasification reactor (1300 K maximum temperature), a high temperature TPD/annealing reactor (0.4 MPa maximum pressure), and a mass spectrometer/vacuum system (gas analysis). A schematic of the overall system is given in Figure 7.

2.2.1. High Pressure Reactor

The high pressure reactor consists of a horizontally mounted 51 mm OD x 19 mm ID Haynes Superalloy pressure vessel capable of operation at 1300 K and 6.6 MPa, with a flange closure on one end. It is externally heated with a Lindberg 1400 watt electric furnace, driven by an Omega programmable temperature controller. It has been used and described in previous studies [71,72], but has undergone several modifications described in the following sections.

2.2.1.1. Internal Microreactor

A small packed bed reactor was designed and constructed to fit inside the main pressure vessel to maximize mass transfer at the

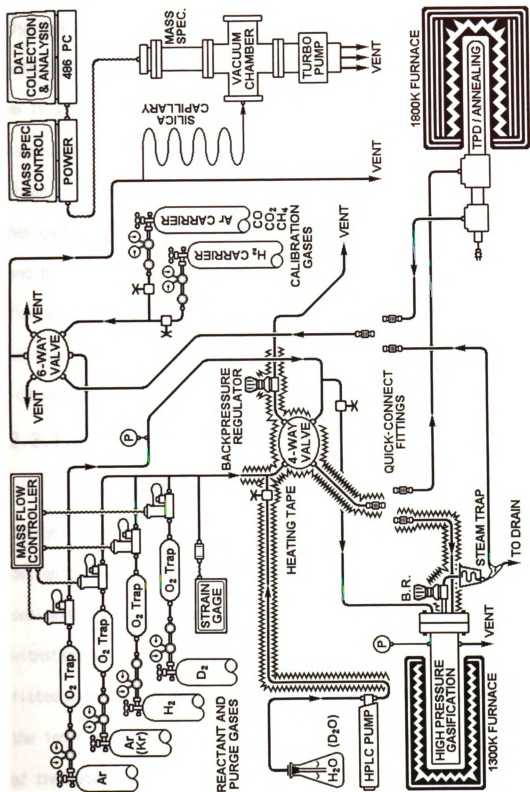


Figure 7: Overall Experimental Apparatus

2000

2001

2002

2003

2004

2005

2006

2007

2008

2009

2010

2011

2012

2013

2014

2015

2016

2017

2018

2019

2020

2021

2022

2023

particle level and to prevent steam condensation in parts of the reactor that are not located inside the furnace or can not be kept warm enough with heating tape. The main pressure vessel houses this 19 mm OD x 11 mm ID x 57 mm length Inconel 625 packed bed microreactor, which is capped at both ends with Swagelok® Monel fittings. The microreactor, shown in Figure 8, is quartz lined, has quartz frits on both ends, and has quartz wool gaskets to prevent sample contact with metal surfaces and to prevent small entrained particles from reaching the sample bed. This provides an 8 mm diameter x 31 mm length sample chamber that can hold up to 300 mg of -60+100 mesh Saran char powder, or 800 mg of -60+100 mesh coal char powder.

2.2.1.2. Flange Modifications

Figure 9 shows the main pressure vessel with the modified flange design. The flange sealing groove has been altered from the original design to hold a 41 mm OD x 32 mm ID x 3 mm deep Variseal internal face seal with Turcite polymer compound and a 301 Stainless Steel spring to withstand an operating temperature of 573 K. The flange has also been fitted with several more taps for feeding purge and reactant gases to the inner microreactor, to facilitate inert gas purging and pressurizing of the outer vessel, and to allow for optimal thermocouple placement. The flange closure contains ports for reactant gas inlet and outlet.

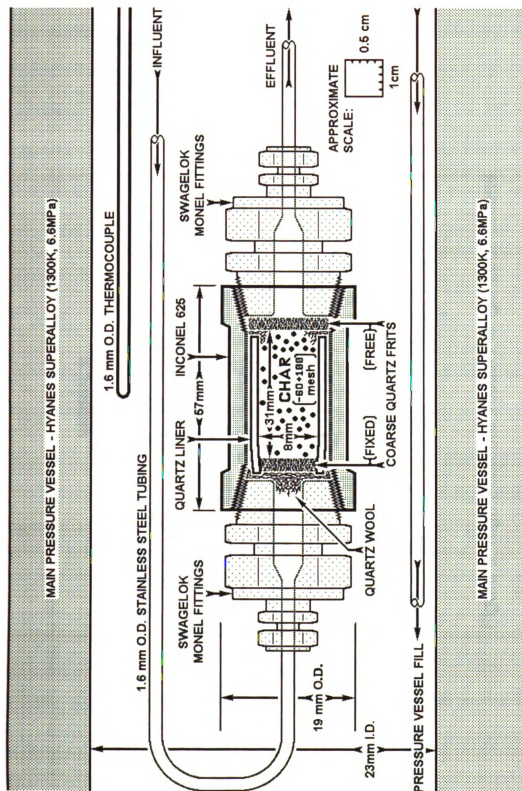


Figure 8: High Pressure Vessel Internal Microreactor

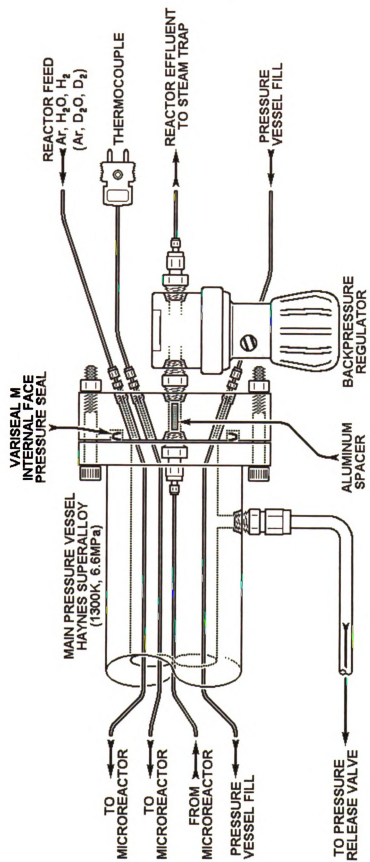


Figure 9: High Pressure Vessel Flange Modifications

thermocouple probes, and purge. The gas inlet and outlet tubing, as well as the sample holder, have been designed to have the lowest possible dead volume so that transients in gas composition can be followed. A Conoflow ABP Series backpressure regulator has also been added for immediate pressure reduction downstream of the reactor, which also minimizes effluent gas residence time between the reactor and detection equipment. During operation, reactant gases have residence times of one to two seconds in the sample bed.

2.2.2. Flow Control and Mixing System

The mass flow control and mixing system, which can be seen in Figure 7, allows rapid switching and mixing of up to four gas streams at flow rates of 0–300 ml(STP)/min per stream. Pressure equalization between active and vented gases is crucial so that backflow of gases does not occur upon rapid switching of the two streams. Unused streams are exhausted during switching, because mass flow controllers may take long periods of time to equilibrate. For introduction of steam into the manifold system, a Series 1350 Bio-Rad Laboratories HPLC pump is used to inject water into the reactant gas stream at flow rates as low as 0.6 cc/hr (10 ml(STP)steam/min). The HPLC grade water is boiled to drive off dissolved oxygen, then stored under argon to prevent dissolution of more oxygen. All lines upstream of the reactor are traced with heating

tape and heated up to 470 K for steam formation and prevention of condensation. Steam can not be introduced into the vacuum chamber for detection with the mass spectrometer, so it is condensed immediately upon exiting the reactor in a cooled 1.6 mm OD copper tube and separated in a 3 ml glass trap to minimize dead space and backmixing. This item is described in detail in section 2.2.2.2.

2.2.2.1. Gas Blending/Rapid Switching System

Also shown in Figure 7 is an externally heated low dead volume gas manifold system which has been added and built to allow for rapid switching and accurate blending of purge and reactant gases. Gas flow is controlled with four Porter 201-FSVB Mass Flow Controllers capable of 0-300 ml(STP)/min and a Porter PCIM4 Four Channel Interface Module. Reactant gas pressure upstream of the reactor is measured with an Omega DP 2000 Strain Gage for minimization of internal volume. A Valco Instruments UW Series 2-Position 4-Port valve is used to rapidly switch between reactant and purge gases, and is also heated. Pressure is controlled with two Veriflo Series ABP-1 Back Pressure Regulators, also heated, one on the reactor line and one on the vent line. Aluminum pegs have been placed inside all sections of the flow control system that contain space greater than 0.125" diameter, including the mass flow

controller fittings, strain gage, reactor fittings, and backpressure regulators as a last step to minimize internal volume.

2.2.2.2. Low Dead Volume Steam Trap

The capacity to use steam as a reactant gas has been added to the high pressure reactor, however it cannot be introduced into the vacuum chamber for detection as are the other effluent species. The assembly that allows for rapid steam condensation with minimum internal volume is shown in Figure 10. Product gases from the high pressure reactor pass through a backpressure regulator to reduce pressure to roughly atmospheric. The steam is condensed and trapped out of the effluent gas immediately as it exits the regulator. Condensation is achieved by directing flow through a 1.6 mm OD x 750 mm length copper tube that is coiled inside an ice bath, while separation is achieved just below the bath where the copper tube empties into a 10 mm OD x 45 mm length glass trap. The trap is very small in order to reduce dead volume between the reactor and detection system. Water level in the trap is controlled by opening a Nupro fine metering valve just enough to allow a drip rate equal to that of the condensation rate. Such separation is reported in the literature by Saber et al. [77].

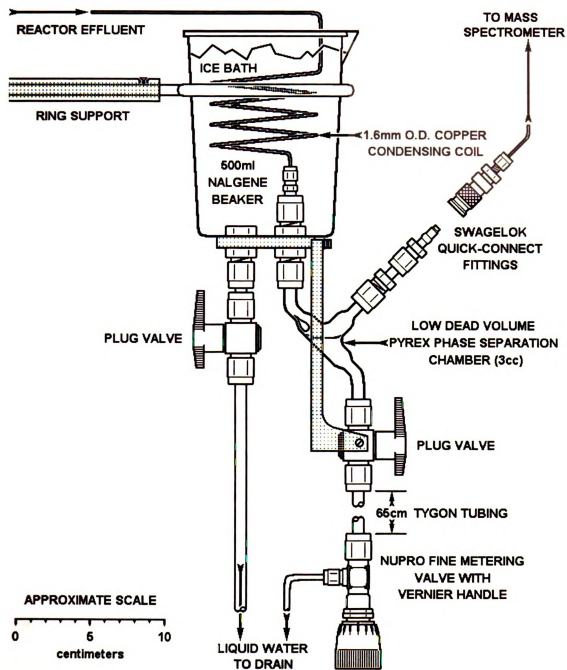


Figure 10: Low Dead Volume Steam Trap

2.2.3. High Temperature Reactor

The high temperature reactor, shown in Figure 11, has been designed and constructed for this work specifically for TPD to high temperatures. Alumina tubes are set in an annular arrangement to facilitate influent gas preheating and low dead volume. Samples are held in a packed bed by a stationary porous alumina frit on one end and thin layers of alumina beads on the other. The beads prevent the char from spilling into the annular space between the thermocouple well and the middle tube because they are too large to fit in the annular space themselves, but are small enough to prevent the char from spilling past them. Hand-tightened fittings have been used for the parts that must be disconnected each time a sample is loaded or unloaded to facilitate rapid sample transfer. The reactor can be operated at pressures slightly above atmospheric and fits inside a Mellen Series 3 8400 watt split design 1800 K tube furnace equipped with a Eurotherm programmable temperature controller to facilitate linear temperature ramping.

2.2.4. Mass Spectrometer

An Ametek Dycor M100M Quadrupole Mass Spectrometer is used to analyze product gases from gasification and TPD. It is mounted on a vacuum chamber that is capable of achieving pressures down to 10^{-8} torr.

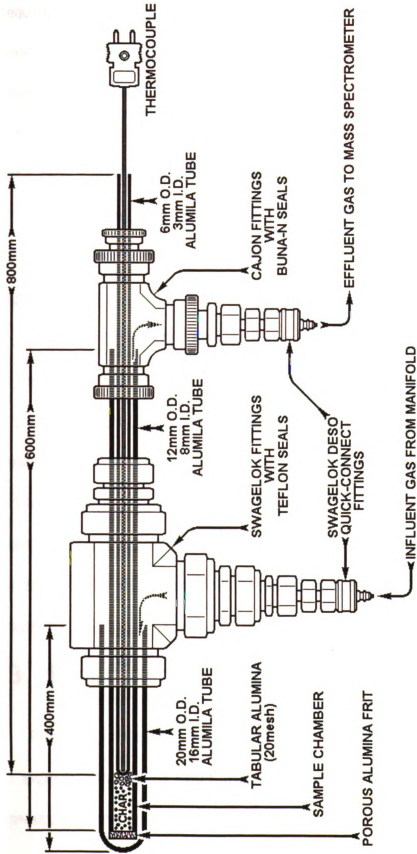


Figure 1: High Temperature Ceramic Reactor

is equipped with an electron multiplier for analysis of species concentrations down to 100 ppm, and is interfaced with a personal computer for data collection and manipulation. Product gases from both reactors as well as calibration gases pass by one end of a one meter quartz fine capillary tube which continuously withdraws sample gases to the vacuum chamber, and achieves the final pressure reduction of 10^{-4} - 10^{-5} torr. A list of all mass spectrometer controller settings is given in Appendix B.

A Marvac Scientific A20 rotary vane vacuum pump was connected to the tubing system near the fine capillary draw point in order to vary the pressure there, and therefore vary the pressure inside the vacuum chamber. A Nupro fine metering valve was installed between the capillary draw point and the rotary vane vacuum pump to precisely control vacuum chamber pressure. The valve was sized in order to be able to vary the capillary feed pressure above or below atmospheric pressure.

2.3. Experimental Techniques

Figure 12 illustrates the basic experimental technique used for most experiments, which start with heating the sample to reaction temperature under an inert purge gas in the high pressure reactor. Once

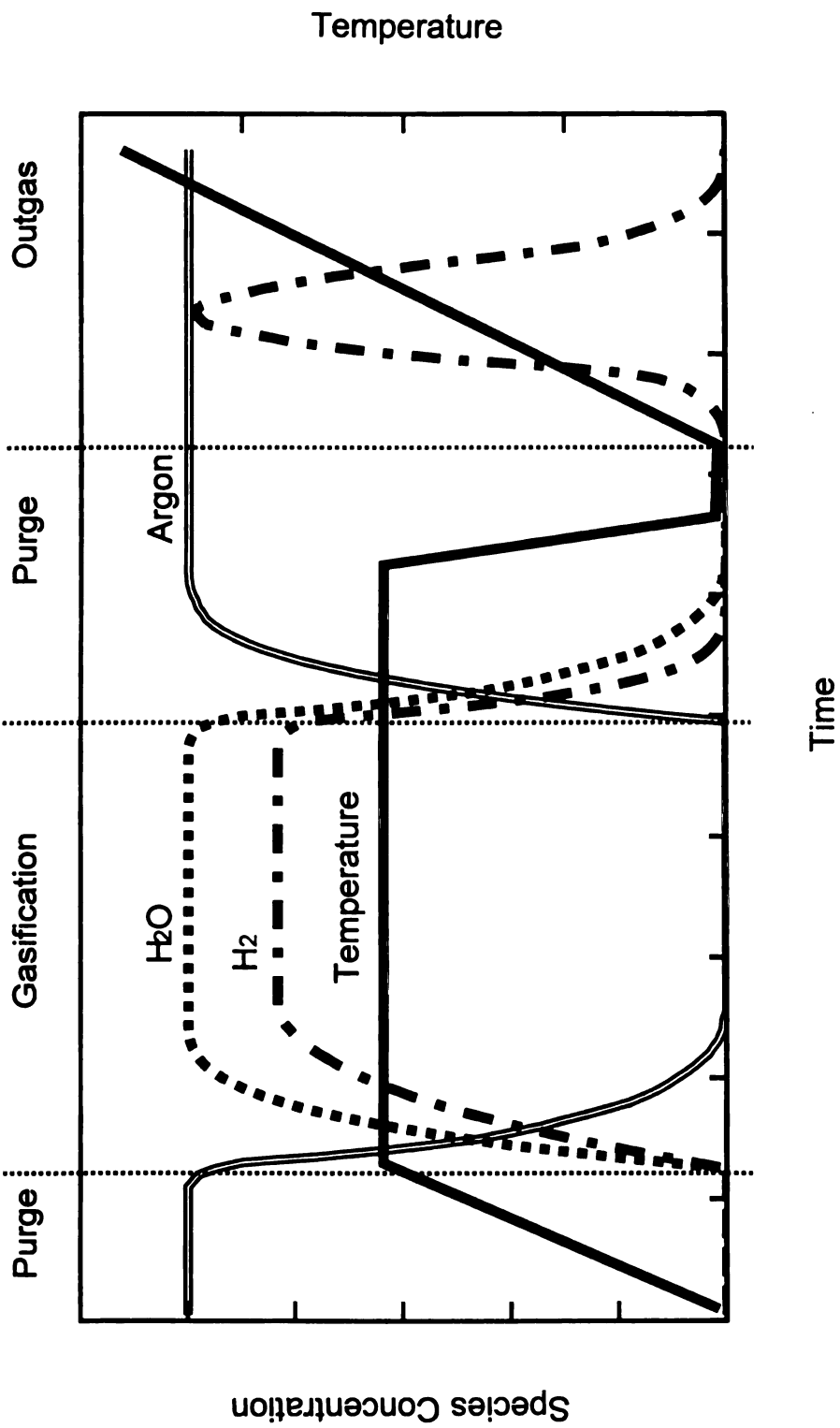


Figure 12: Experimental technique for gasification and subsequent temperature programmed desorption of chars.

temperature has stabilized, the system is pressurized. Gasification of char samples to characterize rate behavior begins when the reactor feed is switched from argon to a mixture of steam, hydrogen, and argon using a Valco 4-port valve.

The reaction is then interrupted after a predetermined length of time by a step change in reactor feed from reactant gas to argon, and transient desorption of active species is monitored. The system transient response is caused primarily by convective backmixing in the volume between the 4-port valve and the detector, and is determined by monitoring the decay of 1.0 vol% krypton in the reactant gas argon. The system response is subtracted from the decay of transient species to get actual desorption behavior.

Figure 13 shows the system transient response to a switch from 5% hydrogen in argon (1% krypton) to pure argon during a blank run through the high pressure reactor at 3.1 MPa heated to 1123 K. The mass spectrometer detects a change in the effluent gas composition 15 seconds after the step change in feed gas composition, and takes another 25 seconds to reach steady state. A high scan rate was used for this experiment, which caused the krypton concentration to be resolved to only $\pm 0.2\%$. This high value is a result of the trade-off between scan rate and detector resolution.

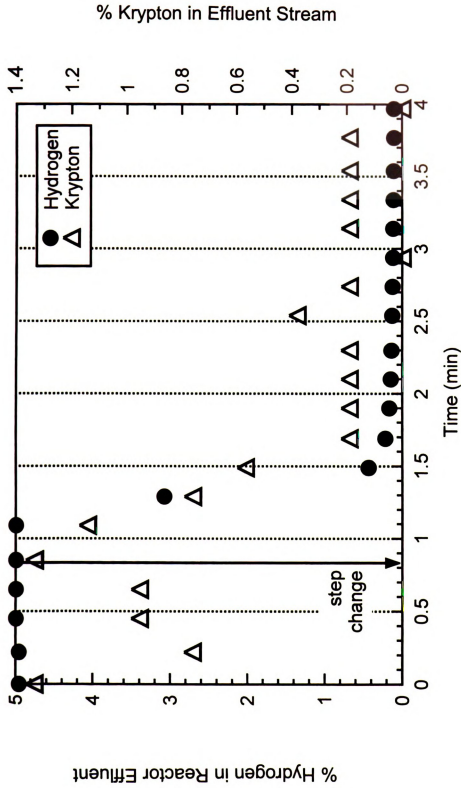


Figure 13: Step change in feed gas composition during heated blank run from 5/95 H₂/Ar(Kr) to 100% Ar at 50 seconds.

The experimental response time is very close to the theoretical purge time of 32 seconds. The reactant gases spend most of the time in the high-pressure section of the apparatus between the 4-way switching valve and the backpressure regulator. The internal volume of this section is about 5 cc, dividing this by a gas flowrate of 10 sccm (3.1 MPa) gives 30 seconds. The internal volume between the backpressure regulator and the detector is also about 5 cc, dividing this by a gas flowrate of 180 sccm (steam condensed) gives 2 seconds.

Once desorption of transients is complete, the char is subjected either to further reaction, or is transferred to the high temperature reactor for TPD to 1773 K to analyze residual adsorbed hydrogen. Mass spectroscopic analysis of effluent gas species, as well as calibration gases, is done throughout the course of all experiments. Software for data deconvolution and manipulation is presented in Appendix C.

2.3.1. Gasification

2.3.1.1. Gasification Conditions

Temperature, pressure, hydrogen/steam ratio, and time of reaction are the four parameters that can be varied for a given gasification in the high pressure reactor. Temperature is fixed at 1123 K, since it produces detectable effluent species concentrations and no significant

mass transport resistances (see Arrhenius plot analysis in section 3.1.). Reactions are conducted at 0.3, 1.0, and 3.1 MPa, with flow rates up to 300 ml(STP)/min and sample sizes of 300-800 mg. Steam fraction is fixed at 40%, and the hydrogen/steam ratio is varied by changing the relative amounts of argon and hydrogen added. Some reactions are conducted with no steam to clarify or extend initial results.

The use of D₂O/D₂ mixtures as reactant gases allows distinction between hydrogen fixed on char surfaces during gasification, and hydrogen initially present on and in the bulk char. This distinction is critical because measurement of hydrogen fixed on char surfaces during gasification is the primary focus of this investigation. Since reaction rate and adsorption rate differ when conducting gasification in H₂O/H₂ or D₂O/D₂, the isotopic effect is measured experimentally. Gaseous species containing H and D are not allowed to contact each other to avoid the possibility of H-D exchange masking important results; however, specific H-D exchange experiments are performed to gain further insight into reaction phenomena.

2.3.1.2. Gasification Procedure

The first step in all experiments is to open the vacuum chamber to the capillary inlet line and flood the vacuum chamber from 1×10^{-8} torr

when sealed to 3×10^{-5} torr with argon. Once pressure stabilizes, the mass spectrometer is turned on so the background has adequate time to stabilize. As the vacuum chamber purges, samples are weighed in the quartz microreactor liner on a Mettler AE100 Analytical Balance (0.1 mg), then loaded into the microreactor. The sample chamber is then sealed with a quartz frit and quartz wool gasket, which are held in place by a fitting inserted into the open end of the microreactor. The microreactor is then purged with argon, loaded into the high pressure reactor, and purged with argon again along with the main pressure vessel and bypass lines. As the reactor system is purged, a mass spectra of background levels of various key species is recorded and subtracted from a mass spectra of the calibration gas to obtain the true response of CO, CO₂, and CH₄.

The heating tape and furnace are switched on after a reactor purge of 20 minutes and stabilize at the reaction temperature after about 1.5 hours. At this time the reactor is pressurized with argon, the bypass line is pressurized with reactant gas, and the steam trap condensing coil vessel is filled with crushed ice. Once the entire system stabilizes, continuous mass spectra collection is initiated. After five or more scans a step change in reactor feed from argon to reactant gas is made to initiate gasification by switching the 4-port valve (see

Figure 7) that interchanges the flow paths of these two streams. Pressure, temperature, and reactant gas flowrate are all monitored and require small periodic adjustments during the course of experiments; some experiments require intentional alteration of reactant gas composition. After a predetermined length of time, the 4-port valve position is switched to create a step change in reactor feed composition from reactant gas to argon and the transients are continuously monitored. Once the reactor effluent composition stabilizes, mass spectral scans are discontinued and the vacuum chamber is isolated unless the experiment duration is longer than eight hours and requires another calibration. The reactor and bypass lines are then depressurized, the furnace and heating tapes are shut off, and the system is allowed to cool overnight under an argon purge of 2 ml(STP)/min. After the furnace has cooled overnight, samples are removed and weighed as quickly as possible.

2.3.2. Temperature Programmed Desorption

2.3.2.1. TPD Conditions

Temperature programmed desorption (TPD) is performed in the high temperature reactor by linearly heating char samples at 5 K/min to 1773 K in 30 ml(STP)/min argon and holding for 30 minutes while monitoring

relative to

green cross

hydrogen

ring rates

astrometer

23.2.2.

After

aged, the

framing is

driven on

descriptive

descriptive

DE To ch

between read

to Jiang [79

can.

As in

DE vacuum c

nitrogen,

DE loaded i

DE Alcoa C

the evolution of species from the char surface. This method of analysis has been chosen over others such as XPS and AES because it is sensitive to hydrogen and is easily integrated into our experimental system. Heating rates and argon flow rates are adjusted depending upon mass spectrometer sensitivity.

2.3.2.2. TPD Procedure

After samples are removed from the gasification reactor and weighed, they are loaded into the TPD reactor. Exposure of samples to air during sample transfer is minimized and does not affect adsorbed hydrogen on the char surface. Exposure to air can result in chemisorption of oxygen to samples, since it is reported that oxygen physisorption reaches equilibrium in 15 minutes at 348 K and 0.1 MPa [78]. To check this, TPD profiles of samples that were transferred between reactors were compared to TPD profiles of samples that were not by Zhang [79], and no differences were observed over a half hour time span.

As in gasification, the first steps in performing TPD are to open the vacuum chamber to the capillary inlet line, flood the vacuum chamber with argon, and turn on the mass spectrometer. During this time samples are loaded into the ceramic reactor, followed by a small amount of 20 mesh Alcoa Chemicals tabular alumina. This is done to prevent sample

spillage into the annular portion of the reactor since the alumina is too big to enter this area, but small enough to prevent char from passing through it. The reactor is then assembled, sealed by tightening elastomer o-ring fittings, loaded into the high temperature furnace, and purged with argon. As the reactor system purges, calibration of CO, CO₂ and CH₄ is done. The furnace is switched on after calibration and a reactor purge of 30 minutes, and the mass spectra of desorption species are continuously monitored as the temperature increases to 1773 K over the course of about 2.5 hours. After a hold time of 30 minutes, the furnace is shut off, mass spectral scans are discontinued, the vacuum chamber is isolated, and the system is allowed to cool overnight.

2.3.3. Gas Detection and Calculation of

Effluent Rates

Gas composition is determined by collecting raw mass spectra of effluent species and calibration gases, subtracting background spectra from these values, and deconvoluting the corrected values to account for molecular fragmentation and peak overlap between species. Raw mass spectra consists of partial pressures of the various molecular masses in the vacuum chamber; however all species can produce different partial pressures for the same influent mole fraction. A percentage of each

species will double ionize or fragment, causing further complications in mass spectra. Extensive calibration and data deconvolution is done to account for these phenomena of mass spectrometry.

Calibration gases are used to determine the relationship between partial pressures of various species inside the vacuum chamber and the actual concentrations of key species. Background pressure in the vacuum chamber is fairly low at about 10^{-8} torr, mainly from water and hydrogen. The only reactor effluent species that is not sent to the mass spectrometer for detection is steam, which is condensed and collected in a small trap immediately upon exit of the reactor. Computer software developed by Zhang [79] is used to deconvolute the peak overlap between species, and is shown in Appendix C.

2.3.3.1. Mass Spectrometer Calibration

Calibration of the mass spectrometer is performed by scanning a blend of two AGA Certified Standard Multicomponent Gas Mixtures. The first contains 2.00% CO, 2.03% CO₂, 2.00% CH₄, and balance argon, while the second contains 2.05% CO, 2.03% CO₂, 2.01% CH₄, and balance hydrogen. Five scans of a blend of pure argon and pure hydrogen (containing no key species of interest) are taken to obtain background levels, averaged, and then subtracted from the average of five scans of the same blend ratio of calibration gases to obtain actual peak values.

The mole fractions of key species in the calibration gas are then divided by the corrected mass spectrometer peak values to obtain actual responses.

An extensive calibration of the mass spectrometer was done prior to the core gasification reactions in order to ensure as much accuracy and consistency as possible throughout the course of this investigation. Detector response can be a function of inlet pressure, time, carrier gas composition, and species concentration. Molecular species fragment to varying degrees upon detection by mass spectrometer, causing overlap between the spectra of different species. These phenomena have been investigated and are detailed in the following sections.

2.3.3.1.1. Variation of Pressure at Capillary Inlet

Mass spectra of both purge Ar (AGA UHP, 99.999%) and carrier Ar (Matheson UHP, 0.9910% Kr) were taken at various capillary inlet pressures in order to find the pressure at which detector response is the highest and to help identify the source of possible contaminant oxygen in the system. Figure 14 shows the pressure inside the vacuum chamber as read by the ion gauge and the mass spectrometer as a function of pressure at the upstream end of the inlet capillary tube. The ion gauge gives an overall pressure from all species present in the vacuum chamber, while the mass spectrometer pressure is a sum total of the

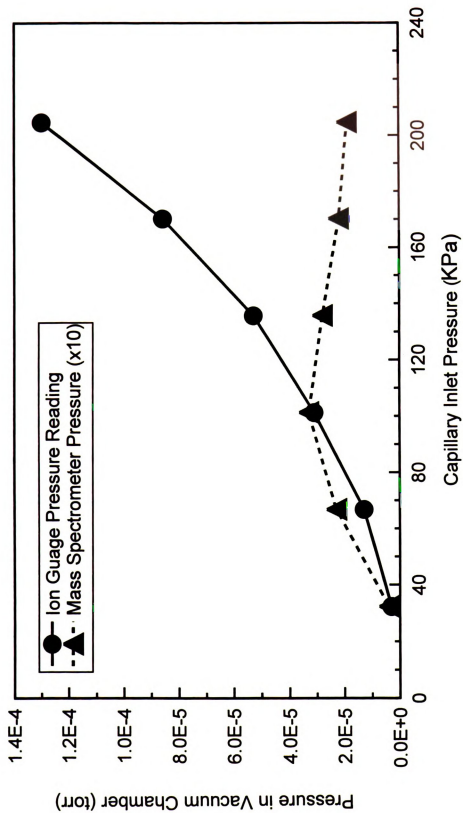


Figure 14: Pressure in vacuum chamber as a function of capillary inlet pressure with argon purge gas.

partial pressures of all individual species. The ion gauge shows an increasing vacuum chamber pressure for increasing inlet pressure, while the mass spectrometer maximum response is at an atmospheric inlet pressure. The ion gauge gives values that are about an order of magnitude greater than the mass spectrometer. This is because the numerical value of the mass spectrometer total pressure is arbitrarily set and can be calibrated.

Figures 15 and 16 show mass spectrometer background partial pressures of species as a function of total vacuum chamber pressure for pure argon and Ar/1% Kr purge gases. They all go through maxima between 2×10^{-5} and 5×10^{-5} torr, with lighter species having maxima shifted toward lower pressure and heavier species shifted toward higher pressure. Mass 32 (O_2) behaves quite similarly to the other species and has roughly 1/4 the partial pressure of Mass 28 (N_2 + small amount CO) over the course of all inlet pressures tested. This indicates that the source of oxygen is one or several small leaks in the vacuum system, not contamination in the purge and carrier gases. The average maximum response for the various species occurs at an inlet pressure that is roughly atmospheric, so it was for this reason and for ease of experimentation that an atmospheric inlet pressure was chosen.

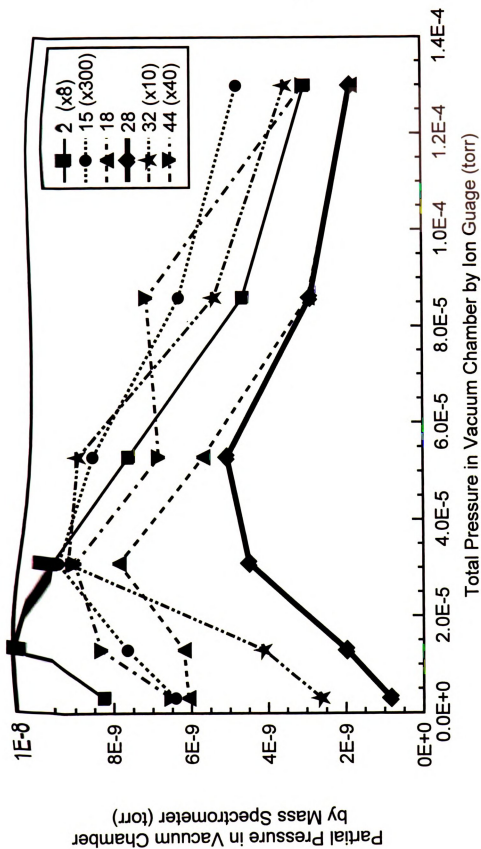


Figure 15: Background partial pressure of various masses vs. vacuum chamber pressure (Purge gas = UHP Argon 99.9999%).

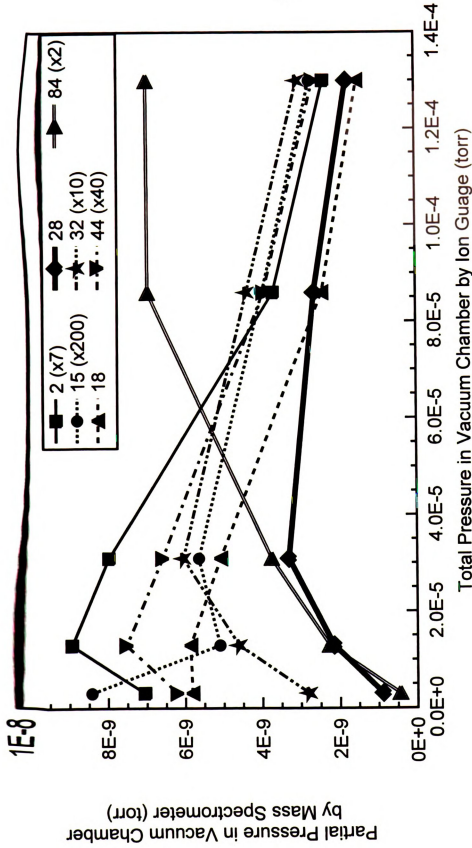


Figure 16: Background partial pressure of various masses vs. vacuum chamber pressure (Purge gas = UHP Argon /1% Krypton).

2.3.3.1.2. Linearity of Response

The relationship between key component concentration and mass spectrometer response was determined by changing the ratio of the Ar/1% Kr carrier gas to the calibration gas (2.00% CO, 2.03% CO₂, 2.00% CH₄, and balance Ar). Figure 17 shows the partial pressure of key components as detected by the mass spectrometer inside the vacuum chamber as a function of feed partial pressure. Varying the ratio between the two gases allows the key component concentrations to vary from 0.2% at 10% calibration gas to 2.0% at 100% calibration gas. The response of all key species is linear with concentration, which indicates that only one representative calibration needs to be made to determine the response over the detectable range of key component concentrations.

2.3.3.1.3. Response as a Function of Time

An investigation of mass spectrometer response over a five hour period was done to ensure that factors such as significant background changes, detector drift, and unknown phenomena do not significantly change system responses over time. A five hour interval was chosen because this is about an hour longer than an average experiment. Figure 18 shows two sets of peak heights of each of the three key components of the calibration gas mixture. The peak heights for all species remain almost constant over the five hours, even though Figure 18 shows the two

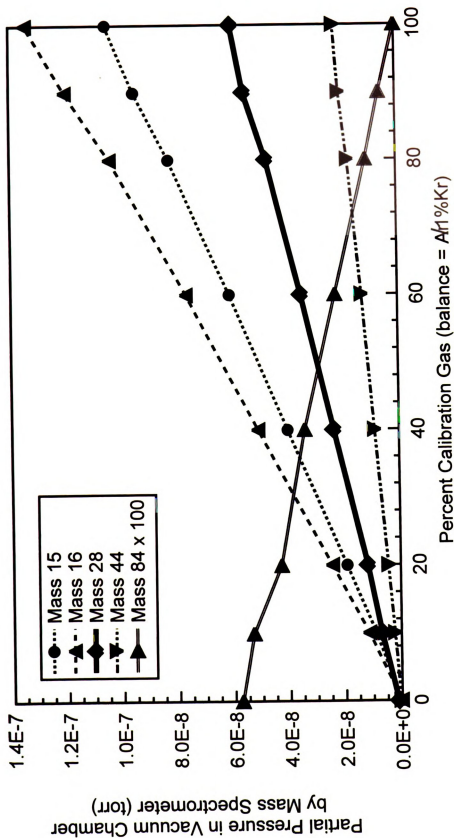


Figure 17: Linearity of mass spectrometer response with key species concentration - calibration carrier gas is Argon.

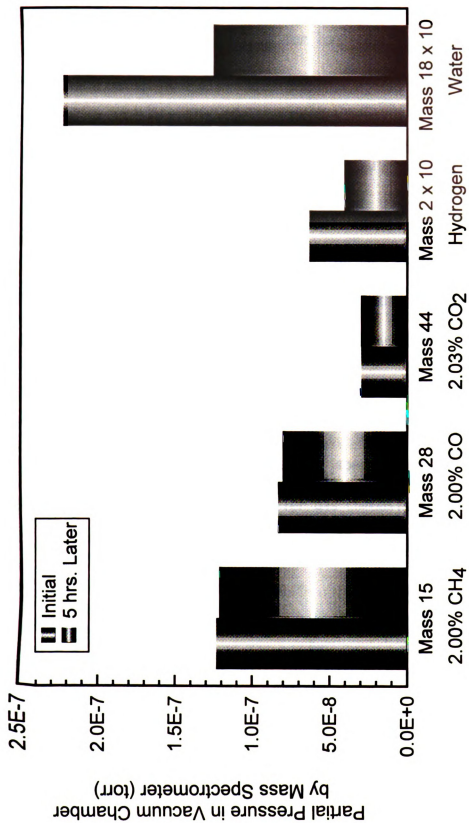


Figure 18: Change in mass spectrometer peak height of key components and major background species over five hour time interval.

major background peak heights, H_2 and H_2O , change significantly.

Multiple calibrations must be done for long experiments, but most are of short enough duration so that one representative calibration is sufficient.

2.3.3.1.4. Response as a Function of Carrier Gas

Composition

It is important that the argon to hydrogen ratio in the calibration carrier gas matches the argon to hydrogen ratio in the actual reactant gas, because the response of key species is a function of carrier gas composition. Figure 19 shows the vacuum chamber total pressure and partial pressures as a function of carrier gas composition ranging from pure Ar to pure D_2 . Neither species nor the sum total give responses that are linear with carrier gas composition, which prompted another similar experiment to analyze the key component responses as a function of carrier gas composition.

Figure 20 shows that the key component responses are not linear with carrier gas composition, with the largest response occurring at 100% D_2 as the carrier gas. It was for this reason that a second calibration gas with H_2 only as the carrier was used. For ease of calculation both calibration gases have the same key component composition; blending them in the right proportions to match the

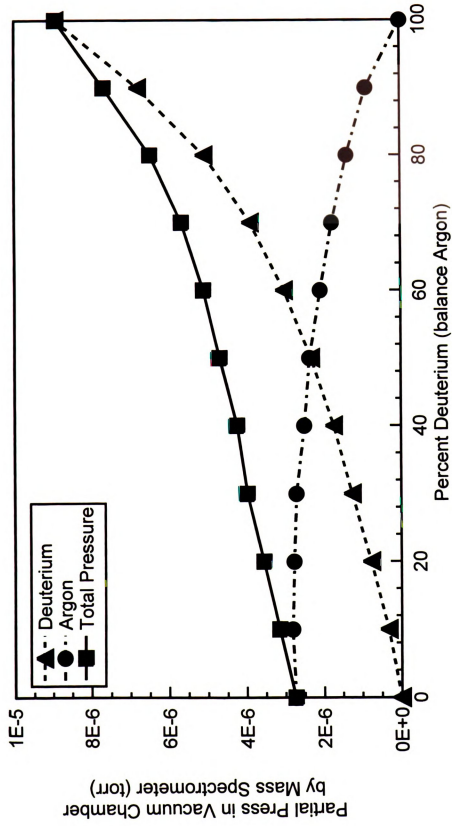


Figure 19: Partial pressures of carrier gases in vacuum chamber vs. carrier gas composition.

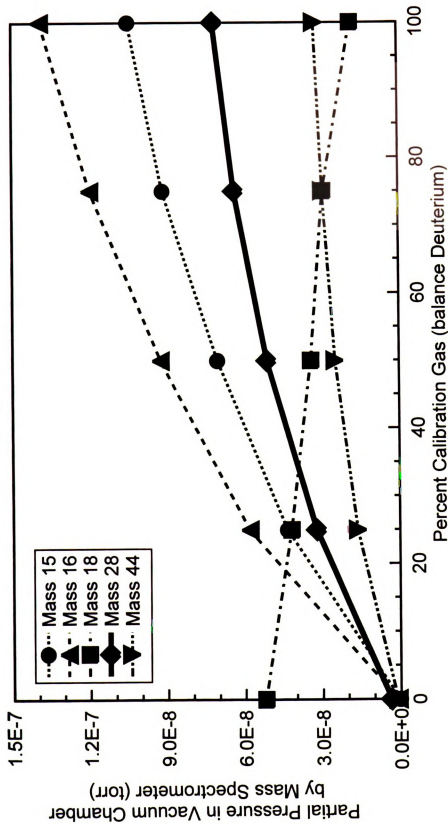


Figure 20: Partial pressures of key components in vacuum chamber vs. carrier gas composition - calibration gas is Argon.

expected reactor effluent carrier/reactant gas composition will give the appropriate responses for each experiment.

2.3.3.1.5. Fragmentation Investigation

A fragmentation study of CO₂ was done so that the contribution to the mass 28 peak from fragmented CO₂ can be subtracted so that a correct CO concentration can be calculated. Figure 21 shows partial pressure of selected atomic masses as a function of partial pressure CO₂ and varying carrier gas compositions. The response of the primary CO₂ peak (mass 44) is linear with CO₂ partial pressure, as is the mass 28 peak for the fragment species.

2.3.3.1.6. CD₄/CH₄ Response Ratios

A comparative study of the mass spectrometer responses of CD₄ and CH₄ has been done to investigate the feasibility of using CH₄-containing gas as a calibration gas for the isotopic investigations which require analysis of CD₄-containing effluent streams. Response ratios in pure Argon and 33% Ar/67% D₂ have been calculated to be 0.6590 and 0.3420 respectively, and are defined as follows:

$$\text{CH}_4 \text{ response} = \frac{\text{CH}_4 \text{ peak height}}{\% \text{ CH}_4 \text{ in carrier gas}} \quad (16)$$

$$\text{CD}_4 \text{ response} = \frac{\text{CD}_4 \text{ peak height}}{\% \text{ CD}_4 \text{ in carrier gas}} \quad (17)$$

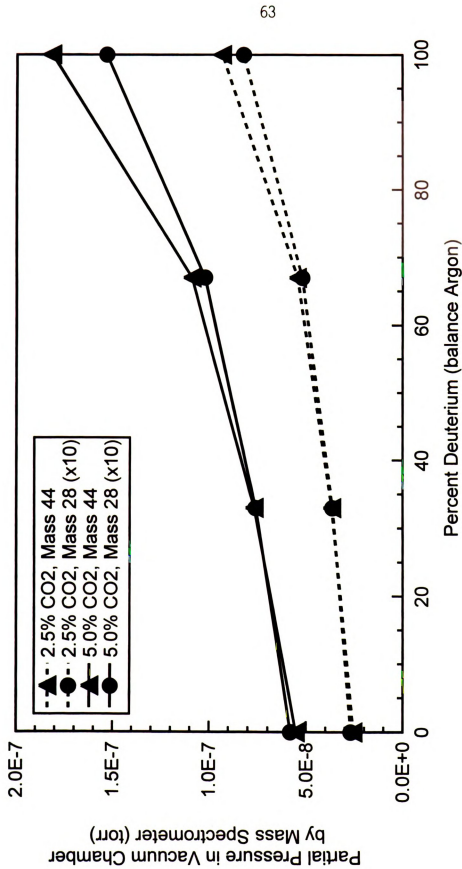


Figure 21: Partial pressures of CO₂ and CO fragments vs. carrier gas composition and inlet percent CO₂.

$$\text{CD}_4 / \text{CH}_4 \text{ response ratio} = \frac{\text{CD}_4 \text{ response}}{\text{CH}_4 \text{ response}} \quad (18)$$

The response ratios are clearly dependent upon carrier gas composition.

2.3.3.2. Mass Spectrometer Data Deconvolution

Peak overlap between species is caused by a number of factors, including fragmentation, double ionization, and isotopes. Deconvolution is accomplished by using mass 84 as the primary peak for Kr, mass 44 for CO₂, mass 40 for Ar, mass 28 for CO (after subtraction of contribution from CO₂ fragmentation), mass 15 for CH₄ (to avoid confusion with fragmentation of species containing oxygen), mass 4 for D₂, mass 3 for HD, and mass 2 for H₂ (after subtraction of contribution from D₂ fragmentation). The Registry of Mass Spectral Data [80] contains the mass spectra of most of the species involved in the gasification reactions of this study.

Gasification and desorption rates are determined by combining knowledge of the relative amounts of effluent species, and knowledge of the total gas flowrate. Relative amounts of various species in the reactor effluent streams are obtained from deconvolution of mass spectral data. The total gas flowrate is calculated from addition of the separate influent stream flowrates minus water, which is possible because the mass flow control system is quite accurate and the

contribution to total effluent flowrate due to gasified char is negligible.

Programs were developed by Zhang [79] in Basic to convert the raw mass spectral data into spreadsheet form, deconvolute the mass peaks, and convert the peaks into species concentrations, and are shown in Appendix C. The first program, named "back.bas", averages the calibration background scans and converts them into a matrix form. The second program, named "cal_h.bas", averages the hydrogen calibration scans, subtracts the background peaks calculated from running "back.bas", then divides the fraction of hydrogen in the calibration gas by the corrected peak height to get the mass spectrometer hydrogen response. The third program, named "cal_c_m.bas", performs identical tasks based on scans of the CO, CO₂, and CH₄ containing calibration gas with the added task of subtracting the contribution from fragmented CO₂ to the CO peak.

The next set of programs processes the mass spectrometer data taken during gasification experiments, initial sample weight, total gas flowrate, and calibration information, and calculates effluent rates and carbon conversion. The fourth program, named "backt.bas", organizes the mass spectrometer output data into matrix form. The fifth program, named "main-dem.bas", reads the matrix organized in "back.bas" and the

calibration information calculated in "cal_h.bas" and "cal_c_m.bas", and calculates the evolution rates of various species as a function of time. The sample weight and total gas flowrate are input to this program directly, while background scans are taken during the initial scans of an experiment and subtracted out accordingly. The fifth program, named "main-ins.bas", reads all of the information from "main-dem.bas", performs the actual peak deconvolution, and calculates the corrected effluent rates based on carbon conversion. Total carbon conversion is also calculated and is usually about 2% less than that calculated based on weighing the sample before and after an experiment. This discrepancy is because of the loss due to a small amount of sample kept in the core reactor quartz liner by static electrical charge.

2.3.4. Char Characterization

The three methods of characterizing char samples chosen for this investigation include mercury intrusion, nitrogen adsorption, and X-ray diffraction. Information such as pore size distribution and volume can be gained down to the mesopore level (2–50 nm) with mercury intrusion and down to the micropore level (<2 nm) with nitrogen adsorption. Crystal structure information such as unit cell dimensions and ordered domain sizes can be gained with analysis by X-ray diffraction.

2.3.4.1. Mercury Intrusion

Annealed chars are tested with a Micromeritics Model 9310 Mercury Poresizer to determine macro and mesopore size distributions. Approximately 200–500 mg of char are weighed and loaded into sample tubes that have been accurately calibrated for internal volume. Mercury pressure about the sample is increased from 80 torr to 340 MPa in 35–40 steps, and the intrusion volume recorded. Analysis software included with the poresizer determines the distribution of pore diameters and their corresponding internal volumes and surface areas.

2.3.4.2. Nitrogen Adsorption

The total surface area of chars at varying extents of conversion are tested by nitrogen adsorption at 77 K with a Micromeritics Pulse Chemisorb 2700. The BET method is used for analysis based on an adsorbed nitrogen area of 16.2 \AA^2 . Twenty to fifty milligrams of char are loaded into a quartz sample tube which is sealed to the Chemisorb apparatus and heated to 423 K for 20 minutes to drive off any weakly adsorbed species, most of which is water. After calibration a continuous flow of 5% nitrogen in helium is passed over the sample and the effluent gas composition is tested for nitrogen concentration. After the sample is saturated with nitrogen, the same procedure is

followed for 10% nitrogen and 18.75% nitrogen in helium. The volume of nitrogen adsorbed at a given composition along with pressure is used in BET analysis to determine char surface areas down to the micropore level.

2.3.4.3. X-ray Diffraction

The unit cell dimensions and ordered domain sizes of the crystal structure of Saran char are tested by X-ray diffraction with a Rigaku X-ray Diffractometer. Copper K α radiation at a wavelength of 1.541838 Å is sent through 0.5 mm slits at 45 kV and 100 mA to the sample. A few milligrams of char are stuck to a microscope slide with double stick scotch tape. The scan is initiated with the detector positioned at 5 $^{\circ}$ and is terminated after the detector has swept through 30 $^{\circ}$ at a rate of 0.5 degrees/min.

The angle to which the X-rays are scattered corresponds to a specific unit cell dimension which can be calculated with Bragg's Law [81,82].

Bragg's Law:
$$n\lambda = (2d)\sin\theta \quad (19)$$

The width to which the X-ray peak is broadened indicates the domain size over which the peak's corresponding unit cell is repeated. This is given by the Scherrer Formula [81,82].

Scherrer Formula:
$$k\lambda = (t\beta)\cos\theta_B \quad (20)$$

Chapter 3

GASIFICATION EXPERIMENTS

The main body of results reported in this investigation centers upon char gasification rate data, char surface area, and adsorbed hydrogen concentration. Results for the determination of the appropriate gasification temperature and the isotopic study are also presented.

3.1. Determination of Appropriate Gasification Temperature

Gasification temperature is fixed at a value that gives reasonably high reaction rates, but is low enough to ensure that the reaction rate is limited by kinetics and not diffusion rate. Figure 22 shows an Arrhenius plot of annealed Saran char steam gasification at conditions that favor relatively high reaction rates, e.g., with no H₂ in the feed gas. The plot gives reasonable and closely matching values for the activation energy of CO and CH₄ formation up to 1123 K. The values of 56.1 and 58.3 Kcal/mol match those found in literature by Juntgen, 51 Kcal/mol [24] and Long and Sykes, 55 Kcal/mol [29]. The fact that they are so close in value is consistent with the accepted theory that the rate limiting step in all uncatalyzed char gasification is cleavage of the carbon-carbon bond.

Above 1123 K, diffusion limitations begin to control reaction rate, as can be seen by the lower and less closely matching values for apparent activation energy of CO and CH₄ formation of 22.8 and 33.8 Kcal/mol. Based on the results in Figure 22, a reaction temperature of 1123 K was chosen even though it is close to the transition range between kinetic and diffusion rate limitations. A bulk modulus

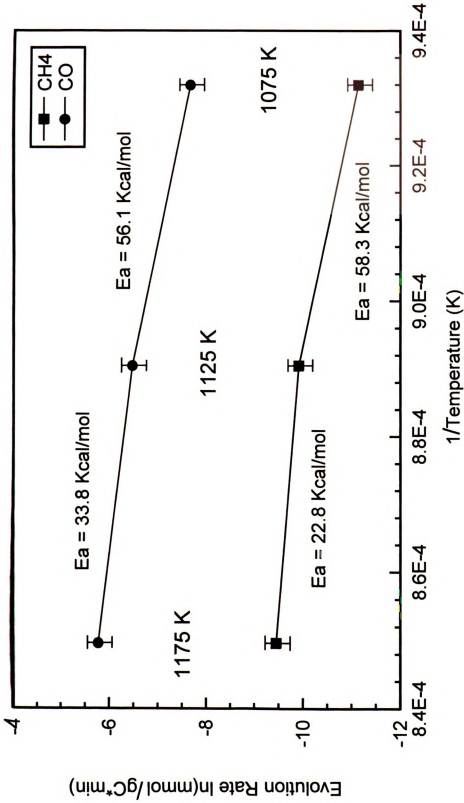
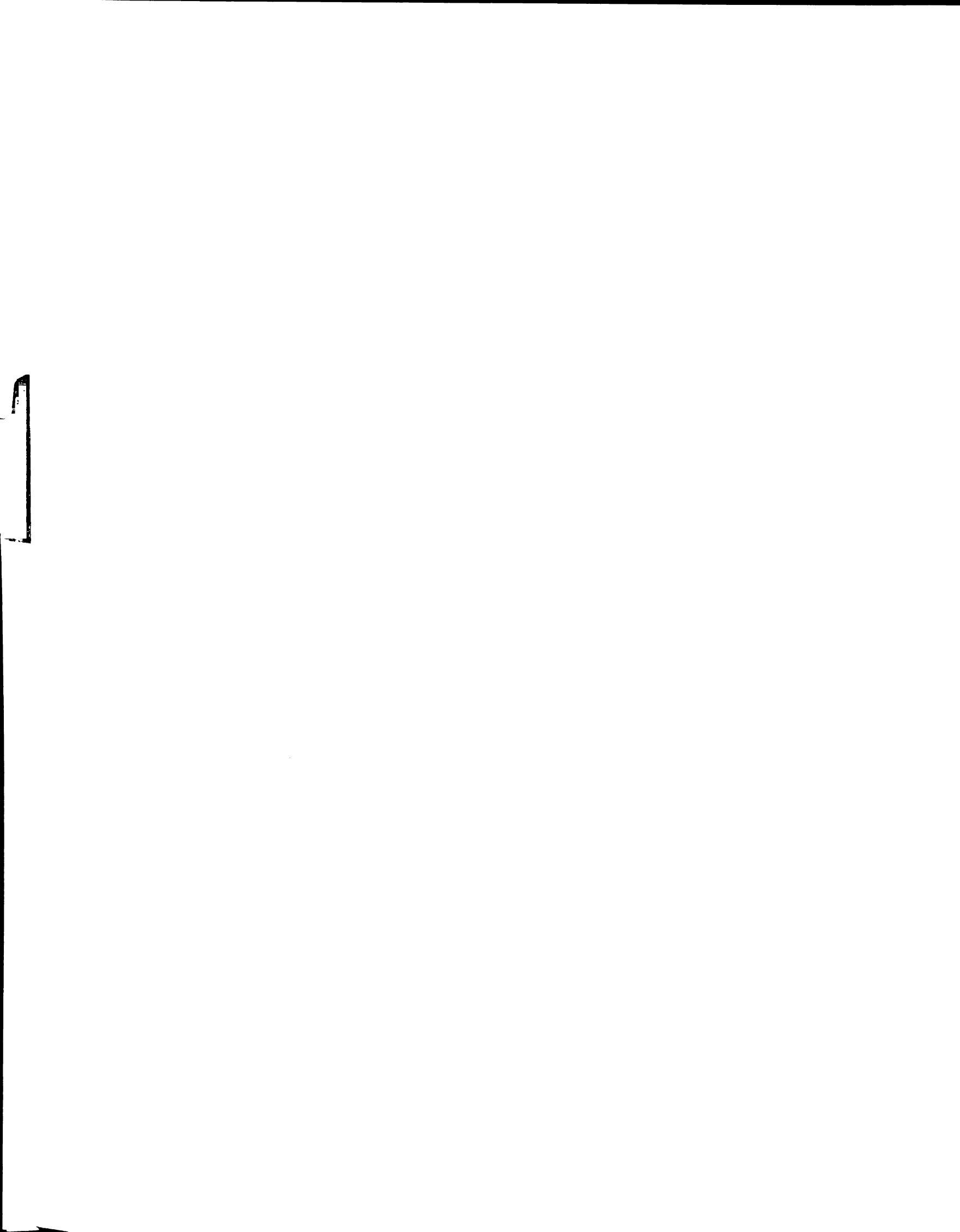


Figure 22: Arrhenius plot of annealed Saran char steam gasification at 1.0MPa; reactant gas composition is 40/60 H₂O/Ar.



calculation of the system at these conditions yields a value of 0.0072, which is more than an order of magnitude lower than the transition range of 0.1 to 3 [83]. Details of the bulk modulus calculations can be found in Appendix D.

3.2. Char Gasification in Steam

3.2.1. Evolution of Char Surface Area

Figure 23 shows total (BET) surface area as measured by nitrogen adsorption for annealed Saran and coal char following H_2O/H_2 gasification at 1.0 MPa as a function of conversion for varying reactant gas compositions. The annealed Saran char has an initial surface area of $800 \text{ m}^2/\text{g}$ and increases linearly to about $1500 \text{ m}^2/\text{g}$ at 30% conversion. Surface area remains fairly constant over the rest of the char conversion, and is independent of reactant gas composition. The annealed coal char has a surface area that is about an order of magnitude less than that of the Saran. CO_2 adsorption was used to measure char surface areas in previous studies [37,73,84] and produced similar results.

Mercury intrusion was also performed on annealed Saran char to characterize porosity at the macropore ($>50 \text{ nm}$) and mesopore ($2\text{-}50 \text{ nm}$) levels. The macropore/mesopore surface area is $0.12 \text{ m}^2/\text{g}$, along with an average pore diameter of $47.5 \text{ }\mu\text{m}$.

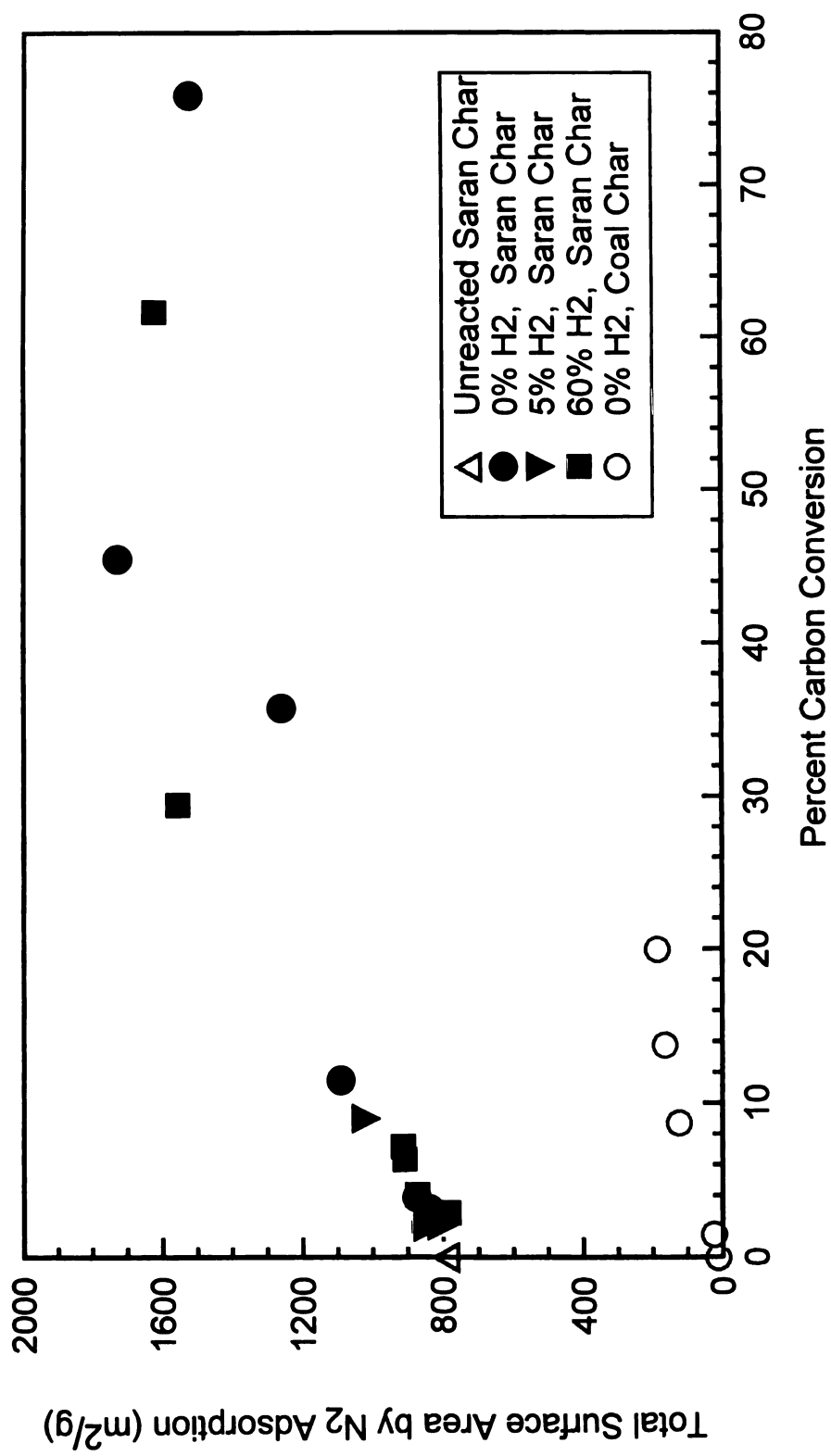


Figure 23: Total surface of of annealed chars by nitrogen adsorption after gasification in steam at 1.0 MPa.

3.2.2. Rate Dependence on Pressure, Composition, and Conversion

Steam gasification rate of chars at all conditions tested is reported in this section. Annealed Saran char is used for most of the experiments, with annealed coal char and unannealed chars used for a few representative runs. Unannealed materials were chosen in order to relate findings in this investigation with previous research in our laboratory (Section 1.3). Steam gasification rate is reported as the sum of CO and CO₂ formation rates because CO₂ is formed in the gas phase from CO by the shift reaction [8], shown in Equation 4. Effluent compositions for two reactions are compared to the equilibrium composition of the shift reaction in Figure 24. The gasifications were performed under conditions of minimum and maximum hydrogen concentration to ensure that the two extremes of effluent composition were tested. At the chosen reaction temperature of 1123 K, it can be seen that the effluent composition under both sets of conditions lies below the equilibrium value, therefore the CO₂ concentration is lower than its equilibrium value. Though this does not prove that CO₂ is not formed at the char surface, if CO₂ concentration was above its equilibrium value

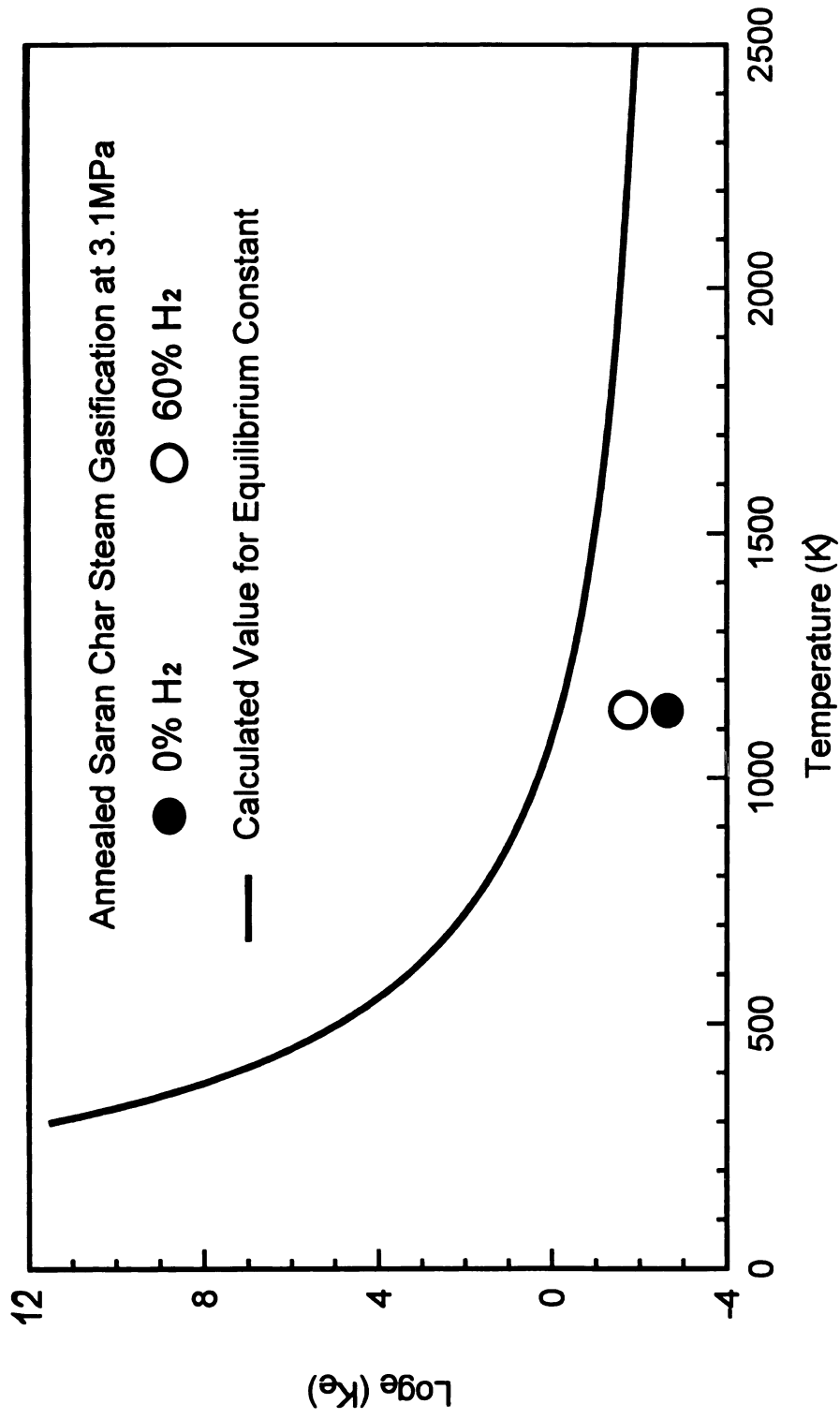
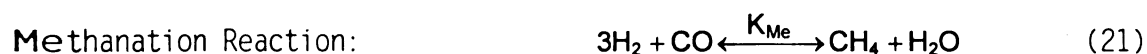


Figure 24: Equilibrium composition of the shift reaction ($\text{CO} + \text{H}_2\text{O} = \text{H}_2 + \text{CO}_2$) and reactor effluent composition vs. temperature.

in the reactor effluent it would prove that it is formed on the char surface.

Effluent compositions of the same two reactions are also compared to the equilibrium composition of the methanation reaction, which takes place in the gas phase.



Huttinger and Merdes [8] performed char gasification under similar conditions and concluded that methane formation was on the char surface only, not in the gas phase. Figure 25 shows the effluent composition of one reaction to be close to the equilibrium curve, but the composition of the other reaction is significantly above it. Both effluent compositions should lie on the equilibrium curve if methanation dominates. Both points lie above the curve and indicate greatly differing compositions, indicating that methanation does not control outlet concentration of key species.

3.2.2.1. Annealed Char Steam Gasification

3.2.2.1.1. Annealed Saran Char Steam Gasification

Several runs of Annealed Saran char gasified under identical conditions are shown in Figure 26. This set of conditions, 1.0 MPa and 40/0/60 H₂O/H₂/Ar, was chosen for analysis because there were more

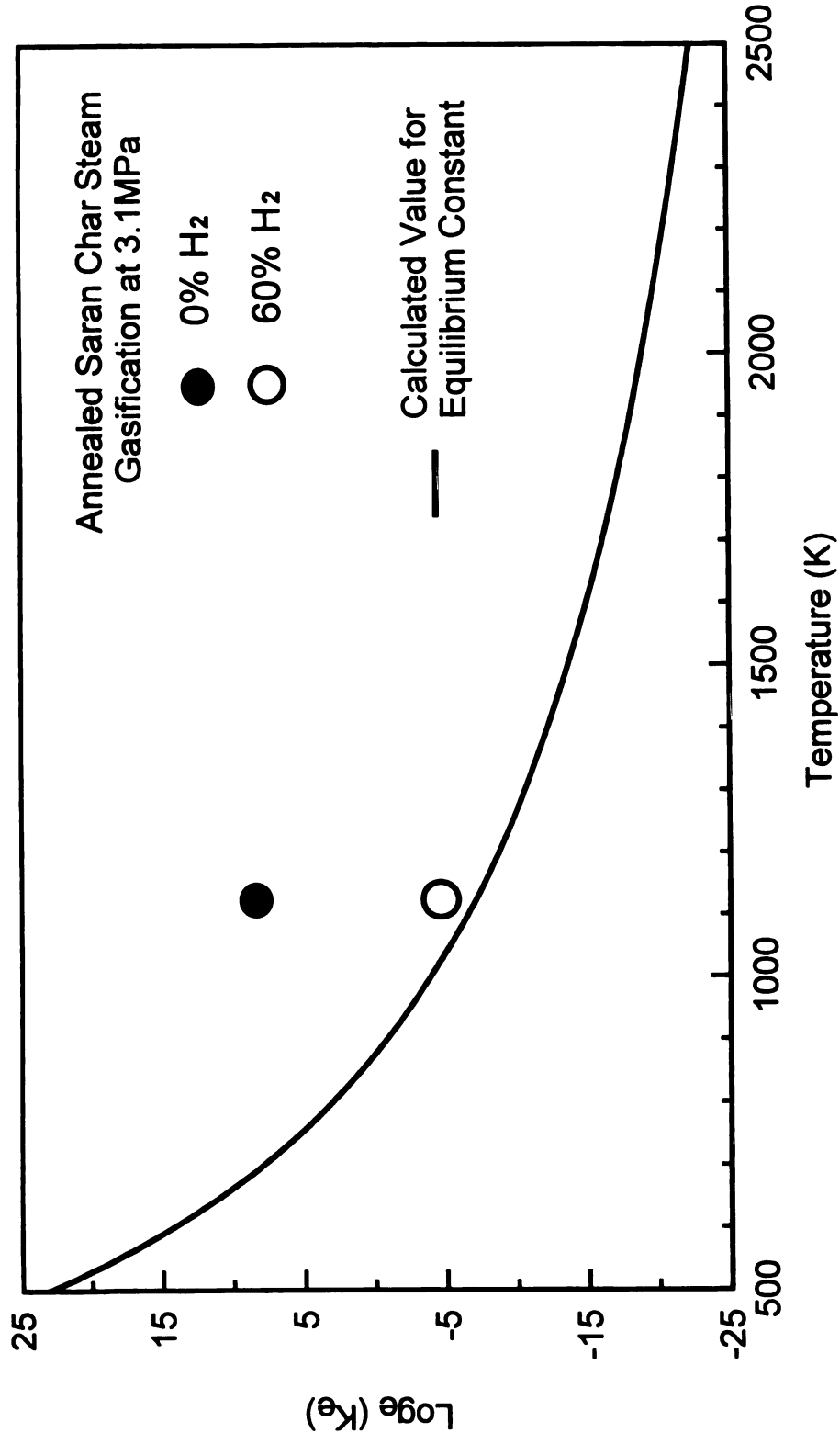


Figure 25: Equilibrium composition of the methanation reaction ($\text{CO}+3\text{H}_2=\text{H}_2\text{O}+\text{CH}_4$) and reactor effluent composition vs. temperature.

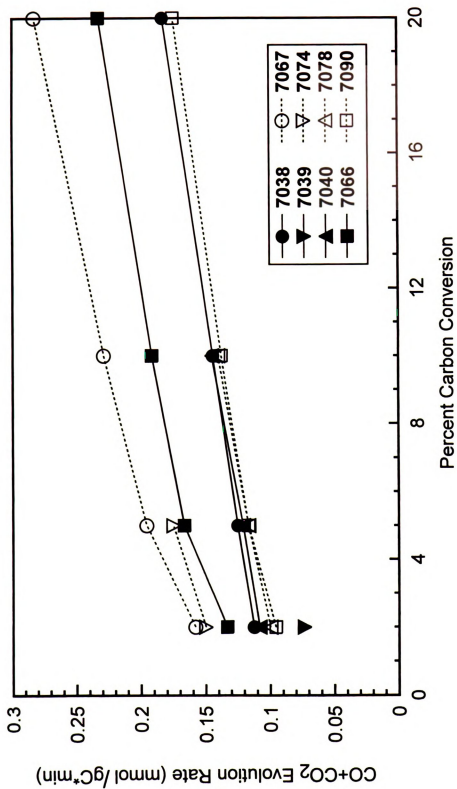


Figure 26: CO+CO₂ evolution rate from several runs of annealed Saran char steam gasification at 1.0 MPa in 40/0/60 H₂O/H₂/Ar.

experiments performed under this set of conditions than any other. Error analysis for these runs is shown at 2% conversion in Figure 27. A conversion of 2% was chosen for analysis because it represents steady state gasification, and it has the greatest number of values to analyze at steady state.

The average rate at 1.0 MPa and 40/0/60 H₂O/H₂/Ar is 1.43 mmol/gC*min with a standard deviation of 25%. This error is substantial, however char gasification rate varies well outside of this range at other sets of conditions used in this investigation. The gasification rate curves, which were calculated from mass spectral data, are accurate representations of actual reaction rate because the weight loss calculated from integration of the rate curves matches closely with measured weight loss. Calculated weight loss is consistently 1-3% less than measured weight loss, mostly due to a small amount of sample retention in the microreactor due to static electricity.

Rate data at all conditions tested are presented in Figures 28-33. Annealed Saran char was gasified under mixtures of Ar, H₂O, and H₂ at pressures of 0.3, 1.0, and 3.1 MPa. Reactant gases for all experiments contain 40% H₂O and varying ratios of H₂/Ar, with the exception of two experiments presented in Figure 29, in which reactant gas contained no

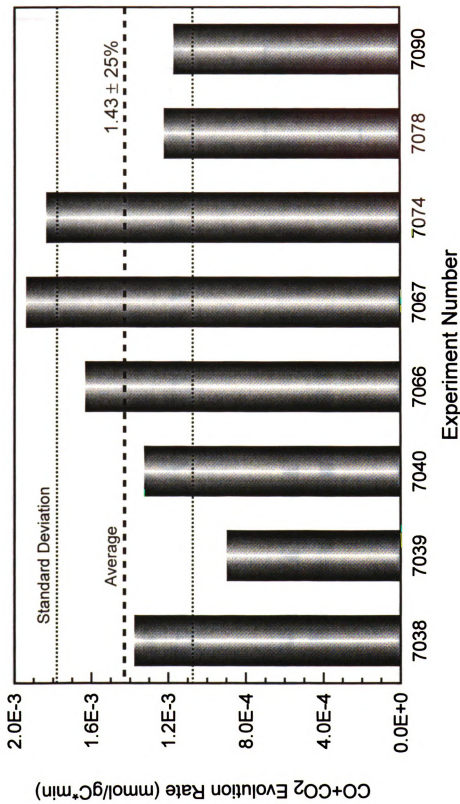


Figure 27: CO+CO₂ evolution rate from annealed Saran char steam gasification at 1.0 MPa in 40/0/60 H₂O/H₂/Ar; several runs at 2% carbon conversion.

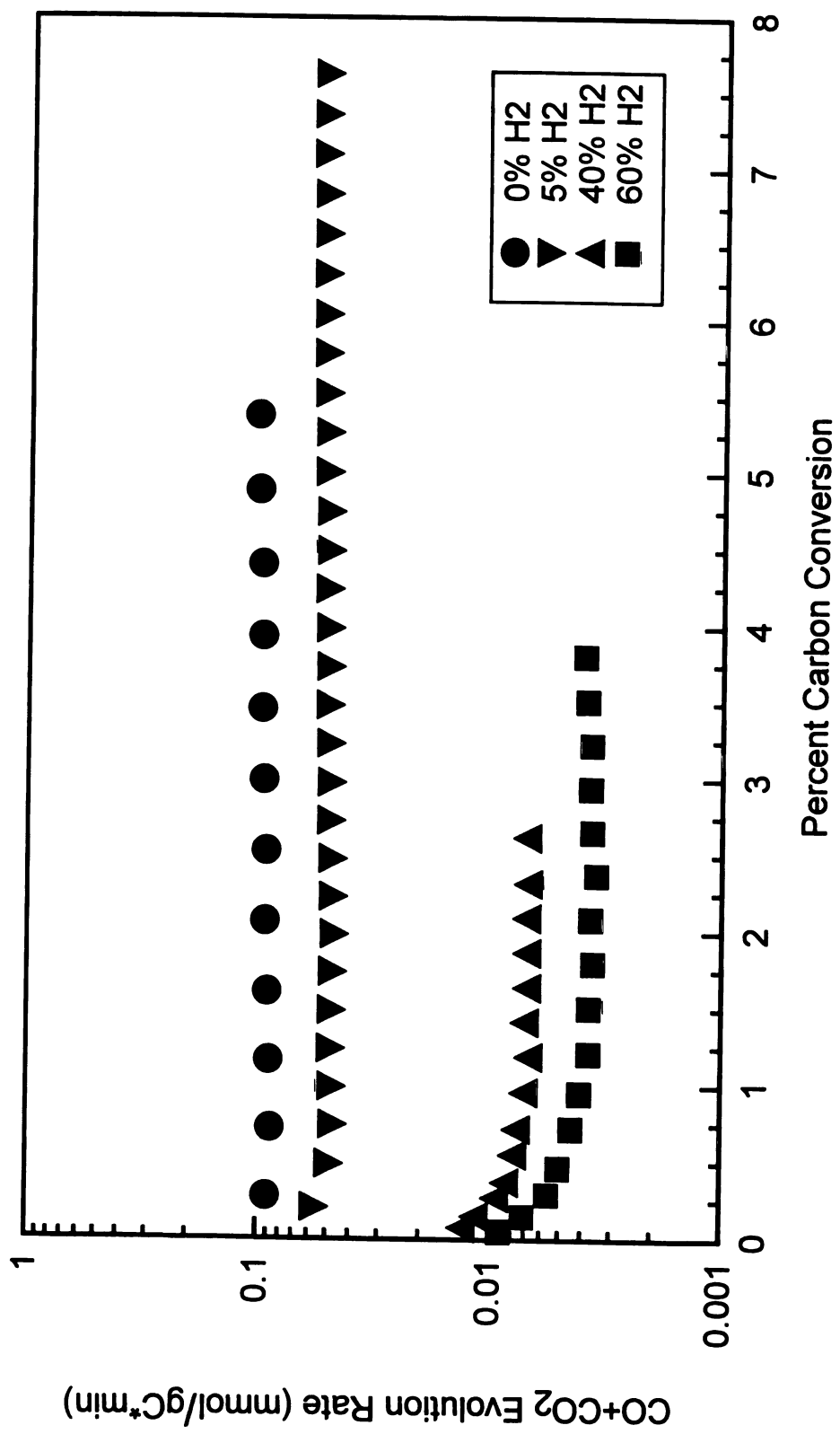


Figure 28: CO+CO₂ evolution rate from annealed Saran char steam gasification at 3.1 MPa.

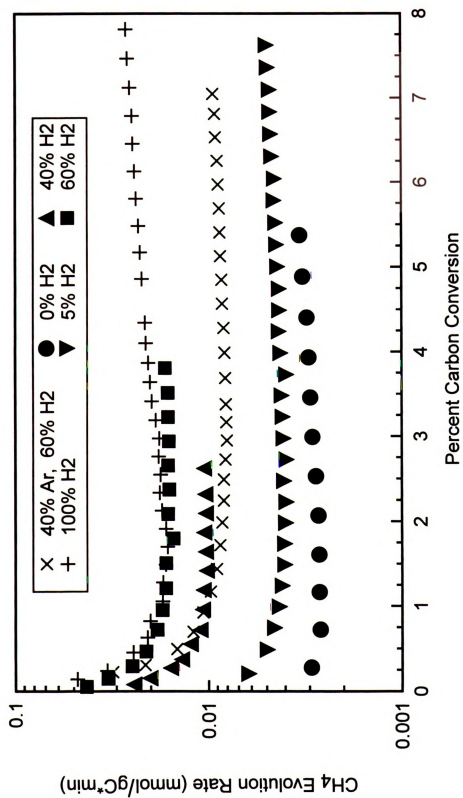


Figure 29: CH₄ evolution rate from annealed Saran char steam gasification at 3.1 MPa .

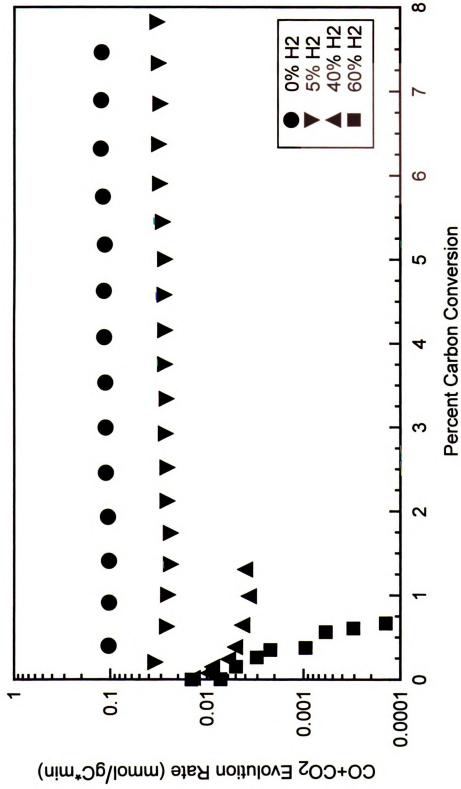


Figure 30: CO+CO₂ evolution rate from annealed Saran char steam gasification at 1.0 MPa.

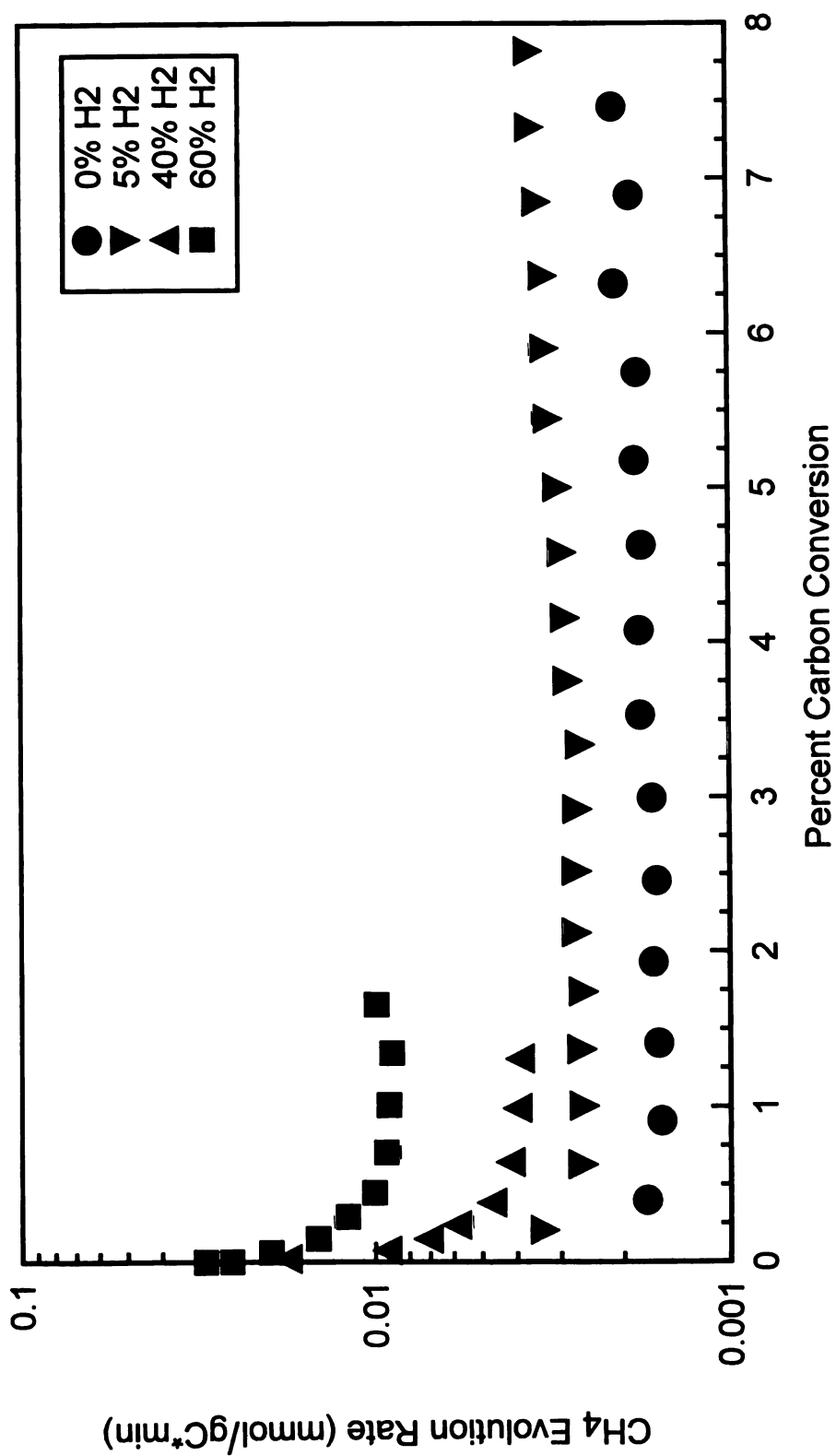


Figure 31: CH₄ evolution rate from annealed Saran char steam gasification at 1.0 MPa.

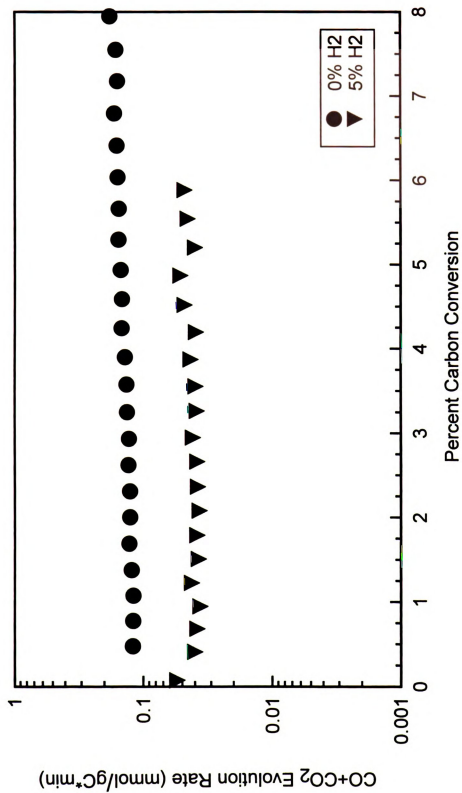


Figure 32: CO+CO₂ evolution rate from annealed Saran char steam gasification at 0.3 MPa.

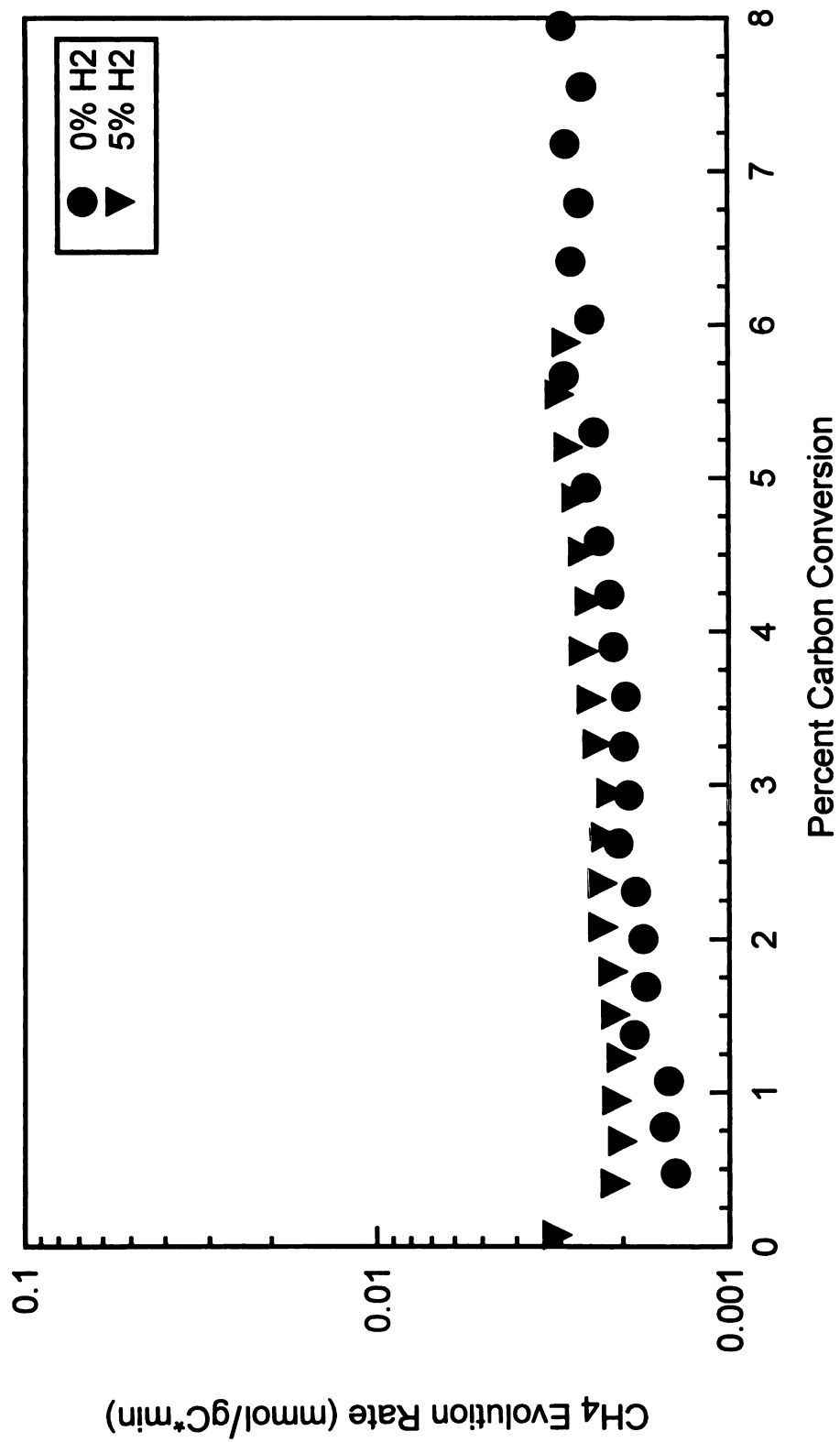


Figure 33: CH₄ evolution rate from annealed Saran char steam gasification at 0.3 MPa .

ti

gati

nost

sign

pres

ier

con

in

ack

tea

am

1981

frs

800

35

1980

hadr

pres

case

H₂O. Deuterated reactant gases were not chosen for the bulk of the gasification reactions for reasons given in Section 3.2.3.

Reaction rates at all tested pressures share several trends, the most obvious being a significant decrease in CO+CO₂ formation rate and significant increase in CH₄ formation rate with increasing H₂ partial pressure. A decrease in reaction rate for both CO+CO₂ and CH₄ formation over the first 1% conversion is also easily noted, and is much more pronounced under higher H₂ partial pressures. There is added difficulty in observing this phenomenon at higher reaction rates because of the lack of detector resolution with conversion. In the extreme case of a total pressure of 1.0 MPa and 60% H₂ in the reactant gas, the CO+CO₂ formation rate approaches zero. This has been observed by Weeda et al. [85] at higher H₂ partial pressures. Reaction rate stabilizes after the first 1% conversion for all conditions tested, and appears to remain at a constant value or increase slightly at higher conversions.

Gasification at 3.1 MPa and 1.0 MPa are compared in Figures 34 and 35 to show the effect of total pressure on species evolution rates. CO+CO₂ formation rate does not change with total pressure when no hydrogen is present in the reactant gas, but increases with total pressure when hydrogen is present. This is extremely pronounced in the case of 60% H₂ in the feed gas where CO+CO₂ formation rate declines to

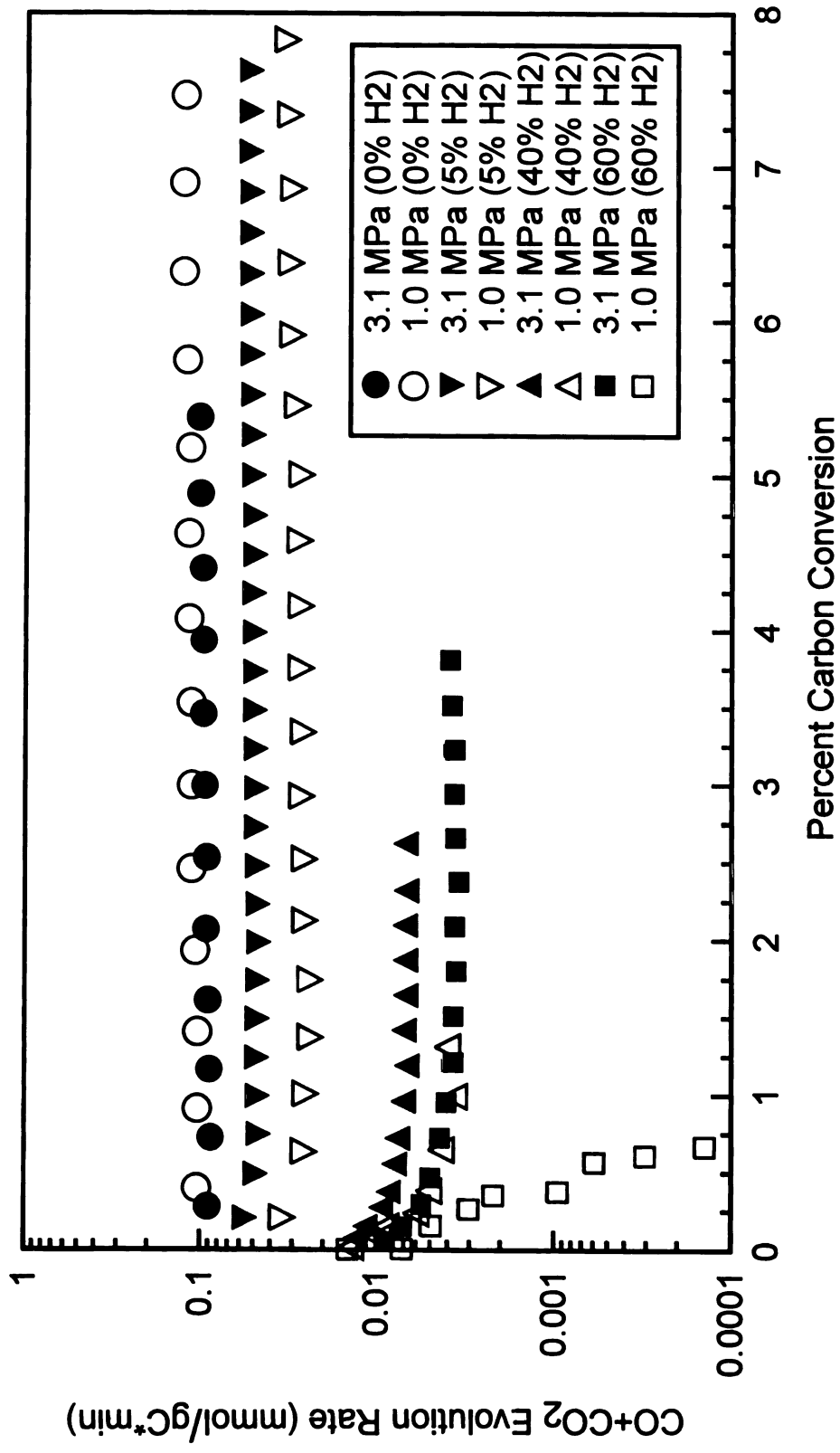


Figure 34: CO+CO₂ evolution rate from annealed Saran char steam gasification.

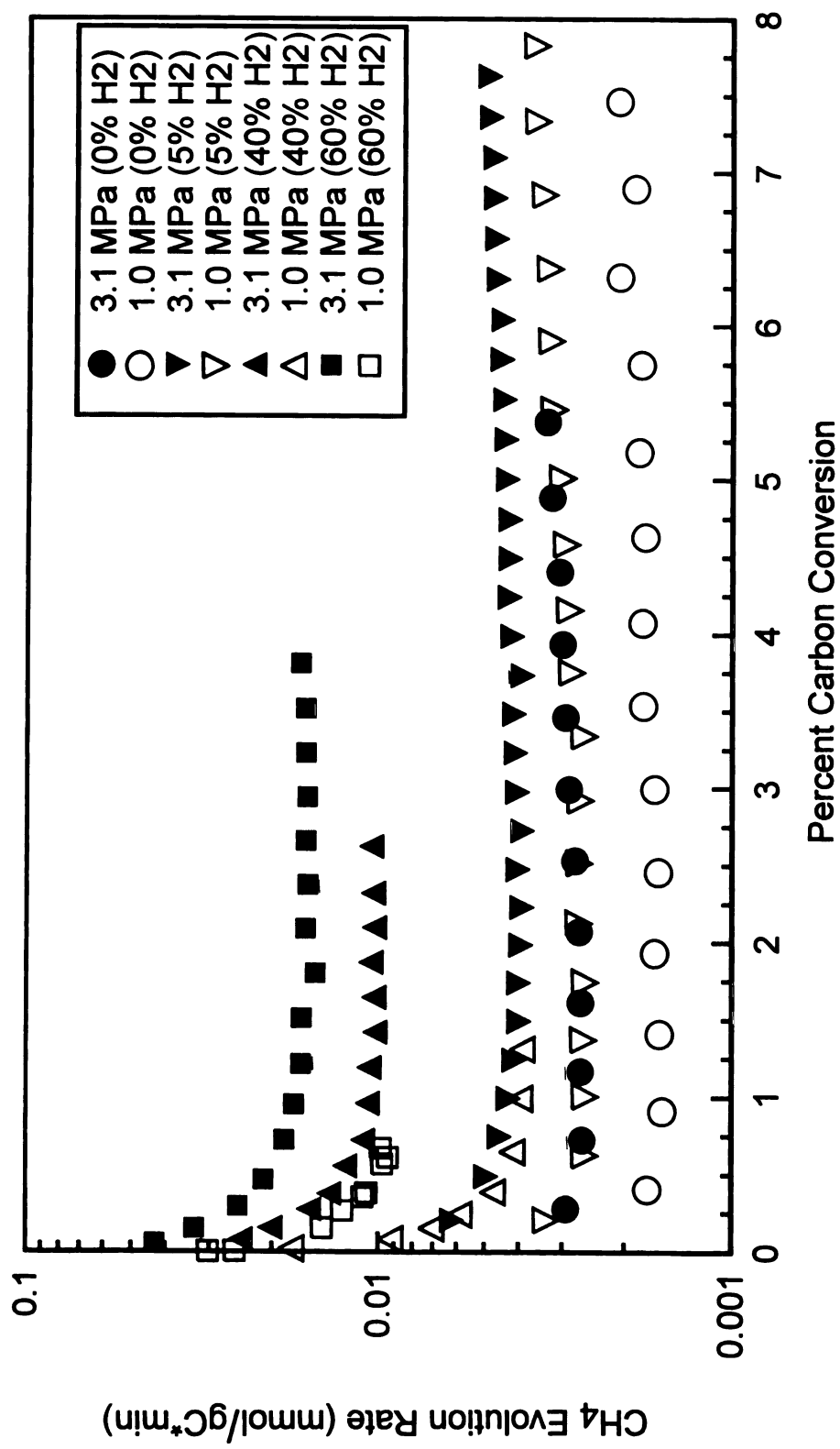


Figure 35: CH₄ evolution rate from annealed Saran char steam gasification.

zero at

directly

increase

shows a

En

negative

constant

the angle

evolution

the H₂A

zero up

results

to the t

have been

This shows

complete

done by

C

increased

includes

equation

zero at a total pressure of 1.0 MPa, but maintains a low but easily detectable value at a total pressure of 3.1 MPa. CH_4 formation rate increases with increasing total pressure at all compositions tested, and shows a more pronounced increase at higher hydrogen partial pressures.

Figure 36 shows the $\text{CO}+\text{CO}_2$ evolution rate of an experiment at 1.0 MPa in which the steam partial pressure in the reactant gas was kept constant at 40%, but the balance of the reactant gas was cycled between 60% Argon and 60% H_2 . Included on this graph as a reference is a $\text{CO}+\text{CO}_2$ evolution rate curve for a char gasification at 1.0 MPa with 40/0/60 $\text{H}_2\text{O}/\text{H}_2/\text{Ar}$ feed. The $\text{CO}+\text{CO}_2$ evolution rate rapidly declines to nearly zero upon a step change to 60% H_2 in the feed, which is consistent with results presented previously. After switching back to a feed containing no H_2 , the $\text{CO}+\text{CO}_2$ evolution rate rapidly increases back to what it would have been if there had been no step change in feed gas composition. This shows that beyond the first 1% conversion hydrogen inhibition is completely reversible. Though the conclusion drawn was different, work done by Huttinger and Merdes [8] shows a similar result.

Quadratic polynomials have been fit to both annealed Saran and annealed coal char surface areas as a function of conversion. Software included in Stanford Graphics (version 3.0) was used to calculate the equation for this curve based on a least squares fit, which can be seen

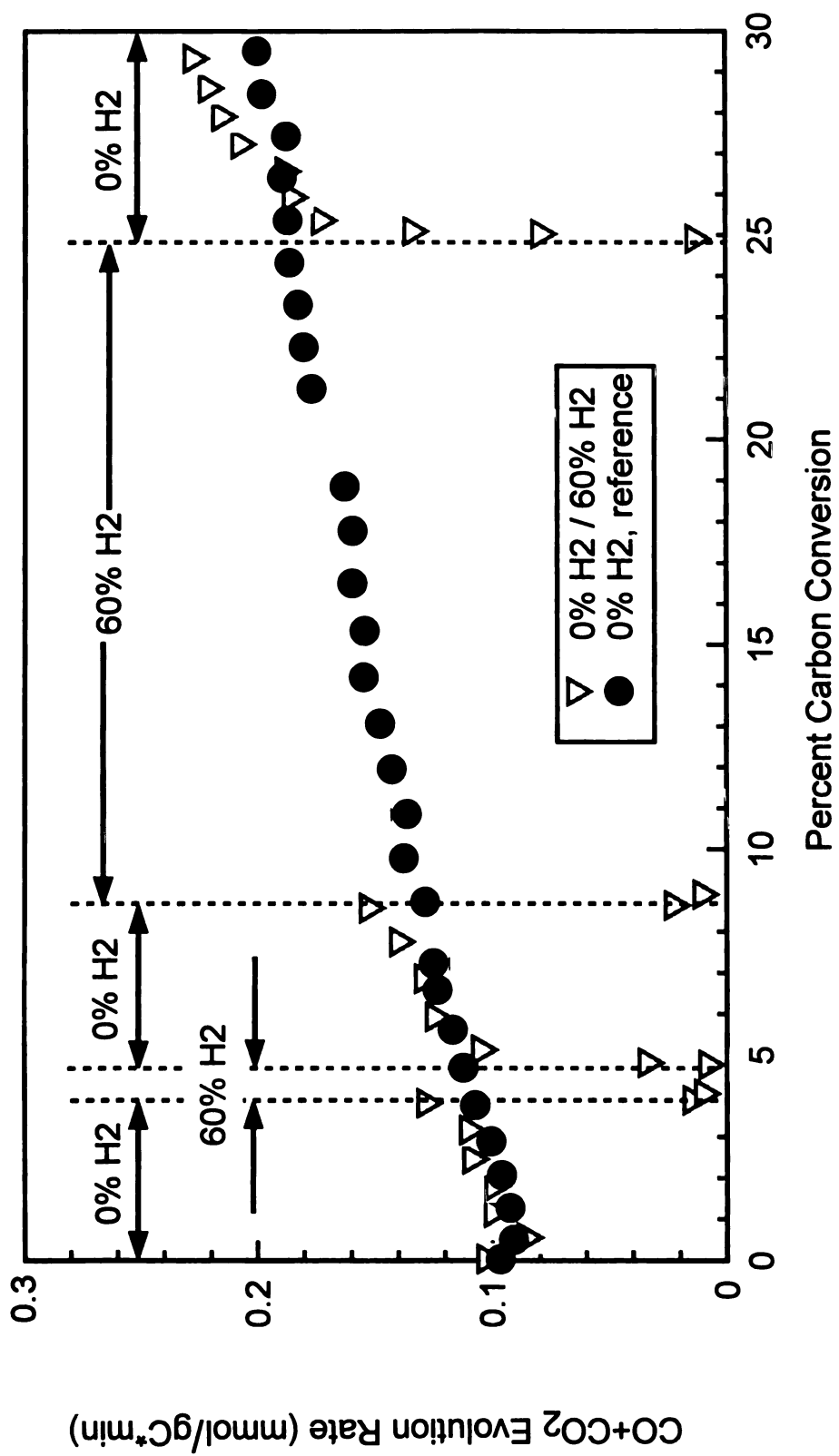


Figure 36: CO+CO₂ evolution rate from annealed Saran char steam gasification at 1.0M Pa with cycled reactant gas composition.

in Fig
follow
Percent
the c
area
rates
40-6
area
the fi
Except
Exper
Past 4
19-00
react
trend
also s
fact
ty a f

in Figures 37 and 38. For annealed Saran char the TSA curve fit is as follows:

$$\text{TSA (m}^2\text{/gC)} = 756 + 30.1x - 0.26x^2 \quad (22)$$

Percent carbon conversion is represented by x . The TSA for annealed coal char is as follows:

$$\text{TSA (m}^2\text{/gC)} = 8.15 + 16.6x - 0.38x^2 \quad (23)$$

Figures 39 and 40 compare $\text{CO}+\text{CO}_2$ and CH_4 formation rates from annealed Saran char gasification reported on a weight basis to formation rates reported on a surface area basis for a reactant gas composition of 40/0/60 $\text{H}_2\text{O}/\text{H}_2/\text{Ar}$ and 1.0 MPa total pressure. An increase in surface area is mainly responsible for the increase in $\text{CO}+\text{CO}_2$ evolution rate for the first 40% conversion. The rate is constant at $0.02 \text{ mmol/m}^2\cdot\text{min}$ except for the first 3% conversion, which is thought to be an experimental anomaly as it is inconsistent with all other experiments. Past 40% conversion, the surface area remains fairly constant but the $\text{CO}+\text{CO}_2$ evolution rate still increases, indicating an increase in reactivity of the char surface by a factor of about two. A similar trend can be seen with CH_4 formation in Figure 40, but the first 40% also shows a mild increase in reactivity of the char on a surface area basis. Overall, the char surface reactivity for CH_4 formation increases by a factor of about four. Figures 41 and 42 show the results of an

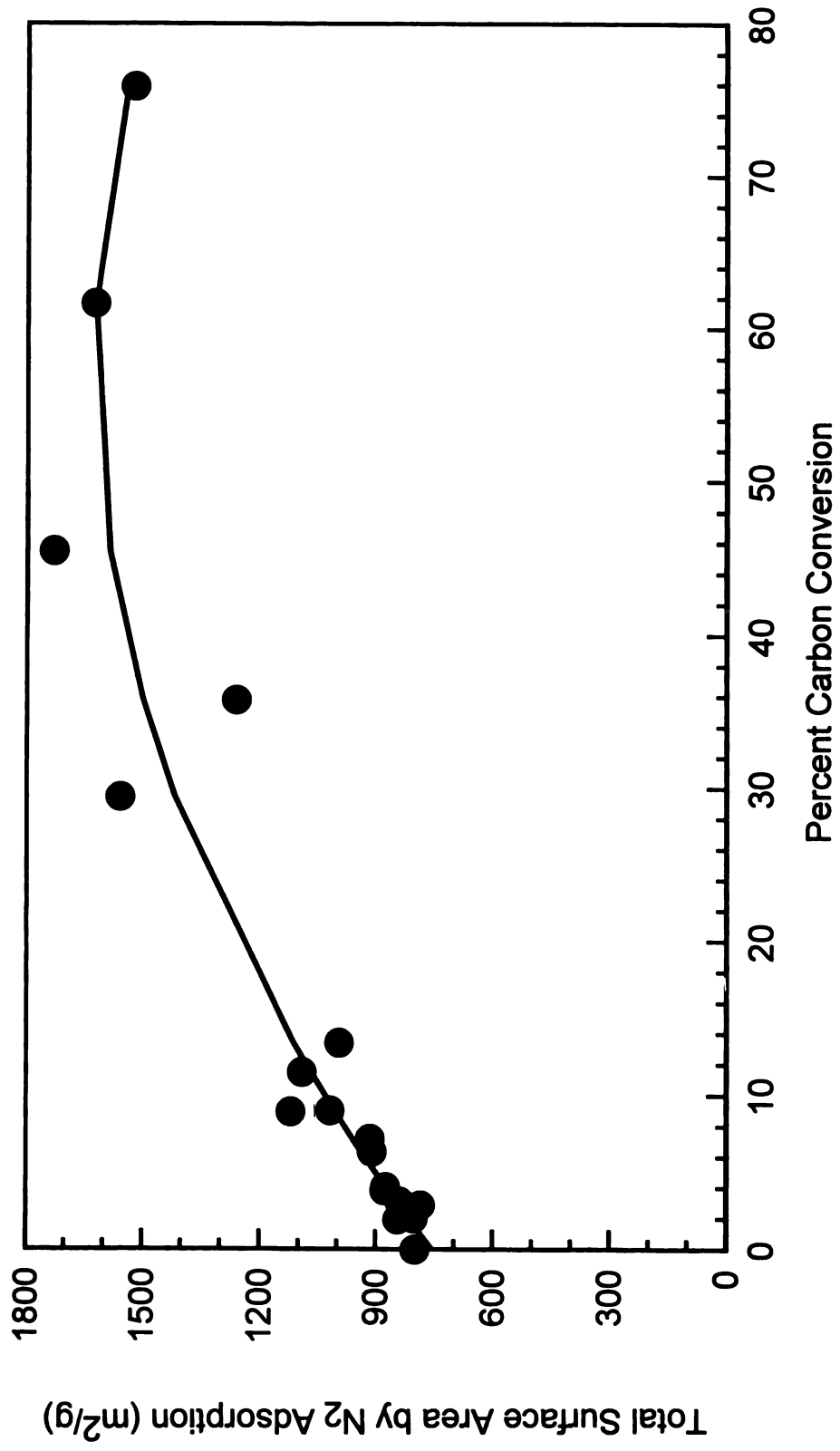


Figure 37: Quadratic polynomial least squares fit to annealed Saran char total surface area following gasification in steam.

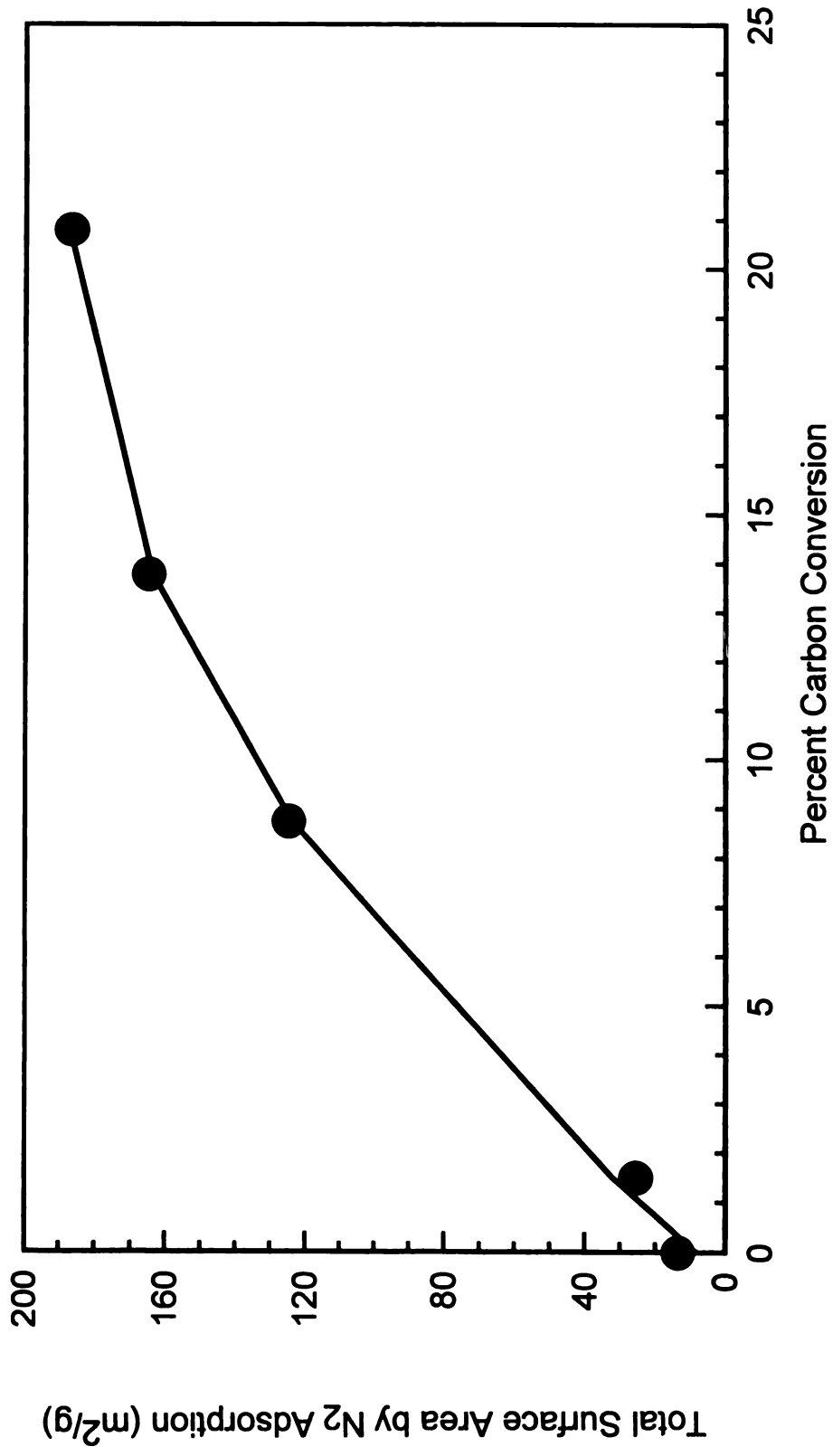


Figure 38: Quadratic polynomial least squares fit to annealed coal char total surface area following gasification in steam.

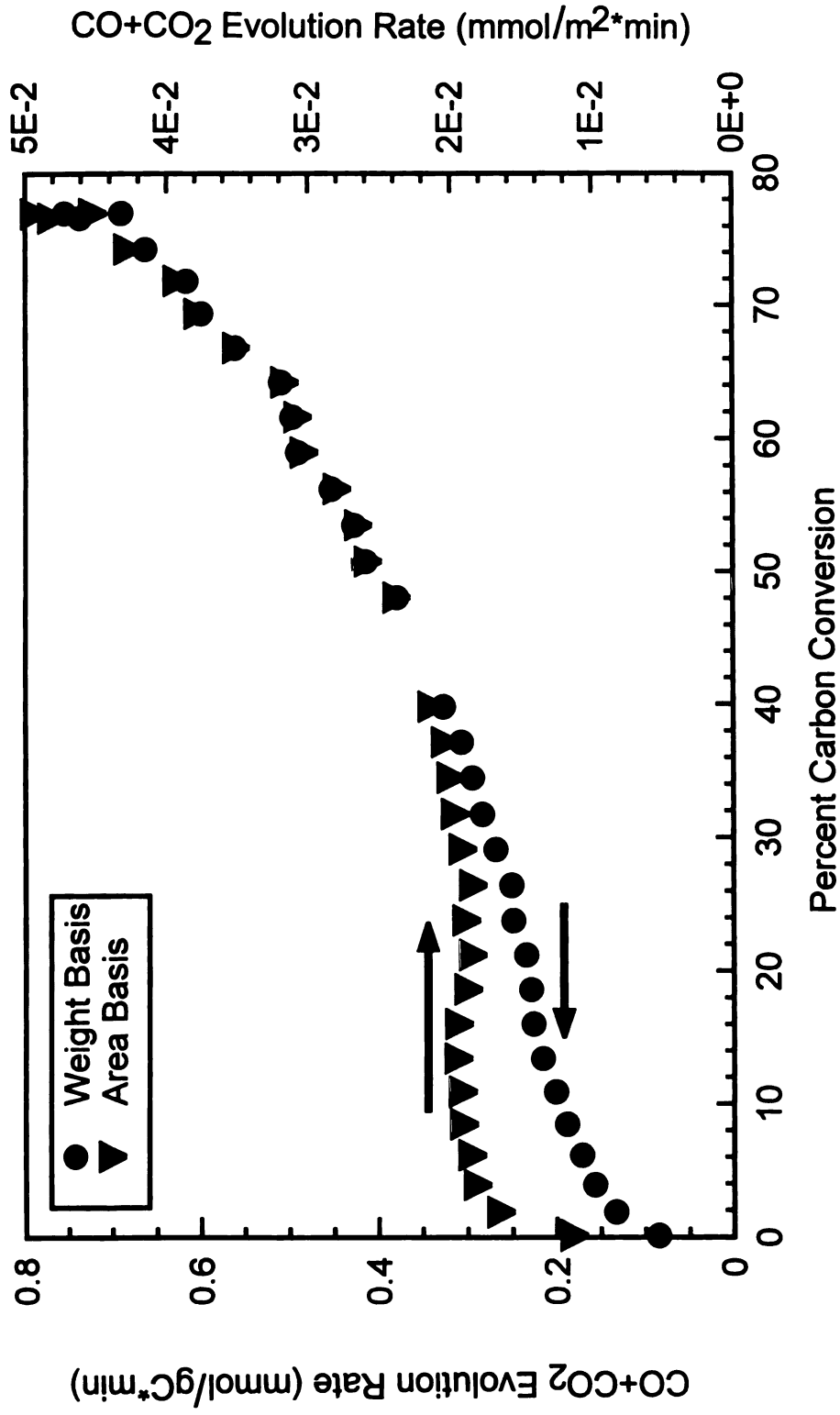


Figure 39: CO+CO₂ evolution rate from annealed Saran char steam gasification at 1.0 MPa in 40/0/60 H₂O/H₂/Ar; rate per unit weight and unit surface area basis.

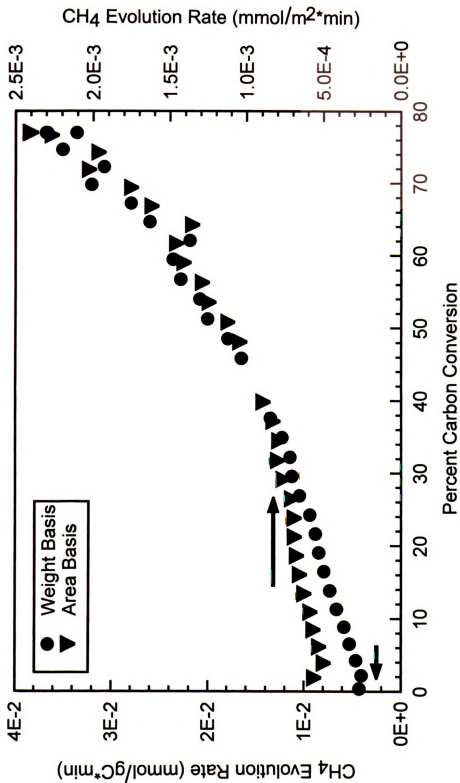


Figure 40: CH₄ evolution rate from annealed Saran char steam gasification at 1.0 MPa in 40/0/60 H₂O/H₂/Ar; rate per unit weight and unit surface area basis.

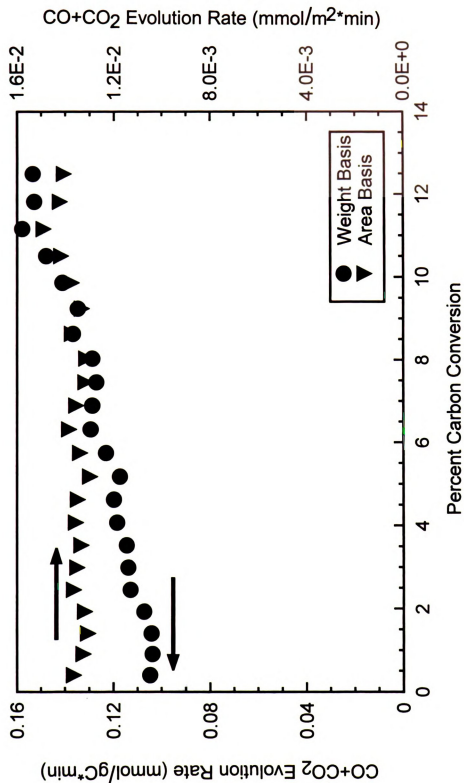


Figure 41: CO+CO₂ evolution rate from annealed Saran char steam gasification at 1.0 MPa in 40/0/60 H₂O/H₂/Ar; rate per unit weight and unit surface area basis.

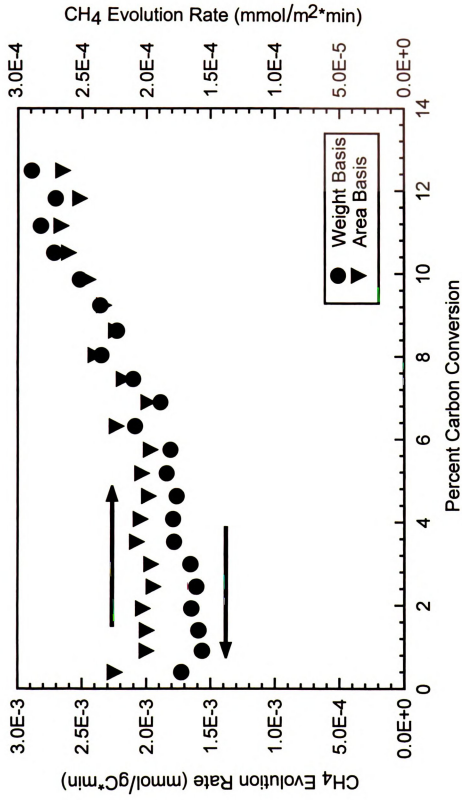


Figure 42: CH₄ evolution rate from annealed Saran char steam gasification at 1.0 MPa in 40/0/60 H₂O/H₂/Ar; rate per unit weight and unit surface area basis.

experiment that was performed under identical conditions, but to a much lower conversion. The rate behavior over the first 3% conversion is consistent with the rest of the experiments performed in this investigation.

Figure 43 compares $\text{CO}+\text{CO}_2$ and CH_4 formation rates from annealed Saran char gasification reported on a weight basis to formation rates reported on a surface area basis for a reactant gas composition of 40/60/0 $\text{H}_2\text{O}/\text{H}_2/\text{Ar}$ and 1.0 MPa total pressure. This experiment had to be performed for 24 hours because the reaction rate under these conditions is much lower than that of the previously described experiment, hence the missing rate data between 3-8% conversion representing the overnight period. The low reaction rate is also the reason why there is so much more scatter in these data compared to the previously described experiment. The $\text{CO}+\text{CO}_2$ formation rate appears to abruptly increase at the start of data collection after the first range of missing data, but this is an artifact of opening the inlet valve to the vacuum chamber that the mass spectrometer is attached to. There is essentially no $\text{CO}+\text{CO}_2$ formation under these conditions, which is consistent with other experiments in this investigation. The increase in CH_4 formation is partially compensated for by the increase in char surface area, but

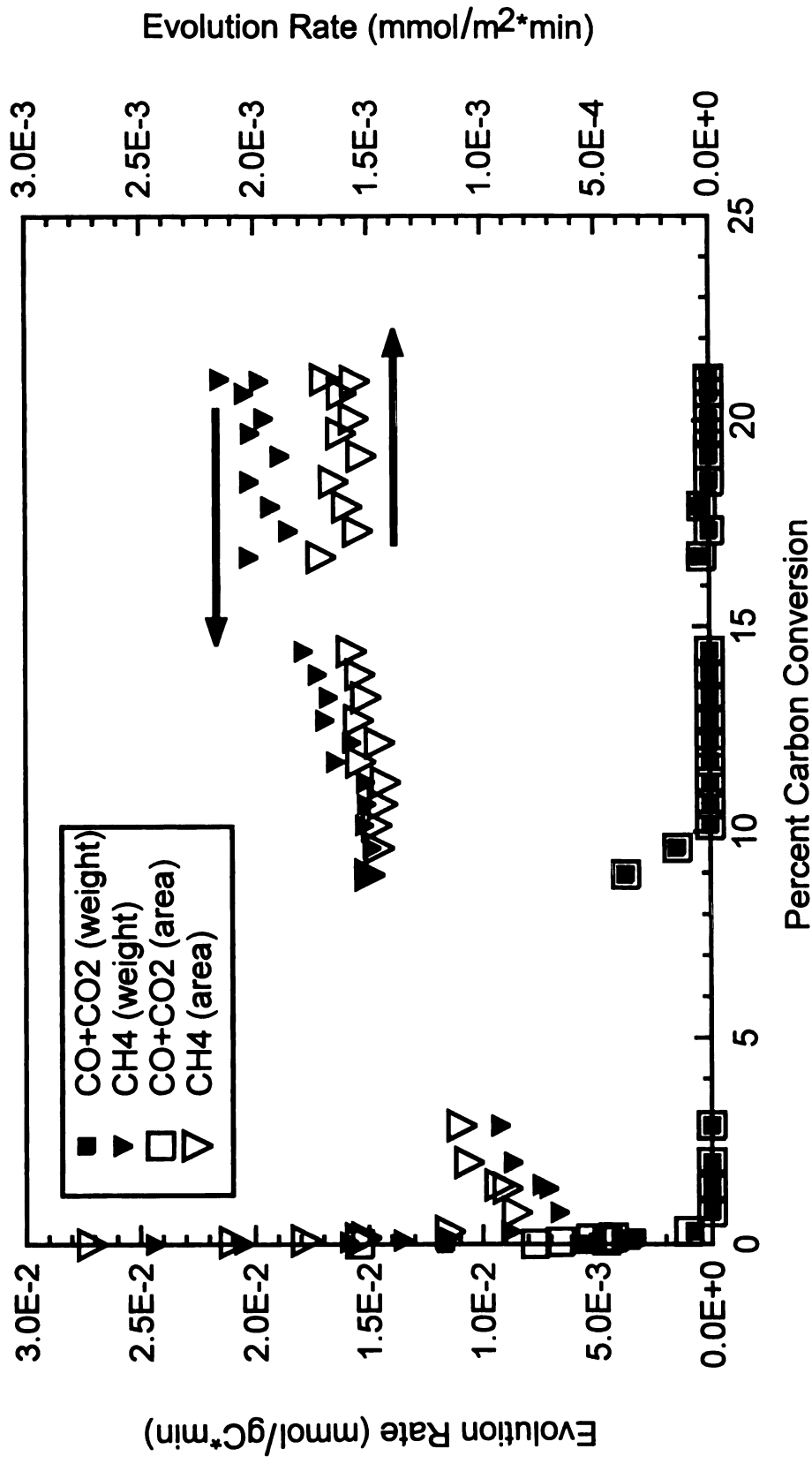


Figure 43: Evolution rate from annealed Saran char steam gasification at 1.0 MPa in 40/60/0 H₂O/H₂/Ar; rate per unit weight and unit surface area basis.

reactivity per unit surface area still increases slightly over the first 20% conversion.

3.2.2.1.2. Annealed Coal Char Steam Gasification

Annealed coal char steam gasification rate is shown in Figure 44. The $\text{CO}+\text{CO}_2$ and the CH_4 formation rates are about half that of annealed Saran char on a weight basis. Rate increases gradually over the first 10% and appears to be stable up to 20%. Pressure fluctuations at the initiation of the reaction have made analysis of possible transient behavior difficult.

Figures 45 and 46 compare $\text{CO}+\text{CO}_2$ and CH_4 formation rates from annealed coal char gasification reported on a weight basis to formation rates reported on a surface area basis for a reactant gas composition of 40/0/60 $\text{H}_2\text{O}/\text{H}_2/\text{Ar}$ and 1.0 MPa total pressure. Formation rates of all species on a surface area basis are actually several times higher for coal than for Saran, because of the catalytic effect of ash.

Unlike rate curves for formation of species on a weight basis, rate curves for formation of species on a surface area basis clearly show initial transient behavior. The initial decrease in $\text{CO}+\text{CO}_2$ as well as CH_4 formation persists to almost 10% conversion, compared to annealed Saran char which displays initial transient behavior over the first 1% conversion. This is most likely due to a higher content of dangling and

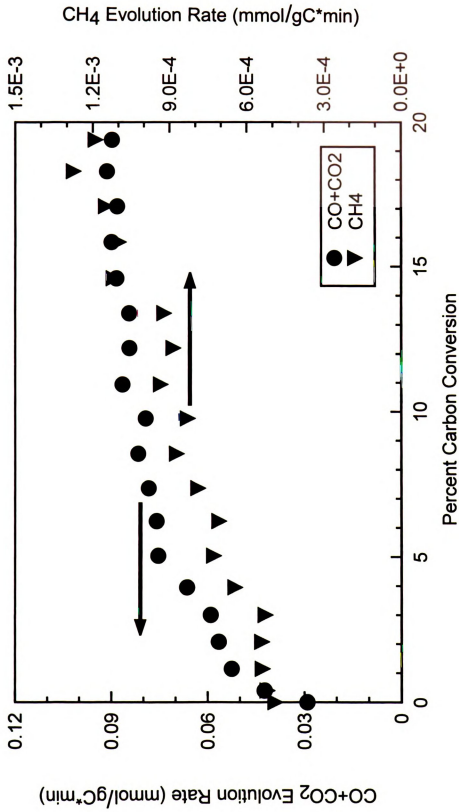


Figure 44: Product gas evolution rate from annealed coal char steam gasification at 1.0 MPa in 40/0/60 H₂O/H₂/Ar.

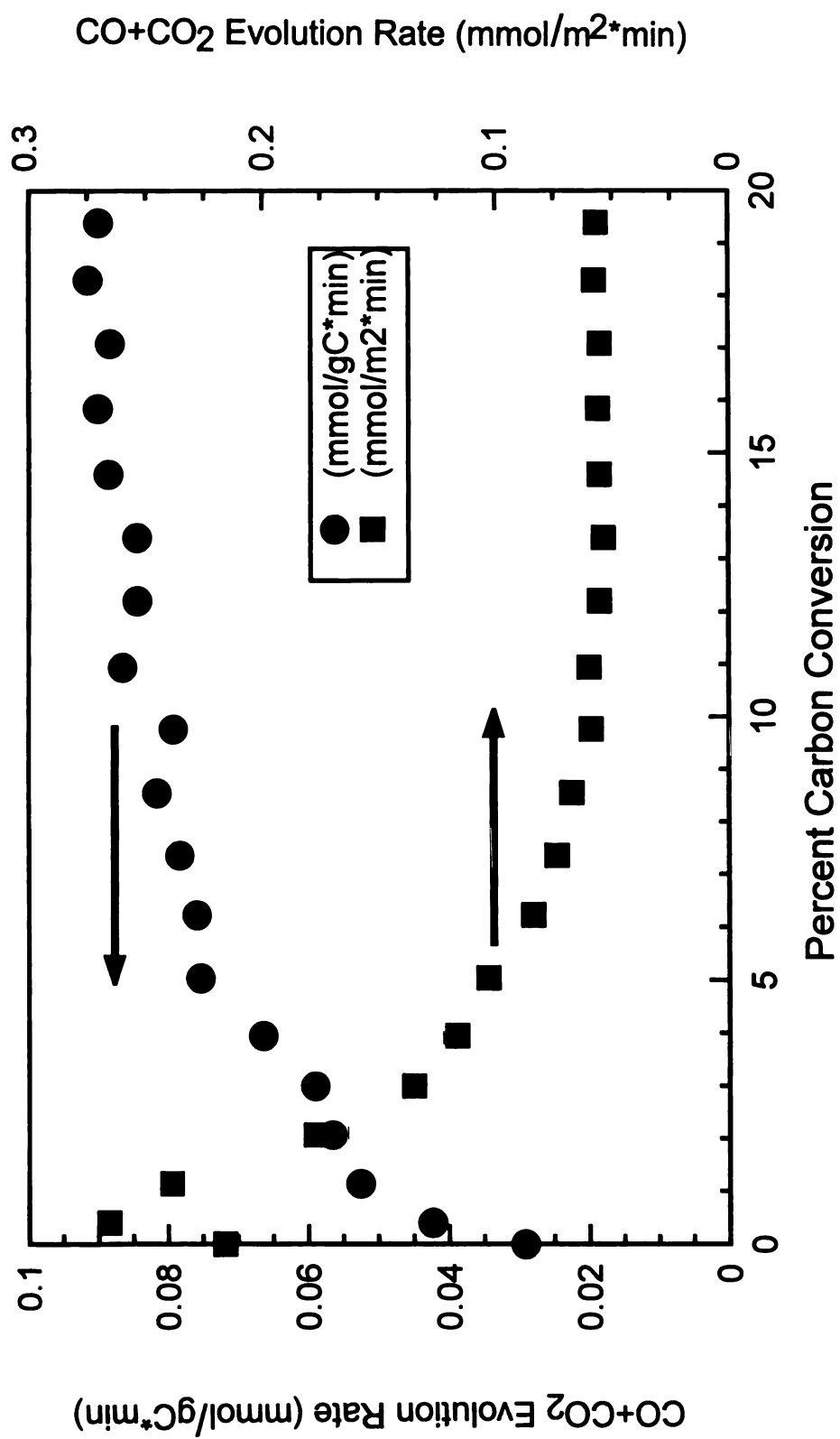


Figure 45: CO+CO₂ evolution rate from annealed coal char steam gasification at 1.0 MPa in 40/0/60 H₂O/H₂/Ar; unit weight and unit surface area basis.

1

1 25 3

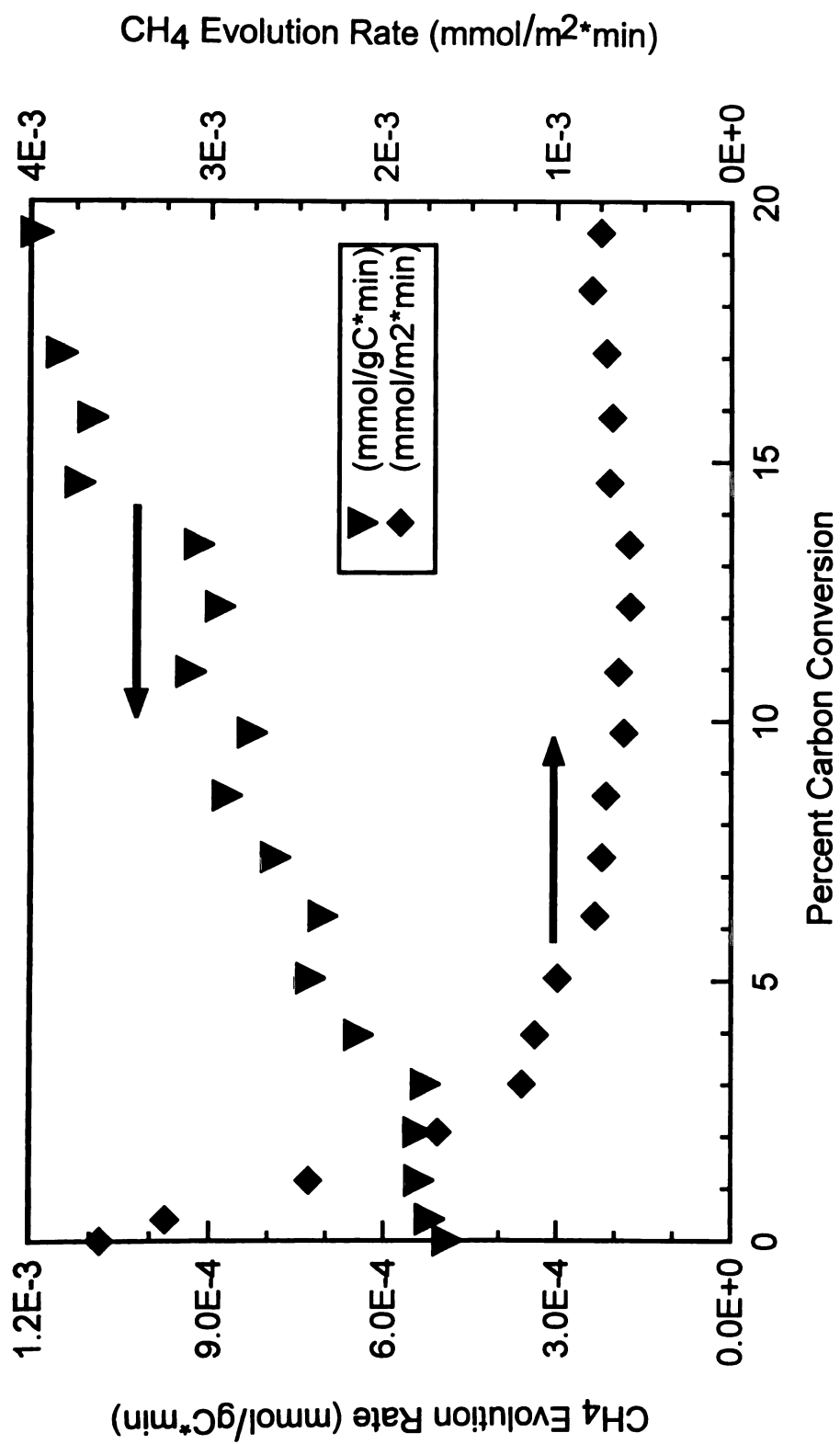


Figure 46: CH₄ evolution rate from annealed coal char steam gasification at 1.0 MPa in 40/0/60 H₂O/H₂/Ar; unit weight and unit surface area basis.

amorphous carbons in annealed coal char, and perhaps the ash in the coal can catalyze the rapid reaction of carbons that are semi-ordered that would not be subject to this kind of reaction in the low ash Saran. Both $\text{CO}+\text{CO}_2$ and CH_4 formation rates remain constant up to 20% conversion after the initial transient behavior.

3.2.2.2. Unannealed Char Steam Gasification

Unannealed Saran char was gasified in H_2O at a lower temperature than the annealed material with and without the presence of H_2 in the reactant gas. Reactivity profiles at 1000 K and 3.1 MPa are shown in Figure 47 and share most of the same trends with annealed Saran char, including a decrease in $\text{CO}+\text{CO}_2$ formation and an increase in CH_4 formation with increasing H_2 partial pressure. Gasification rate declines over the first 3% conversion and then stabilizes with no H_2 present in the reactant gas, but when H_2 is present the rate continues to decline over at least 18% conversion.

Unannealed coal char was also gasified in H_2O under the same conditions as the unannealed Saran char, and shares the same trends as well. Figure 48 shows that the only differences in reaction rate behavior between unannealed coal and Saran chars are that the effect of hydrogen inhibition is less pronounced with coal char, and it takes up

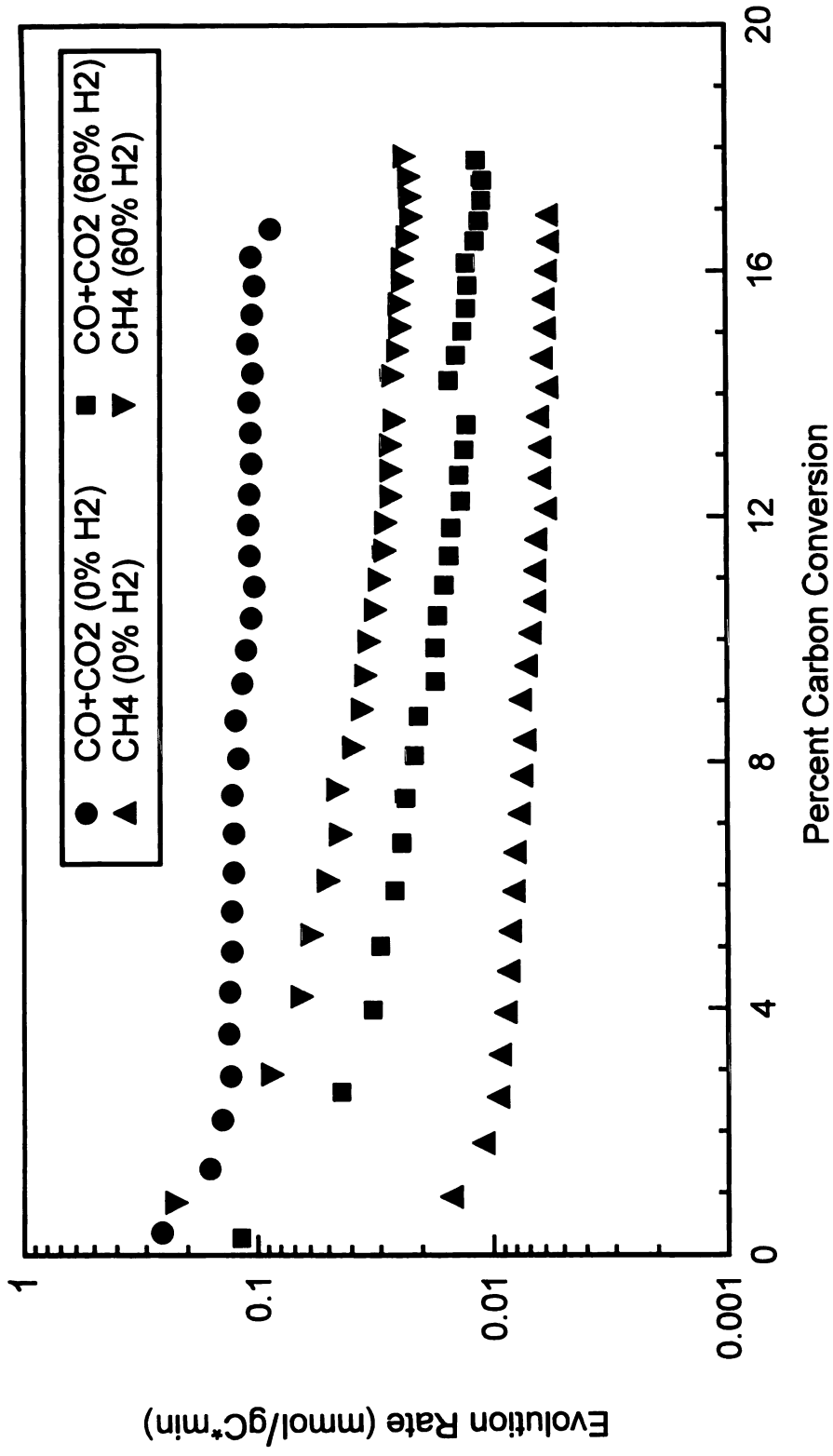


Figure 47: Product gas evolution rate from unannealed Saran char steam gasification at 1000K and 3.1 MPa.

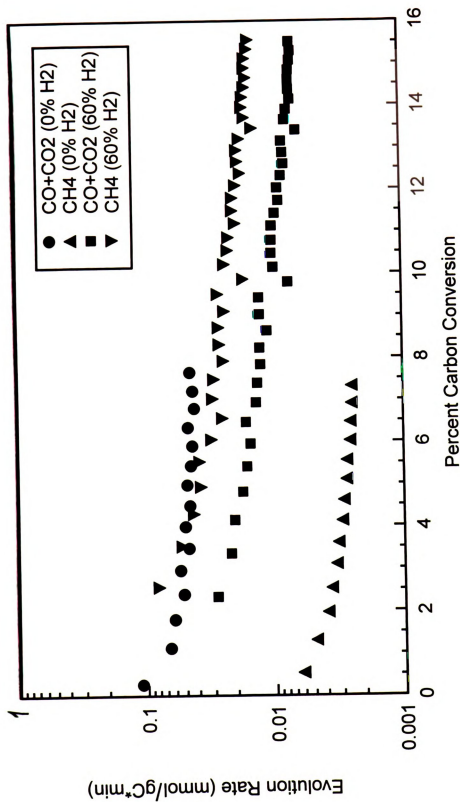


Figure 48: Product gas evolution rate from unannealed coal char steam gasification at 1000 K and 3.1 MPa.

to 5% conversion for the coal char gasification rate to stabilize under conditions of no H_2 in the reactant gas.

3.2.3. Isotopic Studies

Annealed Saran char was gasified in 40%/60% D_2O/Ar at 3.1 MPa for a kinetic comparison between gasification rates of annealed Saran char in deuterated and non-deuterated reactant gases. Figure 49 shows that the rate in D_2O is about three fourths of the rate in H_2O and follows the same behavior, which is consistent with results of Mims and Pabst [61]. Initial rate declines over the first 1% conversion, followed by a gradual increase over the rest of conversion. The difference in gasification rate between the two isotopes indicates that the breaking of hydrogen bonds is definitely involved in rate limitation.

3.3. Adsorbed Hydrogen Concentration

3.3.1. Transient Hydrogen Desorption

Verifying and quantifying the existence of transient species on sample surfaces during gasification is crucial to development of an understanding of reaction phenomenon. H_2 (or D_2) immediately desorbing from the newly quenched surface of a gasified char would be indicative of weakly and perhaps "associatively" bound hydrogen, which would have to be included in active site balances and mechanistic models of the

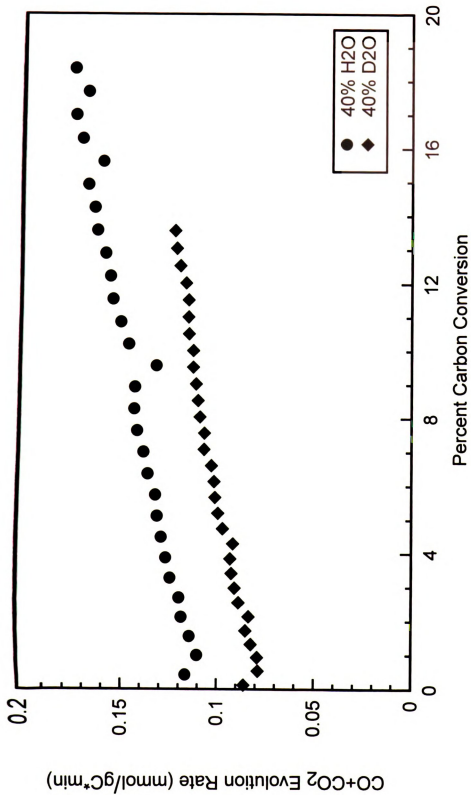


Figure 49: CO+CO₂ evolution rate from annealed Saran char H₂O or D₂O gasification at 3.1 MPa; reactant gas balance is 60% Argon.

char gasification reaction. Further, the system transient response must be subtracted from any transient species desorption to obtain an actual species transient response.

Figure 50 shows high-resolution scans of the end of a D_2O gasification, where there has been a step change from reactant gas to purge gas. Both the D_2 and the Kr show abrupt declines in effluent concentration after about 30 seconds. The D_2 transient response curve matches the Kr curve exactly, indicating that there is no loosely bound D on the char surface that is lost with the removal of D_2 partial pressure. This finding shows that all of the surface D_2 (or H_2) can be quantified with TPD; high-resolution scans for transient surface D_2 (or H_2) do not need to be done at the end of each char gasification.

3.3.2. Adsorbed Hydrogen: Unit Weight Basis

Adsorbed hydrogen concentration was measured on annealed chars following H_2O/H_2 gasification by TPD in flowing Argon at 5 K/min to 1773 K and holding for 1 hour. Figure 51 shows two typical hydrogen TPD profiles for annealed Saran char following H_2O/H_2 gasification to different extents of char conversion. There is a large and distinct peak for each TPD from 1100-1600 K that indicates dissociatively bound hydrogen, but no peaks at lower temperatures which would indicate "associatively" bound hydrogen.

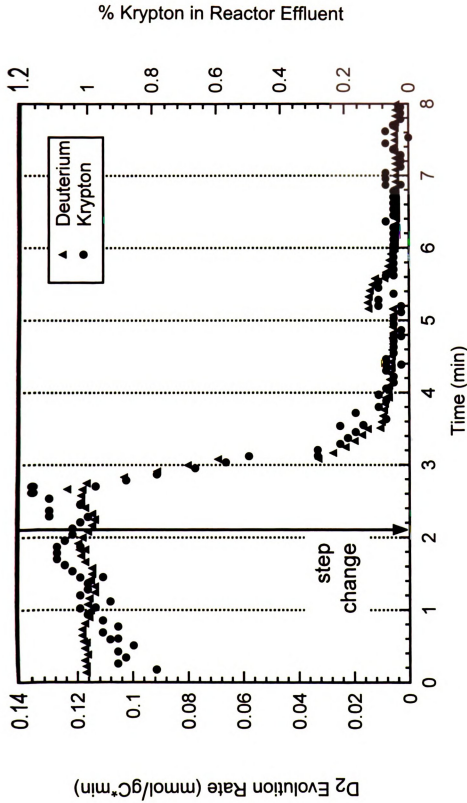


Figure 50: Step change in feed gas composition during annealed Saran char gasification from 40 /60 D₂O/Ar(Kr) to 100% Ar at 2.11 minutes.

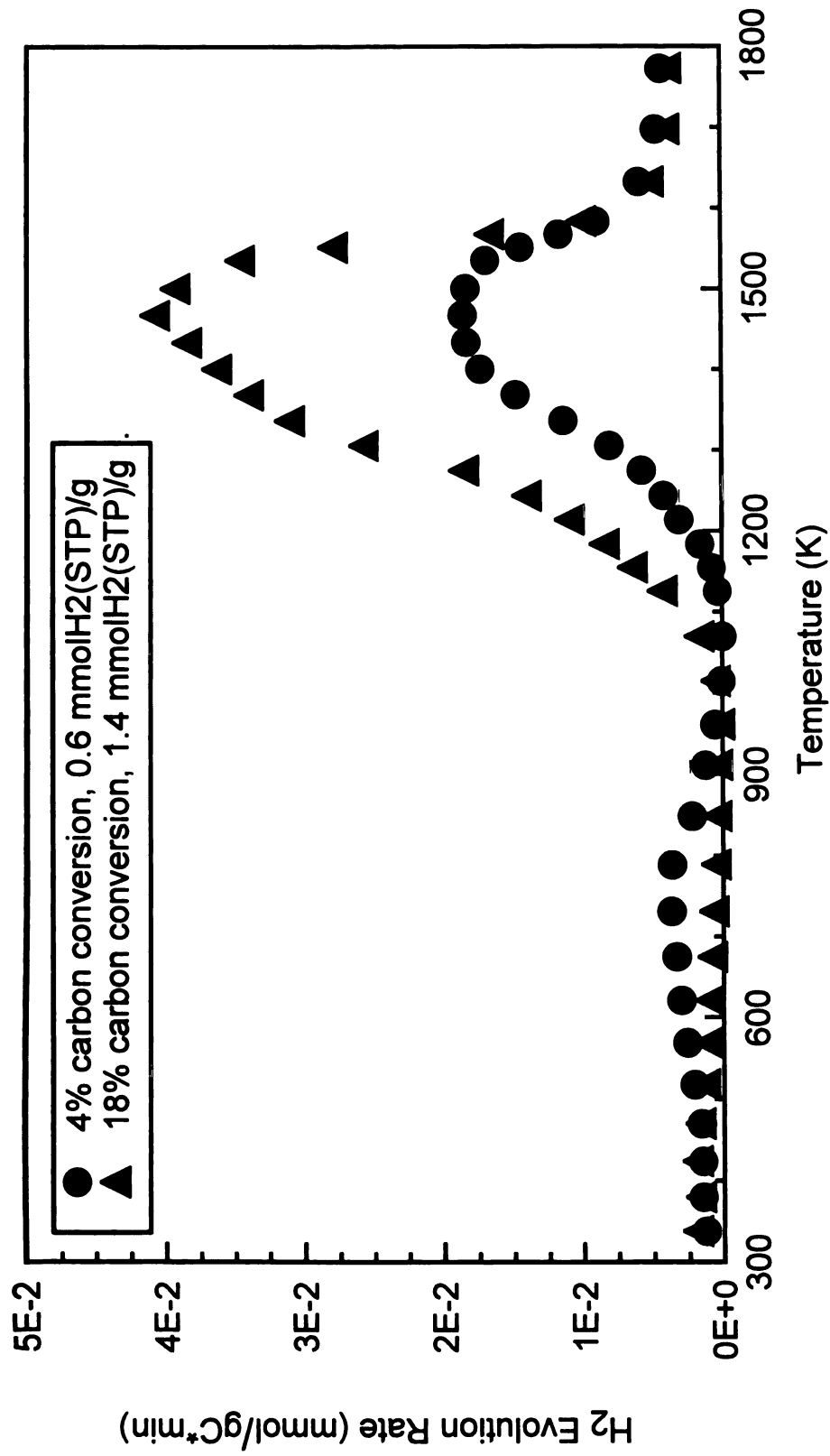


Figure 51: Temperature programmed desorption profile of H₂ from annealed Saran char following steam gasification at 1123 K.

"Associatively" bound hydrogen will adsorb onto chars if they are cooled in the presence of hydrogen after gasification. Figure 52 shows TPD profiles for annealed Saran char after hydrogasification and subsequent cooling in argon or hydrogen. The char quenched in argon shows only dissociatively adsorbed hydrogen, while the char quenched in hydrogen produces another TPD peak centered upon 900 K, indicating 0.02 mmolH₂(STP)/gC of "associatively" bound hydrogen. This hydrogen is not stable on char surfaces during gasification because the TPD peak center is 223 K lower than the experimental gasification temperature of 1123 K.

Figure 53 shows adsorbed hydrogen concentration on annealed chars at several conditions. Surprisingly, the adsorbed hydrogen concentration appears to be independent of reactant gas composition and pressure, spanning the range from 0% H₂ at 0.3 MPa to 100% H₂ at 3.1 MPa. The value starts out very low at 0.02 mmolH₂(STP)/g for unreacted chars, increases rapidly over the first 1-1.5% conversion to 1.2 mmolH₂(STP)/g for Saran char, and increases gradually over the rest of conversion to about 4.0 mmolH₂(STP)/g. The initial adsorbed hydrogen concentration is close to the value given by ultimate analysis of 0.019 wt%, (0.09 mmolH₂(STP)/g). The average adsorbed hydrogen concentration over the bulk of conversion is about 2.5 mmolH₂(STP)/g, which matches the quantity given by the ultimate analysis for unannealed Saran char of

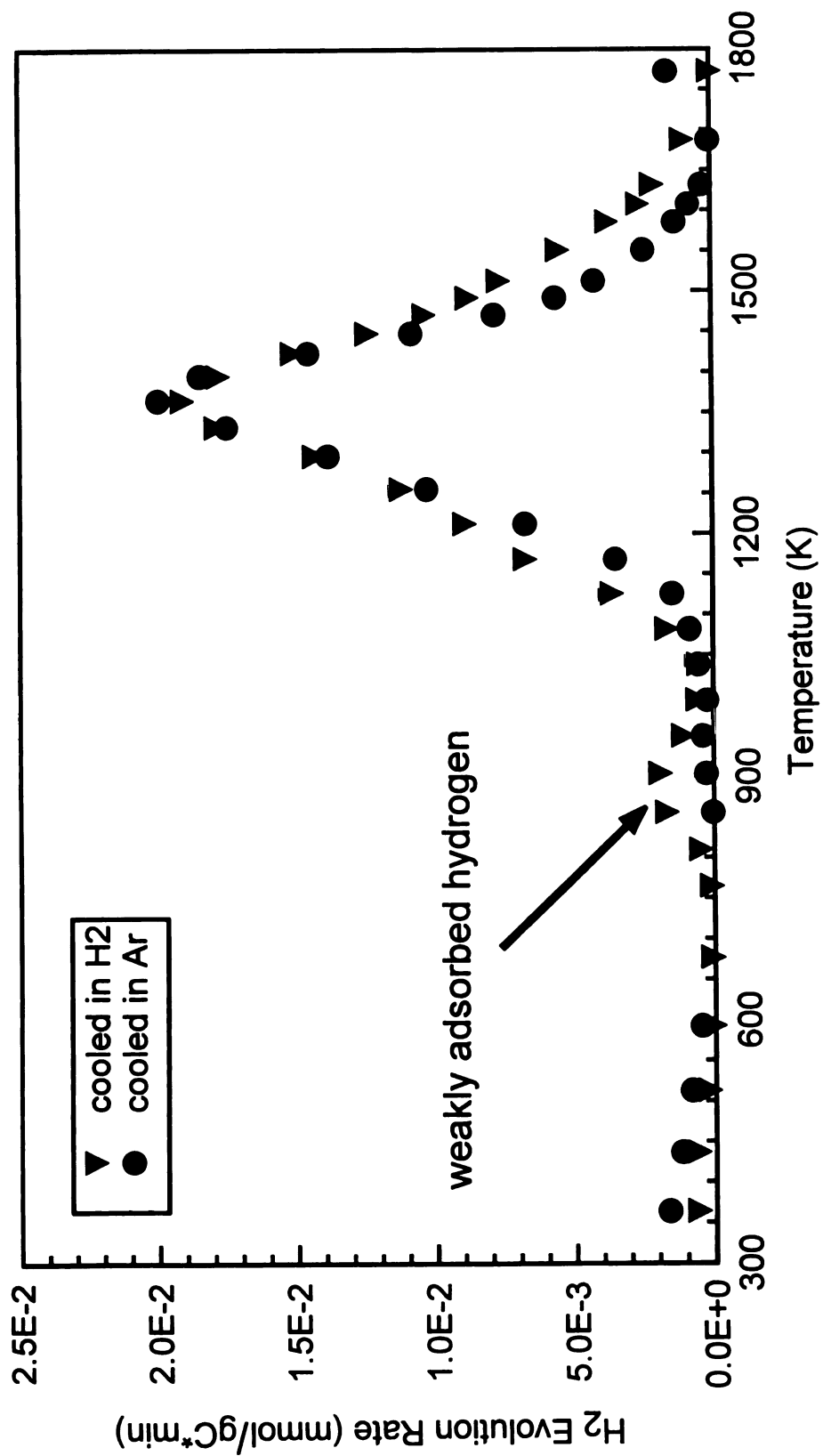


Figure 52: Hydrogen TPD profile for annealed Saran char after hydrogasification at 3.1 MPa and cooling in hydrogen or argon.

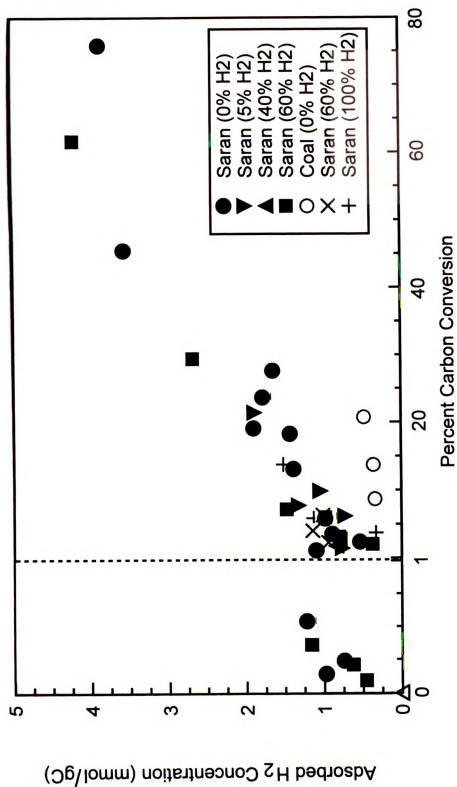


Figure 53: Adsorbed hydrogen concentration from annealed chars following gasification in steam at 1123 K.

0.5 wt% (2.5 mmolH₂(STP)/g). Adsorbed hydrogen concentration on gasified annealed coal char is about one fifth that of gasified annealed Saran char on a unit weight basis.

Initial rapid hydrogen adsorption over the first 0.4% carbon conversion is shown in Figure 54, along with the product gas evolution rates. A reactant gas composition of 40/60/0 H₂O/H₂/Ar was used to produce the most pronounced rate decline with conversion, and to ensure that the initial rapid hydrogen adsorption is not limited by the availability of hydrogen. Figure 54 shows that the initial transient behavior of gasification rate and hydrogen adsorption take place over the same range of carbon conversion. The reason why deuterated reactant gases were not to be used for the bulk of the gasification experiments is because the initial hydrogen concentration on the unreacted annealed Saran char is so low. The original purpose for using D₂O and D₂ as reactant gases was to be able to distinguish between hydrogen that was already present on the char and that which was fixed on the char during the course of reaction, but the temperature chosen for pretreatment is high enough to remove essentially all of the hydrogen in the Saran char, therefore this distinction does not need to be made.

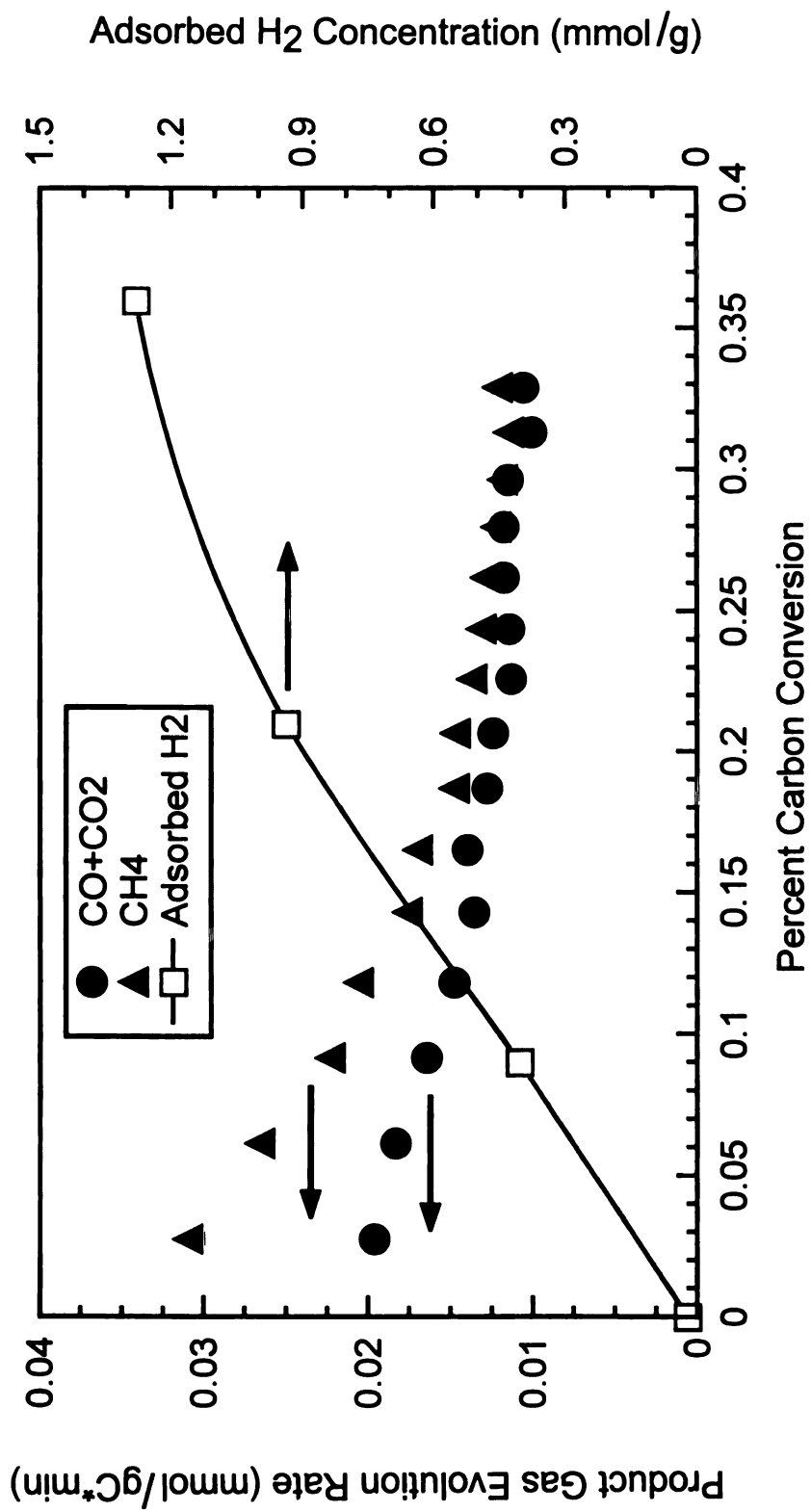


Figure 54: Product gas evolution rate and adsorbed hydrogen concentration from annealed Saran char steam gasification at low conversion; 1.0 MPa and 40/60/0 H₂O/H₂/Ar.

3.3.3. Adsorbed Hydrogen: Unit Area Basis

Figure 55 shows adsorbed hydrogen concentration on annealed chars at all conditions on a surface area basis. Initial rapid adsorption over the first 1% conversion is followed by a steady, gradual increase over the rest of the char conversion. The increase in surface area with conversion partially offsets the increase in adsorbed hydrogen concentration. Adsorbed hydrogen concentration on a surface area basis roughly doubles from 1% to 80% conversion, which indicates an increase in the ratio of exposed edge carbon atoms to those of the graphitic basal planes. Since edge carbons have a much higher potential for becoming gasification sites, this is consistent with the conclusion drawn of an increased surface reactivity from gasification rate curves presented on a surface area basis. Adsorbed hydrogen concentration on gasified annealed coal char on a surface area basis is about twice that of gasified annealed Saran char, which is consistent with char gasification behavior.

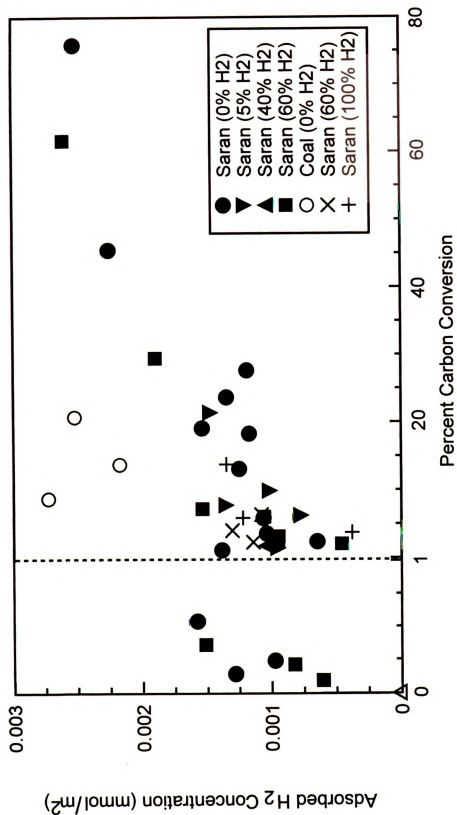


Figure 55: Adsorbed hydrogen concentration from annealed chars following gasification in steam at 1123 K.

Chapter 4

MODEL FITTING - LINEAR

REGRESSION ANALYSIS

The most surprising result of this investigation is that adsorbed hydrogen concentration is **independent** of reactant gas composition and extent of reaction past the first 1% char conversion. Because of this, the linearized rate expressions originally developed, which include explicit adsorbed hydrogen concentration, cannot be used. In developing the rate expressions presented in Chapter 1, it was expected that adsorbed hydrogen would increase in concentration on the char surface over the course of reaction, causing a decline in gasification rate with conversion. It was also assumed that higher hydrogen partial pressures

would lead to higher adsorbed hydrogen concentrations, also causing a decline in rate. However, none of these assumptions proved to be true. What was found was that, after a very short period of transient behavior, the adsorbed hydrogen concentration increased only slightly with conversion, as did gasification rate. Application of the original linearized rate expressions (Equations 10 and 11) to the data leads to the left hand side being negative, which cannot work because rate constants and partial pressures must all be positive. Further, the lack of resolution of data over the first 1% conversion prevents these rate expressions from being applied, where the adsorbed hydrogen and gasification rate appear to behave more like what was originally assumed.

Instead of using the original equations with adsorbed hydrogen concentration expressed explicitly, basic rate expressions were developed from Equations 1-8 which contain a term that includes the total number of active sites in a lumped parameter. Hydrogen surface concentration, as well as surface oxides and surface "free" sites, are all expressed implicitly. The equations have been linearized and used in regression of the rate data for several postulated hydrogen inhibition mechanisms. Rate data at all conditions tested were regressed as a function of carbon conversion to see how well the various

models describe actual rate behavior at different stages of char gasification in steam.

Rate data was then normalized with char surface area for the best representative models and regressed over the entire span of tested conversion and conditions. The regression coefficients, F statistics, rate constants, and the error on rate constant terms were then compared to determine which inhibition model gives the best fit and therefore helps to identify the most dominant hydrogen inhibition mechanism. Methane formation rate data has also been regressed to develop a better understanding of the mechanism of methane formation.

4.1. Char Gasification in Steam

The basic rate expression for gasification of chars in steam/hydrogen mixtures (Equation 8), as well as other similar expressions, have been linearized so that all gasification data can be fit to them to determine which expression best describes the rate behavior. These expressions have been derived from the elementary reaction steps given in Equations 2-7, excluding the shift reaction given in Equation 4. Also included in the derivation of all expressions is the active site balance, given in Equation 9. Common to all expressions are the two elementary steps of steam gasification: oxygen exchange and CO desorption. The mode of hydrogen inhibition is what

differentiates the various expressions. Rate expressions include one or more of the elementary reaction steps of reverse oxygen exchange, “associative” hydrogen adsorption, and dissociative hydrogen adsorption. To further investigate possible reaction mechanisms, oxygen exchange and reverse oxygen exchange are assumed to be rapid enough to be at equilibrium in some rate expressions, which alters their form by removing a term.

4.1.1. Reverse Oxygen Exchange

The first hydrogen inhibition elementary step reaction investigated was reverse oxygen exchange, which involves no hydrogen adsorption on the carbon surface; the $C(H)$ term is not included in the active site balance. The resulting rate expressions include the partial pressure of hydrogen in the denominator raised to the first power ($n=1$).

4.1.1.1. Reverse Oxygen Exchange

Equation 24 is the rate expression for H_2O/H_2 gasification of chars including reverse oxygen exchange as the inhibitory elementary step.

$$r_{CO} = \frac{k_1 C_T P_W}{1 + (k_1/k_2) P_W + (k_{-1}/k_2) P_{H_2}} \quad (24)$$

The key assumption made in the derivation of this expression is that the concentration of the intermediate surface species $C(O)$ is constant.

which is typical of Langmuir-Hinshellwood expressions. The numerator term includes contributions from the reactant gas partial pressure, forward reaction rate constant, and total active site concentration. The first term in the denominator is unity and represents the oxygen exchange elementary step, while the second term in the denominator represents CO desorption from the char surface. The last term in the denominator represents hydrogen inhibition by reverse oxygen exchange, and is proportional to hydrogen partial pressure raised to the first power ($n=1$).

Equation 25 is the linearized version of the previous rate expression.

$$\frac{1}{r_{CO}} = \left[\frac{1}{k_2 C_T} \right] + \left[\frac{1}{k_1 C_T} \right] \left(\frac{1}{P_W} \right) + \left[\frac{1}{k_1 C_T} \right] \left[\frac{k_{-1}}{k_2} \right] \left(\frac{P_{H_2}}{P_W} \right) \quad (25)$$

Figure 56 shows the regression coefficient of determination (r^2) as calculated using the LINEST function in Microsoft Excel 5.0. Rate data at all gasification conditions tested were regressed simultaneously at 0, 0.5, 1, 2, 5, 10, and 20% conversion. The first 2% conversion has an r^2 value of about 0.7, while the rest of the conversion range shows an r^2 value above 0.9. An F test was performed on the data to make sure the good fit above 1% conversion did not occur by chance. Figure 57 shows the F statistic and the F critical values for 95% and 99% confidence. It is easily seen that the F statistic is near or below the

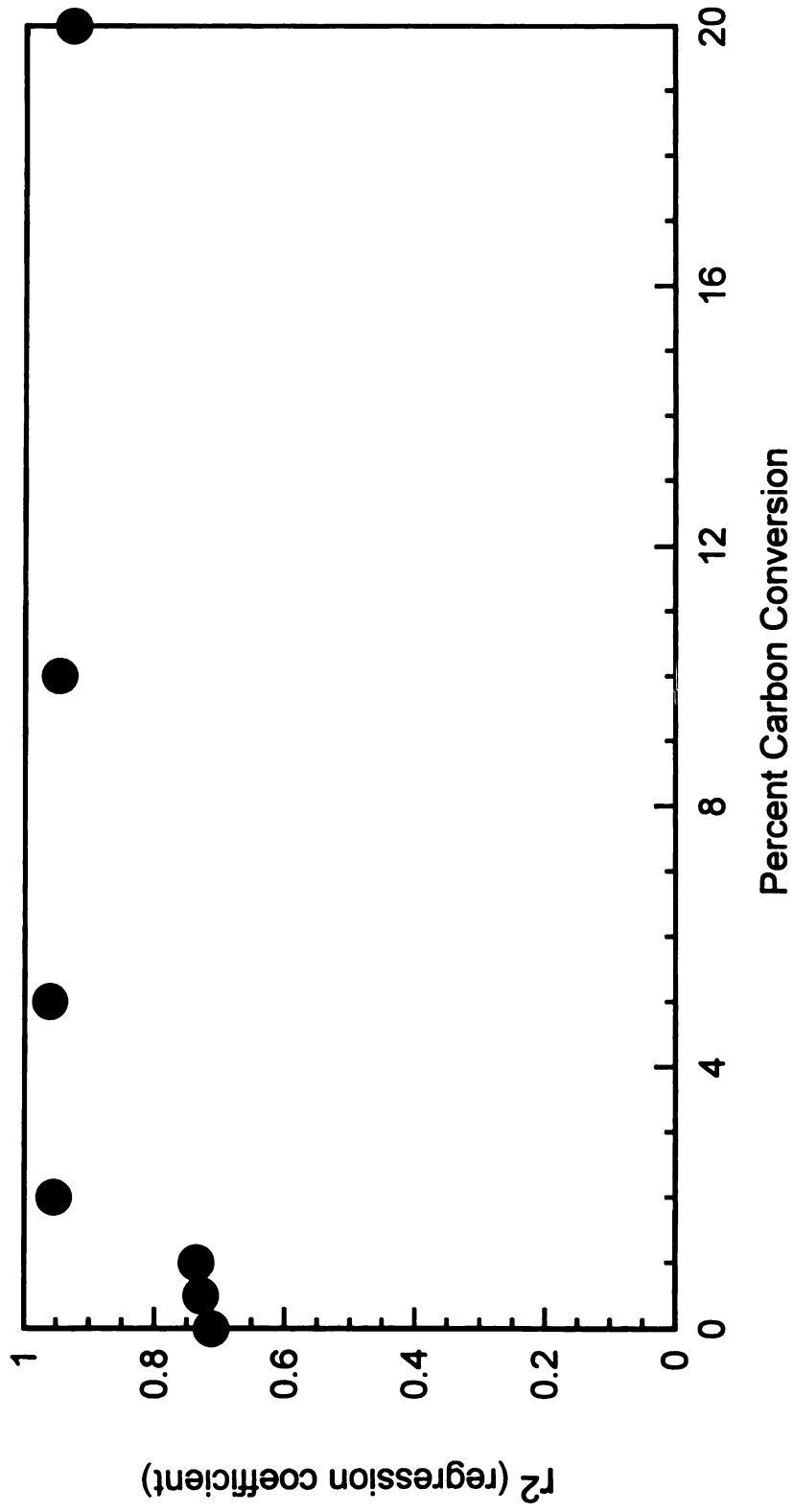


Figure 56: Correlation coefficient for linear regression of rate data from steam gasification of annealed Saran char at all conditions tested, "n"=1 reverse oxygen exchange (ROE).

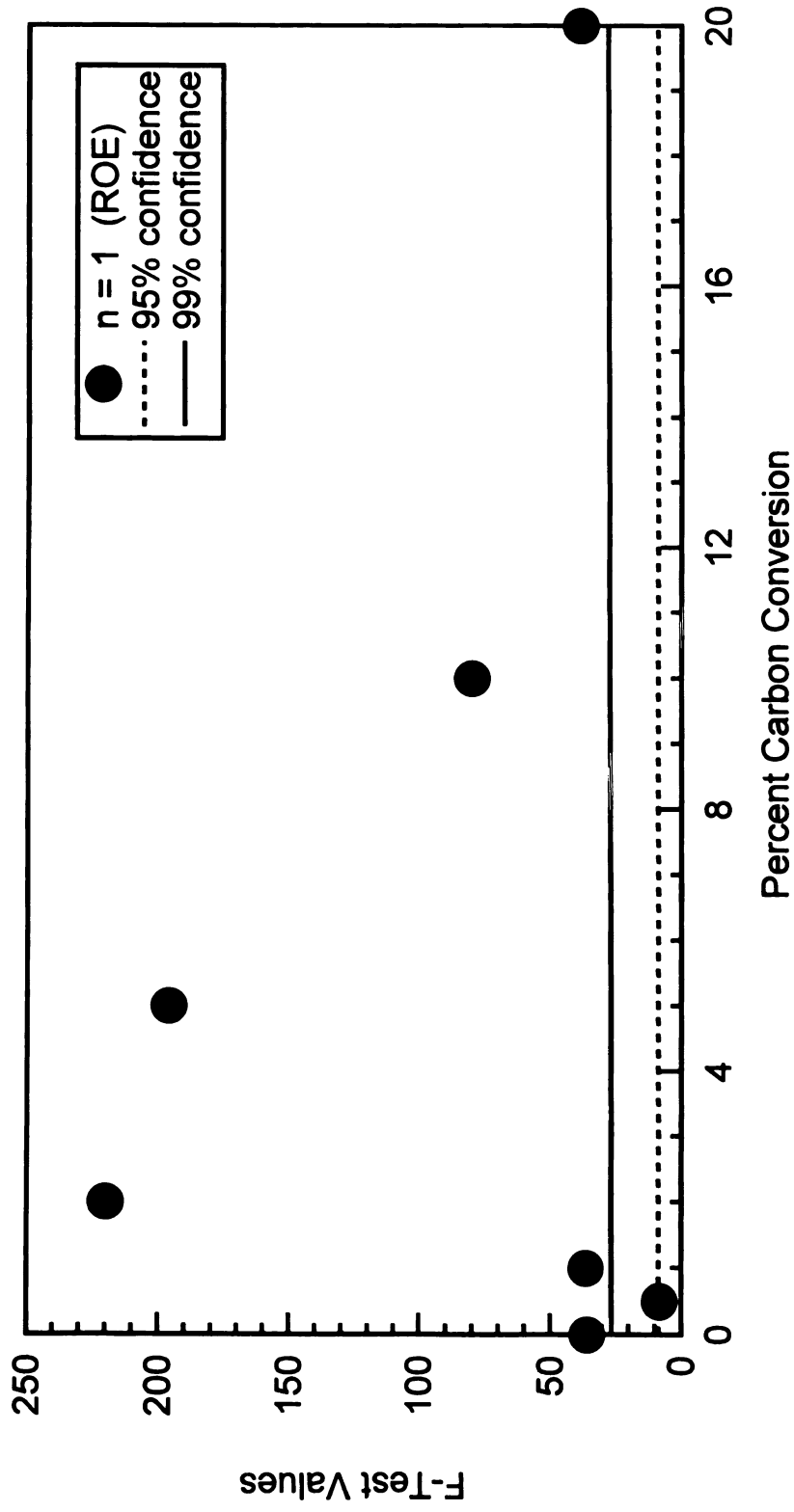


Figure 57: F-Test values for linear regression of rate data from steam gasification of annealed Saran char at all conditions tested, "n"=1 reverse oxygen exchange (ROE).

critical values at and below 2% conversion, but is well above them for the rest of carbon conversion.

4.1.1.2. Rapid Equilibrium Reverse Oxygen Exchange

Equation 26 is another rate expression for H₂O/H₂ gasification of chars including reverse oxygen exchange as the inhibitory elementary step.

$$r_{\text{CO}} = \frac{k_1 C_T P_W}{(k_1/k_2) P_W + (k_{-1}/k_2) P_{\text{H}_2}} \quad (26)$$

The key assumption made in the derivation of this expression is that reverse oxygen exchange and oxygen exchange are in rapid equilibrium making desorption of the C(O) surface complex rate limiting, also typical of Langmuir-Hinshellwood expressions. The numerator term includes contributions from the reactant gas partial pressure, forward reaction rate constant, and total active site concentration. Unlike the previous rate expression, the unity term in the denominator is no longer present. This is because the first term in Equation 26, which represents CO desorption from the char surface, is now the dominant reaction term. The second term in the denominator represents hydrogen inhibition, and as with the previous expression it is proportional to the hydrogen partial pressure raised to the first power (n=1).

Equation 27 is the linearized version of the previous rate expression.

$$\frac{1}{r_{\text{CO}}} = \left[\frac{1}{k_2 C_T} \right] + \left[\frac{1}{k_1 C_T} \right] \left[\frac{k_{-1}}{k_2} \right] \left(\frac{P_{\text{H}_2}}{P_{\text{W}}} \right) \quad (27)$$

Figure 58 shows the regression coefficient of determination (r^2) as calculated by the same method outlined for the previous expression. The results are slightly worse, but almost the same as those of non-rapid reverse oxygen exchange, included in this figure for comparison. The first 2% conversion has an r^2 value of about 0.7, while the rest of the conversion range shows an r^2 value above 0.9. An F test was performed on these data as well. Figure 59 shows the F statistic and the F critical values for 95% and 99% confidence. As with the previous rate expression it is easily seen that the F statistic is near or below the critical values at and below 2% conversion, but is well above them for the rest of carbon conversion.

4.1.2. “Associative” Hydrogen Adsorption

The second hydrogen inhibition elementary step reaction investigated was “associative” hydrogen adsorption, which involves a diatomic hydrogen molecule adsorbing onto one surface carbon atom to form two discrete C-H bonds on the same carbon atom, noted as $\text{C}(\text{H})_2$. Hydrogen blocks water molecules from reacting with formerly unsaturated

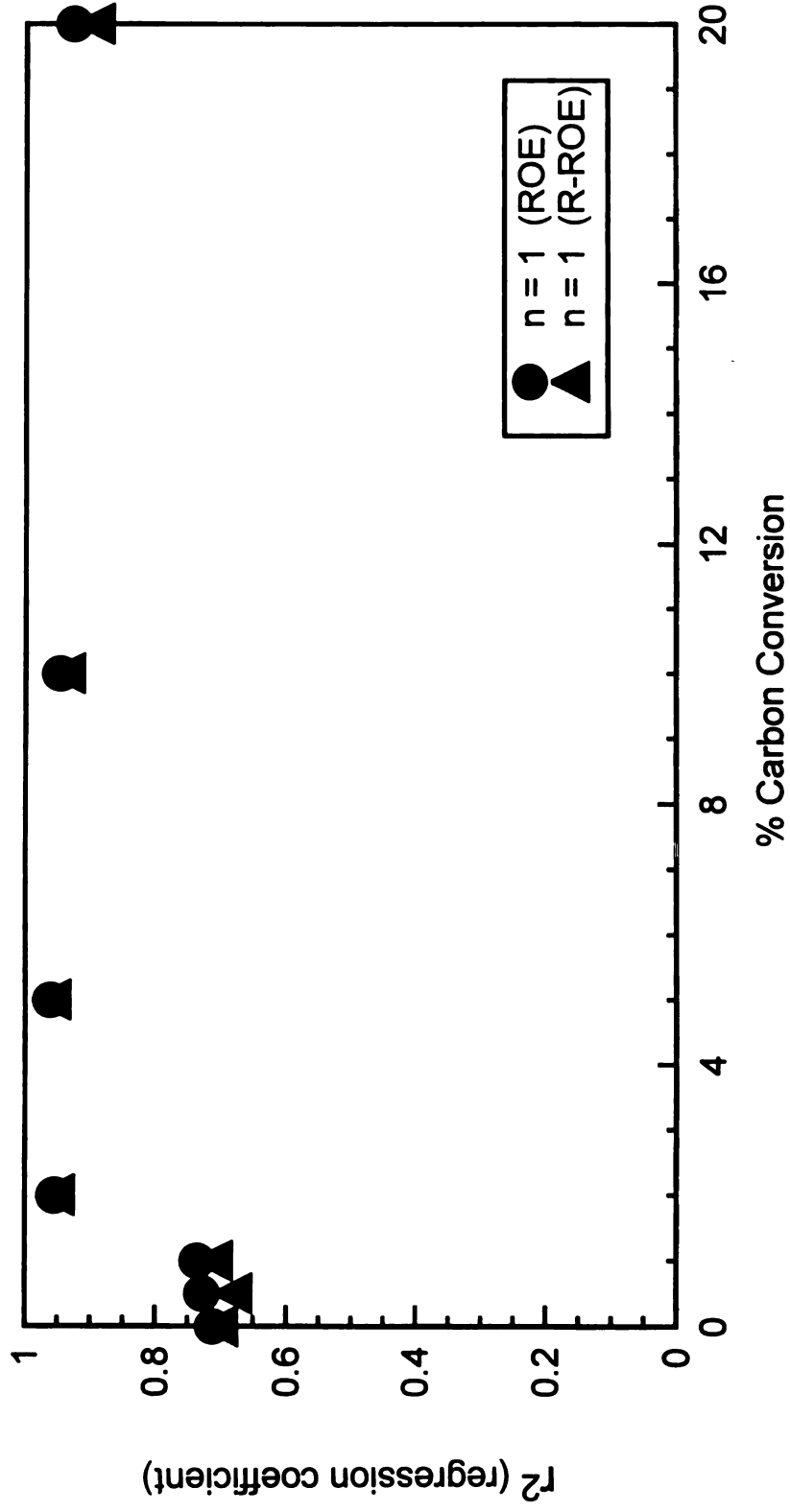


Figure 58: Correlation coefficient for linear regression of rate data from steam gasification of annealed Saran char at all conditions tested, "n"=1 (ROE) and "n"=1 with rapid reverse oxygen exchange (R-ROE).

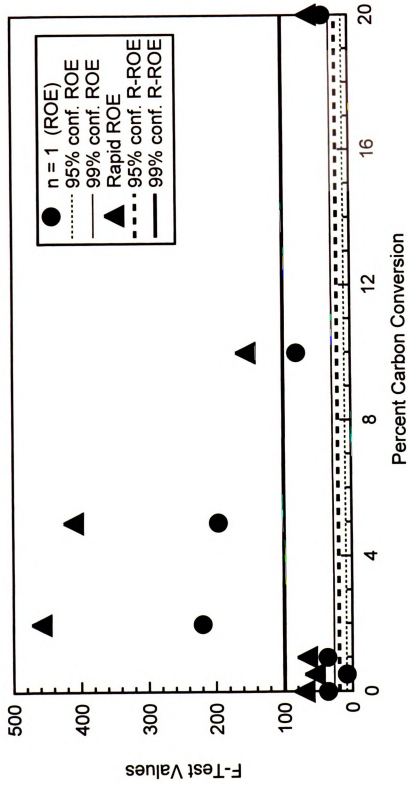


Figure 59: F-Test values for linear regression of rate data from steam gasification of annealed Saran char at all conditions tested, "n" $=$ 1 (ROE) and "n" $=$ 1 with rapid reverse oxygen exchange (R-ROE).

surface carbon atoms, thereby inhibiting oxygen exchange by decreasing the surface concentration of free sites, noted as C_f . The active site balance, seen in equation 9, contains a $C(H)_2$ term instead of a $C(H)$ term.

4.1.2.1. "Associative" Hydrogen Adsorption Only

Equation 28 is the rate expression for H_2O/H_2 gasification of chars including "associative" hydrogen adsorption as the inhibitory elementary step.

$$r_{CO} = \frac{k_1 C_T P_W}{1 + (k_1/k_2) P_W + (k_3/k_{-3}) P_{H_2}} \quad (28)$$

The key assumptions made in the derivation of this expression are that the concentration of the intermediate surface species $C(O)$ and $C(H)_2$ are constant, which is typical of Langmuir-Hinshellwood expressions. The form and terms are all identical to those of hydrogen inhibition by reverse oxygen exchange except the last term in the denominator. The last term in the denominator represents hydrogen inhibition by "associative" hydrogen adsorption and is proportional to the hydrogen partial pressure raised to the first power ($n=1$), which is also the case with hydrogen inhibition by reverse oxygen exchange.

Equation 29 is the linearized version of the previous rate expression.

$$\frac{1}{r_{CO}} = \left[\frac{1}{k_2 C_T} \right] + \left[\frac{1}{k_1 C_T} \right] \left(\frac{1}{P_W} \right) + \left[\frac{1}{k_1 C_T} \right] \left[\frac{k_3}{k_{-3}} \right] \left(\frac{P_{H_2}}{P_W} \right) \quad (29)$$

Figures 60 and 61 can be referred to for the regression coefficient of determination (r^2) and F statistic. The form of this expression is identical to that of hydrogen inhibition by reverse oxygen exchange, so the conclusions drawn from these figures are also identical: a poor fit from 0-2% conversion, and a good fit above 2% conversion.

4.1.2.2. “Associative” Hydrogen Adsorption and Reverse Oxygen Exchange

Equation 30 is the rate expression for H_2O/H_2 gasification of chars including “associative” hydrogen adsorption and reverse oxygen exchange as the inhibitory elementary steps.

$$r_{CO} = \frac{k_1 C_T P_W}{1 + (k_1/k_2) P_W + \{(k_{-1}/k_2) + (k_3/k_{-3})\} P_{H_2} + \{(k_{-1}/k_2)(k_3/k_{-3})\} P_{H_2}^2} \quad (30)$$

The key assumptions made in the derivation of this expression are the same as those made for “associative” hydrogen adsorption only. The form and terms are a combination of those for “associative” hydrogen adsorption only and reverse oxygen exchange only except the last term in the denominator. The second to last denominator term is proportional to the hydrogen partial pressure raised to the first power ($n=1$), and represents a simple addition of the separate contributions of

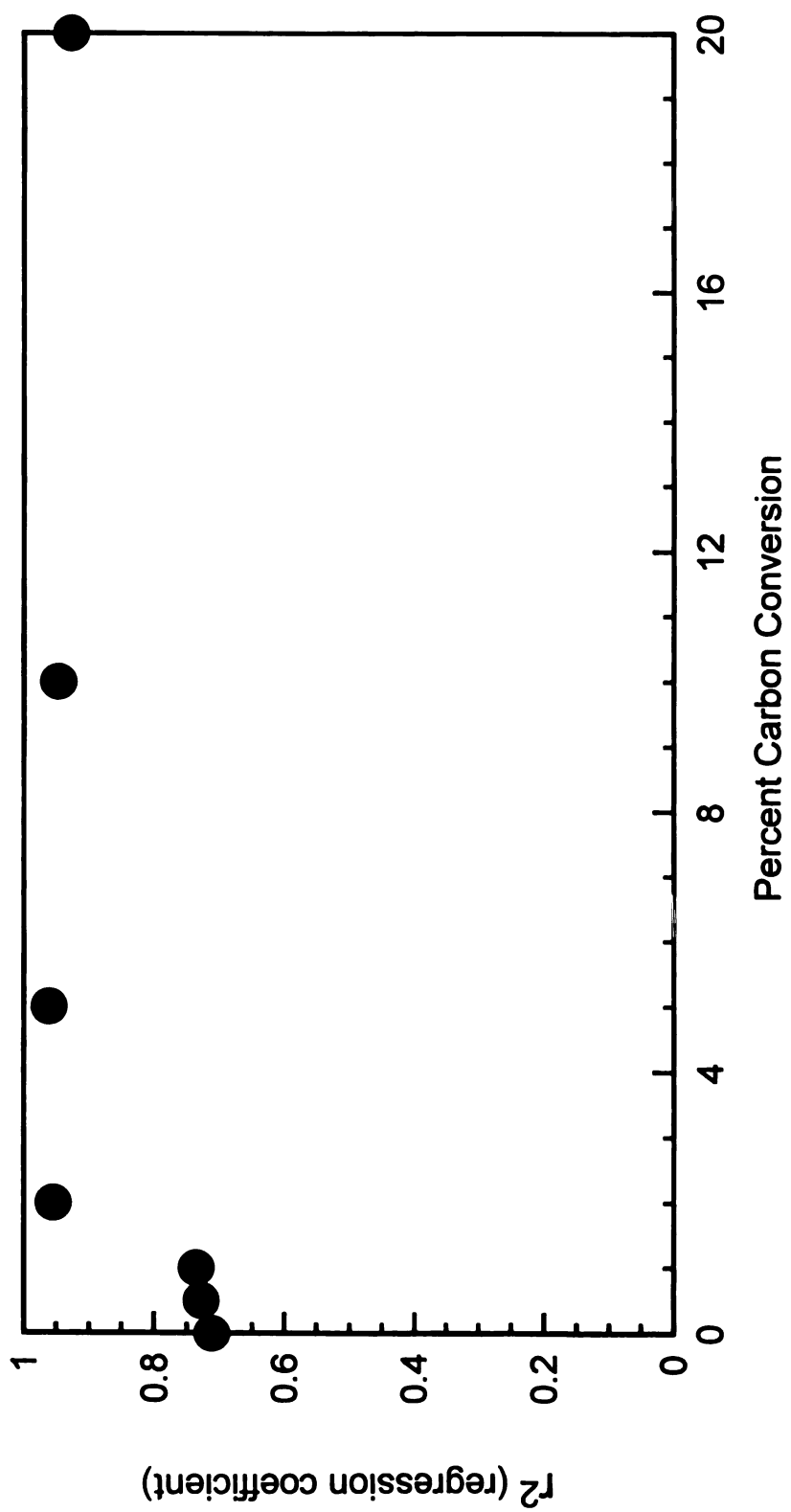


Figure 60: Correlation coefficient for linear regression of rate data from steam gasification of annealed Saran char at all conditions tested, "n"=1 "associative" hydrogen adsorption (AHA).

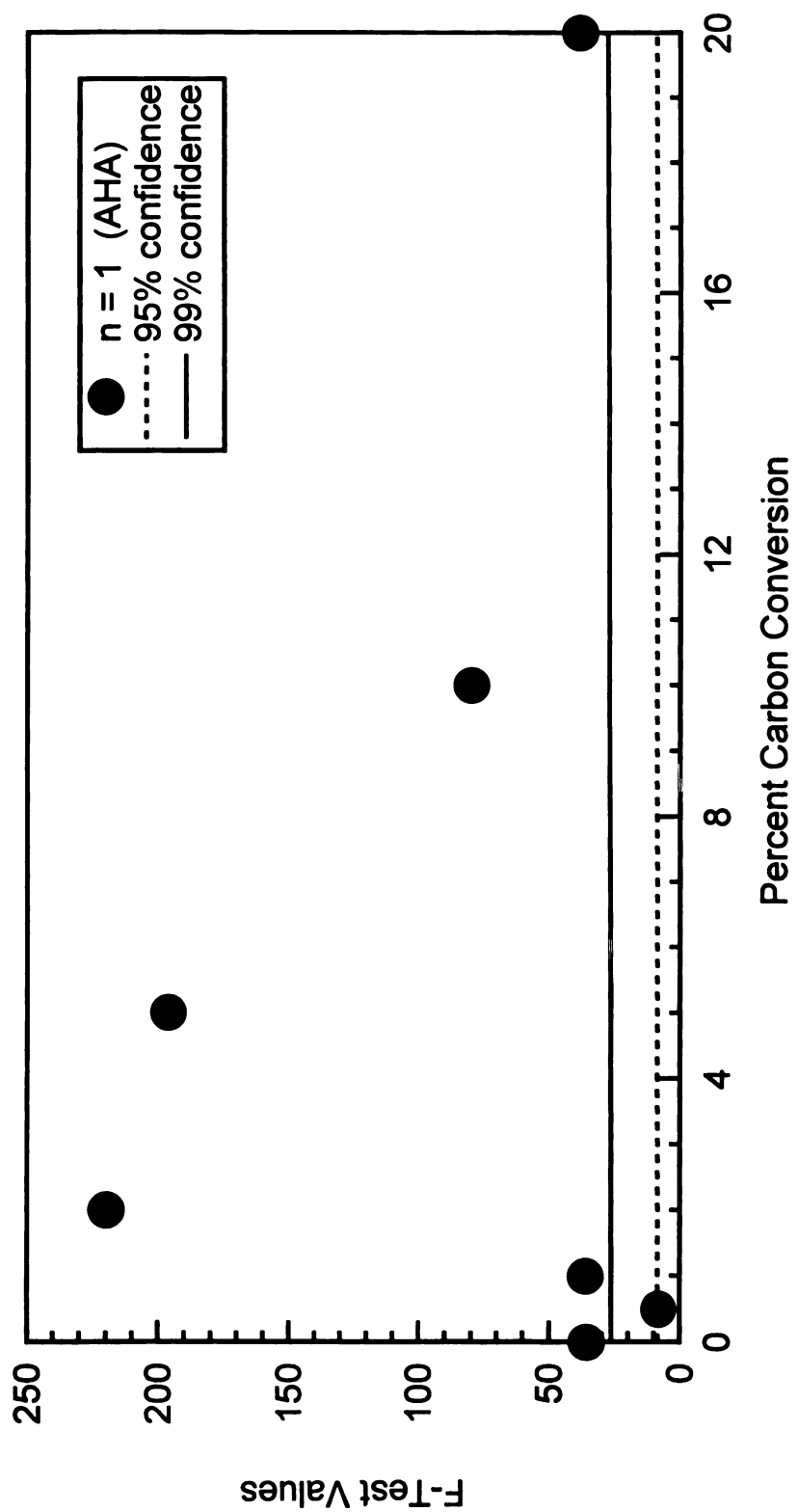


Figure 61: F-Test values for linear regression of rate data from steam gasification of annealed Saran char at all conditions tested, "n"=1 "associative" hydrogen adsorption (AHA).

“associative” hydrogen adsorption and reverse oxygen exchange. The last denominator term is the product of the two separate inhibition terms, and is therefore proportional to the hydrogen partial pressure squared (n=2).

Equation 31 is the linearized version of the previous rate expression.

$$\frac{1}{r_{CO}} = \left[\frac{1}{k_2 C_T} \right] + \left[\frac{1}{k_1 C_T} \right] \left(\frac{1}{P_W} \right) + \left[\frac{1}{k_1 C_T} \right] \left\{ \left[\frac{k_{-1}}{k_2} \right] + \left[\frac{k_3}{k_{-3}} \right] \right\} \left(\frac{P_{H_2}}{P_W} \right) + \left[\frac{1}{k_1 C_T} \right] \left[\frac{k_{-1}}{k_2} \right] \left[\frac{k_3}{k_{-3}} \right] \left(\frac{P_{H_2}^2}{P_W} \right) \quad (31)$$

Figures 62 and 63 show the regression coefficient of determination (r^2), the F statistic and the F critical values for 95% and 99% confidence as calculated by the same method outlined for the previous expressions. Results for reverse oxygen exchange/“associative” hydrogen adsorption only have been included for comparison. The results are nearly identical to those of reverse oxygen exchange only and reversible “associative” hydrogen adsorption only, with only a very slight improvement over either one. This slight improvement caused by the addition of the term in which hydrogen partial pressure is raised to the second power is due to the fact that the model has another parameter by which it can regress the data and not by an improvement in the reaction description by including both elementary steps.

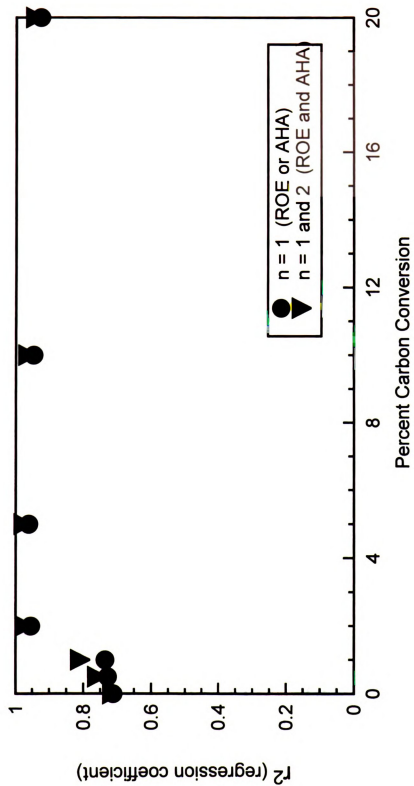


Figure 62: Correlation coefficient for linear regression of rate data from steam gasification of annealed Saran char at all conditions tested, "n"=1 (ROE or AHA) and "n"=1 and 2 (ROE and AHA).

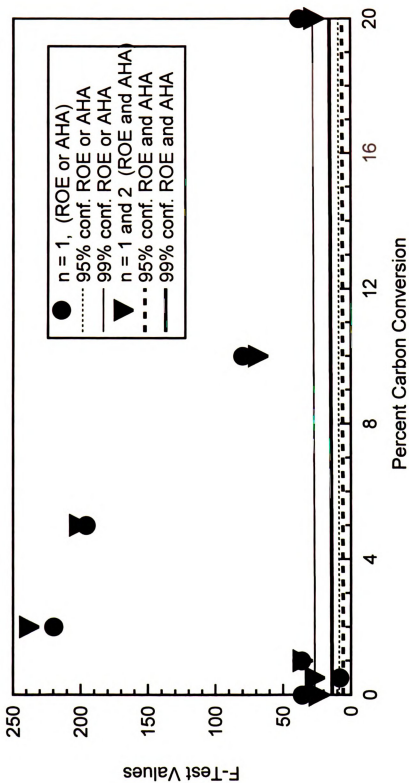


Figure 63: F-Test values for linear regression of rate data from steam gasification of annealed Saran char at all conditions tested, "n"=1 (ROE or AHA) and "n"=1 and 2 (ROE and AHA).

4.1.3. Dissociative Hydrogen Adsorption

The third hydrogen inhibition elementary step reaction investigated was dissociative hydrogen adsorption, which involves a diatomic hydrogen molecule splitting and adsorbing onto two surface carbon atoms to form two discrete C-H bonds, each noted as C(H). Hydrogen blocks water molecules from reacting with formerly unsaturated surface carbon atoms, thereby inhibiting oxygen exchange by decreasing the surface concentration of free sites. The active site balance, seen in equation 9, contains a C(H) term.

4.1.3.1. Dissociative Hydrogen Adsorption Only

Equation 32 is the rate expression for H₂O/H₂ gasification of chars including dissociative hydrogen adsorption as the inhibitory elementary step.

$$r_{\text{CO}} = \frac{k_1 C_T P_W}{1 + (k_1/k_2) P_W + (k_4/k_{-4}) P_{\text{H}_2}^{1/2}} \quad (32)$$

The key assumptions made in the derivation of this expression are that the concentrations of the intermediate surface species C(O) and C(H) are constant, which is typical of Langmuir-Hinshellwood expressions. The form and terms are all identical to those of hydrogen inhibition by reverse oxygen exchange or “associative” hydrogen adsorption except the last term in the denominator. The last term in the denominator

represents hydrogen inhibition by dissociative hydrogen adsorption and is proportional to the hydrogen partial pressure raised to the one half power ($n=0.5$), as opposed to $n=1$ as is the case with hydrogen inhibition by reverse oxygen exchange or "associative" hydrogen adsorption.

Equation 33 is the linearized version of the previous rate expression.

$$\frac{1}{r_{\text{CO}}} = \left[\frac{1}{k_2 C_T} \right] + \left[\frac{1}{k_1 C_T} \right] \left(\frac{1}{P_W} \right) + \left[\frac{1}{k_1 C_T} \right] \left[\frac{k_4}{k_{-4}} \right] \left(\frac{P_{\text{H}_2}^{1/2}}{P_W} \right) \quad (33)$$

Figure 64 shows the regression coefficient of determination (r^2) as calculated by the same method outlined for the previous expressions, with r^2 values for reverse oxygen exchange or "associative" hydrogen adsorption included for comparison. The first 5% conversion has an r^2 value of about 0.6 for dissociative hydrogen adsorption, but the rest of the conversion range shows an r^2 value above 0.9. It is clear that reverse oxygen exchange or "associative" hydrogen adsorption models describe the actual reaction mechanism much better than dissociative hydrogen adsorption over the first 5% conversion. At higher conversions both models show similar fits. An F test was performed on the data to make sure the good fit above 10% conversion did not occur by chance. Figure 65 shows the F statistic and the F critical values for 95% and 99% confidence. It is easily seen that the F statistic is near or below

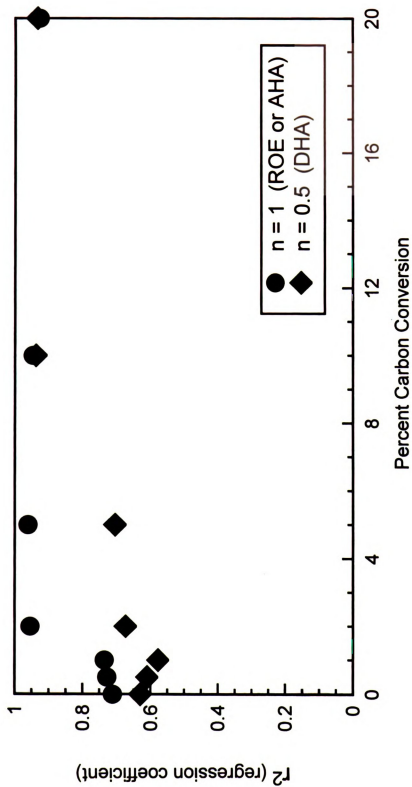


Figure 64: Correlation coefficient for linear regression of rate data from steam gasification of annealed Saran char at all conditions tested, " n "=0.5 dissociative hydrogen adsorption (DHA) and " n "=1 (ROE or AHA).

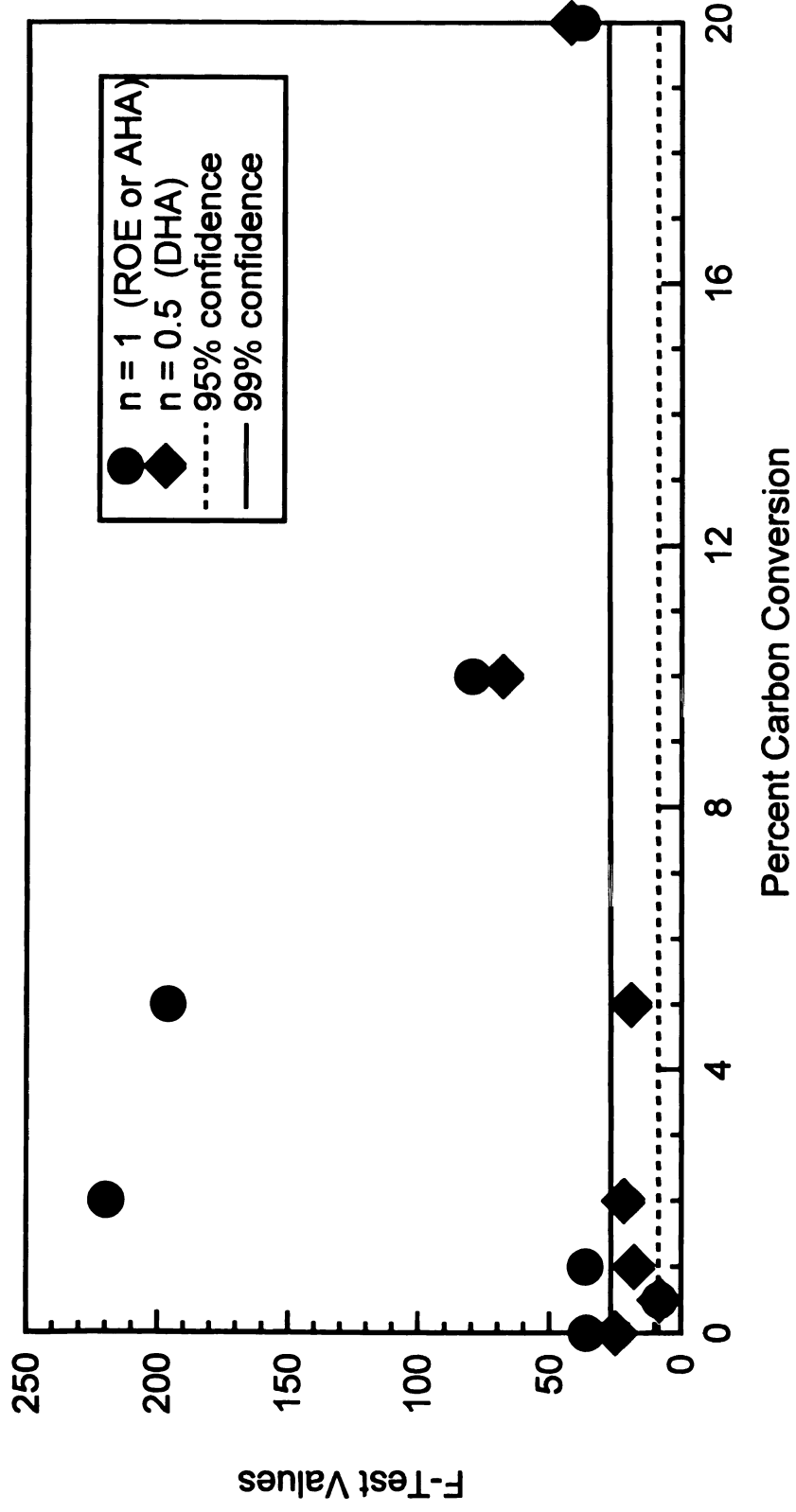


Figure 65: F-Test values for linear regression of rate data from steam gasification of annealed Saran char at all conditions tested, " n "=0.5 dissociative hydrogen adsorption (DHA) and " n "=1 (ROE or AHA).

the C

the n

4.1.

trans

exha

The W

same

and t

on re

thing

rais

The t

press

disso

two s

hydro

the critical values at and below 5% conversion, but is above them for the rest of carbon conversion.

4.1.3.2. Dissociative Hydrogen Adsorption and Reverse Oxygen Exchange

Equation 34 is the rate expression for H₂O/H₂ gasification of chars including dissociative hydrogen adsorption and reverse oxygen exchange as the inhibitory elementary steps.

$$r_{\text{CO}} = \frac{k_1 C_T P_W}{1 + (k_1/k_2)P_W + (k_{-1}/k_2)P_{\text{H}_2} + (k_4/k_{-4})\{P_{\text{H}_2}^{1/2} + (k_{-1}/k_2)P_{\text{H}_2}^{3/2}\}} \quad (34)$$

The key assumptions made in the derivation of this expression are the same as those made for dissociative hydrogen adsorption only. The form and terms are a combination of those of dissociative hydrogen adsorption or reverse oxygen exchange, plus another term in the denominator. The third denominator term is proportional to the hydrogen partial pressure raised to the first power (n=1), and represents reverse oxygen exchange. The fourth denominator term is proportional to the hydrogen partial pressure raised to the one half power (n=0.5), and represents dissociative hydrogen adsorption. The last term is the product of the two separate inhibition terms, and is therefore proportional to the hydrogen partial pressure raised to the three halves power (n=1.5).

expre

Fig. 2

the

calc

with

asso

The

exch

ellen

Oxyg

then

powe

mode

powe

Equation 35 is the linearized version of the previous rate expression.

$$\begin{aligned} \frac{1}{r_{CO}} = & \left[\frac{1}{k_2 C_T} \right] + \left[\frac{1}{k_1 C_T} \right] \left(\frac{1}{P_W} \right) + \left[\frac{1}{k_1 C_T} \right] \left[\frac{k_{-1}}{k_2} \right] \left(\frac{P_{H_2}}{P_W} \right) \\ & + \left[\frac{1}{k_1 C_T} \right] \left[\frac{k_4}{k_{-4}} \right] \left(\frac{P_{H_2}^{1/2}}{P_W} \right) + \left[\frac{1}{k_1 C_T} \right] \left[\frac{k_{-1}}{k_2} \right] \left[\frac{k_4}{k_{-4}} \right] \left(\frac{P_{H_2}^{3/2}}{P_W} \right) \end{aligned} \quad (35)$$

Figures 66 and 67 show the regression coefficient of determination (r^2), the F statistic and the F critical values for 95% and 99% confidence as calculated by the same method outlined for the previous expressions, with results for reverse oxygen exchange/“associative” hydrogen adsorption and dissociative hydrogen adsorption included for comparison. The results show a clear improvement upon inclusion of reverse oxygen exchange with dissociative hydrogen adsorption as the inhibition elementary steps. The results are nearly identical to those of reverse oxygen exchange or “associative” hydrogen adsorption. This is because there is a term with hydrogen partial pressure raised to the first power, which appears to create a much better fit between the data and models than a term with hydrogen partial pressure raised to the one half power.

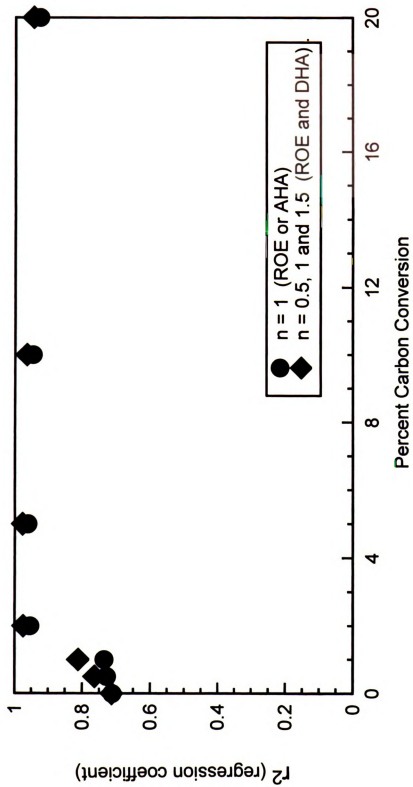


Figure 66: Correlation coefficient for linear regression of rate data from steam gasification of annealed Saran char at all conditions tested, "n"=1 (ROE or AHA) and "n"=0.5, 1 and 1.5 (ROE and DHA).

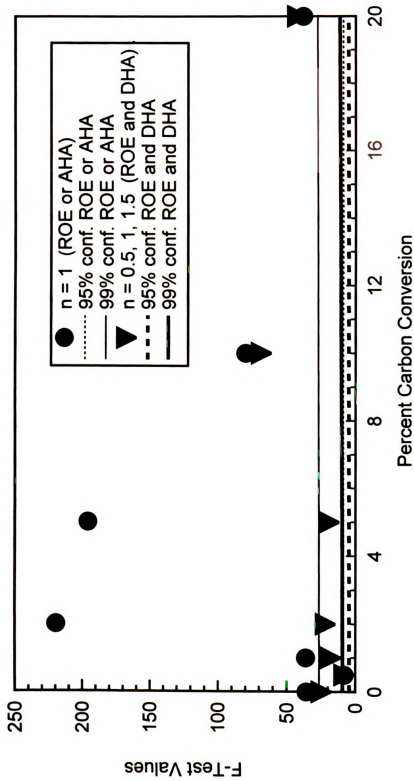


Figure 67: F-Test values for linear regression of rate data from steam gasification of annealed Saran char at all conditions tested, "n"=1 (ROE or AHA) and "n"=0.5, 1, and 1.5 (ROE and DHA).

4.

4.

exc

bet

ads

ven

hyd

tha

fit

inv

cyo

Tat



4.2. Comparison of Hydrogen Inhibition

Models

4.2.1. Linear Regression Parameters

The models which incorporate hydrogen inhibition by reverse oxygen exchange or "associative" hydrogen adsorption ($n=1$) correlate much better with actual data than models based on dissociative hydrogen adsorption ($n=0.5$) for steam gasification of annealed Saran char. A very slight improvement to the models can be made by combining modes of hydrogen inhibition in a single expression, but this is due to the fact that there are more parameters with which the data can be regressed to fit the model, as seen in Table 2. Other rate expressions were investigated involving methane formation as well as a combination of hydrogen adsorption and rapid equilibrium reverse oxygen exchange, but

Table 2: Number of parameters in various kinetic models of H_2O/H_2 gasification of annealed Saran char.

<u>Number of Model Parameters</u>	<u>"n" = ?</u>
2	1 for Rapid-ROE (no constant term)
3	1 for ROE, 1 for AHA, 0.5 for DHA
4	1 and 2 for ROE + AHA
5	0.5, 1, and 1.5 for ROE + DHA

the

to

the

had

of

gro

de

had

the

high

Ta



they yielded unnecessarily complicated rate expressions similar to those given in Sections 4.1.2.2. and 4.1.3.2.

None of the models fit the data well up to 1% conversion because the reaction is not at steady state over this range. Hydrogen is rapidly adsorbing onto the carbon surface, therefore the concentration of various surface intermediates is not constant. Constant surface group concentrations are one of the key assumptions made in the development of the mechanistic models.

It is not surprising to find the dissociative hydrogen inhibition model fitting kinetic data well at 10% and 20% carbon conversion because there are significantly fewer degrees of freedom for the models at the higher conversions. Table 3 shows degrees of freedom as a function of

Table 3: Degrees of freedom for linear regression of various kinetic models of H₂O/H₂ gasification of annealed Saran char as a function of conversion.

<u>Percent Carbon Conversion</u>	<u>2 Model Parameters</u>	<u>3 Model Parameters</u>	<u>4 Model Parameters</u>	<u>5 Model Parameters</u>
0	30	29	28	27
0.5	27	26	25	24
1	27	26	25	24
2	22	21	20	19
5	17	16	15	14
10	10	9	8	7
20	7	6	5	4

proven

proven

proven

proven

proven

proven

proven

proven

proven

proven

proven

proven

proven

proven

proven

proven

proven

proven

proven

conversion for linear regression of the various kinetic models. Carbon conversions lower than 10% have enough degrees of freedom to show a significant difference between the way models which include reverse oxygen exchange as an inhibitory mechanism describe kinetic data and those that do not include reverse oxygen exchange. At 10% and 20% carbon conversion the number of degrees of freedom approach the number of model parameters, making it much more likely that a good fit between the model and data will occur by chance as seen by decreasing F test values at these conversions.

A further attempt was made to identify the actual inhibitory mechanism by comparison of the regression results of two different forms of the linearized rate expressions for both reverse oxygen exchange/"associative" hydrogen adsorption and dissociative hydrogen adsorption. Equations 36–38 show the alternate forms of the linearized rate expressions. The difference between these expressions and the ones presented previously (Equations 24, 28, and 32) is that each side of the new expressions has been multiplied through by the water partial pressure.

$$\frac{P_w}{r_{CO}} = \left[\frac{1}{k_2 C_T} \right] \left(\frac{P_w}{1} \right) + \left[\frac{1}{k_1 C_T} \right] + \left[\frac{1}{k_1 C_T} \right] \left[\frac{k_{-1}}{k_2} \right] \left(\frac{P_{H_2}}{1} \right) \quad (36)$$

P.w.
foo

P.w.
foo

Ta

the prev

formaliz

independ

diversi

Fe

tech the

but nei

of the

slight

rate co

value t

also a

4.2.1

H

gives a

Oxygen

$$\frac{P_W}{r_{CO}} = \left[\frac{1}{k_2 C_T} \right] \left(\frac{P_W}{1} \right) + \left[\frac{1}{k_1 C_T} \right] + \left[\frac{1}{k_1 C_T} \right] \left[\frac{k_3}{k_{-3}} \right] \left(\frac{P_{H_2}}{1} \right) \quad (37)$$

$$\frac{P_W}{r_{CO}} = \left[\frac{1}{k_2 C_T} \right] \left(\frac{P_W}{1} \right) + \left[\frac{1}{k_1 C_T} \right] + \left[\frac{1}{k_1 C_T} \right] \left[\frac{k_4}{k_{-4}} \right] \left(\frac{P_{H_2}^{1/2}}{1} \right) \quad (38)$$

Table 4 shows the regression results for both linearized forms of the previous expressions. Rate data from 2–20% conversion has been normalized to the total surface area, so it is relatively constant and independent of conversion. These parameters therefore represent char conversion over the entire 2–20% conversion range.

Form 2 of the $n=0.5$ model shows an improvement over Form 1 for both the regression coefficient of determination and the F statistic, but neither is as good as the $n=1$ models. The r^2 value for both forms of the $n=1$ model are the same, while the F statistic for Form 2 shows slight improvement over that of Form 1. Inspection of the rate constants shows that Form 1 is better because it yields a positive value for the constant $1/k_2 C_T$. A positive value for the group $1/k_2 C_T$ also allows a positive value for the group k_1/k_{-1} to be calculated.

4.2.2. Calculated Rate Constants

Hydrogen inhibition by rapid equilibrium reverse oxygen exchange gives almost as good a fit to the data as the model derived for reverse oxygen exchange. The difference between the linearized rate expressions

Table 4: Regression results for linearized rate expressions.

Linear Regression Parameters <u>H₂O/H₂ Gasification of Char</u>	n=1 <u>Form 1</u>	n=1 <u>Form 2</u>	n=0.5 <u>Form 1</u>	n=0.5 <u>Form 2</u>
r ²	0.96	0.96	0.66	0.87
F stat.	659	739	59	200
F crit. (99% confidence)	4.1	4.1	4.1	4.1
1/k ₂ C _T (gC*min/mmol)	4.6	-1.0	12	-22
1/k ₂ C _T error	3.1	5.4	8.9	11
k ₂ C _T (mmol/gC*min)	0.22	-1.0	0.08	-0.05
1/k ₁ C _T (gC*min*MPa/mmol)	0.38	2.5	-7.0	-1.2
1/k ₁ C _T error	0.77	3.5	2.0	6.5
k ₁ C _T (mmol/gC*min*MPa)	2.6	0.40	-1.4	-0.83
k ₋₁ /k ₁ k ₂ C _T (gC*min/mmol)	163	166		
k ₋₁ /k ₁ k ₂ C _T error	4.7	5.0		
k ₁ /k ₋₁ (unitless)	0.029	-5.7		
k ₃ /k ₋₃ k ₁ C _T (gC*min/mmol)	163	166		
k ₃ /k ₋₃ k ₁ C _T error	4.7	5.0		
k ₃ /k ₋₃ (1/MPa)	425	66		
k ₄ /k ₋₄ k ₁ C _T (gC*min*MPa ^{1/2} /mmol)			149	221
k ₄ /k ₋₄ k ₁ C _T error			14	13
k ₄ /k ₋₄ (1/MPa ^{1/2})			-21	-184

Equati

reverse

group (C

the len

tyger

effect

exchan

betwee

test o

for tr

for re

fract

sites

adson

$O(H)_2$

const

found

$O(H)_2$

cover

(Equations 25 and 27) is the term $(1/k_1C_T)(1/P_w)$, which appears in the reverse oxygen exchange expression. Inspection of the rate constant group $(1/k_1C_T)$ in Table 4 shows that it has a very low value, lower than the error calculated for this parameter. This indicates that reverse oxygen exchange is at rapid equilibrium, because this term is effectively zero.

Comparison of the equilibrium constants for reverse oxygen exchange and "associative" hydrogen adsorption helps to distinguish between the two mechanisms as inhibitory reaction steps, which is the most difficult distinction to make because the forms of rate expressions for these two mechanisms is identical. The equilibrium rate constant for reverse oxygen exchange (k_1/k_{-1}) is 0.029, which indicates a low fractional coverage of C(O) surface groups compared to the free surface sites, C_f . The equilibrium rate constant for "associative" hydrogen adsorption (k_3/k_{-3}) is 425, which indicates a high fractional coverage of C(H)₂ surface groups compared to C_f . Table 5 shows that the rate constant groups found in this investigation are closely matched to those found by other workers.

TPD studies by Zhang [79] have shown that the surface coverage of C(H)₂ groups is negligible at reaction conditions, much lower than the coverage of C(O) groups. 0.02 mmolH₂/gC of "associatively" bound

Table 5

Rate
k_0
k_1
k_2
k_3

hydrog

was co

experi

assoc

at gas

cove

gasifi

gasifi

steam

maxima

dur

in ste

This i

Table 5: Comparison of rate constant groups.

<u>Rate Constant Group</u>	<u>Regressed Data</u>	<u>Huttinger and Merdes [8]</u>	<u>Weeda and Kapteijn[86]</u>
$k_2\tau$ (mmol/gC*min)	0.22	6.4 (0.33)*	
$k_1\tau$ (mmol/gC*min*MPa)	2.6	10 (0.52)*	2.3
k_1/k_{-1} (unitless)	0.029	0.025	
k_3/k_{-3} (1/MPa)	425	68.3	

* rate normalized to 1123 K via $E_A = 56.1$ Kcal/mol

hydrogen was seen at 900 K from the TPD of an annealed Saran char that was cooled in hydrogen after gasification. This range is below the experimental gasification temperature of 1123 K, therefore "associatively" adsorbed hydrogen should not be stable on char surfaces at gasification conditions and therefore have a very low fractional coverage.

TPD studies have shown some surface coverage of C(O) groups at gasification conditions. CO desorption peaks up to 0.07 mmol/g for gasification in steam and less than 0.04 mmol/g for gasification in steam/hydrogen are produced after gasification at 1123 K, with peak maxima at 1200 K. Larger CO desorption peaks were also produced at 1200 K during TPD for gasification at 1000 K; 0.21 mmol/gC after gasification in steam and less than 0.04 mmol/gC for gasification in steam/hydrogen. This indicates a small but significant surface coverage of C(O) groups

with a

and

with

4.2

the m

$n=1$

hydro

Figure

3.3

cerf

over

regr

$n=1$

the

Dres

hydr

the

that are stable at gasification conditions, which is consistent with the equilibrium constant calculated when reverse oxygen exchange is the inhibitory mechanism.

4.2.3. Theoretical Rate Curves

Theoretical steady-state char gasification rate curves based on the models and calculated rate constants for reverse oxygen exchange ($n=1$), "associative" hydrogen adsorption ($n=1$), and dissociative hydrogen adsorption ($n=0.5$) are compared to actual rate curves in Figures 68-73. Both models fit well for char gasifications performed at 0.3 MPa, but only experiments with 0 and 5% H_2 in the feed gas were performed at this pressure. The $n=1$ model produces a much better overall fit than the $n=0.5$ model, which is supported by linear regression analysis and by comparison of calculated rate constants. The $n=1$ model is off by a factor of 2 at 1.0 and 3.1 MPa and 0% hydrogen in the feed gas, but the fit improves with increasing hydrogen partial pressure. The $n=0.5$ model is very close at 1.0 and 3.1 MPa and 0% hydrogen in the feed gas, but as hydrogen partial pressure increases, the error grows to an order of magnitude.

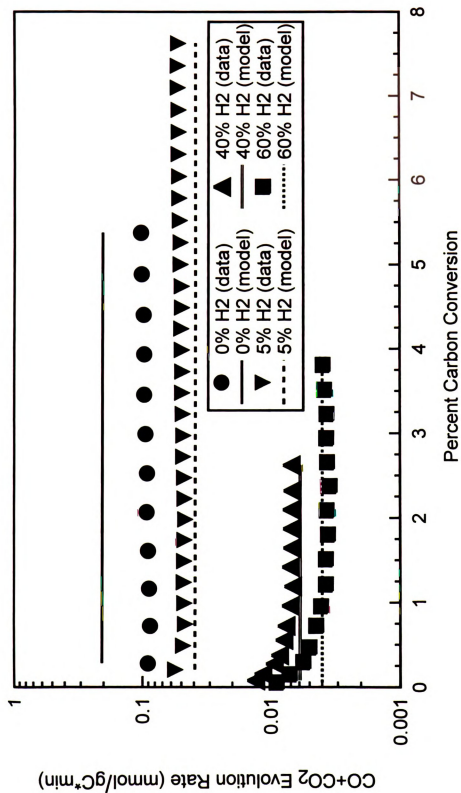


Figure 68: CO+CO₂ evolution rate from annealed Saran char steam gasification at 3.1 MPa and $\eta = 1$ " model.

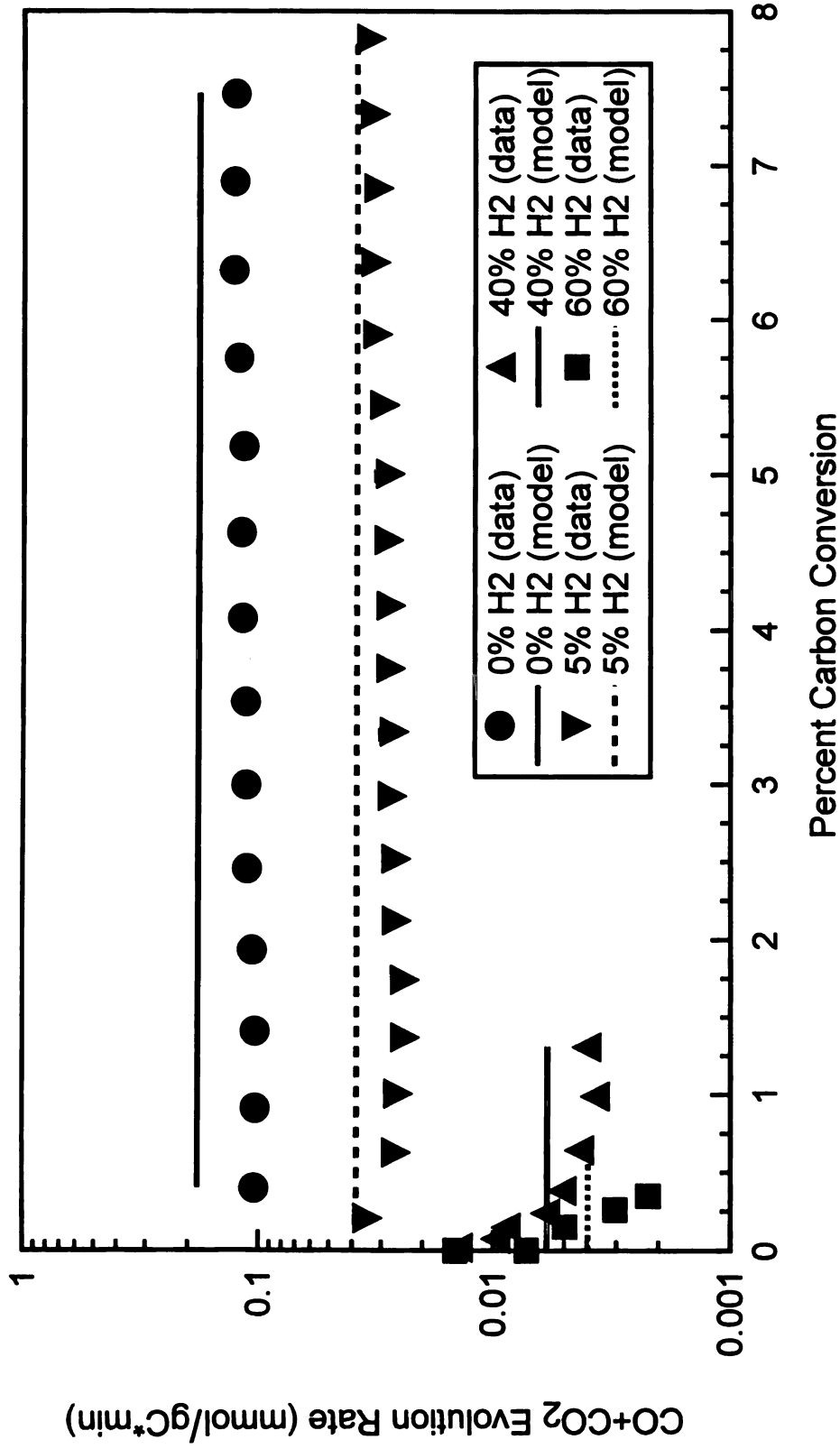


Figure 69: CO+CO₂ evolution rate from annealed Saran char steam gasification at 1.0 MPa and "n = 1" model.

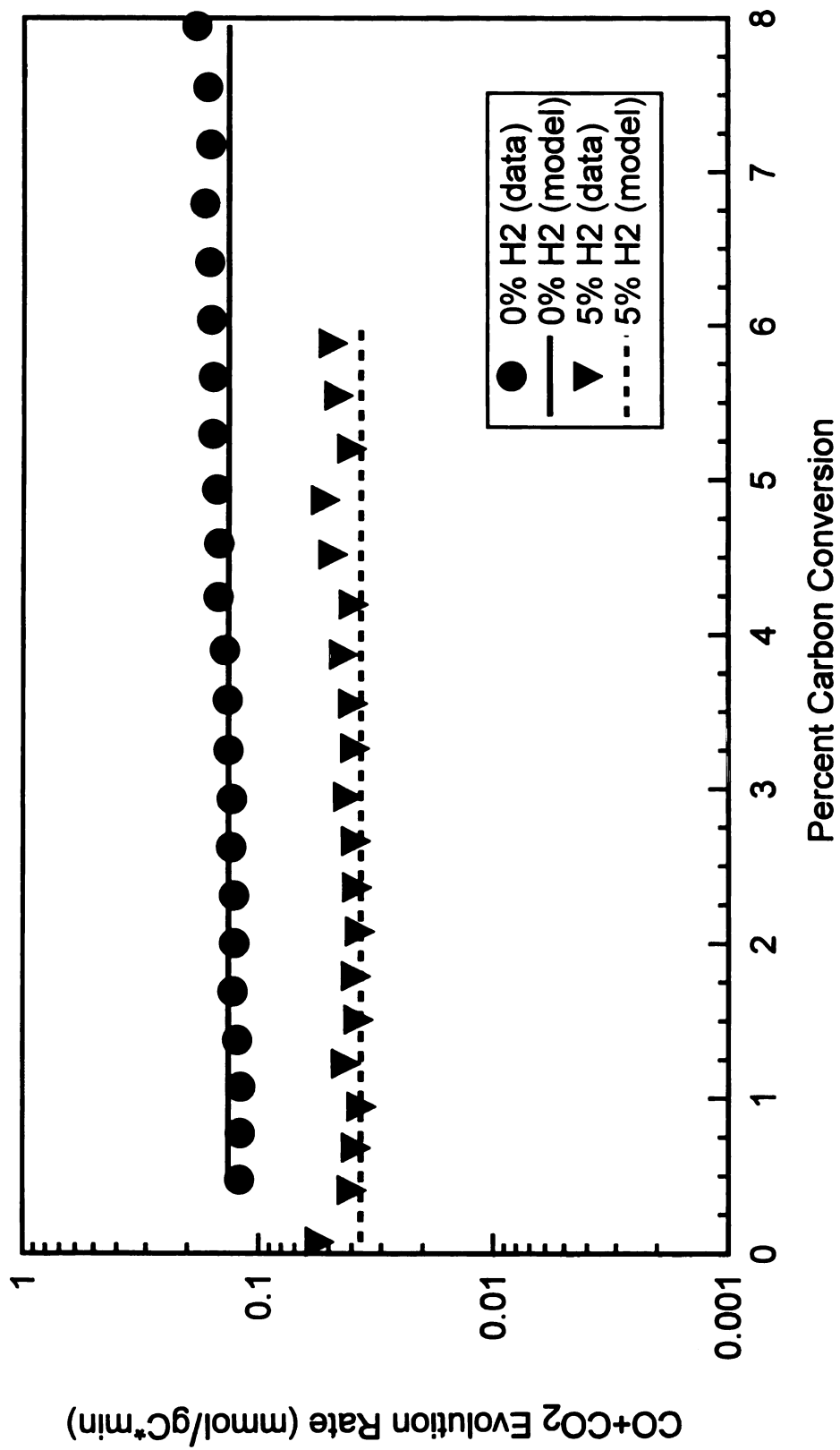


Figure 70: CO+CO₂ evolution rate from annealed Saran char steam gasification at 0.3 MPa and "n = 1" model.

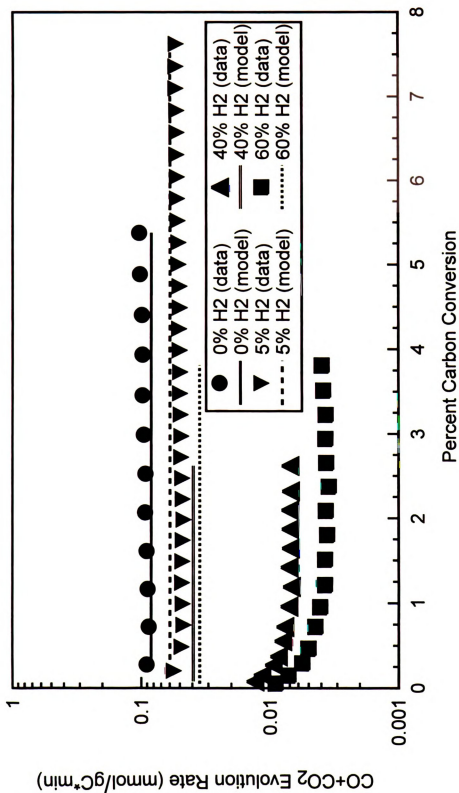


Figure 71: CO+CO₂ evolution rate from annealed Saran char steam gasification at 3.1 MPa and "n = 0.5" model.

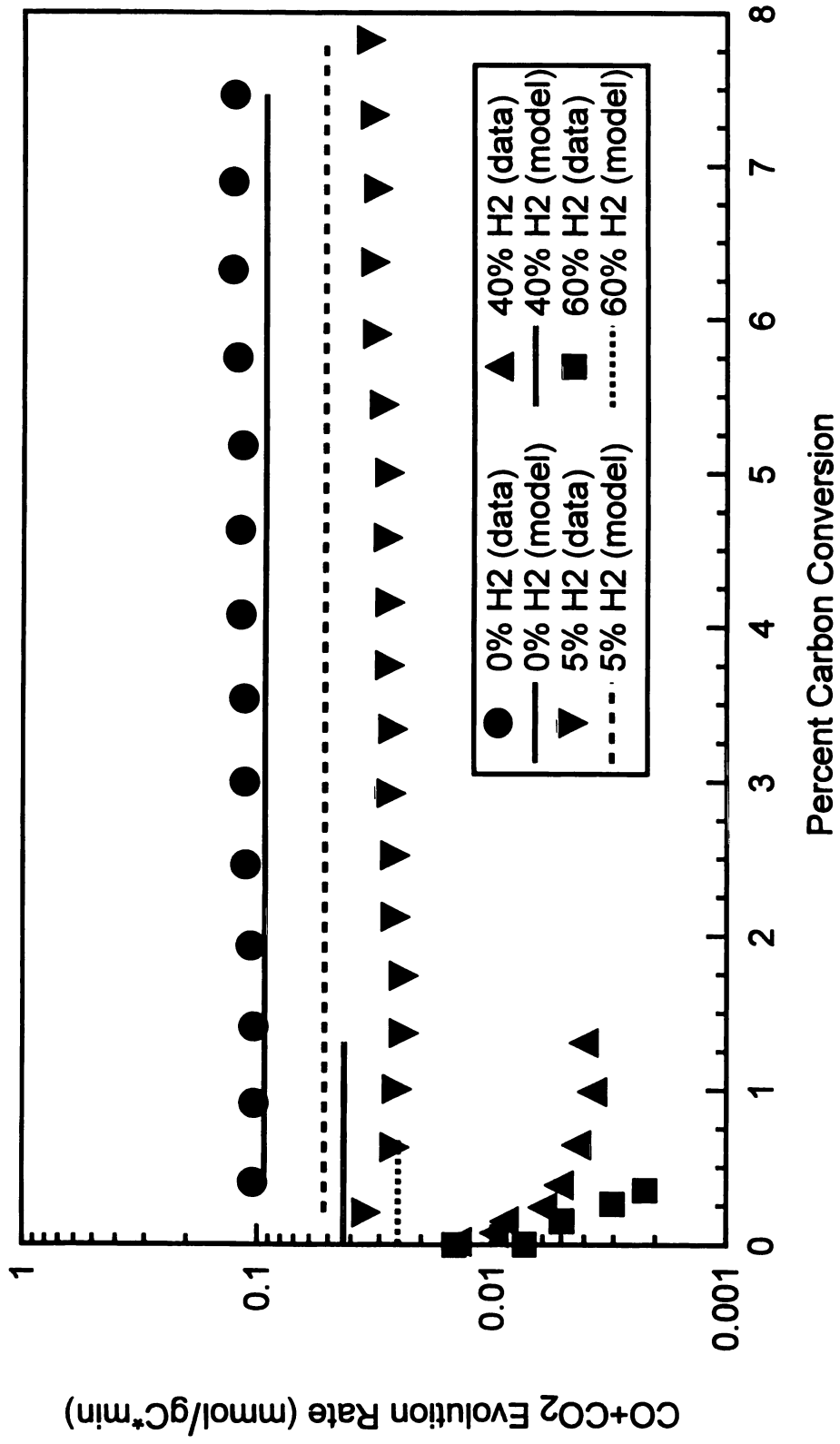


Figure 72: CO+CO₂ evolution rate from annealed Saran char steam gasification at 1.0 MPa and "n = 0.5" model.

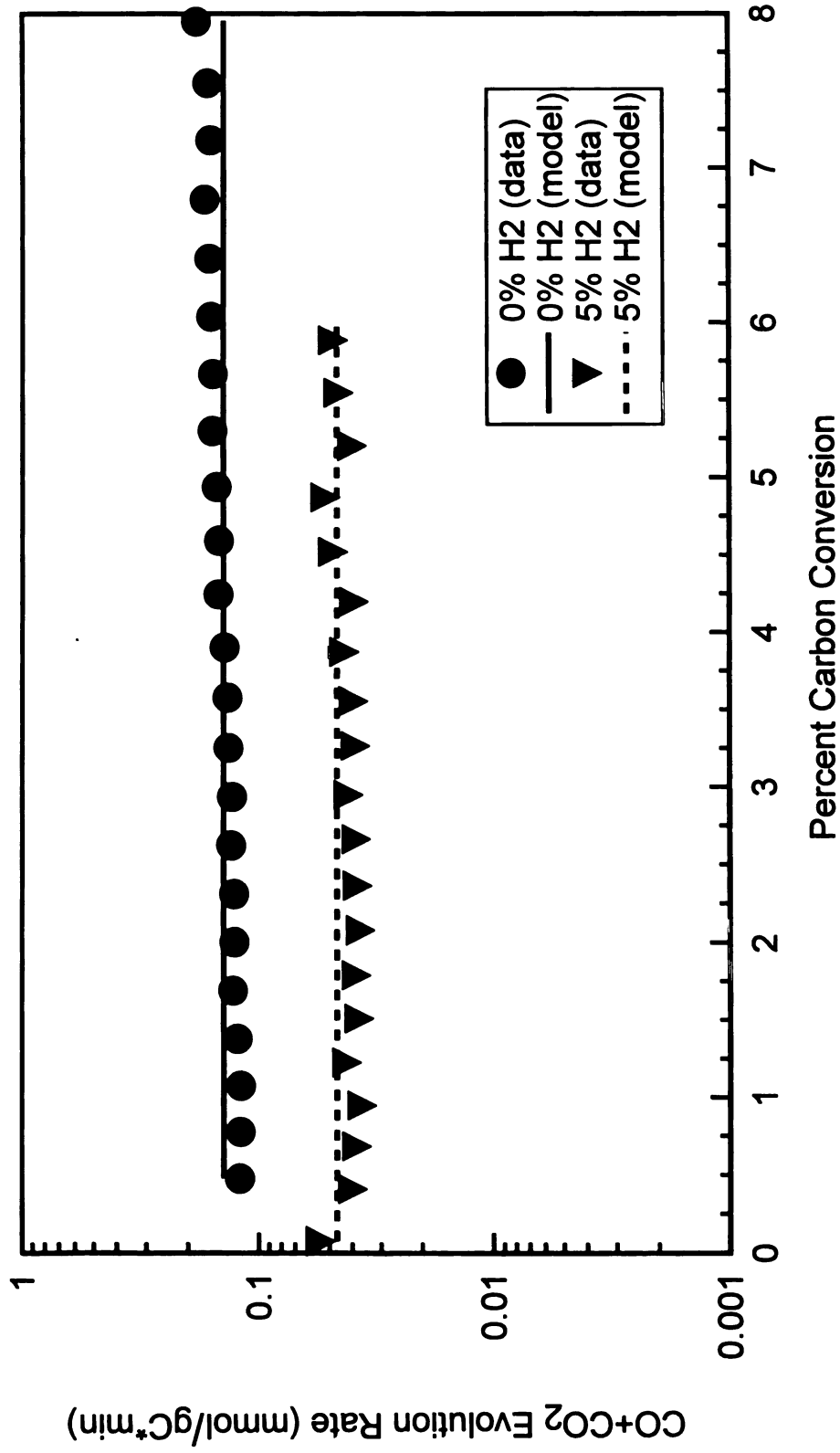


Figure 73: CO+CO₂ evolution rate from annealed Saran char steam gasification at 0.3 MPa and "n = 0.5" model.

4.3. Methane Formation Only

Expressions for methane formation excluding steam gasification were derived to determine the mechanism by which direct hydrogasification takes place. Methane formation by successive "associative" hydrogen adsorption gives a rate expression as follows.

$$r_{\text{CH}_4} = \frac{k_5 C_T P_{\text{H}_2}^2}{(k_{-3}/k_3) + (1 + k_5/k_3) P_{\text{H}_2}} \quad (39)$$

Methane formation by successive dissociative hydrogen adsorption gives a much more complicated expression, with a general form as follows.

$$r_{\text{CH}_4} = \frac{k_8 C_T P_{\text{H}_2}^2}{f_1(k) + f_2(k) P_{\text{H}_2}^{1/2} + f_3(k) P_{\text{H}_2} + f_4(k) P_{\text{H}_2}^{3/2}} \quad (40)$$

Figure 74 shows the natural log of methane formation rate plotted against the natural log of hydrogen partial pressure. The best fit line to the data has a slope of 0.42, which is fairly close to 0.5. The only way that the models can describe this relationship is if the dissociative hydrogen adsorption expression is used with a dominant last term in the denominator, therefore we can conclude that direct hydrogasification takes place by successive dissociative adsorption. This is consistent with the findings of Zielke and Gorin [19] and Cao and Back [20].

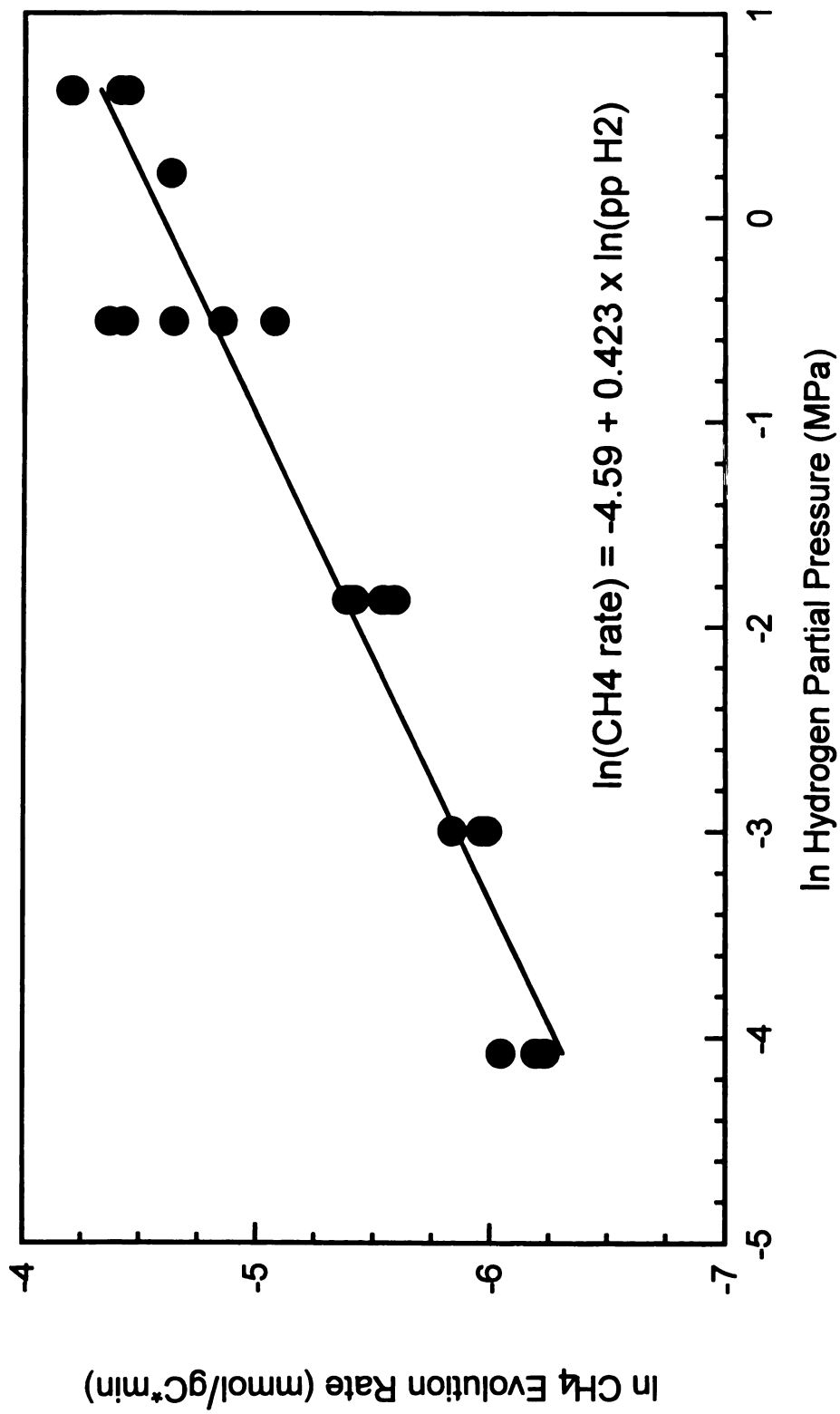


Figure 74: Dependence of methane formation rate on hydrogen partial pressure in steam gasification of annealed Saran char at all conditions tested.

5.1.1

Dir

char conv

chars by

ranges of

effects c

adsorption

with the

Chapter 5

CHAR PROPERTIES

DURING GASIFICATION

5.1. Hydrogen Adsorption

Direct measurement of adsorbed hydrogen over the entire range of char conversion has shown that hydrogen inhibits steam gasification of chars by two distinct mechanisms which remain active over different ranges of conversion. The form of hydrogen inhibition that first affects chars during gasification is initial rapid dissociative hydrogen adsorption over the first 1% conversion. Figure 54 shows this along with the initial rapid decline in steam gasification rate over the same

conversion range. This adsorption decreases rate by covering active sites, termed "free" carbon sites, on the char surface with stable hydrogen atoms. This happens regardless of reactant gas composition and is irreversible at reaction conditions.

The second form of hydrogen inhibition becomes dominant once the dissociatively adsorbed hydrogen is in place. The small number of remaining unblocked active sites (unsaturated surface carbon atoms) are subject to the dynamic equilibrium of oxygen exchange/reverse oxygen exchange with water. Most of the surface oxide complexes are stripped of their oxygen atoms by gaseous hydrogen before they can desorb in the form of CO. Active sites do not become blocked with "associatively" adsorbed hydrogen because it is not stable at reaction temperatures. Other workers that have identified dissociative hydrogen adsorption as the only mode of inhibition have performed char gasifications under conditions of very low reaction rate where this mode may dominate over reverse oxygen exchange [6,43,48,49].

5.1.1. Initial Rapid Adsorption

Hydrogen rapidly adsorbs on char surfaces at the initiation of steam gasification, as seen in Figure 53 and 55, even with no gaseous hydrogen present in the reactor feed. The source of hydrogen must be that which is liberated by CO+CO₂ formation as well as surface oxide

format

general

to the

of the

in the

with

value

that

multi

surface

attached

several

by the

surface

on the

the

the

value

formation, so a comparison has been made between the initial hydrogen generation rate and the initial hydrogen adsorption rate.

Hydrogen adsorbs on annealed char surfaces at a rate of 0.30 mmolH₂/gC*min over the first 0.5% conversion, but is liberated at a rate of 0.18 mmolH₂/gC*min due to CO+CO₂ formation under conditions of 0% H₂ in the reactant gas. The difference between the two values is 0.12 mmolH₂/gC*min, and over the course of 0.5% conversion gives a total value of 0.60 mmolH₂/gC. The CO desorption peak upon outgassing the char sample after several percent conversion accounts for 0.07 mmolH₂/gC, which is about one tenth of the difference.

The most likely explanation for this is that the quantity of surface oxide groups during the initial transient phase of gasification attains a value that is several times greater than that present after several percent conversion. The char surface is not initially blocked by strongly bound hydrogen, so a relatively high concentration of surface oxides can form, liberating hydrogen in the process. These oxides, along with transient char structural properties, contribute to the initial high gasification rate. After the initial transient phase the quantity of adsorbed oxygen declines to a fraction of its former value due to desorption and displacement by strongly bound hydrogen.

5.1.2. Gradual Adsorption over Time

Hydrogen continues to build up very gradually on char surfaces after initial rapid adsorption upon exposure to hydrogen containing reactant gases, as seen in Figures 53 and 56. A final surface concentration of $2.5 \times 10^{-3} \text{ mmolH}_2/\text{m}^2$ corresponds to 25% coverage. Unlike the first 1% conversion, however, the gasification rate also increases very gradually along with surface hydrogen concentration. Even though these changes are very gradual compared to the initial changes in char properties, they indicate that changes in the char morphology also play an important role in determining reactivity.

5.2. Char Structure

Char structure is very important in determining rate behavior because most chars have significant pore structure down to the micropore level, and have surfaces which are heterogeneous and constantly being renewed with reaction. Varying configurations of carbon atoms, as well as heteroatoms, can all affect gasification rate. These properties can also change in relative importance with conversion because of the constant removal of surface carbon atoms throughout the course of gasification.

5.2.1. Total Surface Area and Pore Structure

The annealed Saran char used in this investigation is extremely porous, with a large fraction extending below 2 nm into the micropore range. The first indication of this is the long time required to perform nitrogen adsorption on the annealed chars. The time it takes for nitrogen to intrude into pores is inversely proportional to the pore diameter, and eight hours are required to complete a nitrogen BET on the annealed char samples.

TSA calculated by nitrogen adsorption is very high, about 1500 m²/g, which is also indicative of a microporous material. Figures 37 and 38 show TSA gradually increasing with conversion, indicating that char micropore structure opens up and allows gaseous species greater access to the internal surface. Char reactivity appears to increase even on a unit area basis at higher conversion as seen in Figures 39, 40, and 43, but this may be partly due to the fact that the new char surface area opening up is fresh and more reactive than that which has been exposed to reactant gases for some time.

Further evidence of char microporosity is seen by comparing the N₂ BET surface to that which is calculated by mercury intrusion, which only measures down to the mesopore (2-50 nm) level. Mercury intrusion gives a much lower value of 0.12 m²/g which is four orders of magnitude lower

tra

ing

is

but

of

The

but

one

see

5.1

are

for

gas

the

graph

atom

base

plan

see

than 1500 m²/g. The value calculated by nitrogen adsorption is a significant fraction of the theoretical maximum of 2600 m²/g, but this is due in part to pore condensation. Taking this into account, the surface area created by micropores is still at least two to three orders of magnitude greater than those created by mesopores and macropores. The average pore diameter calculated by mercury intrusion is 47.5 μm, but this is due mainly to the interstitial voids between particles. The chars were ground and sieved to -60+100 mesh, which corresponds to 150-250 μm.

5.2.2. Domain Sizes via H/C Atom Ratio

Values for adsorbed hydrogen concentration and total surface area were combined to calculate an average ideal graphitic crystallite size for annealed Saran char beyond 1% conversion. At steady state gasification, the adsorbed hydrogen concentration is approximately 4 mmolH₂/gC, which corresponds to an H/C ratio of 0.1. Assuming an ideal graphitic hexagonal crystallite with zig-zag configured edge carbon atoms, dissociatively adsorbed hydrogen, no hydrogen adsorbed on the basal planes, and a C-C bond length of 0.1421 nm [87] a graphitic basal plane width of 3.8 nm was calculated. The number of graphitic layers per crystallite was calculated based on the above plate width, a total

surfa

0.336

comp

hydr

cryst

the

the

1000

data

5.2

cryst

scat

1000

beta

beta

beta

beta

beta

beta

surface area of approximately 1000 m²/g, and an interlayer spacing of 0.3364 nm [88] to be three.

The theoretical hydrogen fractional coverage of these crystallites compares closely to that which was calculated based on the experimental hydrogen surface coverage of 2.5×10^{-3} mmolH₂/m². Assuming an ideal crystallite oriented so its basal planes are horizontal, the ratio of the area of the sides to the area of the top and bottom corresponds to the hydrogen fractional coverage. A value of 35% is calculated for the ideal crystallite, which is close to 25% calculated from experimental data.

5.2.3. X-ray Analysis

An attempt to confirm the previously stated theoretical values of crystallite dimensions with X-ray spectroscopy using both angle scattering (Bragg's Law) for unit cell dimensions and peak broadening (Scherrer Formula) for ordered domain size shows that there is almost no detectable ordered structure in annealed Saran char. Reference graphites tested included a 325 mesh and -10+60 mesh Alpha Graphite and a 360 mesh Ultra "F" Graphite, all of which showed strong peaks corresponding to an interlayer spacing of 0.336 nm and ordered domain sizes corresponding to thicknesses of 18-40 nm, or 50-120 basal planes.

As a

peak

fine

trade

face

Bara

teer

res.

fair

is

grat

ann

ony

idge

100

stia

de

de

the

X-ray spectra for all carbons tested are shown in Figures 75-78. As can be seen in Figure 75, the annealed Saran char shows no detectable peaks corresponding to spacing between graphitic basal planes. The finer mesh graphites show relatively small peaks corresponding an ordered spacing of 0.426 nm, which is the spacing between the zig-zag faces along the basal planes. This peak was detectable in annealed Saran char, but was nearly beyond the resolution of the detector, as seen in Figure 79. Analysis of materials for ordered domain size resulted in 20-40 nm for the reference materials, while the extremely faint peak in Saran char corresponded to a domain size of 3.2 nm, which is fairly close to the theoretical calculated value of 3.8 nm for ideal graphitic crystallite basal plane widths.

The lack of prominent X-ray diffraction peaks in Saran char annealed at 1773 K is consistent with small highly disordered graphitic crystallites, which are similar in dimension to those calculated for ideal graphitic crystallites based on an H/C ratio of 0.1 and TSA of 1000 m²/g. Several investigators have shown an abundance of defects in small crystallites, such as increased interlayer spacing in networks below 5 nm [89] and turbostratic structure [90]. The latter type of defect is misalignment of adjacent basal planes, which contributes to the lack of lines in powder photographs. These investigators also make

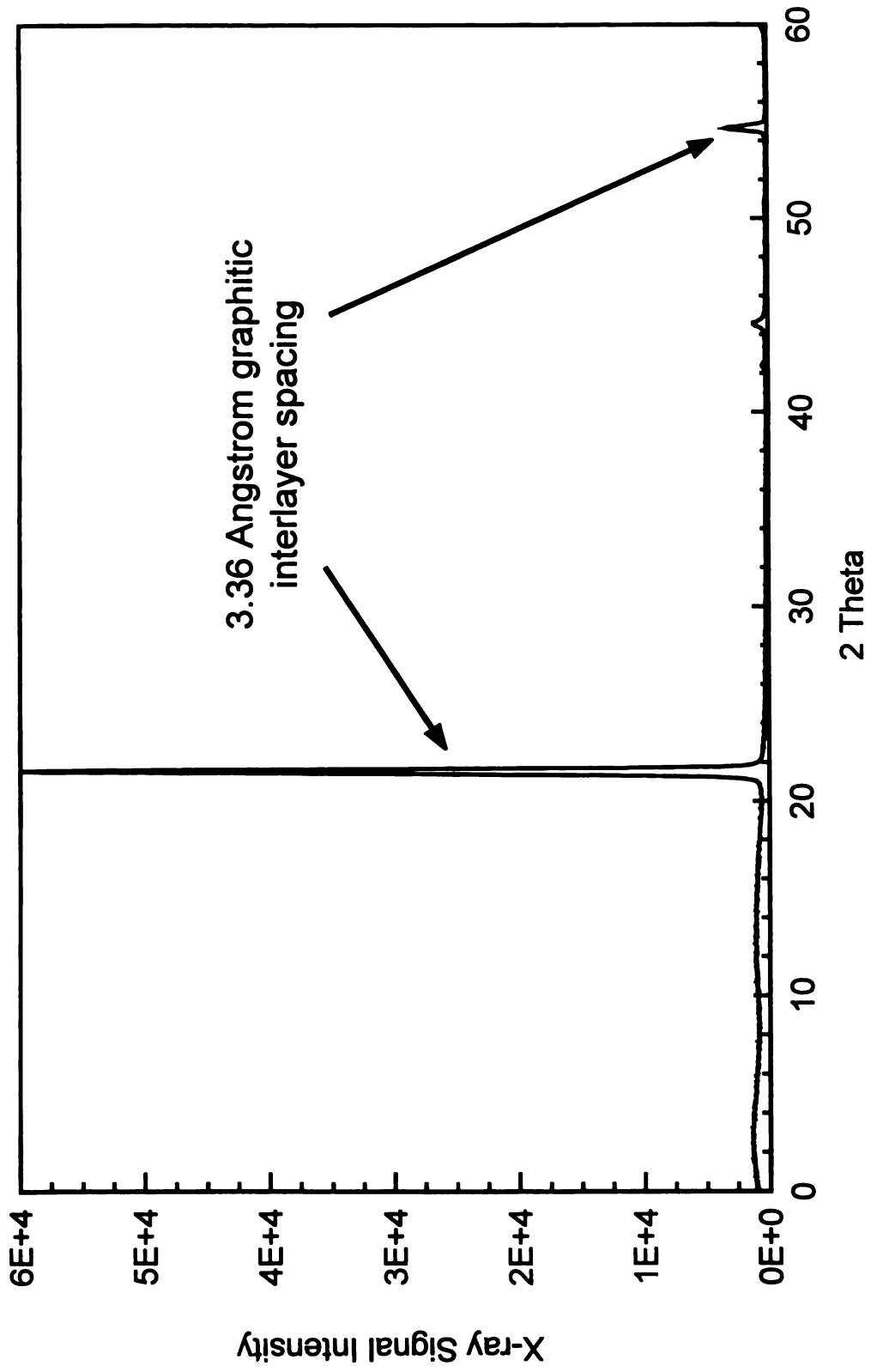


Figure 75: X-ray spectrum of 360 mesh Ultra "F" graphite.

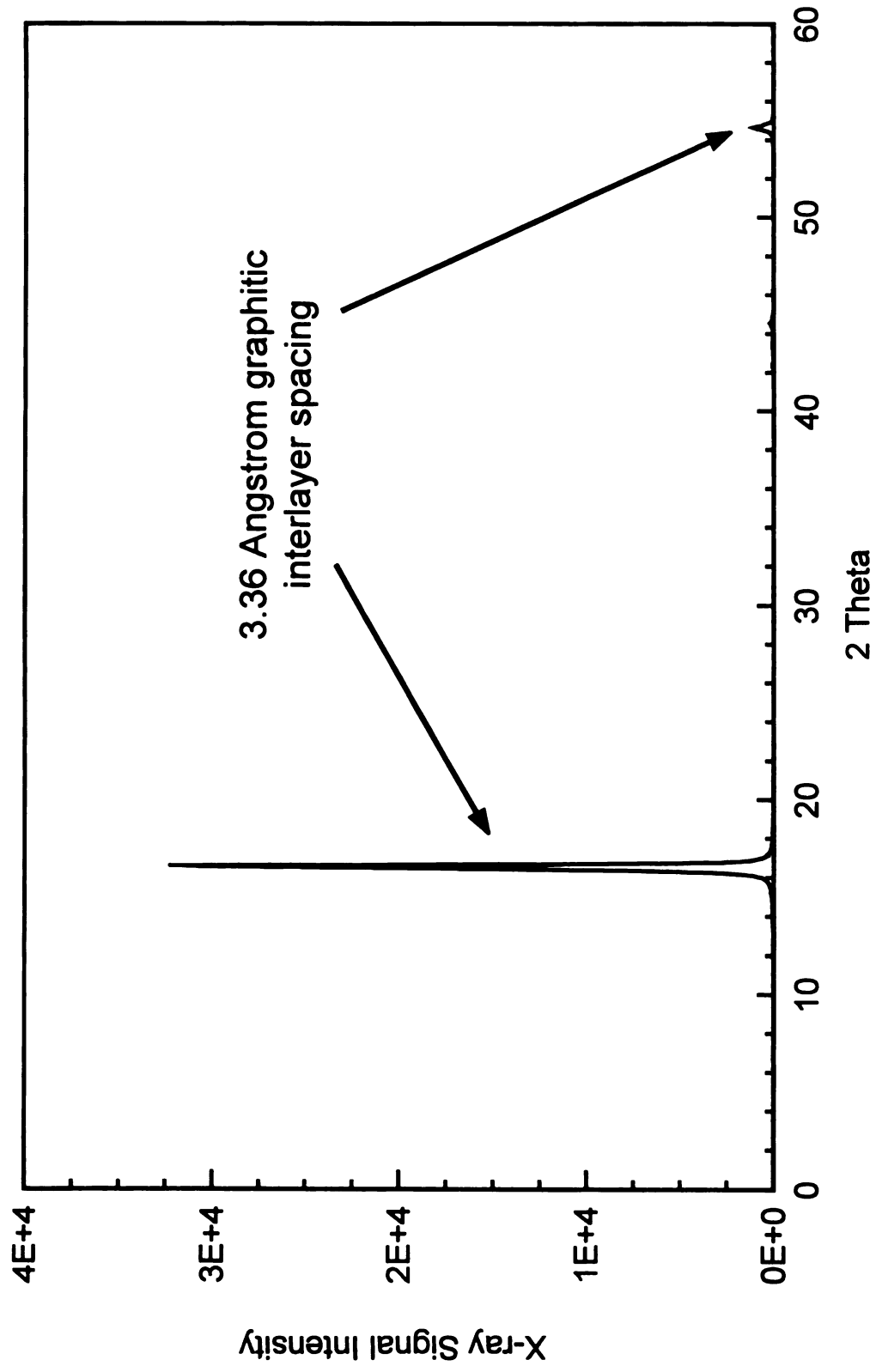


Figure 76: X-ray spectrum of 325 mesh Alpha graphite.

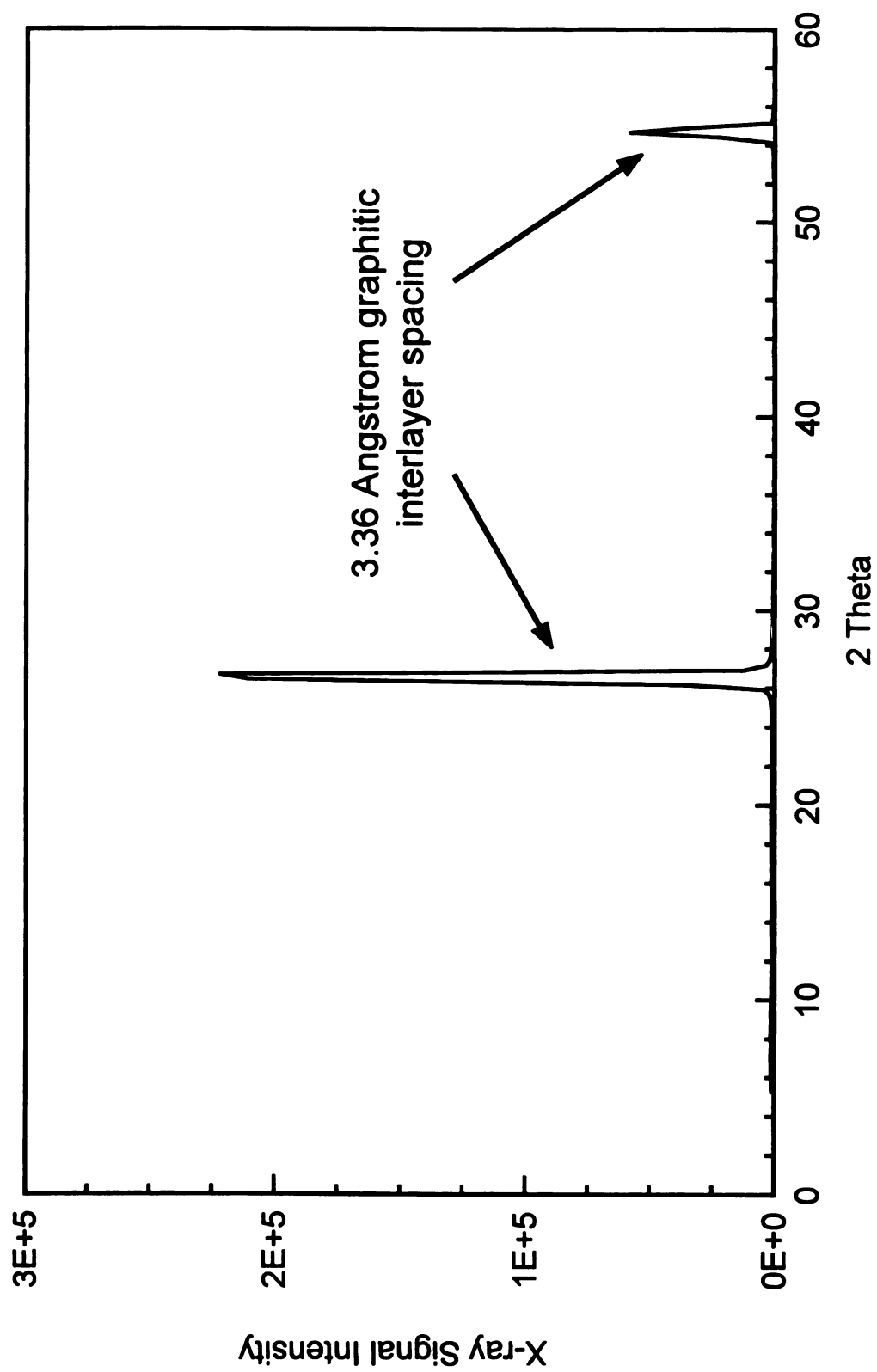


Figure 77: X-ray spectrum of -10+60 mesh Alpha graphite.

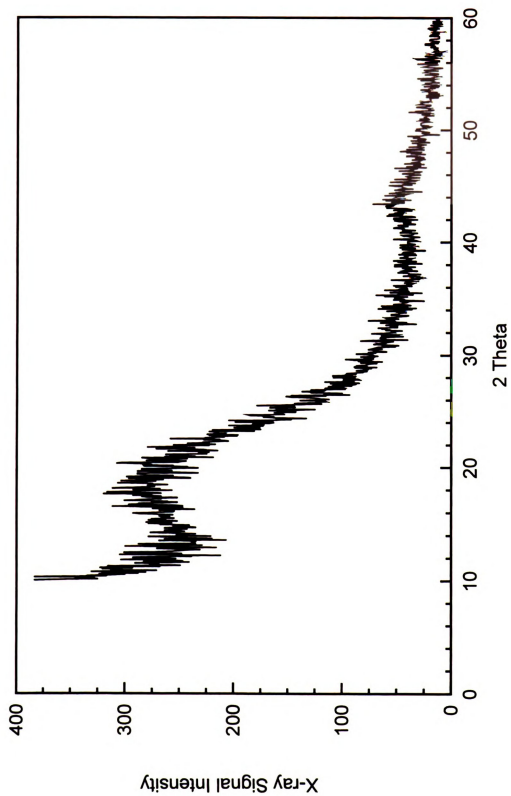


Figure 78: X-ray spectrum of -60+100 mesh annealed Saran char.

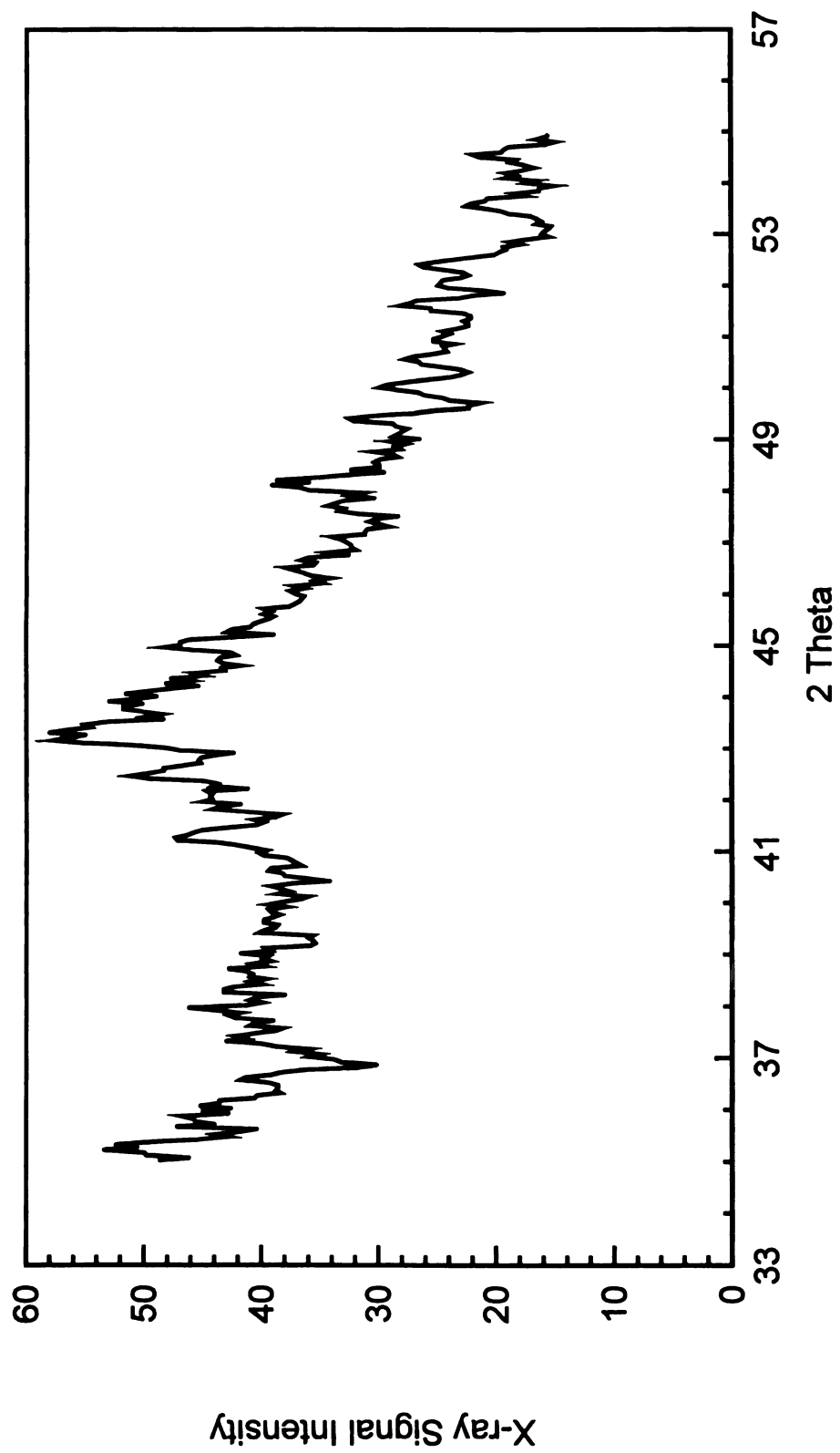


Figure 79: Magnified view of X-ray spectrum of -60+100 mesh annealed Saran char.

the point that X-ray methods become less precise with decreasing domain size, as this broadens peaks. Graphitic crystallite size of dimensions similar to those obtained in this investigation were formed by annealing a cellulose carbon at 5 K/min to 1573 K, yielding a thickness of 4-5 layers and basal plane width of 2.1 nm [90].

5.2.4. Char Morphology

Annealed Saran char has a very high surface area, is highly microporous, contains graphitic structure over small domains, but also contains a fair amount of disordered structure. Initial rapid char gasification rate can be partly attributed to reaction of a small amount of highly disordered "dangling" or "glassy" carbon atoms which form as a result of char preparation. These amorphous carbon atoms are much more likely than graphitic carbon atoms to be bound to heteroatoms and have strained C-C bonds.

Figure 80 shows CH_4 formation rate during hydrogasification of untreated (1023 K), outgassed (1273 K under vacuum), and annealed (1773 K) Saran char. It appears as if the rate curves are approaching each other as carbon conversion increases. Untreated Saran char has the highest reactivity because it has the highest initial concentration of amorphous carbon atoms and heteroatoms, while the outgassed char has a lower concentration and the annealed char has the lowest. The amorphous

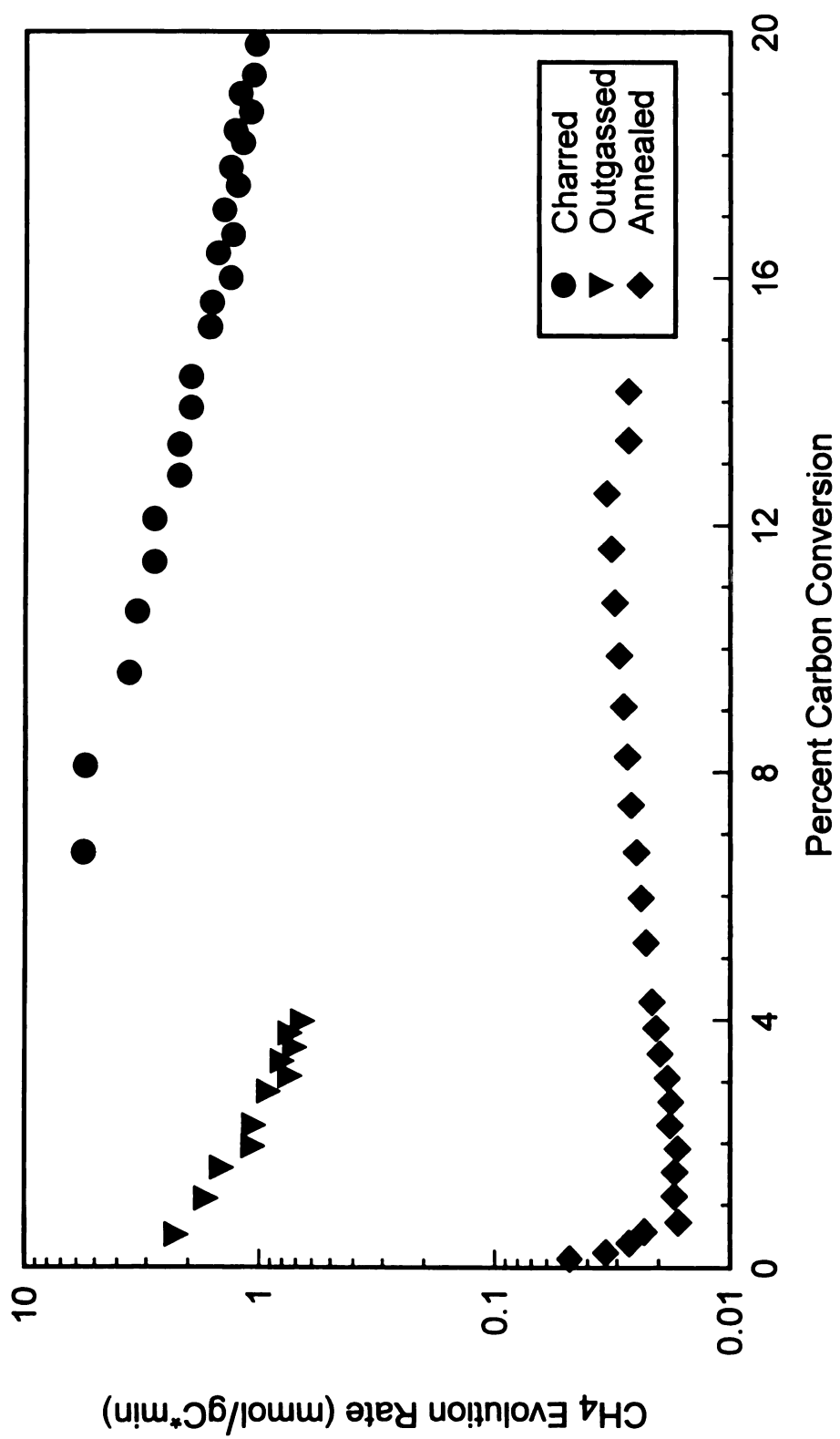


Figure 80: CH₄ evolution rate from Saran char hydrogasification at 3.1 MPa, temperature at or normalized to 850°C via $E_a=75$ Kcal/mol.

carbon atoms and heteroatoms react rapidly, leaving behind a more ordered, homogeneous, and inert graphitic structure.

The graphitic base structure is also critical to reactivity because carbon atoms of the basal planes are practically inert while edge carbon atoms are much more reactive. The ratio of edge to basal plane carbon atoms may be partly responsible for the apparent increase in char gasification rate in steam on a unit area basis for conversions above 50%. This ratio could easily increase if the edges of the basal planes react away simultaneously and at a relatively constant rate, but would decrease if individual basal planes reacted away sequentially.

The configuration of the edge carbon atoms can also change with conversion. A graphitic basal plane with edge carbon atoms in both zig-zag and armchair configurations can be seen by referring back to Figure 2. Reactant gases which contain hydrogen have been shown by other workers to preferentially react with edge carbon atoms of the armchair configuration, leaving behind the less reactive zig-zag edges. This phenomenon lends a great deal of insight into the steam gasification mechanism, and is addressed further in the following sections.

5.2.5. Char Active Sites

An active site in char gasification is a surface carbon atom that is not saturated with chemical bonds and has the potential to react with

one or more gaseous or migrating surface species. If the unsaturated surface carbon atom reacts in such a way as to be removed from the char matrix in gaseous form and leave one or more adjacent unsaturated surface carbon atoms, it has successfully propagated. If the unsaturated surface carbon atom reacts in such a way as to bind to one or more species but remain on the char matrix, it has been blocked. If it becomes bound to a relatively unstable functional group, the group may desorb and re-expose the active site. If it becomes bound to a stable group, such as dissociatively adsorbed hydrogen, the propagation of the active site terminates as it is blocked.

Edge carbon atoms have the potential to become active sites in the case of a graphitic char, but the vast majority of these are strongly bound to hydrogen during steam gasification. Those that are not bound to dissociatively adsorbed hydrogen are bound to other less stable functional groups or are unsaturated. Some functional groups may destabilize adjacent carbon atoms and increase their chances of becoming active sites, most notably the off-plane oxygen functional groups of the recently proposed "universal" char gasification mechanism [55,56].

5.2.5.1. Etch Pit Analysis

Of critical importance to understanding how hydrogen affects edge carbon atoms during gasification is a series of experiments on etch pit

00

Tr

Se

Dr

Pe

Se

Et

Pr

Co

Cr

Re

Et

De

De

Co

Co

Et

Tr

Dr

Et

Se

conformation performed by Yang and Duan [43] and Yang and Yang [6]. They used etch decoration/transmission electron microscopy on graphite samples after gasification at 923-1023 K to identify the shape and orientation of etch pits on the basal planes of graphite samples. Reaction with O_2 or CO_2 produced round etch pits on graphite surfaces, seen in Figure 81, which indicate a combination of zig-zag and armchair edge configurations. Hexagonal etch pits with zig-zag edges only, also pictured in Figure 81, were produced by reaction with H_2O , H_2O then CO_2 , CO_2 then H_2O , CO_2 plus H_2 , and H_2O plus H_2 . They conclude that hydrogen chemisorption is preferred on the zig-zag edges and therefore responsible for the anisotropy of reactivity toward the two principal edge configurations.

This is clear evidence that the presence of hydrogen changes the behavior of active sites on the char surface, or at least limits behavior to mechanisms which preserve the zig-zag edge configuration and consume the armchair edge configuration. Of particular interest are two experiments performed with successive exposure of graphite to H_2O and then CO_2 . The CO_2 gasification rate at 1023 K was greatly reduced after H_2O gasification, while no gasification with CO_2 at 923 K was observed after reaction with H_2O . Hexagonal etch pits with zig-zag edges were detected following both experiments.

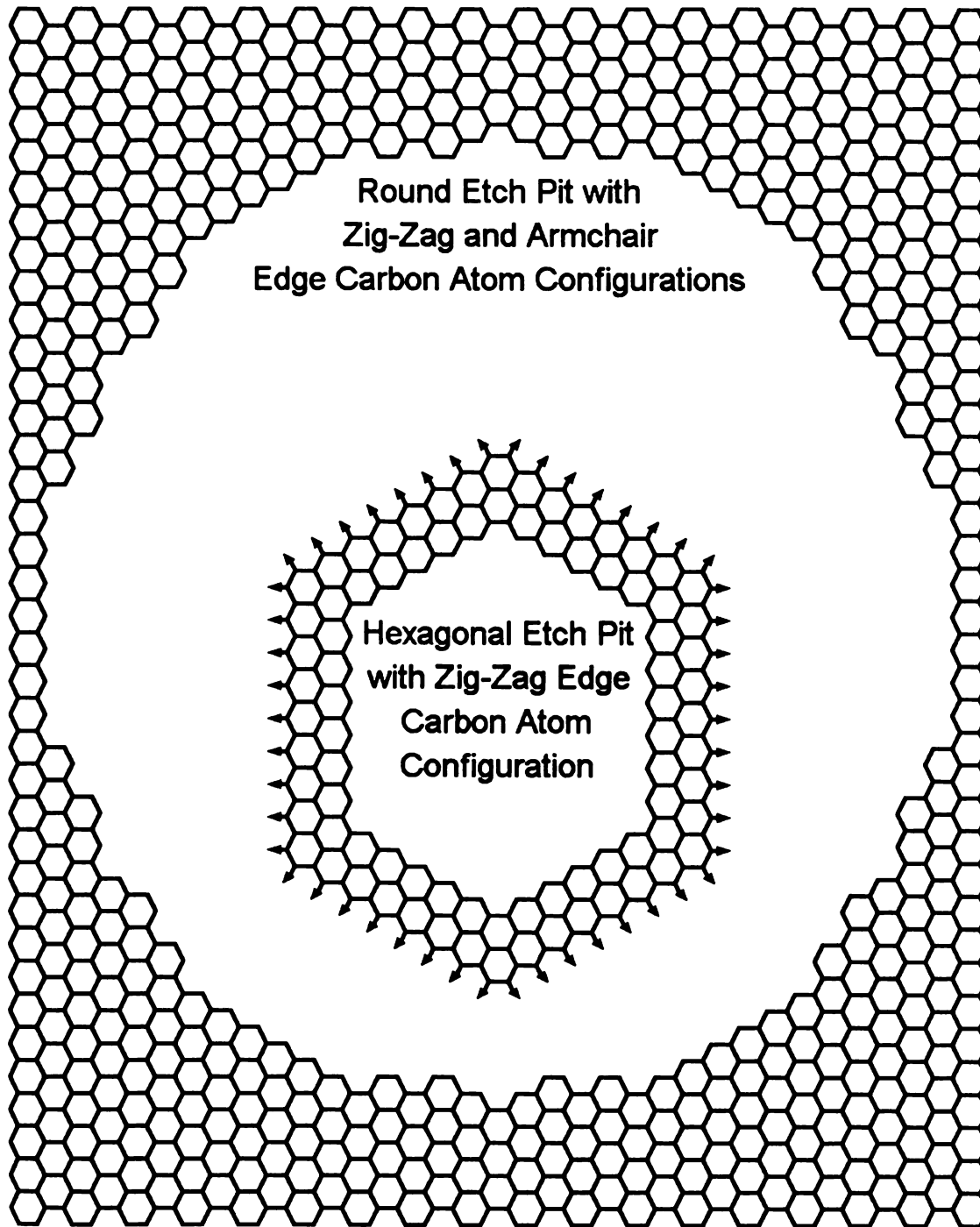


Figure 81: Round and hexagonal etch pits of the graphite basal plane.

These experiments show how strongly hydrogen is bound at gasification conditions on zig-zag edge carbon atoms. The preserved zig-zag edge configurations must be caused by residual surface hydrogen since CO_2 gasification alone produces round etch pits. This hydrogen is stable enough at 923 K to completely inhibit gasification, indicating complete blockage of active sites. At 1023 K CO_2 gasification takes place at a greatly reduced rate, but in such a way as to preserve the zig-zag edge configuration. Since no hydrogen is present in the reactant gas, the hydrogen must be migrating from one zig-zag edge to the next zig-zag edge exposed by gasification.

5.2.5.2. Active Site Propagation

The work cited above shows that the presence of hydrogen during char gasification changes the behavior of active sites from those which show no preference for leaving zig-zag or armchair edge configurations to those which show a strong preference for leaving zig-zag edge configurations. The most reasonable explanation for this is that under the presence of hydrogen, most steady-state gasification takes place via active site propagation along zig-zag edges.

Reactant gases that produce round etch pits show no preference for leaving zig-zag or armchair edge carbon atoms under conditions of no hydrogen. Graphitic basal plane edges are unsaturated or covered



primarily with oxygen functional groups which are less stable than hydrogen, and therefore more likely to react and initiate active sites. If some active sites do propagate, they do so in a chaotic sequence.

Reactant gases produce hexagonal etch pits with zig-zag edges in the presence of hydrogen because there is a much more ordered sequence of desorption of edge carbon atoms. The lack of armchair edge carbon atom configurations indicates that they are more reactive and less prone to hydrogen inhibition, while zig-zag edges are preserved. If active sites were generated on the zig-zag edges they would become pitted and rounded out, especially if the active sites only propagated to a few adjacent carbon atoms before termination. Evidence of the difficulty of initiating active sites on hydrogen-blocked zig-zag edges was seen by Yang and Duan [43] and Yang and Yang [6] in the greatly reduced CO₂ gasification rates following H₂O gasification.

Active sites are generated at defects in the zig-zag edges such as armchair-like arrangements, crystallite corners, crystallite defects, and unstable functional groups. These active sites propagate along the zig-zag edges and remove the outer row of carbon atoms, preserving the edge intact. Figure 82 shows two possible modes of active site propagation along a zig-zag edge. They are both two-step mechanisms which alternate between the removal of a cyclic carbon atom (step a) and

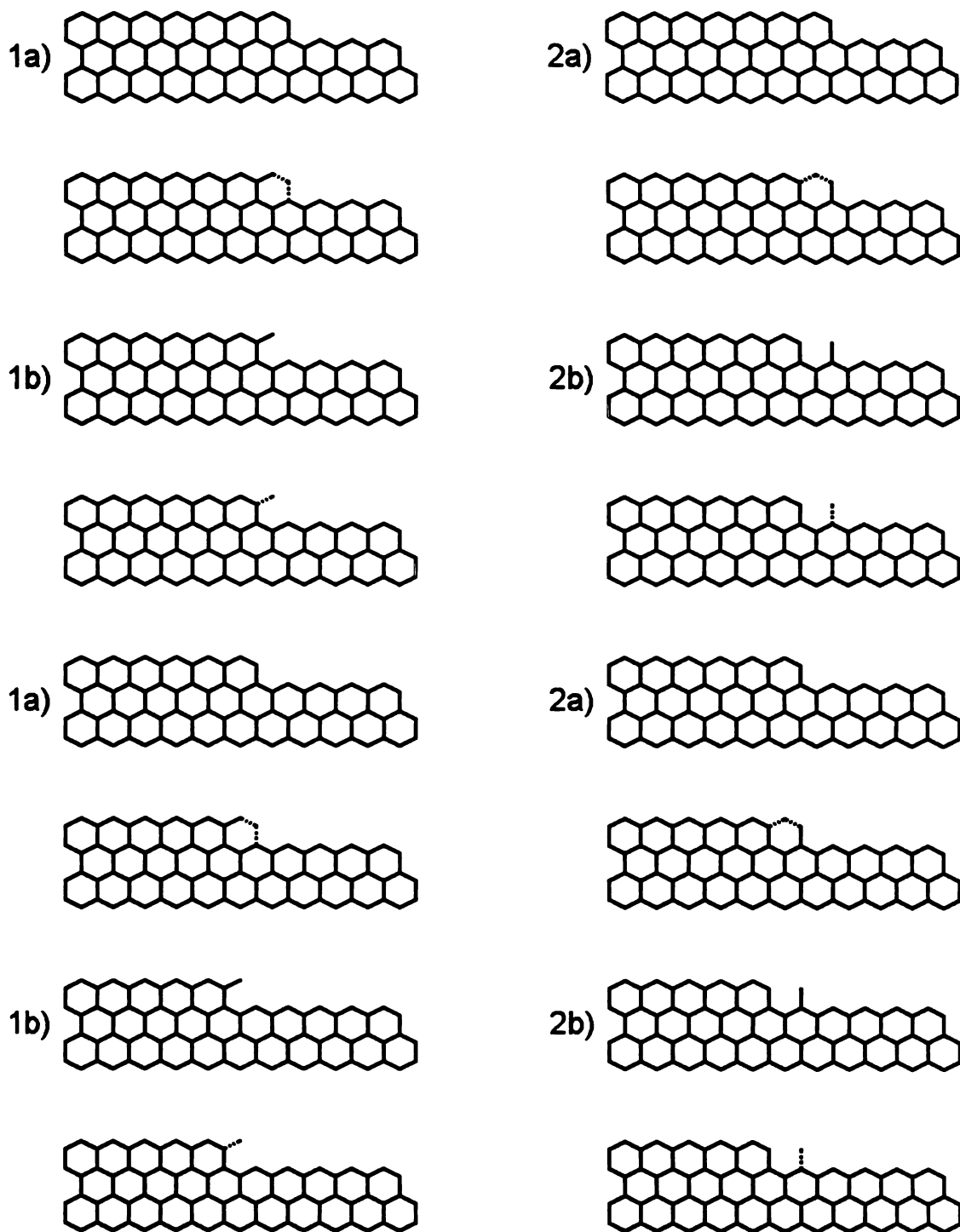


Figure 82: Active site propagation along graphite zig-zag edge.

a

c

a

s

a

a

c

t

d

.

t

w

r

E

c

.

c

c

c

f

n

a dangling carbon atom (step b). It is more likely that mechanism 1 is correct because it entails sequential desorption of the edge carbon atoms, while mechanism 2 does not and requires transfer of the active site between non-adjacent carbon atoms.

Figure 83 shows two possible modes of active site propagation along the armchair edge carbon atom configuration. Mechanism 3 alternates between two configurations which consist of removing a cyclic carbon atom and removing a dangling carbon atom. The major problem with this mechanism is that two adjacent carbon atoms in the "sheltered" position must be skipped for every two adjacent carbon atoms in the "exposed" position that desorb. This is an even more extreme example of transfer of the active site between non-adjacent carbon atoms. Mechanism 4 entails sequential desorption, but is fairly complex as it must alternate between four different configurations.

5.2.5.3. Active Site Behavior with Conversion

Char surfaces are covered with active sites and easily gasified carbon atoms at the start of gasification. Those that react rapidly include loosely bound secondary carbon atoms that may be glassy, dangling, or saturated with a greater concentration of heteroatoms. Desorption of the secondary carbon atoms, as well as low-stability functional groups, generates active sites (unsaturated carbon atoms) on

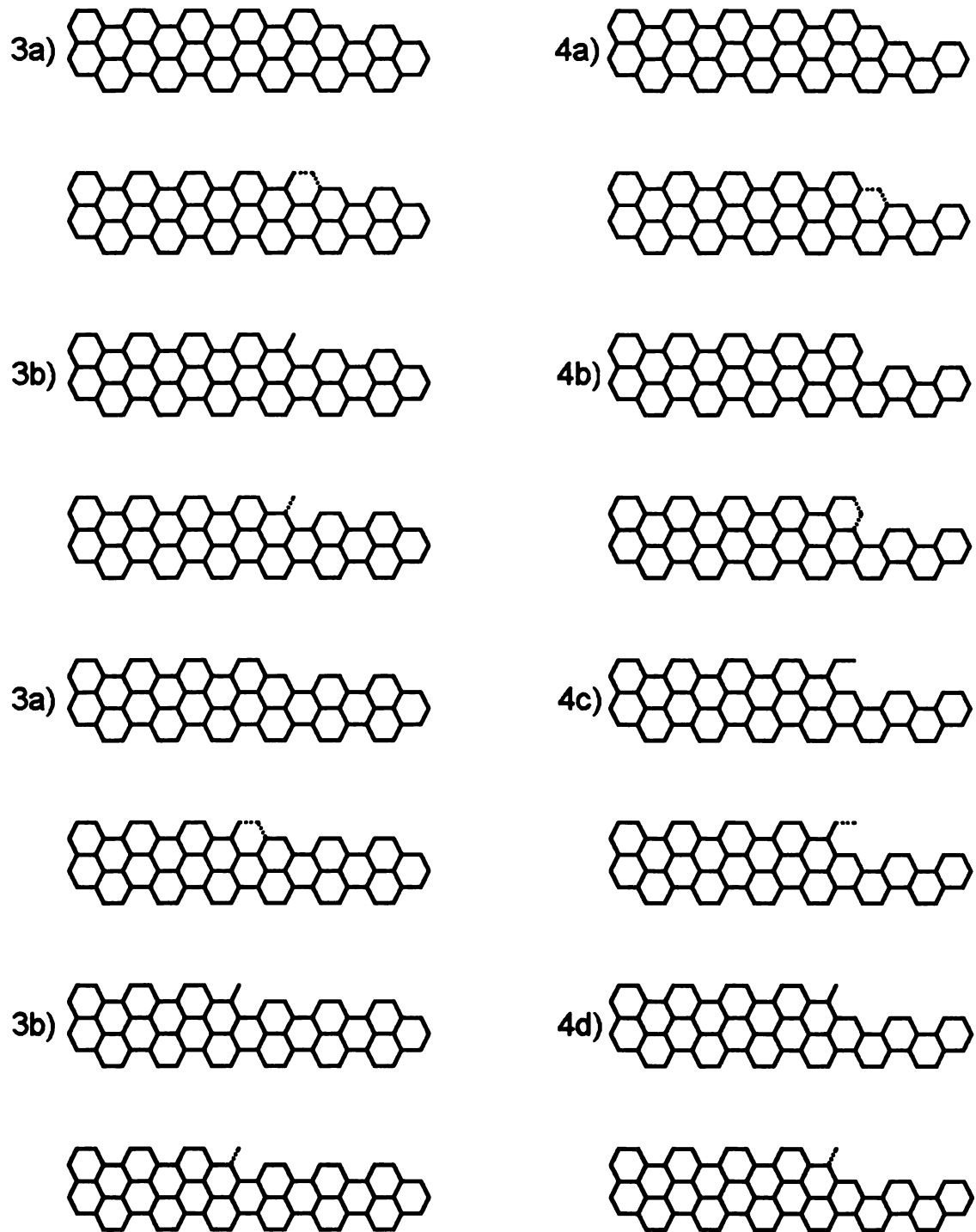


Figure 83: Active site propagation along graphite armchair edge.

the char edge surfaces. The annealing pretreatment process also generates active sites by causing strongly bound hydrogen to desorb from edge carbon atoms, leaving them unsaturated.

Over the course of the first 1% conversion for annealed Saran char, 10% for annealed coal char, and 5-15% for unannealed chars, the high concentration of active sites decreases rapidly. The "secondary" carbon atoms are rapidly consumed, and hydrogen rapidly and strongly adsorbs to most unsaturated surface carbon atoms. Also decreasing is the ratio of the more reactive armchair to the less reactive zig-zag edge carbon atom configurations. Figure 84 shows how an etch pit or graphitic crystallite can change in shape from rounded features displaying zig-zag and armchair edge configurations to hexagonal features with zig-zag edges.

It is over the initial transient conversion range that the active site termination rate is much greater than the active site generation rate, causing a significant decrease in char gasification rate. Dissociative hydrogen adsorption is responsible for the blockage and termination of nearly all active sites over this range. Other examples of active site termination include "collision" or "canceling out" of two active sites together, complete gasification of an entire graphitic basal plane, or excessive steric hindrance from adjacent basal planes.

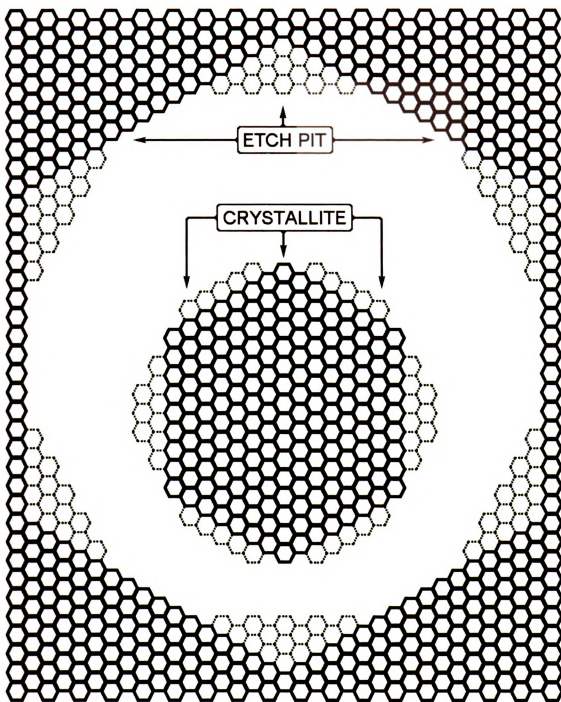


Figure 84: Round etch pit and crystallite converting to hexagonal features with zig-zag edges.

In the last case the active site may just be “stalled out” and resume propagation after adjacent layers have gasified.

After the first 1-15% conversion (depending upon char type) the “secondary” carbon atoms have reacted away, very few armchair edge carbon atom configurations are left, and dissociatively adsorbed hydrogen is in place. The active site termination rate is low and now roughly equals the generation rate, and the char shows a fairly constant reactivity with conversion. Most gasification takes place via active site propagation along zig-zag edges. Active sites are in a dynamic equilibrium with species that weakly adsorb, such as oxygen functional groups, but the effect of reverse oxygen exchange usually removes the functional groups before they can desorb in the form of CO and leave another unsaturated surface carbon atom. The abundance of defects in annealed Saran char, as well as most other chars, ensures that there will always be surface carbon atoms that are more prone to active site initiation than those of the zig-zag edge.

5.2.5.4. Comparison to the “Universal” Mechanism

The char gasification mechanism identified as universal by Chen, Yang, Kapteijn, and Moulijn [55] and Kapteijn, and Moulijn [56] represents an extensive and thorough body of work, however it is very unlikely that this mechanism plays a role in char gasification when

3

.

3

a

a

F

t

t

a

g

i

g

g

5

A

t

t

S

t

W

gaseous hydrogen is present. The effects of reverse oxygen exchange, identified in this investigation as the major mode of hydrogen inhibition in steady-state steam gasification, should be even greater for off-plane oxygen atoms because they only form a single bond to the adjacent carbon atom. Also, the universal gasification mechanism (see Figure 3) is shown with all edge carbon atoms saturated with oxygen, but in steam gasification nearly all edge carbon atoms are saturated with hydrogen. Chen et al. do state that off-plane oxygen atoms are not abundant in CO_2 and H_2O char gasification compared to O_2 char gasification, but in the presence of hydrogen they are probably in such low concentration that they do not contribute significantly to char gasification rate.

5.3. Rate Enhancement

The practical application of the knowledge of actual mechanisms by which steam/hydrogen gasification of chars is inhibited by hydrogen is to enhance the reaction rate. Hydrogen presents problems for achieving this goal because small quantities bind rapidly and strongly to char surfaces, covering and blocking the majority of surface carbon atoms that are at the edges of the graphitic basal planes. Gaseous hydrogen will always be present in steam gasification of chars because one

hydrogen molecule is liberated for every water molecule that reacts with a surface carbon atom.

5.3.1. Partial Combustion

Intermittent treatments of annealed Saran char with molecular oxygen at 700 K were done by Zhang [79] to test the duration over which fixing oxygen functional groups on char surfaces enhances steam gasification rate. Mild rate enhancements were produced during gasification at 998 K, which could be due to contributions from fixation of surface oxygen functional groups as well as changes in char morphology.

Rate enhancement was not achieved for char gasifications at 1123 K given the same oxidative treatments. The reason for the differences in rate enhancement is because a much greater concentration of oxygen functional groups fixed during intermittent oxidation remains on char surfaces during gasification at 998 K. These groups are not stable at the temperature chosen for the majority of gasifications performed in this investigation (1123 K), so they do not remain on the char surface and do not enhance rate.

5.3.2. Catalysis

Catalysis with alkali salts and transition metals is the most common method of significantly increasing char gasification rate. Gasification rates can be 2-3 orders of magnitude higher in catalyzed systems. The effect of hydrogen inhibition is greatly reduced because of the dissociation site/spillover action of catalysts, increasing gasification rate by increasing the number of active sites, not by lowering the activation energy [61].

Sulfur poisoning, not hydrogen, is the main form of inhibition in catalyzed char gasification. Sulfur is present as both a heteroatom in coal and as a mineral component in the coal ash. Charring can volatilize most of the sulfur initially present in the carbon matrix, but not the sulfur in the ash. Most model chars have very low concentrations of sulfur and very little ash, so poisoning is not a problem. Coal, on the other hand, always contains sulfur and ash. Charring to volatilize sulfur in the carbon matrix is not a problem, but getting rid of the ash is expensive and time-consuming. Complete demineralization of coal samples during previous experiments in our laboratory required heated baths of hydrofluoric, hydrochloric, and nitric acid [74]. Ash particles can catalyze steam gasification in some systems as is seen by comparison of rates based on surface areas of

annealed Saran and coal char, but this enhancement is fairly mild compared to catalysis with alkali or transition metals.

Chapter 6

CONCLUSIONS/RECOMMENDATIONS

6.1. Char Gasification Mechanism

Identification

Char gasification rate behavior and properties of annealed Saran and coal char during gasification in steam were studied in order to identify the mode(s) of hydrogen inhibition at various stages of char conversion. Langmuir-Hinshellwood type linearized rate expressions based on the three principal modes of hydrogen inhibition were regressed

with rate data collected at 1123 K and varying reactant gas compositions and pressures. None of the three principal modes of hydrogen inhibition give rate expressions that fit the data from 0-1% conversion, where transient rate and adsorbed hydrogen behavior is observed. Beyond this range gasification rate and char properties are nearly constant. The expressions derived for reverse oxygen exchange and "associative" hydrogen adsorption, which are identical in form, fit the data much better than the expressions derived for dissociative hydrogen adsorption.

Further comparison of the linearized rate expressions for reverse oxygen exchange and "associative" hydrogen adsorption shows that the equilibrium constant for reverse oxygen exchange indicates low fractional coverage of intermediate surface oxides, while the equilibrium constant for "associative" hydrogen adsorption indicates high fractional coverage of "associatively" bound hydrogen. Transient desorption and temperature programmed desorption of chars following gasification show low concentrations of surface oxides and no "associatively" bound hydrogen, therefore reverse oxygen exchange is the active mechanism by which hydrogen inhibits char gasification in steam above 1% conversion.

Temperature programmed desorption has been used to identify the major mode by which hydrogen inhibits gasification in steam over the initial transient range of char conversion. Dissociatively bound hydrogen covers the annealed char surface very rapidly at the onset of gasification, going from nearly zero to nearly saturated over the first 1% conversion. This adsorption behavior was found to be independent of hydrogen partial pressure. Gasification rate decreases significantly over the first 1% conversion, and is more pronounced under higher hydrogen partial pressures. It is concluded that dissociative hydrogen adsorption is the dominant mode of hydrogen inhibition over the initial stage of char conversion, however changes in char morphology also play an important role.

6.2. Char Structure During Gasification

Char structure significantly affects rate behavior because most chars, including those used in this investigation, have a significant micropore network as well as several different carbon atom configurations. These properties can change in relative importance with conversion because of the constant removal of surface carbon atoms throughout the course of gasification. Initial "dangling" and "glassy" carbon is the result of charring, and contributes to initial high gasification rate. On the more ordered graphitic features, gasification

rate is affected by the ratio of edge to basal plane carbon atoms, as well as the ratio of zig-zag to armchair edge configured carbon atoms.

The largest features that display ordered structure in annealed Saran char were found by TSA, H/C atom ratio, and X-ray scattering to be graphitic crystallites about 3.5 nm wide and three to five basal plane layers thick. These crystallites are quite small and filled with defects, which are more prone to become active sites than crystallite lattice carbon atoms. A gradual increase in the ratio of reactive edge carbon atoms to inert basal plane carbon atoms can explain the very gradual increase in gasification rate and adsorbed hydrogen concentration past 50% conversion. A more abrupt increase in the ratio of inert zig-zag edge carbon atoms to the more reactive armchair edge carbon atoms can contribute to the initial rapid decline in gasification rate over the first 1% char conversion.

Edge carbon atoms have the potential to become active sites, but the vast majority of these are strongly bound to hydrogen during gasification in steam. Experiments on etch pit conformation performed by Yang and Duan [43] and Yang and Yang [6] identify the shape and orientation of etch pits on the basal planes of graphite samples to be round in the case of gasification with non-hydrogen containing reactant gases, and hexagonal with zig-zag edges in the case of gasification with

hydrogen containing reactant gases. They conclude that hydrogen chemisorption is preferred on the zig-zag edges and therefore responsible for the anisotropy of reactivity toward the two principal edge configurations.

The presence of hydrogen limits behavior of active sites to mechanisms which preserve the zig-zag edge configuration and consume the armchair edge configuration. The most reasonable explanation for this is that under the presence of hydrogen, most gasification takes place via active site propagation along zig-zag edges. Zig-zag edges alone are produced in the presence of hydrogen because there is a much more ordered sequence of desorption of edge carbon atoms. If active sites were generated on the zig-zag edges, the edges would become pitted and rounded out. Most active sites are generated on armchair edge, amorphous, and dangling carbon atoms, which is why these features are consumed rapidly with conversion. A much smaller number of active sites are generated at defects in the zig-zag edges such as armchair-like arrangements, crystallite corners, crystallite defects, and unstable functional groups. These active sites propagate down the zig-zag edges and remove the outer row of carbons, preserving the edge intact.

It is very unlikely that the char gasification mechanism identified as universal by Chen, Yang, Kapteijn, and Moulijn [55] and

Kapteijn, and Moulijn [56] plays a role in char gasification when gaseous hydrogen is present. The effects of reverse oxygen exchange, identified in this investigation as the major mode of hydrogen inhibition in steady-state steam gasification, should be even greater for the "off-plane" oxygen atoms because they only form single bonds to the adjacent carbon atoms. Also, the universal gasification mechanism (see Figure 3) is shown with all edge carbon atoms saturated with oxygen, but in steam gasification nearly all edge carbon atoms are saturated with hydrogen.

6.3. Recommendations

Recommendations for further research in this investigation of the mode(s) of hydrogen inhibition in char gasification by steam include transient desorption of oxygen functional groups and molecular modeling of the proposed active site behavior in this investigation. Transient desorption of oxygen functional groups following gasification in steam gives the concentration of metastable groups which are most active in char gasification. The concentration of these metastable groups should be directly proportional to char reactivity. Relating the concentration of these groups and char reactivity to hydrogen partial pressure and adsorbed hydrogen concentration should lend a great deal of insight into the mode(s) of hydrogen inhibition.

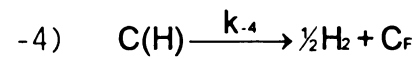
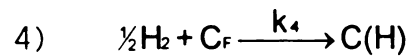
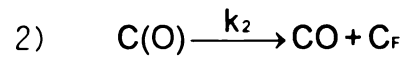
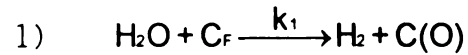
Molecular modeling of active site propagation in steam gasification of chars is much more important than molecular modeling of active site formation. The majority of carbon atoms should desorb via active site propagation, as concluded in this investigation. Reaction schemes proposed by most other workers [21,45,55,56,91] are based on the removal of a carbon atom from a straight, defect-free zig-zag edge. This is a form of active site formation, which should also be able to take place readily on amorphous surface carbon atoms, defect sites, and carbon atoms that are adjacent to functional groups. A few other workers have proposed reaction schemes which include active site propagation [8,52], but dissociatively adsorbed hydrogen on the zig-zag edges has been neglected.

APPENDICES

Appendix A:

Linearized Rate Expressions with Explicit Adsorbed Hydrogen Concentration

Appendix A-1: Dissociative Hydrogen Adsorption Linearized Rate Expression with Explicit Adsorbed Hydrogen Concentration



$$\text{Site Balance: } [\text{C}_T] = [\text{C}_F] + [\text{C}(\text{O})] + [\text{C}(\text{H})]$$

$$\text{Pseudo Steady State: } r_{\text{C}(\text{O})} = 0$$

Derivation of Rate Expression:

$$r_{\text{CO}} = k_2[\text{C}(\text{O})]$$

$$r_{\text{C}(\text{O})} = 0 = k_1[\text{H}_2\text{O}][\text{C}_F] - k_2[\text{C}(\text{O})]$$

$$r_{\text{CO}} = k_1[\text{H}_2\text{O}][\text{C}_F]$$

$$r_{\text{CO}} = k_1[\text{H}_2\text{O}][\text{C}_T - \text{C}(\text{O}) - \text{C}(\text{H})]$$

$$r_{\text{CO}} = k_1[\text{H}_2\text{O}][\text{C}_T - (r_{\text{CO}}/k_2) - \text{C}(\text{H})]$$

$$r_{\text{CO}}\{1 + (k_1/k_2)[\text{H}_2\text{O}]\} = k_1[\text{C}_T - \text{C}(\text{H})][\text{H}_2\text{O}]$$

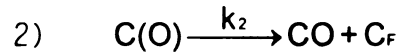
$$[\text{C}_T - \text{C}(\text{H})]/r_{\text{CO}} = \{1 + (k_1/k_2)[\text{H}_2\text{O}]\}/k_1[\text{H}_2\text{O}]$$

$$[\text{C}_T - \text{C}(\text{H})]_i - [\text{C}_T - \text{C}(\text{H})]/r_{\text{CO},i} - r_{\text{CO}} = \{1 + (k_1/k_2)[\text{H}_2\text{O}]\}/k_1[\text{H}_2\text{O}]$$

$$\boxed{\frac{\text{C}(\text{H}) - \text{C}(\text{H})_i}{r_{\text{CO},i} - r_{\text{CO}}} = \left(\frac{1}{k_1}\right) \frac{1}{P_w} + \frac{1}{k_2}}$$



**Appendix A-2: Dissociative Hydrogen Adsorption and Rapid
Reverse Oxygen Exchange Linearized Rate
Expression with Explicit Adsorbed Hydrogen
Concentration**



Site Balance: $[\text{C}_T] = [\text{C}_F] + [\text{C}(\text{O})] + [\text{C}(\text{H})]$

Rapid Equilibrium: $K_1 = k_1/k_{-1} = [\text{H}_2][\text{C}(\text{O})]/[\text{H}_2\text{O}][\text{C}_F]$

Derivation of Rate Expression:

$$r_{\text{CO}} = k_2[\text{C}(\text{O})]$$

$$[\text{C}(\text{O})] = k_1[\text{H}_2\text{O}][\text{C}_F]/k_{-1}[\text{H}_2]$$

$$r_{\text{CO}} = k_2k_1[\text{H}_2\text{O}][\text{C}_F]/k_{-1}[\text{H}_2] = k_2k_1[\text{H}_2\text{O}][\text{C}_T - \text{C}(\text{O}) - \text{C}(\text{H})]/k_{-1}[\text{H}_2]$$

$$r_{\text{CO}} = k_2k_1[\text{H}_2\text{O}][\text{C}_T - (r_{\text{CO}}/k_2) - \text{C}(\text{H})]/k_{-1}[\text{H}_2]$$

$$r_{\text{CO}} + r_{\text{CO}}\left\{k_1[\text{H}_2\text{O}]/k_{-1}[\text{H}_2]\right\} = k_2k_1[\text{H}_2\text{O}][\text{C}_T - \text{C}(\text{H})]/k_{-1}[\text{H}_2]$$

$$r_{\text{CO}}\left\{1 + k_1[\text{H}_2\text{O}]/k_{-1}[\text{H}_2]\right\} = k_2k_1[\text{H}_2\text{O}][\text{C}_T - \text{C}(\text{H})]/k_{-1}[\text{H}_2]$$

$$[\text{C}_T - \text{C}(\text{H})]/r_{\text{CO}} = \left\{1 + k_1[\text{H}_2\text{O}]/k_{-1}[\text{H}_2]\right\}k_{-1}[\text{H}_2]/k_2k_1[\text{H}_2\text{O}]$$

$$[\text{C}_T - \text{C}(\text{H})]_i - [\text{C}_T - \text{C}(\text{H})]/r_{\text{CO},i} - r_{\text{CO}} = (k_{-1}/k_2k_1)[\text{H}_2]/[\text{H}_2\text{O}] + 1/k_2$$

$$\boxed{\frac{\text{C}(\text{H}) - \text{C}(\text{H})_i}{r_{\text{CO},j} - r_{\text{CO}}} = \left(\frac{k_{-1}}{k_1k_2}\right) \frac{P_{\text{H}_2}}{P_{\text{W}}} + \frac{1}{k_2}}$$

Appendix B: Mass Spectrometer Controller Settings

RS-232	COMPUTER	.	
BAUD RATE	9600	ELEC CUR	1.000E-03
STOP BITS	7	EL ENERGY	-30.0
DATA BITS	1	FOCUS	-20.0
PARITY	NONE	ELEC MULT	OFF
PROTOCOL	XON / XOFF	FIL RES	0.73
ECHO	OFF	FIL VOLTS	2.2
DELTA_D	0.50	FIL CUR	3.1
HOURS	1	FIL	ON
MINUTES	44	TOT SENS	20.0
DAY	3	FREQUENCY	2.803E+06
MONTH	7	RF TUNE	6.984
YEAR	94	EMISSION	1.0E-03
FIL PROT	1.0E-03	AMP CAL	5.0E+03
MULT VOLT	-800	CAL MASS 1	1
DIST MODE	TAB	LO RES	3945
CHANNEL	12	LO POS	1.00
TAB MASS	84	LO SENS	6.00
TAB DWELL	120 msec	CAL MASS 2	100
NO. SCANS	0	HI RES	1000
TAB HI	1.0E+00	HI POS	-0.10
TAB LO	1.0E-15	HI SENS	7.00
TAB CALIB	1.0E+00	QUAD HEAD	1
AUTO ZERO	ON	TOT PRES	7.4E-06

Appendix C: Basic Programs for Deconvolution and Rate Calculation from Mass Spectrometer Data

Program 1: Determination of Background Levels of Various Masses for Calibration

Filename = back.bas

```
10 DIM B(17,5),BA(17),F(30)
15 READ XXX,RAW$
20 OPEN "I",#1,RAW$
30 FOR N=1 TO XXX
40 INPUT#1,F(N)
50 NEXT N
60 FOR N=1 TO F(1)
70 INPUT#1,B(1,N),B(2,N),B(3,N),B(4,N),B(5,N),B(6,N),B(7,N),
B(8,N),B(9,N),B(10,N),B(11,N),B(12,N),B(13,N),B(14,N),
B(15,N),B(16,N),B(17,N)
80 NEXT N
85 PRINT B(1,4) : IF B(1,4)=1234 THEN GOTO 90
86 LIST 200
90 CLOSE
100 FOR T=1 TO 17
110 BA(T)=(B(T,1)+B(T,2)+B(T,3)+B(T,4)+B(T,5))/5 :REM average
120 NEXT T
140 OPEN "O",#1,"BACKAVEG.dat"
145 FOR T=1 TO 17
150 PRINT#1 ,BA(T)
154 PRINT BA(T)
155 NEXT
160 CLOSE
200 DATA 25 ,"0006-1.tab"
```

Program 2: Hydrogen Calibration and Response Calculation

Filename = cal_h.bas

```

10 DIM H(17,5),HA#(17),BA#(17),P#(17),F(30)
15 READ XXX,RAW$,HPER
20 OPEN "I",#1,RAW$
30 FOR N=1 TO XXX
40 INPUT#1,F(N)
50 NEXT N
60 FOR N=1 TO F(1)
70 INPUT#1,H(1,N),H(2,N),H(3,N),H(4,N),H(5,N),H(6,N),H(7,N),
H(8,N),H(9,N),H(10,N),H(11,N),H(12,N),H(13,N),H(14,N),
H(15,N),H(16,N),H(17,N)
80 NEXT N :CLOSE
95 PRINT H(1,4) :IF H(1,4)=1234 GOTO 100
97 LIST 300
100 OPEN "I",#1,"BACKAVEG.DAT"
110 FOR T=1 TO 17
120 INPUT#1,BA#(T)
125 NEXT :CLOSE
140 FOR T=6 TO 17
150 HA#(T)=(H(T,1)+H(T,2)+H(T,3)+H(T,4)+H(T,5))/5 :REM average
160 P#(T)=HA#(T)-BA#(T) :REM subtract background
170 NEXT T
180 REM deconvolution
210 HS#=HPER/(P#(6)-.034*P#(8)) :REM get the response
230 OPEN "O",#1,"H_RESPON.DAT"
240 PRINT#1 ,HS# :CLOSE
260 PRINT HS#
300 DATA 25,"7011a.TAB" ,0.0126

```

Program 3: CO, CO₂, CH₄ Calibration and Response Calculation

Filename = cal_c_m.bas

```

10 DIM C(17,5),CA#(17),BA#(17),S#(17)
15 READ XXX,RAW$
16 PRINT RAW$
20 OPEN "I",#1,RAW$
30 FOR N=1 TO XXX
40 INPUT#1,F      :PRINT F:NEXT
60 FOR N=1 TO 5
70 INPUT#1,C(1,N),C(2,N),C(3,N),C(4,N),C(5,N),C(6,N),C(7,N)
  .C(8,N),C(9,N),C(10,N),C(11,N),C(12,N),C(13,N),C(14,N),
  C(15,N),C(16,N),C(17,N)
80 NEXT N :CLOSE
90 PRINT C(1,4)  :IF C(1,4)=1234 GOTO 100
95 LIST 300
100 OPEN "I",#1,"BACKAVEG.DAT"
110 FOR T=1 TO 17
120 INPUT#1,BA#(T)
130 NEXT      :CLOSE
140 FOR T=6 TO 17
150 CA#(T)=(C(T,1)+C(T,2)+C(T,3)+C(T,4)+C(T,5))/5  :REM average
160 S#(T)=CA#(T)-BA#(T)      :REM subtract background
170 NEXT T      :REM deconvolution and get the response:
180 RCO#=.02/(S#(14)-.105*S#(16))  :REM get the response CO
190 RCO2#=.0203/S#(16)      :REM get the response CO2
200 RCH4#=.02/S#(9)      :REM get the response CH4
210 OPEN "O",#1,"C_respon.dat"
220 PRINT#1 ,RCO#,RCO2#,RCH4#
230 CLOSE
235 PRINT " CO                CO2                CH4"
240 PRINT   RCO#,RCO2#,RCH4#
300 DATA 25,"7020_d.tab"

```

Program 4: Organization of Mass Spectrometer Output Data into Matrix Format

Filename = backt.bas

```

10 DIM V(17,200),S#(17,200),TIME(200),F(30),CO(200),CO2(200)
   ,CH4(200),H2(100)
20 READ XXX,RAWDAT$,SAVEDAT$ ,K
30 OPEN "I",#1,RAWDAT$
40 IF EOF(1) THEN END
50 FOR N=1 TO XXX
60 INPUT#1,F(N)
70 PRINT F(N)
80 NEXT N
85 REM K=F(1)
90 FOR N=1 TO K
100 INPUT#1,V(1,N),V(2,N),V(3,N),V(4,N),V(5,N),V(6,N),V(7,N)
   ,V(8,N),V(9,N),V(10,N),V(11,N),V(12,N),V(13,N),V(14,N),V(15,N),V(16,N),V
   (17,N)
102 PRINT N
110 NEXT N
120 CLOSE
130 PRINT V(1,3) ,"To see if this value is 1234"
145 TI=60*V(2,1)+V(3,1)+V(4,1)/60
160 FOR N=1 TO K
170 TIME(N)=V(2,N)*60+V(3,N)+V(4,N)/60
180 NEXT N
400 OPEN "O",#1,SAVEDAT$
410 PRINT#1,"Time M2 M3 M4 M15 M16 M17 M18 M20 M28 M32 M44 M84
415 PRINT "Time      M2      M3      "
420 FOR N=1 TO K
430 PRINT#1,INT(100*TIME(N))/100,V(6,N),V(7,N),V(8,N),V(9,N)
   ,V(10,N),V(11,N),V(12,N),V(13,N),V(14,N),V(15,N),V(16,N),
   V(17,N)
440 PRINT  INT(10*TIME(N))/10,V(6,N),V(7,N),N
450 NEXT
460 CLOSE
480 DATA 25,"0003-1.tab",0003-1r.DAT" ,93

```

Program 5: Deconvolution and Calculation of Evolution Rates of Various Species

Filename = main-dem.bas

```
10 DIM V(13,300),S#(13,300),TIME(300),A0(13),CO(300),
CO2(300),CH4(300),H2(300)
20 READ RAWDAT$,SAVEDAT$,GASFL,SAMW,RH2
30 OPEN "I",#1,RAWDAT$
40 IF EOF(1) THEN END
50 INPUT#1,A,B
60 FOR L=1 TO B
70 INPUT#1,Q$
80 PRINT Q$
90 NEXT L
100 A=A-1
110 PRINT A,B
120 FOR N=1 TO A
130 FOR J=1 TO B
140 INPUT#1,V(J,N)
150 NEXT J
160 PRINT N,V(1,N),V(2,N)
170 NEXT N
180 REM *****
190 FOR J=1 TO B
200 A0(J)=V(J,1)
210 FOR N=1 TO A
220 IF V(J,N) < A0(J) THEN A0(J)=V(J,N)
230 REM PRINT A0(J),J
240 NEXT N
250 NEXT J
260 REM *****
270 CLOSE
280 FOR J=1 TO B
290 FOR N=1 TO A
300 V(J,N)=V(J,N)-A0(J)
310 NEXT N
320 NEXT J
325 PRINT "below is the found background"
330 FOR T=2 TO B
340 PRINT A0(T)
```

```
350 NEXT
360 INPUT "The backgroud is OK?",K$
370 REM *****
380 OPEN "I",#1,"C_RESPON.DAT"
390 INPUT#1,RCO,RCO2,RCH4
400 CLOSE
410 X=GASFL/SAMW
420 FOR N=1 TO A
430 H2(N)=(V(2,N)-.034*V(3,N))*RH2*X
440 CO(N)=(V(10,N)-.105*V(12,N))*RCO*X
450 CO2(N)=V(12,N)*RCO2*X
460 CH4(N)=V(5,N)*RCH4*X
470 NEXT
480 OPEN "O",#1,SAVEDAT$
490 PRINT#1,"Time(min) H2 CH4 CO CO2/ml/min"
500 FOR N=1 TO A
510 PRINT#1 ,V(1,N),H2(N),CH4(N),CO(N),CO2(N)
520 PRINT V(1,N),CO2(N),N
530 NEXT
540 CLOSE
550 DATA "7020raw.dat",7020dec.DAT",300,0.3735,300000
```

Program 6: Calculation of Evolution Rates Based on Carbon Conversion

Filename = main-ins.bas

```

10 DIM TIME(200),CO(200),CO2(200),CH4(200),H2(200),
X(200),Y(200)
20 DIM COX(200),CO2X(200),CH4X(200),W(200),SUM1(200),
SUM2(200),SUM3(200)
30 DIM WSUM(200),INSCO(200),INSCH4(200),INSCO2(200)
40 READ RAWDAT$,SAVEDAT$,GASFL,W0
50 OPEN "I",#1,RAWDAT$
60 REM IF EOF(1) THEN END
70 INPUT#1 ,A,B
80 INPUT#1 ,Q1$,Q2$,Q3$,Q4$,Q5$
81 PRINT Q1$,Q2$,Q3$,Q4$,Q5$
82 A=A-1
90 FOR N=1 TO A
100 INPUT#1 ,TIME(N),H2(N),CH4(N),CO(N),CO2(N)
110 PRINT TIME(N),CO(N),N
120 NEXT N :CLOSE
125 PRINT
"-----"
130 INPUT "The Data Read[time(min) and CH4 CO CO2 cc/min.g(initial)] is
OK";T$
140 FOR N=1 TO A
150 COX(N)=CO(N)*W0 :CO2X(N)=CO2(N)*W0 :CH4X(N)=CH4(N)*W0
160 NEXT
165 SUM1(1)=0:SUM2(1)=0:SUM3(1)=0
170 FOR J=2 TO A
200 SUM1(J)=SUM1(J-1)+((CH4X(J)+CH4X(J-1))/2)*(TIME(J)-TIME(J-1))
210 SUM2(J)=SUM2(J-1)+((COX(J)+COX(J-1))/2)*(TIME(J)-TIME(J-1))
220 SUM3(J)=SUM3(J-1)+((CO2X(J)+CO2X(J-1))/2)*(TIME(J)-TIME(J-1))
230 WSUM(J)=(SUM1(J)+SUM2(J)+SUM3(J))/(22.41*1000)*12.011
240 REM wsum(J) is total Carbon loss (gram)
250 PRINT USING "###.###" :SUM1(J),SUM2(J),SUM3(J),W0-WSUM(J),J
260 NEXT J
263 PRINT "CH4 (ML) CO (ML) CO2 (ML) left sample Data Point "
265 PRINT "-----"
267 PRINT 100*SUM1(A)/(SUM1(A)+SUM2(A)+SUM3(A)), " CH4 Carbon lose
percent%"

```

```
268 PRINT 100*SUM2(A)/(SUM1(A)+SUM2(A)+SUM3(A)), " CO Carbon lose
percent%"
269 PRINT 100*SUM3(A)/(SUM1(A)+SUM2(A)+SUM3(A)), " CO2 Carbon lose
percent%"
270 INPUT "The Gas volume(ML) of CH4 CO CO2 is correct ?".T$
280 FOR N=1 TO A
291 W(N)=W0-WSUM(N)
310 INSCO(N)=COX(N)/W(N)
320 INSCO2(N)=CO2X(N)/W(N)
330 INSCH4(N)=CH4X(N)/W(N)
340 NEXT N
350 OPEN "0",#1,SAVEDAT$
360 PRINT#1,"Time(min) CH4(cc/min) CO(cc/min) CO2(cc/min) conversion(%)"
370 FOR N=1 TO A
380 PRINT#1 .TIME(N),INSCH4(N),INSCO(N),INSCO2(N),100*WSUM(N)/W0
390 X(N)=INT(10000*(W0-W(N)))/10000: Y(N)=INT(1000000!*(W0-
W(N))/W0)/10000
400 PRINT "W_Loss":X(N):"g ";Y(N):"%";TAB(35);N;"TH DATA POINT"
410 NEXT
420 CLOSE :P1=INT(10000*WSUM(A))/10000 :P2=INT(10000*(W0-WA))/10000
440 PRINT "Among the lose,CH4% CO% CO2%"
441 Z1=SUM1(A)/(SUM1(A)+SUM2(A)+SUM3(A))
442 Z2=SUM2(A)/(SUM1(A)+SUM2(A)+SUM3(A))
443 Z3=SUM3(A)/(SUM1(A)+SUM2(A)+SUM3(A))
445 PRINT Z1*Y(A),Z2*Y(A),Z3*Y(A)
450 PRINT "Calculated W-Loss is:":P1;"g ";100*WSUM(A)/W0:"% of sample
weight"
510 DATA "7020de.dat","7020-ins.DAT",180 ,0.3735
```


Appendix D: Annealed Saran Char Bulk Modulus

$$\Phi_G = L\sqrt{r_C/CD_e} \quad (\text{eq.4.74, Lee})$$

$$\Phi_G = (4.17 \times 10^{-3}) \sqrt{\frac{2.40 \times 10^{-6}}{(1.33 \times 10^{-4})(0.00607)}} = 0.00719$$

$$L = D_P/6 \quad (\text{Table 4.1, Lee})$$

$$L = (250 \mu\text{m}/6)(\text{cm}/10^4 \mu\text{m}) = 4.17 \times 10^{-3} \text{ cm}$$

$$r_C = \left(\frac{0.9 \text{gCconv.}}{100 \text{gC} \cdot \text{min}} \right) \left(\frac{\text{molC}}{12.01 \text{gC}} \right) \left\{ \frac{(0.3 \text{gC})(1000 \text{mm}^3/\text{cm}^3)}{\pi[(4 \text{mm})^2(31 \text{mm})]} \right\} \left(\frac{\text{min}}{60 \text{sec}} \right)$$

$$r_C = 2.40 \times 10^{-6} \text{ mol}/\text{cm}^3 \cdot \text{sec}$$

$$C = (0.4)(3.1 \text{MPa}) \left(\frac{\text{mol} \cdot \text{K}}{8.314 \text{cm}^3 \cdot \text{MPa}} \right) / 1123 \text{K} = 1.33 \times 10^{-4} \text{ mol}/\text{cm}^3$$

$$\frac{1}{D_e} = \frac{1 + (m^{1/2} - 1)x}{D_{e,12}} + \frac{1}{D_{e,k}} \quad (\text{eq.14.2, Lee})$$

$$\frac{1}{D_e} = \frac{1 + ((18/40)^{1/2} - 1)(0.4)}{2220} + \frac{1}{0.00607} = \frac{1}{0.00607} \text{ s}/\text{cm}^2$$

$$D_{e,12} = D_{m,12} f_e(\epsilon/k) \quad (\text{eq.14.3, Lee})$$

$$D_{e,12} = (2804)(0.792) = 2220 \text{ cm}^2/\text{s}$$

$$D_{e,k} = D_k f_e(\epsilon/k) \quad (\text{eq.14.4, Lee})$$

$$D_{e,k} = (0.00766)(0.792) = 0.00607 \text{ cm}^2/\text{s}$$

$$D_{m,12} = 0.0018583 \left\{ \left[T^3 \left(\frac{1}{M_1} + \frac{1}{M_2} \right) \right]^{1/2} / \left[P \sigma_{12}^2 \Omega_{12} \right] \right\} \quad (\text{eq.14.5, Lee})$$

$$D_{m,12} = 0.0018583 \left\{ \frac{\left[1123^3 \left(\frac{1}{18} + \frac{1}{40} \right) \right]^{1/2}}{\left[(316)(3.36)^2 (0.745) \right]} \right\} = 2804 \text{ cm}^2/\text{s}$$

$$\sigma_{12} = (\sigma_1 + \sigma_2)/2 \quad (\text{p.484, Lee})$$

$$\sigma_{12} = (3.30 + 3.418)/2 = 3.36 \text{ \AA}$$

$$\Omega_{12} = f(\epsilon_{12}) \quad (\text{Table 14.2, Lee})$$

$$\Omega_{12} = 0.745$$

$$\epsilon_{12} = \sqrt{\epsilon_1 \epsilon_2} \quad (\text{p.484, Lee})$$

$$\epsilon_{12} = \sqrt{(124\text{k})(110\text{k})} = 117\text{k}$$

$$f_e(\epsilon/k) = \epsilon^2 \quad (\text{eq.14.12, Lee})$$

$$f_e(\epsilon/k) = 0.89^2 = 0.792$$

$$D_k = 9.7 \times 10^3 r \sqrt{T/M} \quad (\text{eq.14.7, Lee})$$

$$D_k = 9.7 \times 10^3 (1 \times 10^{-7}) \sqrt{1123/18} = 0.00766 \text{ cm}^2/\text{s}$$

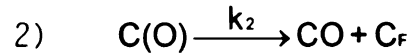
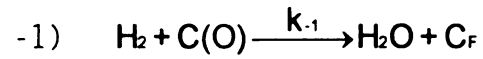
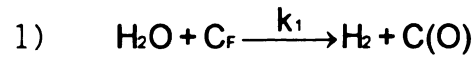
Appendix D Nomenclature:

- Φ_G = generalized Thiele modulus for first order reaction (unitless)
 L = characteristic length of particles (cm)
 r_c = intrinsic reaction rate (mol/m³*sec)
 C = concentration of key species (mol/cm³)
 D_e = effective binary diffusivity of H₂O in Ar (cm²/s)
 D_p = diameter of particle (cm)
 $D_{e,12}$ = effective molecular diffusivity of H₂O in Ar (cm²/s)
 $D_{e,k}$ = Knudsen diffusivity of H₂O (cm²/s)
 m = ratio of molecular weights of H₂O to Ar (unitless)
 x = mole fraction of H₂O (unitless)
 f_e = correction factor for porous medium (unitless)
 ϵ = porosity of medium (unitless)
 k = tortuosity of medium (unitless)
 T = temperature (K)
 M = molecular weight (g/mol)
 P = pressure (atm)
 σ = Lennard-Jones parameter (Å)
 Ω = Lennard-Jones parameter (unitless)
 ϵ_{12} = Lennard-Jones parameter (unitless)
 r = average pore radius (cm)

Appendix E:

Linearized Rate Expression Derivations for Various Rate Expressions

Appendix E-1: Linearized Rate Expression Derivation for Reverse Oxygen Exchange



Site Balance: $[\text{C}_T] = [\text{C}_F] + [\text{C}(\text{O})]$

Pseudo Steady State: $r_{\text{C}(\text{O})} = 0$

Derivation of Rate Expression:

$$r_{\text{C}(\text{O})} = 0 = k_1[\text{H}_2\text{O}][\text{C}_F] - k_{-1}[\text{H}_2][\text{C}(\text{O})] - k_2[\text{C}(\text{O})]$$

$$0 = k_1[\text{H}_2\text{O}]\{[\text{C}_T] - [\text{C}(\text{O})]\} - k_{-1}[\text{H}_2][\text{C}(\text{O})] - k_2[\text{C}(\text{O})]$$

$$k_1[\text{H}_2\text{O}][\text{C}_T] = [\text{C}(\text{O})]\{k_1[\text{H}_2\text{O}] + k_{-1}[\text{H}_2] + k_2\}$$

$$[\text{C}(\text{O})] = k_1[\text{H}_2\text{O}][\text{C}_T] / \{k_1[\text{H}_2\text{O}] + k_{-1}[\text{H}_2] + k_2\}$$

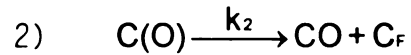
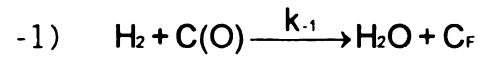
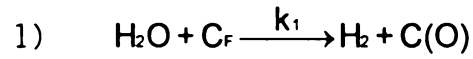
$$r_{\text{CO}} = k_2[\text{C}(\text{O})]$$

$$r_{\text{CO}} = k_2 k_1 [\text{H}_2\text{O}][\text{C}_T] / \{k_2 + k_1[\text{H}_2\text{O}] + k_{-1}[\text{H}_2]\}$$

$$r_{\text{CO}} = \frac{k_1 \text{C}_T \text{P}_W}{1 + (k_1/k_2)\text{P}_W + (k_{-1}/k_2)\text{P}_{\text{H}_2}}$$

$$\frac{1}{r_{\text{CO}}} = \left[\frac{1}{k_2 \text{C}_T} \right] + \left[\frac{1}{k_1 \text{C}_T} \right] \left(\frac{1}{\text{P}_W} \right) + \left[\frac{1}{k_1 \text{C}_T} \right] \left[\frac{k_{-1}}{k_2} \right] \left(\frac{\text{P}_{\text{H}_2}}{\text{P}_W} \right)$$

Appendix E-2: Linearized Rate Expression Derivation for Rapid Equilibrium Reverse Oxygen Exchange



Site Balance: $[\text{C}_T] = [\text{C}_F] + [\text{C}(\text{O})]$

Rapid Equilibrium: $K_1 = k_1/k_{-1} = [\text{H}_2][\text{C}(\text{O})]/[\text{H}_2\text{O}][\text{C}_F]$

Derivation of Rate Expression:

$$[\text{C}_F] = k_{-1}[\text{H}_2][\text{C}(\text{O})]/k_1[\text{H}_2\text{O}]$$

$$[\text{C}_T] = \left\{ (k_{-1}/k_1)[\text{H}_2][\text{C}(\text{O})]/[\text{H}_2\text{O}] \right\} + [\text{C}(\text{O})]$$

$$[\text{C}(\text{O})] = [\text{C}_T] / \left\{ 1 + (k_{-1}/k_1)[\text{H}_2]/[\text{H}_2\text{O}] \right\}$$

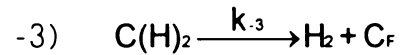
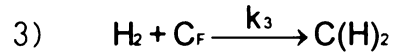
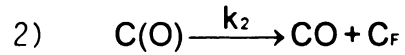
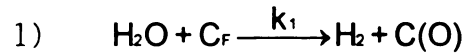
$$r_{\text{CO}} = k_2[\text{C}(\text{O})]$$

$$r_{\text{CO}} = k_2[\text{C}_T] / \left\{ 1 + (k_{-1}/k_1)[\text{H}_2]/[\text{H}_2\text{O}] \right\}$$

$$r_{\text{CO}} = \frac{k_1 \text{C}_T P_W}{(k_1/k_2)P_W + (k_{-1}/k_2)P_{\text{H}_2}}$$

$$\frac{1}{r_{\text{CO}}} = \left[\frac{1}{k_2 \text{C}_T} \right] + \left[\frac{1}{k_1 \text{C}_T} \right] \left[\frac{k_{-1}}{k_2} \right] \left(\frac{P_{\text{H}_2}}{P_W} \right)$$

Appendix E-3: Linearized Rate Expression Derivation for "Associative" Hydrogen Adsorption



$$\text{Site Balance: } [\text{C}_T] = [\text{C}_F] + [\text{C}(\text{O})] + [\text{C}(\text{H})_2]$$

$$\text{Pseudo Steady State: } r_{\text{C}(\text{O})} = 0, \quad r_{\text{C}(\text{H})_2} = 0$$

Derivation of Rate Expression:

$$r_{\text{C}(\text{H})_2} = 0 = k_3[\text{H}_2][\text{C}_F] - k_{-3}[\text{C}(\text{H})_2]$$

$$[\text{C}(\text{H})_2] = (k_3/k_{-3})[\text{H}_2][\text{C}_F]$$

$$r_{\text{C}(\text{O})} = 0 = k_1[\text{H}_2\text{O}][\text{C}_F] - k_2[\text{C}(\text{O})]$$

$$k_2[\text{C}(\text{O})] = k_1[\text{H}_2\text{O}][\text{C}_F]$$

$$[\text{C}_F] = (k_2/k_1)[\text{C}(\text{O})]/[\text{H}_2\text{O}]$$

$$[\text{C}(\text{H})_2] = (k_3/k_{-3})(k_2/k_1)[\text{H}_2][\text{C}(\text{O})]/[\text{H}_2\text{O}]$$

$$k_2[\text{C}(\text{O})] = k_1[\text{H}_2\text{O}][\text{C}_F]$$

$$k_2[\text{C}(\text{O})] = k_1[\text{H}_2\text{O}] \{ [\text{C}_T] - [\text{C}(\text{O})] - [\text{C}(\text{H})_2] \}$$

$$k_2[\text{C}(\text{O})] = k_1[\text{H}_2\text{O}] \{ [\text{C}_T] - [\text{C}(\text{O})] - (k_3/k_{-3})(k_2/k_1)[\text{H}_2][\text{C}(\text{O})]/[\text{H}_2\text{O}] \}$$

$$k_2[\text{C}(\text{O})] = k_1[\text{H}_2\text{O}][\text{C}_T] - k_1[\text{H}_2\text{O}][\text{C}(\text{O})] - (k_3/k_{-3})k_2[\text{H}_2][\text{C}(\text{O})]$$

“Associative” Hydrogen Adsorption Continued...

$$k_1[\text{H}_2\text{O}][\text{C}_T] = [\text{C}(\text{O})] \{ k_2 + k_1[\text{H}_2\text{O}] + (k_3/k_{-3})k_2[\text{H}_2] \}$$

$$[\text{C}(\text{O})] = k_1[\text{H}_2\text{O}][\text{C}_T] / \{ k_2 + k_1[\text{H}_2\text{O}] + (k_3/k_{-3})k_2[\text{H}_2] \}$$

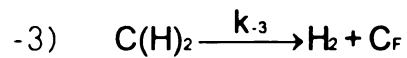
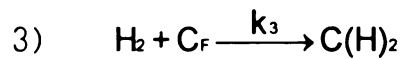
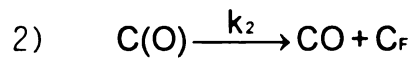
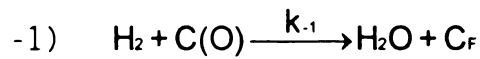
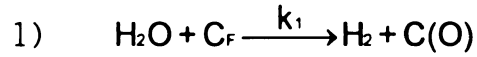
$$r_{\text{CO}} = k_2[\text{C}(\text{O})]$$

$$r_{\text{CO}} = k_2 k_1 [\text{H}_2\text{O}][\text{C}_T] / \{ k_2 + k_1[\text{H}_2\text{O}] + (k_3/k_{-3})k_2[\text{H}_2] \}$$

$$r_{\text{CO}} = \frac{k_1 \text{C}_T \text{P}_W}{1 + (k_1/k_2)\text{P}_W + (k_3/k_{-3})\text{P}_{\text{H}_2}}$$

$$\frac{1}{r_{\text{CO}}} = \left[\frac{1}{k_2 \text{C}_T} \right] + \left[\frac{1}{k_1 \text{C}_T} \right] \left(\frac{1}{\text{P}_W} \right) + \left[\frac{1}{k_1 \text{C}_T} \right] \left[\frac{k_3}{k_{-3}} \right] \left(\frac{\text{P}_{\text{H}_2}}{\text{P}_W} \right)$$

Appendix E-4: Linearized Rate Expression Derivation for Reverse Oxygen Exchange and “Associative” Hydrogen Adsorption



Site Balance: $[\text{C}_T] = [\text{C}_F] + [\text{C}(\text{O})] + [\text{C}(\text{H})_2]$

Pseudo Steady State: $r_{\text{C}(\text{O})} = 0$, $r_{\text{C}(\text{H})_2} = 0$

Derivation of Rate Expression:

$$r_{\text{C}(\text{H})_2} = 0 = k_3[\text{H}_2][\text{C}_F] - k_{-3}[\text{C}(\text{H})_2]$$

$$[\text{C}(\text{H})_2] = (k_3/k_{-3})[\text{H}_2][\text{C}_F]$$

$$r_{\text{C}(\text{O})} = 0 = k_1[\text{H}_2\text{O}][\text{C}_F] - k_{-1}[\text{H}_2][\text{C}(\text{O})] - k_2[\text{C}(\text{O})]$$

$$k_1[\text{H}_2\text{O}][\text{C}_F] = k_{-1}[\text{H}_2][\text{C}(\text{O})] + k_2[\text{C}(\text{O})]$$

$$[\text{C}_F] = [\text{C}(\text{O})] \{ k_{-1}[\text{H}_2] + k_2 \} / k_1[\text{H}_2\text{O}]$$

$$[\text{C}(\text{H})_2] = (k_3/k_{-3})[\text{H}_2][\text{C}(\text{O})] \{ k_{-1}[\text{H}_2] + k_2 \} / k_1[\text{H}_2\text{O}]$$

$$k_1[\text{H}_2\text{O}][\text{C}_F] = k_{-1}[\text{H}_2][\text{C}(\text{O})] + k_2[\text{C}(\text{O})]$$

$$k_1[\text{H}_2\text{O}] \{ [\text{C}_T] - [\text{C}(\text{O})] - [\text{C}(\text{H})_2] \} = k_{-1}[\text{H}_2][\text{C}(\text{O})] + k_2[\text{C}(\text{O})]$$

Reverse Oxygen Exchange and "Associative" Hydrogen Adsorption Continued...

$$k_1[\text{H}_2\text{O}] \left\{ [\text{C}_T] - [\text{C}(\text{O})] - (k_3/k_{-3})[\text{H}_2][\text{C}(\text{O})] \left\{ k_{-1}[\text{H}_2] + k_2 \right\} / k_1[\text{H}_2\text{O}] \right\}$$

$$= k_{-1}[\text{H}_2][\text{C}(\text{O})] + k_2[\text{C}(\text{O})]$$

$$k_1[\text{H}_2\text{O}][\text{C}_T] = [\text{C}(\text{O})] \left\{ k_1[\text{H}_2\text{O}] + (k_3/k_{-3})[\text{H}_2] \left\{ k_{-1}[\text{H}_2] + k_2 \right\} + k_{-1}[\text{H}_2] + k_2 \right\}$$

$$[\text{C}(\text{O})] = k_1[\text{H}_2\text{O}][\text{C}_T] / \left\{ k_1[\text{H}_2\text{O}] + (k_3/k_{-3})[\text{H}_2] \left\{ k_{-1}[\text{H}_2] + k_2 \right\} + k_{-1}[\text{H}_2] + k_2 \right\}$$

$$r_{\text{CO}} = k_2[\text{C}(\text{O})]$$

$$r_{\text{CO}} = k_2 k_1 [\text{H}_2\text{O}][\text{C}_T] / \left\{ k_1[\text{H}_2\text{O}] + (k_3/k_{-3})[\text{H}_2] \left\{ k_{-1}[\text{H}_2] + k_2 \right\} + k_{-1}[\text{H}_2] + k_2 \right\}$$

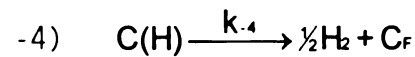
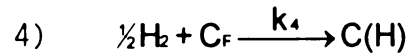
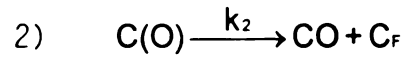
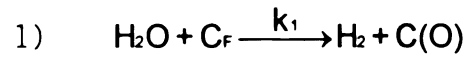
$$r_{\text{CO}} = k_2 k_1 [\text{H}_2\text{O}][\text{C}_T] / \left\{ k_1[\text{H}_2\text{O}] + (k_3/k_{-3})k_{-1}[\text{H}_2]^2 + (k_3/k_{-3})k_2[\text{H}_2] + k_{-1}[\text{H}_2] + k_2 \right\}$$

$$r_{\text{CO}} = \frac{k_1 C_T P_W}{1 + (k_1/k_2)P_W + \left\{ (k_{-1}/k_2) + (k_3/k_{-3}) \right\} P_{\text{H}_2} + \left\{ (k_{-1}/k_2)(k_3/k_{-3}) \right\} P_{\text{H}_2}^2}$$

$$\frac{1}{r_{\text{CO}}} = \left[\frac{1}{k_2 C_T} \right] + \left[\frac{1}{k_1 C_T} \right] \left(\frac{1}{P_W} \right) + \left[\frac{1}{k_1 C_T} \right] \left\{ \left[\frac{k_{-1}}{k_2} \right] + \left[\frac{k_3}{k_{-3}} \right] \right\} \left(\frac{P_{\text{H}_2}}{P_W} \right)$$

$$+ \left[\frac{1}{k_1 C_T} \right] \left[\frac{k_{-1}}{k_2} \right] \left[\frac{k_3}{k_{-3}} \right] \left(\frac{P_{\text{H}_2}^2}{P_W} \right)$$

Appendix E-5: Linearized Rate Expression Derivation for Dissociative Hydrogen Adsorption



Site Balance: $[\text{C}_T] = [\text{C}_F] + [\text{C}(\text{O})] + [\text{C}(\text{H})]$

Pseudo Steady State: $r_{\text{C}(\text{O})} = 0$, $r_{\text{C}(\text{H})} = 0$

Derivation of Rate Expression:

$$r_{\text{C}(\text{H})} = 0 = k_4[\text{H}_2]^2[\text{C}_F] - k_{-4}[\text{C}(\text{H})]$$

$$[\text{C}(\text{H})] = (k_4/k_{-4})[\text{H}_2]^2[\text{C}_F]$$

$$r_{\text{C}(\text{O})} = 0 = k_1[\text{H}_2\text{O}][\text{C}_F] - k_2[\text{C}(\text{O})]$$

$$k_2[\text{C}(\text{O})] = k_1[\text{H}_2\text{O}][\text{C}_F]$$

$$[\text{C}_F] = (k_2/k_1)[\text{C}(\text{O})]/[\text{H}_2\text{O}]$$

$$[\text{C}(\text{H})] = (k_4/k_{-4})(k_2/k_1)[\text{H}_2]^2[\text{C}(\text{O})]/[\text{H}_2\text{O}]$$

$$k_2[\text{C}(\text{O})] = k_1[\text{H}_2\text{O}][\text{C}_F]$$

$$k_2[\text{C}(\text{O})] = k_1[\text{H}_2\text{O}]\{[\text{C}_T] - [\text{C}(\text{O})] - [\text{C}(\text{H})]\}$$

$$k_2[\text{C}(\text{O})] = k_1[\text{H}_2\text{O}]\{[\text{C}_T] - [\text{C}(\text{O})] - (k_4/k_{-4})(k_2/k_1)[\text{H}_2]^2[\text{C}(\text{O})]/[\text{H}_2\text{O}]\}$$

$$k_2[\text{C}(\text{O})] = k_1[\text{H}_2\text{O}][\text{C}_T] - k_1[\text{H}_2\text{O}][\text{C}(\text{O})] - (k_4/k_{-4})k_2[\text{H}_2]^2[\text{C}(\text{O})]$$

Dissociative Hydrogen Adsorption Continued...

$$k_1[\text{H}_2\text{O}][\text{C}_T] = [\text{C}(\text{O})] \{ k_2 + k_1[\text{H}_2\text{O}] + (k_4/k_{-4})k_2[\text{H}_2]^2 \}$$

$$[\text{C}(\text{O})] = k_1[\text{H}_2\text{O}][\text{C}_T] / \{ k_2 + k_1[\text{H}_2\text{O}] + (k_4/k_{-4})k_2[\text{H}_2]^2 \}$$

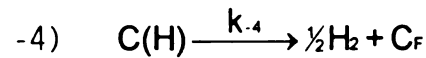
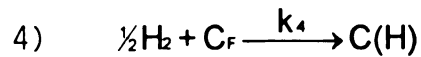
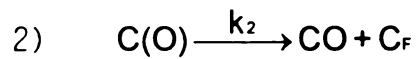
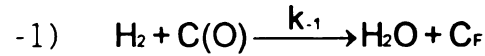
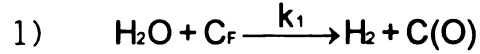
$$r_{\text{CO}} = k_2[\text{C}(\text{O})]$$

$$r_{\text{CO}} = k_2 k_1 [\text{H}_2\text{O}][\text{C}_T] / \{ k_2 + k_1[\text{H}_2\text{O}] + (k_4/k_{-4})k_2[\text{H}_2]^2 \}$$

$$r_{\text{CO}} = \frac{k_1 C_T P_W}{1 + (k_1/k_2)P_W + (k_4/k_{-4})P_{\text{H}_2}^{1/2}}$$

$$\frac{1}{r_{\text{CO}}} = \left[\frac{1}{k_2 C_T} \right] + \left[\frac{1}{k_1 C_T} \right] \left(\frac{1}{P_W} \right) + \left[\frac{1}{k_1 C_T} \right] \left[\frac{k_4}{k_{-4}} \right] \left(\frac{P_{\text{H}_2}^{1/2}}{P_W} \right)$$

**Appendix E-6: Linearized Rate Expression Derivation for
Reverse Oxygen Exchange and Dissociative
Hydrogen Adsorption**



Site Balance: $[\text{C}_T] = [\text{C}_F] + [\text{C}(\text{O})] + [\text{C}(\text{H})]$

Pseudo Steady State: $r_{\text{C}(\text{O})} = 0$, $r_{\text{C}(\text{H})} = 0$

Derivation of Rate Expression:

$$r_{\text{C}(\text{H})} = 0 = k_4[\text{H}_2]^2[\text{C}_F] - k_{-4}[\text{C}(\text{H})]$$

$$[\text{C}(\text{H})] = (k_4/k_{-4})[\text{H}_2]^2[\text{C}_F]$$

$$r_{\text{C}(\text{O})} = 0 = k_1[\text{H}_2\text{O}][\text{C}_F] - k_{-1}[\text{H}_2][\text{C}(\text{O})] - k_2[\text{C}(\text{O})]$$

$$k_1[\text{H}_2\text{O}][\text{C}_F] = k_{-1}[\text{H}_2][\text{C}(\text{O})] + k_2[\text{C}(\text{O})]$$

$$[\text{C}_F] = [\text{C}(\text{O})] \{ k_{-1}[\text{H}_2] + k_2 \} / k_1[\text{H}_2\text{O}]$$

$$[\text{C}(\text{H})] = (k_4/k_{-4})[\text{H}_2]^2[\text{C}(\text{O})] \{ k_{-1}[\text{H}_2] + k_2 \} / k_1[\text{H}_2\text{O}]$$

$$k_1[\text{H}_2\text{O}][\text{C}_F] = k_{-1}[\text{H}_2][\text{C}(\text{O})] + k_2[\text{C}(\text{O})]$$

$$k_1[\text{H}_2\text{O}] \{ [\text{C}_T] - [\text{C}(\text{O})] - [\text{C}(\text{H})] \} = k_{-1}[\text{H}_2][\text{C}(\text{O})] + k_2[\text{C}(\text{O})]$$

Reverse Oxygen Exchange and Dissociative Hydrogen Adsorption Continued...

$$k_1[\text{H}_2\text{O}] \left\{ [\text{C}_T] - [\text{C}(\text{O})] - (k_4/k_{-4})[\text{H}_2]^2[\text{C}(\text{O})] \right\} / \{ k_{-1}[\text{H}_2] + k_2 \} / k_1[\text{H}_2\text{O}]$$

$$= k_{-1}[\text{H}_2][\text{C}(\text{O})] + k_2[\text{C}(\text{O})]$$

$$k_1[\text{H}_2\text{O}][\text{C}_T] = [\text{C}(\text{O})] \left\{ k_1[\text{H}_2\text{O}] + (k_4/k_{-4})[\text{H}_2]^2 \{ k_{-1}[\text{H}_2] + k_2 \} + k_{-1}[\text{H}_2] + k_2 \right\}$$

$$[\text{C}(\text{O})] = k_1[\text{H}_2\text{O}][\text{C}_T] / \left\{ k_1[\text{H}_2\text{O}] + (k_4/k_{-4})[\text{H}_2]^2 \{ k_{-1}[\text{H}_2] + k_2 \} + k_{-1}[\text{H}_2] + k_2 \right\}$$

$$r_{\text{CO}} = k_2[\text{C}(\text{O})]$$

$$r_{\text{CO}} = k_2 k_1 [\text{H}_2\text{O}][\text{C}_T] / \left\{ k_1[\text{H}_2\text{O}] + (k_4/k_{-4})[\text{H}_2]^2 \{ k_{-1}[\text{H}_2] + k_2 \} + k_{-1}[\text{H}_2] + k_2 \right\}$$

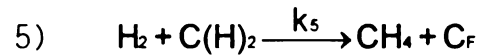
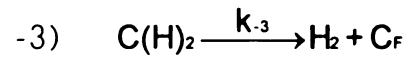
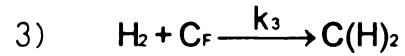
$$r_{\text{CO}} = k_2 k_1 [\text{H}_2\text{O}][\text{C}_T] / \left\{ k_1[\text{H}_2\text{O}] + (k_4/k_{-4}) k_{-1} [\text{H}_2]^{3/2} + (k_4/k_{-4}) k_2 [\text{H}_2]^2 + k_{-1}[\text{H}_2] + k_2 \right\}$$

$$r_{\text{CO}} = \frac{k_1 C_T P_W}{1 + (k_1/k_2) P_W + (k_{-1}/k_2) P_{\text{H}_2} + (k_4/k_{-4}) \{ P_{\text{H}_2}^{1/2} + (k_{-1}/k_2) P_{\text{H}_2}^{3/2} \}}$$

$$\frac{1}{r_{\text{CO}}} = \left[\frac{1}{k_2 C_T} \right] + \left[\frac{1}{k_1 C_T} \right] \left(\frac{1}{P_W} \right) + \left[\frac{1}{k_1 C_T} \right] \left[\frac{k_{-1}}{k_2} \right] \left(\frac{P_{\text{H}_2}}{P_W} \right)$$

$$+ \left[\frac{1}{k_1 C_T} \right] \left[\frac{k_4}{k_{-4}} \right] \left(\frac{P_{\text{H}_2}^{1/2}}{P_W} \right) + \left[\frac{1}{k_1 C_T} \right] \left[\frac{k_{-1}}{k_2} \right] \left[\frac{k_4}{k_{-4}} \right] \left(\frac{P_{\text{H}_2}^{3/2}}{P_W} \right)$$

Appendix E-7: Methane Formation Only "Associative" Hydrogen Adsorption



Site Balance: $[\text{C}_T] = [\text{C}_F] + [\text{C(H)}_2]$

Pseudo Steady State: $r_{\text{C}_F} = 0$, $r_{\text{C(H)}_2} = 0$

Derivation of Rate Expression:

$$r_{\text{C}_F} = 0 = k_3[\text{H}_2][\text{C}_F] - k_{-3}[\text{C(H)}_2] + k_5[\text{H}_2][\text{C(H)}_2]$$

$$k_3[\text{H}_2][\text{C}_F] = k_{-3}[\text{C(H)}_2] + k_5[\text{H}_2][\text{C(H)}_2]$$

$$k_3[\text{H}_2]\{[\text{C}_T] - [\text{C(H)}_2]\} = k_{-3}[\text{C(H)}_2] + k_5[\text{H}_2][\text{C(H)}_2]$$

$$k_3[\text{H}_2][\text{C}_T] = [\text{C(H)}_2]\{k_{-3} + k_5[\text{H}_2] + k_3[\text{H}_2]\}$$

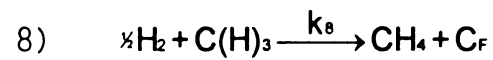
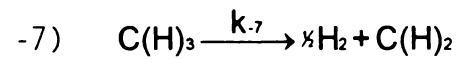
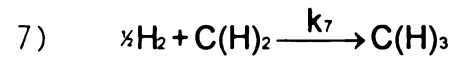
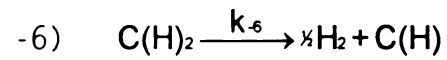
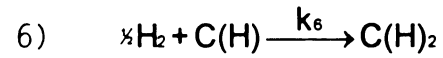
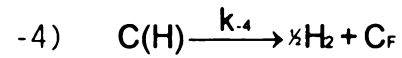
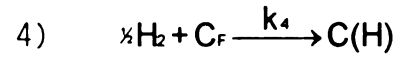
$$r_{\text{CH}_4} = k_5[\text{C(H)}_2][\text{H}_2]$$

$$r_{\text{CH}_4} = k_5[\text{H}_2]k_3[\text{H}_2][\text{C}_T] / \{k_{-3} + k_5[\text{H}_2] + k_3[\text{H}_2]\}$$

$$r_{\text{CH}_4} = k_5[\text{H}_2]^2[\text{C}_T] / \{(k_{-3}/k_3) + (1 + k_5/k_3)[\text{H}_2]\}$$

$r_{\text{CH}_4} = \frac{k_5 \text{C}_T \text{P}_{\text{H}_2}^2}{(k_{-3}/k_3) + (1 + k_5/k_3) \text{P}_{\text{H}_2}}$

Appendix E-8: Methane Formation Only Dissociative Hydrogen Adsorption



Site Balance: $[\text{C}_T] = [\text{C}_F] + [\text{C(H)}] + [\text{C(H)}_2] + [\text{C(H)}_3]$

Pseudo Steady State: $r_{\text{C}_F} = r_{\text{C(H)}} = r_{\text{C(H)}_2} = r_{\text{C(H)}_3} = 0$

$$r_{\text{CH}_4} = \frac{k_8 \text{C}_T P_{\text{H}_2}^2}{f_1(k) + f_2(k) P_{\text{H}_2}^{1/2} + f_3(k) P_{\text{H}_2} + f_4(k) P_{\text{H}_2}^{3/2}}$$

REFERENCES

1. Redmond, J.P. and Walker, P.L. Jr., *J. Phys. Chem.* **64**, 1093 (1960).
2. Bansal, R.C., Vastola, F.J., and Walker, P.L. Jr., *Carbon* **9**, 185 (1971).
3. Bansal, R.C., Vastola, F.J., and Walker, P.L. Jr., *Carbon* **12**, 355 (1974).
4. Tobias, H. and Soffer, A., *Carbon* **23**, 291 (1985).
5. Biederman, D.L. et al., *Carbon* **14**, 351 (1976).
6. Yang, R.T. and Yang, K.L., *Carbon* **23**(5), 537 (1985).
7. Matsumoto, S., Sato, Y., and Setaka, N., *Carbon* **19**, 232 (1981).
8. Huttinger, K.J. and Merdes, W.F., *Carbon* **30**(6), 883 (1992).
9. Mims, C.A. and Krajewski, J.J., *J. Catal.* **102**, 140 (1986).
10. Steinberg, M., *1987 Int. Conf. on Coal Sci.* **11**, J.A. Moulijn, ed., 953 (1987).
11. Steinberg, M., *1987 Int. Conf. on Coal Sci.* **11**, J.A. Moulijn, ed., 1064 (1987).
12. Blackwood, J.D., *Aust. J. Applied Sci.*, 199 (1962).
13. Blackwood, J.D. and McCarthy, D.J., *Aust. J. Chem.* **19**, 797 (1966).
14. Blackwood, J.D. *Aust. J. Chem.* **15**, 397 (1962).
15. Blackwood, J.D. *Aust. J. Chem.* **12**, 14 (1959).

16. Makino, M. and Toda, Y., *Fuel* **60**, 321 (1981).
17. Blackwood, J.D., McCarthy, D.J., and Cullis, B.D., *Aust. J. Chem.* **20**, 2525 (1967).
18. Blackwood, J.D., Cullis, B.D., and McCarthy, D.J., *Aust. J. Chem.* **20**, 1561 (1967).
19. Zielke, C.W. and Gorin, E., *Ind. and Eng. Chem.* **47**(4), 820 (1955).
20. Cao, J.R. and Back, M.H., *Carbon* **30**(6), 505 (1981).
21. Pan, Z.J. and Yang, R.T., *J. Catal.* **123**, 206 (1990).
22. Shaw, J.T., *Proc. Int. Conf. Coal Sci.*, Dusseldorf, Germany, 209 (1981).
23. Cao, J.R. and Back, M.H., *Carbon* **20**, 505 (1982).
24. Juntgen, H., *Carbon* **19**, 167 (1981).
25. Lizzio, A.A., Jiang, H., and Radovic, L.R., *Carbon* **28**, 7 (1990).
26. Huttinger, K.J. and Nill, J.S., *Carbon* **28**, 457 (1990).
27. Muhlen, H.J., Van Heek, H., and Juntgen H., *Fuel* **64**, 944 (1985).
28. Gardner, N., Samuels, E., and Wilkes, K., *ACS Div. In Chem.* **131**, 209 (1974).
29. Cypres, R., Ghodsi, M., and Feron, D., *Thermochemica Acta* **81**, 105 (1984).
30. Blackwood, J.D. and McCarthy, D.J., *Aust. J. Chem.* **20**, 2003 (1967).
31. Carangelo, R.M., Solomon, P.R., and Gerson, D.J., *Fuel* **66**, 960 (1987).
32. Hauge, R.H., et al., *ACS Div. Fuel Chem.* **28**(1), 35 (1983).
33. Walker, P.L. Jr., *Carbon* **28**, 261 (1990).

34. Phillips, R.F., Vastola, F.J., and Walker, P.L. Jr., *Carbon* **8**, 197 (1970).
35. Hart, P.J., Vastola, F.J., and Walker, P.L. Jr., *Carbon* **5**, 363 (1967).
36. Treptau, M.H. and Miller, D.J., *Carbon* **29**, 531 (1991).
37. Toomajian, M., Lussier, M., and Miller, D.J., *ACS Div. Fuel Chem. Prepr.* **36**(1), 139 (1991).
38. Zoheidi, H. and Miller, D.J., *Carbon* **25**, 809 (1987).
39. Saber, M.J., Falconer, J.L., and Brown, L.F., *Fuel* **65**, 1356 (1986).
40. Hashimoto, K., et al., *Chem. Lett.* **5**, 555 (1984).
41. Cao, J.R., and Back M.H., *Carbon* **23**, 141 (1985).
42. Wood, B.J. and Sancier, K.M., *Cata. Rev. Sci. Eng.* **26**, 233 (1984).
43. Yang, R.T. and Duan, R.Z., *Carbon* **23**(3), 325 (1985).
44. McKee, D.W. in '*Chemistry and Physics of Carbon*', Walker, P.L. Jr. and Thrower, P.A., ed. Marcel Dekker, New York, **61**(1) (1981).
45. Hermann, G. and Huttinger, K.J., *Carbon* **24**(6), 705 (1986).
46. Huttinger, K.J., *ACS Div. Fuel Chem. Prepr.* **34**(1), 56 (1989).
47. Huttinger, K.J., *Carbon* **26**(1), 79 (1988).
48. Giberson, R.C. and Walker, J.P., *Carbon* **3**, 521 (1966).
49. Montet, G.L., and Myers, G.E., *Carbon* **9**, 673 (1971).
50. Gadsby, J., Hinshelwood, C.N., and Sykes, K.W., *Proc. Royal Soc. London* **A187**, 129 (1946).
51. Long, F.J., and Sykes, K.W., *Proc. Royal Soc. London* **A193**, 377 (1948).

52. Blackwood, D.J. and McGrory, F., *Aust. J. Chem.* **11**, 16 (1958).
53. Lewis, W.K., Gilliland, E.R., and Hipkin, H., *Ind. Eng. Chem.* **45**, 1698 (1953).
54. Johnstone, H.F., Chen, C.Y., and Scott, D.S., *Ind. Eng. Chem.* **44**, 1564 (1952).
55. Chen, S.G. et al., *Ind. Eng. Chem. Res.* **32**, 2835 (1993).
56. Moulijn, J.A. and Kapteijn, F., *Carbon.* **33**, 8 (1995).
57. Goyal, A., Zabransky, R.F., and Rehmat, A., *Ind. Eng. Chem. Res.* **28**, 1767 (1989).
58. Ozaki, A., *Isotopic Studies of Heterogeneous Catalysis*, New York, Academic Press, Inc. (1977).
59. Melander, L. and Sanders, W.H., *Reaction Rates of Isotopic Molecules*, New York, John Wiley and Sons (1980).
60. Yates, J.T.Jr. and McKee, D.W., *J. Chem. Phys.* **75**, 2211, (1981).
61. Mims, C.A. and Pabst, J.K., *ACS Div. Fuel Chem. Prepr.* **25**(3), 263 (1980).
62. Gulbransen, E.A., *Nature* **212**, 1420 (1966).
63. Ishikawa, Y. et al., *Chem. and Phys. of Carbon* **12**, Walker, P.L.Jr. and Throver, P.A., ed., 40 (1975).
64. Kapteijn, F., Meijer, R., and Moulijn, J.A., *ACS Div. Fuel Chem. Prepr.* **36**(3), 906 (1991).
65. Biloen, P., *J. Molec. Catal.* **21**, 17 (1983).
66. Mims, C.A. et. al., *Surf. Sci. of Catal.* **15**, 230 (1992).
67. Laidler, K.J., *Chemical Kinetics*, New York, Harper Collins Inc., (1987).

68. Steinfeld, J.I., Francisco, J.S., and Hase, W.L., New Jersey, Prentice Hall, (1989).
69. Lide, D.R., *CRC Handbook of Chemistry and Physics 78*, New York, CRC Press, Inc., (1997).
70. Huber, K.P. and Herzberg, G., *Molecular Spectra and Molecular Structure IV, Constants of Diatomic Molecules*, New York, Van Nostrand Reinhold, (1979).
71. Zoheidi, H., *Ph.D. Dissertation*, Michigan State University, (1987).
72. Treptau, M.H., *Ph.D. Dissertation*, Michigan State University, (1989).
73. Toomajian, M.E., Lussier, M.G., and Miller, D.J., *Fuel 71*, 1055 (1992).
74. Lussier, M.L., *M.S. Theses*, Michigan State University, (1992).
75. Commercial Testing and Engineering Co., Lombard, IL (1990).
76. Galbraith Laboratories, Inc., Knoxville, TN (1995).
77. Saber, J.M., Falconer, J.L., and Brown, L.F., *J. Catal.* **90**, 65 (1984).
78. Ismail, I.M.K. and Walker, P.L.Jr., *Carbon 27*(4), 549 (1989).
79. Zhang, Z., *M.S. Theses*, Michigan State University, (1997).
80. Einar, S., Abrahamsson, S., and McLafferty, F.W., *Registry of Mass Spectral Data 1*, (1974).
81. Warren, B.E., *X-ray Diffraction*, Addison-Wesley Publishing Co., Reading, MA (1969).
82. McLachlan, D.Jr., *X-ray Crystal Structure*, McGraw-Hill Book Company, Inc., New York (1957).
83. Lee, H.H. *Heterogeneous Reactor Design*, Butterworth (1985).

84. Toomajian, M.E., *M.S. Thesis*, Michigan State University, (1991).
85. Weeda, M., Abcouwer, H.H., Kapteijn, M. and Moulijn, J.A., *Fuel Proc. Technol.*, **36**, 235 (1993).
86. Weeda, M., *Ph.D. Dissertation*, University of Amsterdam, (1995).
87. Lide, D.R., *CRC Handbook of Chem. And Phys.*, **75** (1995).
88. Takahashi et.al., *The Surface Energies of Graphite*, ref.#3, Abrahmson, J., 338.
89. Ubbelhode, A.R. and Lewis, F.A., *Graphite and Its Crystal Compounds*, Oxford University Press, London (1960).
90. Riley, H.L., *Chemistry and Industry*. **58**, 394 (1939).
91. Skokova, K. and Radovic, L.R., *ACS Div. Fuel Chem. Prepr.*, **41**(1), 143 (1996).

MICHIGAN STATE UNIV. LIBRARIES



31293017721170